

https://dspace.org/

Computational methods in string and field theory

Pontiggia, Luca Terzio

2018

https://hdl.handle.net/10539/25803

Pontiggia, Luca Terzio (2018) Computational methods in string and field theory, University of the Witwatersrand, Johannesburg, <http://hdl.handle.net/10539/25803>

Downloaded from a DSpace repository. https://dspace.org/

University of the Witwatersrand

Doctoral Thesis

Computational Methods in String and Field Theory

Author:
Luca Pontiggia

Supervisor:
Prof. Vishnu Jejjala



A thesis submitted in fulfillment of the requirements
for the degree of Doctor of Philosophy

in the

Faculty of Science

May 9, 2018

Declaration of Authorship

I, Luca Pontiggia, declare that this thesis titled, "Computational Methods in String and Field Theory" and the work presented in it are my own. I confirm that:

- This work was done wholly or mainly while in candidature for a research degree at the University of the Witwatersrand.
- Where any part of this thesis has previously been submitted for a degree or any other qualification at this University or any other institution, this has been clearly stated.
- Where I have consulted the published work of others, this is always clearly attributed.
- Where I have quoted from the work of others, the source is always given. With the exception of such quotations, this thesis is entirely my own work.
- I have acknowledged all main sources of help.
- Where the thesis is based on work done by myself, jointly with others, I have made clear exactly what was done by others and what I have contributed myself.

Signed:

_____

Date:

_____

UNIVERSITY OF THE WITWATERSRAND

Abstract

Faculty of Science

Doctor of Philosophy

Computational Methods in String and Field Theory

by Luca Pontiggia

Like any field or topic of research, significant advancements can be made with increasing computational power - string theory is no exception. In this thesis, an analysis is performed within three areas: Calabi–Yau manifolds, cosmological inflation and application of conformal field theory. Critical superstring theory is a ten dimensional theory. Four of the dimensions refer to the spacetime dimensions we see in nature. To account for the remaining six, Calabi-Yau manifolds are used. Knowing how the space of Calabi-Yau manifolds is distributed gives valuable insight into the compactification process. Using computational modeling and statistical analysis, previously unseen patterns of the distribution of the Hodge numbers are found. In particular, patterns in frequencies exhibit striking new patterns - pseudo-Voigt and Planckian distributions with high confidence and exact fits for many substructures. The patterns indicate typicality within the landscape of Calabi–Yau manifolds of various dimensions. Inflation describes the exponential expansion of the universe after the Big Bang. Finding a successful theory of inflation centres around building a potential of the inflationary field, such that it satisfies the slow-roll conditions. The numerous ways this can be done, coupled with the fact that each model is highly sensitive to initial conditions, means an analytic approach is often not feasible. To bypass this, a statistical analysis of a landscape of thousands of random single and multifield polynomial potentials is performed. Investigation of the single field case illustrates a window in which the potentials satisfy the slow-roll conditions. When there are two scalar fields, it is found that the probability depends on the choice of distribution for the coefficients. A uniform distribution yields a 0.05% probability of finding a suitable minimum in the random potential whereas a maximum entropy distribution yields a 0.1% probability. The benefit of developing computational tools extends into the interdisciplinary study between conformal field theory and the theory of how wildfires propagate. Using the two dimensional Ising model as a basis of inspiration, computational methods of analyzing how fires propagate provide a new tool set which aids in the process of both modeling large scale wildfires as well as describing the emergent scale invariant structure of these fires. By computing the two point and three point correlations of fire occurrences in particular regions within Botswana and Kazakhstan, it is shown that this proposed model gives excellent fits, with the model amplitude being directly proportional to the total burn area of a particular year.

Acknowledgements

I would like to thank my supervisor Prof. Vishnu Jejjala for being a supportive, understanding and always present supervisor. From a personal perspective, it has been, for the most part, stress free working under his supervision. His constant interest in my progress, as well as his ability to give me space has played a central role in enabling me to complete my Ph.D. Academically, I would like to thank him for his insight in choosing projects that both interest me, as well as develop me as an academic professional. In addition to Prof. Jejjala, I would like to thank Prof. Yang-Hui He, who worked with me on many of my collaborations. His input and positive feedback encouraged me and continuously motivated me to keep working hard. Acknowledgment needs to be given to Da Zhou and Yan Xiao, who are students of Prof. Yang-Hui He, for their contributions to some of the collaborations. I want to thank Prof. Kevin Goldstein and Sally Archibald for their input and especially Sally who provided the relevant data needed. I would like to thank my family - mom, dad and sister - for supporting me throughout my academic career, from my undergraduate days until now. They pushed me when I became complacent, and helped me appreciate and celebrate my achievements even when I thought nothing of them. Their love and care have shaped who I am, and who I will grow to become. My friends, for giving me the needed laughs, breaks and fun in various times of pressure. I would like to acknowledge the National Research Foundation, whose grant given to me via my supervisor, has funded me over the past three years. In addition, I want to acknowledge the University of the Witwatersrand, which has also funded me via Postgraduate Merit Award grants, and more generally, for providing an environment rich with diversity and a strong work ethic. This achievement of mine is shared among all those who have helped in their own small way. Lastly, I want to thank Vaughn Ho and Nicolette Stephens for proof reading and giving their editing suggestions regarding to this thesis.

List of Sources

Chapter 2 of this thesis was published in collaboration with Yang-Hui He and Vishnu Jejjala as:

Author : Y.H. He and V. Jejjala and L. Pontiggia

Title : Patterns in Calabi–Yau Distributions

Journal : Commun. Math. Phys.

Volume : 354

Year : 2017

Number : 2

Pages : 477-524

DOI : 10.1007/s00220-017-2907-9

Chapter 3 of this thesis has appeared in a preprint with collaborators Yang-Hui He, Vishnu Jejjala, Yan Xiao and Da Zhou as:

Author : Y.H. He, V. Jejjala, L. Pontiggia, Y. Xiao and D. Zhou

Title : Flatness of Minima in Random Inflationary Landscapes

Year : 2017

E-print : 1704.08351

Archive prefix : arXiv

Primary class : hep-th

Chapter 4 of this thesis was work done in collaboration with Sally Archibald, Kevin Goldstein and Vishnu Jejjala.

Contents

Declaration of Authorship iii

Abstract v

Acknowledgements vii

List of Sources ix

List of Figures xv

1 Introduction 1

1.1 Background - Calabi–Yau Manifolds . . . 5

1.1.1 Complex Manifolds . . . 6

1.1.1.1 Complex Structure . . . 7

1.1.1.2 Kähler Manifolds . . . 9

1.1.2 Cohomology . . . 10

1.1.2.1 Representatives . . . 13

1.1.2.2 Hodge-de Rham cohomology . . . 14

1.1.3 Homology . . . 15

1.1.4 Vector Bundles . . . 18

1.1.5 Calabi–Yau manifolds . . . 21

1.1.5.1 Complex 1 dimensional manifolds . . . 23

1.1.5.2 Complex 2 dimensional manifolds . . . 28

1.1.5.3 Complex 3 dimensional manifolds . . . 29

1.1.5.4 Complex Structure Moduli Space . . . 30

1.1.6 Reflexive Polytopes . . . 32

1.2 Background - Cosmological Inflation . . . 36

1.2.1 Inflation . . . 36

1.2.2 Random Slow-Roll Inflation - A Computational Approach . . . 40

1.2.2.1 Single Field inflation . . . 41

1.2.2.2 Multifield Inflation . . . 43

1.3 Background - Applied Conformal Field Theory . . . 46
1.3.1 Correlation functions . . . 47
1.3.1.1 Two point functions . . . 47
1.3.1.2 Three point functions . . . 48
1.3.1.3 Understanding what correlations show . . . 48

2 Patterns in Calabi–Yau Distributions 53
2.1 Introduction . . . 53
2.2 Calabi–Yau Threefolds . . . 56
2.2.1 Analysis of $h^{1,1} - h^{1,2}$ . . . 57
2.2.1.1 A Pseudo-Voigt Fit . . . 59
2.2.2 Analysis of $h^{1,1} + h^{1,2}$ . . . 67
2.2.2.1 A Planckian Fit . . . 67
2.2.3 The Distribution of the Euler Number . . . 73
2.2.4 Goodness-of-fit . . . 76
2.2.5 Implications for Physics . . . 81
2.3 Calabi–Yau Twofolds: K3 Surfaces . . . 82
2.4 Calabi–Yau Fourfolds . . . 84
2.5 Conclusions and Outlook . . . 86
2.6 Appendix . . . 88
2.6.1 Gamma distribution . . . 88
2.6.2 Supplementary plots for the $h^{1,1} - h^{1,2}$ distribution . . . 90
2.6.2.1 Plots for the odd distribution as counterparts to the even ones . . . 90
2.6.2.2 Comparative plots . . . 91
2.6.2.3 A first approximation to the data . . . 95
2.6.2.4 Table of parameter values and statistics . . . 97
2.6.3 Supplementary plots for the $h^{1,1} + h^{1,2}$ distribution . . . 100
2.6.3.1 Plots for the odd distribution as counterparts to the even ones . . . 100
2.6.3.2 Table of parameter values, coefficient values and statistics . . . 106
2.6.4 Supplementary plots for the fourfold data. . . . 107

3 Flatness of Minima in Random Inflationary Landscapes 109
3.1 Introduction . . . 109
3.2 Random potentials for inflation . . . 111
3.3 Single field models . . . 113
3.3.1 Behavior of slow-roll parameters . . . 115
3.3.1.1 $\beta \geq 0.7789$ . . . 116
3.3.1.2 $0.6021 \leq \beta < 0.7789$ . . . 116
3.3.1.3 $9/32 \leq \beta < 0.6021$ . . . 117
3.3.1.4 $1/4 < \beta < 9/32$ . . . 117
3.3.1.5 $0 < \beta \leq 1/4$ . . . 118
3.3.2 The window . . . 119
3.4 Multi-field models . . . 119

3.4.1 Slow-roll conditions for multi-field inflation . . . 120
3.4.2 Numerical tests . . . 121
3.4.2.1 Setup for numerics . . . 121
3.4.2.2 Numerical results . . . 123
3.5 Discussion and outlook . . . 126

4 New Tools in the Analysis of Large Scale Wildfires 129
4.1 Introduction . . . 129
4.2 Conformal field theory basics . . . 131
4.2.1 Two dimensional CFTs . . . 131
4.2.2 Correlation of Fire Occurrences . . . 133
4.2.3 Directional Correlations . . . 135
4.3 Results . . . 138
4.3.1 Sample Plots . . . 138
4.3.1.1 Botswana - 2002 . . . 141
4.3.1.2 Botswana - 2008 . . . 143
4.3.1.3 Kazakhstan - 2003 . . . 145
4.3.2 Error Estimates . . . 146
4.3.3 All variable values . . . 148
4.3.4 Comparison of Variables with Meteorological Data . . . 153
4.3.4.1 Botswana . . . 154
4.3.4.2 Kazakhstan . . . 157
4.3.5 Comments . . . 159
4.4 Conclusion . . . 161

Bibliography 163

List of Figures

1.1 *A representation of a complex four dimensional Calabi-Yau manifold [19].* . . . 5
1.2 *Parameterization of torus in the complex plane* . . . 24
1.3 *Finding complex moduli structure from homology cycles of a torus* . . . 24
1.4 *A lattice polygon in a plane with integer coordinates* . . . 32
1.5 *Lattice polygon Δ with 3 lattice points on the boundary.* . . . 33
1.6 *Polar lattice polygon Δ^0 with 9 lattice points on the boundary.* . . . 33
1.7 *Cosmic Microwave background captured from the PLANCK satellite* . . . 37
1.8 *Various polynomial functions different degrees* . . . 42
1.9 *Example of a multivariate polynomial functions* . . . 43
1.10 *Three grids each representing a different distribution* . . . 49
1.11 *The plots of average correlation for a given separation distance r* . . . 50

2.1 *Cumulative plots of Calabi–Yau threefolds as hypersurfaces in toric fourfolds.* . . . 55
2.2 *Plots of frequency vs $\frac{1}{2}\chi = h^{1,1} - h^{1,2}$ and $h^{1,1} + h^{1,2}$.* . . . 57
2.3 *Plots highlighting a difference between odd and even values for $h^{1,1} - h^{1,2}$ and $h^{1,1} + h^{1,2}$.* . . . 58
2.4 *Substructure within the distributions of $h^{1,1} - h^{1,2}$ identified by various r curves.* . . . 58
2.5 *Plots of frequency against $h^{1,1} - h^{1,2}$ for various odd values of r.* . . . 60
2.6 *Plots of frequency against $h^{1,1} - h^{1,2}$ for various even values of r.* . . . 61
2.7 *Deviation from the pseudo-Voigt model as values of r increase.* . . . 62
2.8 *Tail behaviour of pseudo-Voigt model over all frequencies.* . . . 63
2.9 *Performance of the model at specific cutoff frequencies.* . . . 64
2.10 *Relationship between variables for the pseudo-Voigt distribution of σ, b, α, A, a with r* . . . 66
2.11 *Three curves ($q = 0, 18, 30$) within the even $h^{1,1} + h^{1,2}$ distribution.* . . . 67
2.12 *Discovery of some subtle structure within the distribution of $h^{1,1} + h^{1,2}$* . . . 68
2.13 *Illustration of how regression curves can be divided into residue classes.* . . . 70
2.14 *The parameter plots are color coded according to what residue class their q value belong to.* . . . 72
2.15 *Example of how the Planckian model begins to break down at large even values of q* . . . 74
2.16 *Various plots illustrating the actual fit of the modified pseudo-Voigt model* . . . 76
2.17 *Using probability plots, we are able to statistically see which model provides the better fit.* . . . 80

2.18 *Probability plots of fitted theoretical Planck model.* . . . 81
2.19 *Using probability plots, we are able to statistically see which model provides the better fit* . . . 83
2.20 *The blue points correspond to manifolds with a mirror symmetric counterpart in the data set.* 84
2.21 *Frequency of Calabi–Yau fourfolds with a given Euler number.* . . . 85
2.22 *The frequency for all the Hodge $h^{i,j}$ numbers* . . . 86
2.23 *A comparison of the new Gamma distribution with the previous Planck distribution* . . . 89
2.24 *Three highlighted curves ($r = 41, 51, 67$) within the odd $h^{1,1} - h^{1,2}$ distribution.* . . . 90
2.25 *The plots of the various parameters A, σ, α, b, a versus r for odd values of r.* . . . 91
2.26 *Probability plot presents all the models analyzing the $h^{1,1} - h^{1,2}$ data.* . . . 95
2.27 *Best fit curve based on the pseudo-Voigt model for the same sets of curves as seen in Figure 2.5.* 96
2.28 *Best fit curve based on the pseudo-Voigt model for the same sets of curves as seen in Figure 2.6.* 97
2.29 *Showcase of the entire distribution modeled using our modified pseudo-Voigt model* . . . 98
2.30 *List of best fit coefficients for all even and odd curves.* . . . 99
2.31 *Number of data points left after increasing the cut off frequency to achieve a perfect fit.* . . . 100
2.32 *Three highlighted curves ($q = 3, 19, 31$) within the odd $h^{1,1} + h^{1,2}$ distribution.* . . . 101
2.33 *Discover some subtle structure within $h^{1,1} + h^{1,2}$ for odd values of q.* . . . 102
2.34 *Division of added structure for odd $h^{1,1} + h^{1,2}$ data into residue classes.* . . . 103
2.35 *The parameter plots are color coded according to what residue class their q value belong to.* . . . 105
2.36 *Break down of the Planck model for large odd q-values* . . . 105
2.37 *List of best fit coefficients for all even and odd q-curves* . . . 106
2.38 *Mirror symmetry is incomplete in the fourfold data set.* . . . 107

3.1 *Roots of $\frac{\partial f}{\partial y}$ and $\frac{\partial g}{\partial y}$.* . . . 116
3.2 *Shapes of $\bar{\epsilon}$ and $\bar{\eta}$ for $\beta \geq 0.7789$.* . . . 116
3.3 *Shapes of $\bar{\epsilon}$ and $\bar{\eta}$ for $0.6021 \leq \beta < 0.7789$.* . . . 117
3.4 *Shapes of $\bar{\epsilon}$ and $\bar{\eta}$ for $9/32 \leq \beta < 0.6021$.* . . . 117
3.5 *Graphs illustrating the local minimum and shapes of $\bar{\epsilon}$ and $\bar{\eta}$ for $1/4 < \beta < 9/32$.* . . . 118
3.6 *Graphs illustrating the local minimum and shapes of $\bar{\epsilon}$ and $\bar{\eta}$ for $0 < \beta < 1/4$* . . . 118
3.7 *The window that opens to non-trivial slow-roll potentials.* . . . 119
3.8 *Two of the 76 slow-roll potentials for the uniform distribution in Table 3.1* . . . 123
3.9 *Stack of all found potentials for both uniform and Gaussian distributions* . . . 125
3.10 *Distribution histogram for $\vec{a}$ and $\vec{b}$ coefficients drawn from uniform distribution.* . . . 126
3.11 *Distribution histogram for $\vec{a}$ and $\vec{b}$ coefficients drawn from Gaussian/Gamma distribution.* . . . 127

4.1 *Comparison of data grids between Ising model and fire occurrences* . . . 133
4.2 *Comparison of correlation functions between Ising model and that of the fire occurrences* . . . 134
4.3 *Comparison of three point correlation functions between Ising model fire occurrences* . . . 134
4.4 *Illustration of directional correlations on 2D grid* . . . 135
4.5 *Directional correlations highlight the different behaviours of the data at different angles.* . . . 135
4.6 *Sample difference in correlations along parallel and perpendicular directions* . . . 136
4.7 *Shape dependence on correlation function variables.* . . . 137
4.8 *Region of Botswana used for analysis* . . . 138
4.9 *Region of Kazakhstan used for analysis* . . . 139

4.10 *Overlay of region with fire occurrences for the year 2002.* . . . 141
4.11 *Two point correlation function analysis for 2002 using both formats in Botswana.* . . . 141
4.12 *Three point correlation function analysis for 2002 using both formats in Botswana.* . . . 141
4.13 *Directional correlation analysis for 2002 using both formats in Botswana.* . . . 142
4.14 *Overlay of region with fire occurrences for the year 2008.* . . . 143
4.15 *Two point correlation function analysis for 2008 using both formats in Botswana.* . . . 143
4.16 *Three point correlation function analysis for 2008 using both formats in Botswana.* . . . 143
4.17 *Directional correlation analysis for 2008 using both formats in Botswana.* . . . 144
4.18 *Overlay of region with fire occurrences for the year 2003.* . . . 145
4.19 *Two point correlation function analysis for 2003 using both formats in Kazakhstan.* . . . 145
4.20 *Three point correlation function analysis for 2003 using both formats in Kazakhstan.* . . . 145
4.21 *Directional correlation analysis for 2003 using both formats in Kazakhstan.* . . . 146
4.22 *Amplitude sampling statistics for both formats* . . . 147
4.23 *Amplitude sampling statistics for both formats.* . . . 147
4.24 *Exponent sampling statistics for both formats.* . . . 147
4.25 *Correlation length sampling statistics for both formats.* . . . 148
4.26 *Table summarizing all fitted variables relating to Botswana* . . . 148
4.27 *Table summarizing all fitted variables relating to Kazakhstan.* . . . 149
4.28 *Plots of amplitude with mean values - Botswana.* . . . 150
4.29 *Plots of amplitude with mean values - Kazakhstan.* . . . 150
4.30 *Plots of exponents with mean values - Botswana.* . . . 151
4.31 *Plots of exponents with mean values - Kazakhstan.* . . . 151
4.32 *Plots of correlation lengths with mean values - Botswana.* . . . 152
4.33 *Plots of correlation lengths with mean values - Kazakhstan.* . . . 152
4.34 *Weather comparison using the* $1/0$ *format for Botswana.* . . . 154
4.35 *Weather comparison using the* $1/-1$ *format for Botswana.* . . . 155
4.36 *Moving average weather comparison of both formats for Botswana.* . . . 156
4.37 *Weather comparison using the* $1/0$ *format for Kazakhstan.* . . . 157
4.38 *Weather comparison using the* $1/-1$ *format for Kazakhstan.* . . . 158
4.39 *Moving average weather comparison of both formats for Kazakhstan.* . . . 159
4.40 *Plots illustrating the relationship of amplitude with total burn area of Botswana and Kazakhstan.* 160

This Ph.D thesis is dedicated to the young child in me. Who; reading encyclopedias, tinkering with electronics and thinking up inventions, one day dreamed of becoming a scientist

Chapter 1

Introduction

The laws of electricity and magnetism were once regarded as separate. Faraday observed that changing magnetic fields produce electric fields. Maxwell then proved that magnetic and electric fields are intrinsically linked to one another. Maxwell's equations provided a unified theory of electricity, magnetism, and light, as well as all other types of electromagnetic radiation. The term unification implies that the different forces must obey the same set of equations. The pursuit to unify more and more fields of physics under a single system of equations has continued ever since.

With the unification of time and space, Einstein's theory of general relativity - describing gravity - began to deviate away from any kind of unification attempt with quantum mechanics - itself a well-established field of subatomic particles. The development of quantum field theory gave a relativistic quantum mechanical field description of electromagnetism and the weak and strong nuclear forces. As an example, the photon is an excitation of the electromagnetic field and the Higgs boson is an excitation of the Higgs field. This field excitation description of particles, also known as particle physics, is what led to the standard model - thus far, one of the most complete descriptions of nature. The standard model contains a classification of all elementary particles, divided into two main categories - fermions (quarks, antiquarks, leptons, antileptons) and bosons (gauge and scalar bosons).

Various attempts at unification of general relativity with the particle physics were unsuccessful. Resultant theories of such unification attempts typically all suffered the same problem of non-renormalizablity[1]. At loop level amplitudes involving gravitons - the force carrier for the gravitational interaction - become divergent. String theory, which is constructed by studying the dynamical behaviour of open or closed vibrating strings, says that particles arise as excitations of different modes of these strings. Because of this, the graviton arises naturally also as a closed string. The extended nature of strings mean string collisions no longer occur at a single point, but over a small, yet finite, distance. The combining of quantum mechanics and gravity thus becomes a viable one in the string theory framework. This allows a sensible argument for a particle which carries the gravitational force - something which cannot be done in quantum field theory. If string theory is to be a theory of quantum gravity, then the average size of a string should be somewhere near

the length scale of quantum gravity, called the Planck length, which is about 10^{-33} centimeters. Initially, string theory only included the description of bosons. However, since a true description of matter includes both bosons and fermions, fermionic string theory or superstring theory was developed [2, 3, 4, 5] . Superstring theory requires supersymmetry; meaning that every boson has a corresponding fermion partner. And so, supersymmetry relates the particles that transmit forces to the particles that make up matter. Through superstring theory, one gains an immediate and natural connection to particle physics - due to the presence of the same supersymmetry in the aforementioned Grand Unified Theories (GUTs) of the standard model. This provides compelling theoretical evidence that superstring theory could be a good mathematical model of nature at extremely small distances.

In its development through the years, string theory has found use in numerous settings: inflationary cosmology, standard model physics, black hole physics, and; due to its heavy mathematical formalism, even fields like number theory and group theory. Most recently, it has become a major field of interest due to a particular duality known as the anti-de Sitter/conformal field theory (AdS/CFT) correspondence proposed by Maldacena [6], through which solutions to previously intractable problems can now be calculated. At one time, it was believed there were five distinct superstring theories: type I, types IIA and IIB, and the two heterotic string theories. Only one of these theories, whose ten dimensional existence when compactified to four dimensions would match known physics, could be correct. It turns out that instead, all these theories are dual[1] to one another under certain conditions. The usefulness of certain dualities is that they link important physical concepts which were once thought to be completely separate and distinct, such as: strong/weak couplings or small/large distance scales [7, 8]. T-duality, for example, arises from the compactification of extra space dimensions in a ten dimensional superstring theory. The compactification process is used to reduce the $9+1$ dimensional (nine spatial, one temporal) space into a $3+1$ dimensional space. This compactification occurs when one of the nine spatial dimensions is compactifed into a circle of radius R, in such a way that traveling a distance $L = 2pR$, in the direction of compatification, results in the end point being the same as the starting point. Any particle which travels around this circle obtains a quantized momentum contributing to the total energy of that particle. A string, however, can wrap around the circle a number of times - this is known as the winding number, which is itself quantized. Interchaging the radius R of the circle with the the quantity l_{st}^2/R, where l_{st} is the string length, creates an interchangeability between particle momentum modes and string winding modes. Naturally making R much smaller than the string length, the quantity l_{st}^2/R will become extremely large. The important aspect is realizing that the interchange between momentum and winding modes means one is exchanging large distance scales with small distance ones. This kind of duality is unique to string theory as of course particles can not wrap themselves around a circle, and thus - if true, large and small distance scales in physics are not separated in a fixed manner, but rather, by the type of probe we use to measure distances, as well how we count the states of this probe.[2].

Ultimately, understanding the real world requires two pieces of data: cosmology and particle physics. It is known that cosmology invokes gravity, whereas, as we have seen, particle physics does not. This is where string theory attempts to unite these two theories into a unified framework. As mentioned previously, string theory is a ten dimensional theory - to describe the real world, we need to go from $9+1$ dimensions

[1] The dualties here are different in nature to the dualities mentioned by the AdS/CFT correspondence. They should not be thought of as related

[2] For a more in depth discussion see [9, 10, 11]

to $3+1$ dimensions. The mathematical setting in which we do the compactification of these dimensions is that of Calabi-Yau geometries [12, 13] . Compactification on a Calabi–Yau preserves four dimensional supersymmetry - an important requirement for superstring theory and particle physics, since it is believed to solve certain problems in particle physics, such as the hierarchy problem. Thus, the motivation in studying the structure of Calabi-Yau manifolds lies in the search for how to go from ten to four dimensions. On certain Calabi-Yaus, we can build supersymmetric standard models of particle physics. This gives us a nice framework where particle physics emerges from a string construction. In fact, the problem is that we can do this in so many ways that there is no unique path from Calabi-Yau manifolds to the real world - understanding the structure of Calabi-Yau geometries is a first step in solving this problem. There are certain properties of these manifolds which are of particular interest, one such being the Euler character χ. In heterotic compactification, this tells, for example, the number of generations in the low energy spectrum.By looking at the distribution of Calabi-Yaus within these potential models, which can be constructed from string theory, something more can be learned about particle physics.

The premise of trying to compactify the extra dimensions within string theory, is to realise our current "real world physics" from the added dimensions, as we live in a $3+1$ dimensional world. Settings like inflation allow for the exploration of how we can reconcile string theory with the real world. Inflation, on a classical level, was originally developed to address several issues in cosmology, the most important of which is the relative homogeneity of the observed universe and the evenness of the CMB temperature (horizon problem). Special relativity teaches us that the speed of light is the maximum velocity at which information can be conveyed. If we look at distant patches of the sky, the cosmic microwave background has the same temperature up to one part in 100000 - this despite the fact that light from one patch of the Universe could not have reached the other in the time elapsed since the Big Bang. In inflation, the Universe underwent a period of exponential expansion during the first 10^{-33} seconds of existence. Prior to inflation, the different patches of the sky were in causal contact with each other, and quantum fluctuations during the inflationary epoch are responsible for the existence of large scale structure in the Universe today.

Despite the speculation of whether string theory is a true theory of nature or not, it has undoubtedly broadened the solution space of opportunities within high energy physics, and for that matter, also mathematics. As the investigation of string theory expands into different sub-fields, so does the opportunity for new methods of analysis - borrowed from within these fields - become available, to enrich how we study string and, in general, field theories. In turn, analytic tools in field theories such as, conformal field theory, can have reach in other disciplines. Earth system scientists, who look to understand a the interaction between climate, vegetation and fire require complex models. Models such as that of Rothermal [14], can often be incredibly sophisticated and too computationally expensive. Instead of trying to describe the exact path of how a fire will spread, to some scientists it is more important to understand how fires burn over large areas across the world. One, common, emergent feature arising from studying extensive burn patterns of wildfires, is the presence of scale invariant structure. In the context of fire behaviour, tests for scale invariance require showing log behaviour in the number of fires versus size of these fires [15]. In physics, however, tools to study and describe scale invariant features in a theory are abundant. Conformal field theory (CFT) serves this purpose well as, in two dimensions, scale invariance of the CFT automatically fixes correlation functions. By computing correlation functions of the burn areas within a region and testing the behaviour of the data against an expected model, provided by CFT, one obtains a quantitative method to study scale invariant

features in the burning of wild fires.

In this thesis, I study the space of Calabi–Yau compactifications, parameters of multifield inflationary potentials, and the application of CFT methods to the propagation of fire within regions of ecological importance. My thesis is divided into five Chapters; Chapter 1 is an introduction to the motivation behind string theory as well as a minimal supplementation of body of knowledge for the topics explored in the thesis, mainly Calabi-Yau manifolds as well as cosmological inflation and applied conformal field theory. Since the aim is ease of legibility as well as the introduction of relevant topics, which create a minimal self-consistent reference of information presented in further Chapters, the overview is written in an informal lecture note style. Thus keeping away from extreme mathematical rigor - if required, the reader has relevant starting points where they can look for more in depth explanations. Chapters 2, 3 and 4 respectively contain research papers and work covered over the course of my Ph.D. Chapter 2 discusses how one obtains a new set of patterns within the distribution of Hodge numbers relating indirectly to the distribution of Calabi-Yau manifolds - something of high importance. Chapter 3 looks at the computation and statistical exploration of random polynomial potential inflationary models and their validity of true slow-roll inflationary models. Lastly, Chapter 4 uses techniques in conformal field theory to analyze data representing the spread of fire occurrences within the regions of Botswana and Kazakhstan, in the attempt to find a more realistic model of fire propagation.

1.1 Background - Calabi–Yau Manifolds

In 2012, the standard model was spectacularly vindicated through the discovery of the Higgs at the Large Hadron Collider [16]. The mass of the Higgs is 125 GeV. Because of the existence of gravity, the natural state of the ultraviolet cutoff is the Planck mass and the Higgs mass ought to acquire radiative corrections and be 10^{17} orders of magnitude more massive. The gauge hierarchy problem attempts to explain why the Higgs is light - see [17] for a review of the gauge hierarchy problem. One theoretical explanation is supersymmetry, which invokes the largest possible symmetries of a quantum field theory. Supersymmetry predicts that every particle in Nature has a superpartner. The effects of a particle and its superpartner in quantum field theory almost exactly cancel, which explains the lightness of the Higgs compared to the Planck scale. In order to realize supersymmetry in four dimensions in a heterotic string compactification, we need a $R^{3,1}$ Minkowski space and some compact manifold. We know that Minkowski space is flat, and thus preserving SUSY in $d = 4$ means that the compact manifolds needs to be Ricci flat. The simplest manifolds which admit the desired properties to preserve SUSY in four dimensions are called Calabi–Yau manifolds, and the term for reducing these six extra dimensions is compactification. Additionally, the fact that we have particle physics in four dimensions, places constrains on the type of scenarios we consider. In particular, because there are three generations of light particles in the standard model, the Calabi–Yau used for a natural compactification should have Euler character $\chi = \pm 6$, where $\chi = 2h^{1,1} - h^{1,2}$. Since $1/2$ of the Euler character is the number of light generations we require, it is the index for the Dirac operator. So far, precision measurements of the $1/r^2$ force of gravity have been made to an accuracy of tens of microns[18]. Thus, at least at these scales, we know for sure that the Universe is $3 + 1$ dimensional. Below this scale, however - say, less than a nanometer - a Calabi–Yau geometry is not necessarily excluded. Even more so, Calabi–Yau geometries at string scale are most certainly allowed.

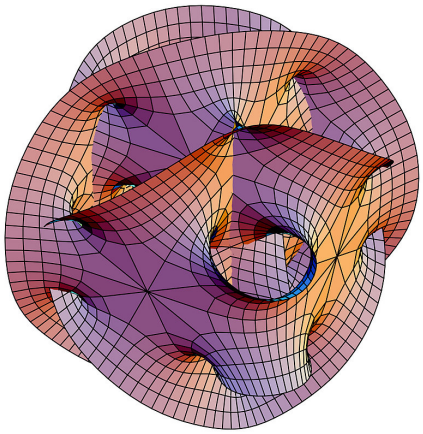


FIGURE 1.1: *A representation of a complex four dimensional Calabi-Yau manifold [19].*

One major problem, is that there are an extraordinarily large number of possible Calabi-Yau manifolds which satisfy the needed requirements. Thus, going about finding which are the "correct" manifolds to choose is a difficult task, and has thus far not been done. In such situations, classification methods can be

of extreme importance. This is the characterization of one particular class of Calabi-Yau manifolds whereby compactifications are done by characterization of reflexive polytopes. This is because reflexive polytopes are used to obtain Calabi-Yau geometries[20]. To do this, we can look at how many Calabi-Yau geometries have a given set of Hodge numbers $h^{1,1}$ and $h^{1,2}$. The weighting of the number of reflexive polytopes for different values of $h^{1,1}$(number of Kähler moduli which indicate the volume parameters of the of the Calabi–Yau) and $h^{1,2}$(number of complex moduli which indicate shape parameters of the Calabi-Yau) is given by the Kreuzer-Skarke data base. It is from this database where we can study the distribution of $h^{1,1}$ and $h^{1,2}$.

Although supersymmetry is a major part of string theory, for the scope of the thesis, the details are not too relevant. Much more important is the mathematics underlying Calabi-Yau manifolds as well as reflexive polytopes, which is quite extensive. What follows is a minimal introduction to a few concepts within differential geometry which are required to give a flavour of how we construct Calabi-Yau manifolds. We make use of the following sections to introduce certain key concepts which are then used as a tool in further sections. Material written in the following section was compiled from various lectures, online videos and text books on differentiable geometry. For more in depth discussion on related sections see [21, 22, 23, 24]

1.1.1 Complex Manifolds

In a 2d complex plane, we have that $z = x + iy$ and $\bar{z} = x - iy$, where x and iy are the real and imaginary coordinates respectively. Of particular interest, is a class of functions within the space of all smooth functions, which are dependent only on z. This then naturally gives us the differential equation:

$$\frac{\partial}{\partial \bar{z}} f(z) = 0.$$

Rewriting

$$\frac{\partial}{\partial z} = \frac{1}{2}\left(\frac{\partial}{\partial x} - i\frac{\partial}{\partial y}\right), \tag{1.1.1}$$

$$\frac{\partial}{\partial \bar{z}} = \frac{1}{2}\left(\frac{\partial}{\partial x} + i\frac{\partial}{\partial y}\right), \tag{1.1.2}$$

we are able to solve the differential equation to get what is called the Cauchy-Riemann relation. In particular if f is a holomorphic, then what we get is a **harmonic function**:

$$\nabla^2 f = 0. \tag{1.1.3}$$

Conversely, we can prove that a solution to the Laplace equation is a sum of a holomorphic function and its complex conjugate. Introducing complex coordinates on a manifold allows us to extend this notion to manifolds.

If the dimension of the manifold is odd, the generalization of the above is difficult as one cannot pair sets of real coordinates into a single complex coordinate. This gives us the requirement that $\dim\mathcal{M} = 2m$. One

might think the coordinate patches U_i on $\mathcal{M}$ get mapped to euclidean space with coordinates $(x^1, \dots x^{2m})$, such that we can pair $2m$ real coordinates into m complex coordinates :

$$z^1 = x^1 + ix^2 \tag{1.1.4}$$
$$z^2 = x^3 + ix^4 \tag{1.1.5}$$
$$\vdots \tag{1.1.6}$$
$$z^m = x^{2m-1} + ix^{2m}, \tag{1.1.7}$$

but this would be incorrect. Suppose we take another coordinate patch U_j, which maps its region to a region of the euclidean space with coordinates $y^1, \dots, y^{2m}$. Then, in the overlapping region $U_i \cap U_j$, there must exist a smooth transition function which takes the set of coordinates $(x^1, \dots, x^{2m})$ to $(y^1, \dots, y^{2m})$. There is however, no guarantee that such a transition function is holomorphic. What we do then, is to introduce another set of coordinates

$$w^1 = y^1 + iy^2 \tag{1.1.8}$$
$$w^2 = y^3 + iy^4 \tag{1.1.9}$$
$$\vdots \tag{1.1.10}$$
$$w^m = y^{2m-1} + iy^{2m}. \tag{1.1.11}$$

From the initial transformation, we get a set of smoth functions $y^i = y^i(x^i)$, therefore $w^i = w^i(x^1, x^2, \dots, x^{2m})$. In order for all coordinate transformations to be done holomorphically, we require that $w^i = w^i(z^1, z^2, \dots, z^{2m})$ not just be a smooth coordinate change, but also a holomorphic one. That is, the coordinate change does not depend on $\bar{z}$, but only on m z coordinates. From the initial discussion, we see that each transition functions satisfies some differential equation:

$$\frac{\partial}{\partial \bar{z}^i} w^j = 0 \; ; \quad i, j = 1, 2, \dots, m. \tag{1.1.12}$$

Similarly to defining a Riemannian manifold, having smooth transition functions is not good enough, one also needs to define a Riemannian structure - the addition of a metric tensor on the manifold. This added structure to the manifold then ensures we have a Riemannian manifold. Similarly then, since again there is no guarantee that, for an arbitrary given choice of coordinates, the transition functions will always be holomorphic. We need to add "complex structure" on the manifold. This will allow us to choose coordinates consistently such that the transition functions are always holomorphic.

1.1.1.1 Complex Structure

Just as a rank 2 metric tensor $g_{\mu\nu}(x)$ is used to impose Riemannian structure on a manifold, we can introduce a rank 2 tensor with mixed indices $J_\mu{}^\nu(x) \; ; \quad \mu, \nu = 1, \dots, 2m$. Moreover we require the following

$$J_\mu{}^\nu(x) J_\nu{}^\rho(x) = -\delta_\mu{}^\rho(x), \tag{1.1.13}$$

simply put $J^2 = -\mathbb{1}$. It is important to note that such a structure is not always possible - for example on a 4 dimensional sphere. However, a motivation for such a choice comes from the idea that in order to define a complex structure, one needs to introduce i whereby $i^2 = -1$, so that the tensor J mimics this property.

The tensor $J_\mu{}^\nu(x)$ is a $2m \times 2m$ matrix which gives a linear map on the tangent space $T_p\mathcal{M}$:

$$J : T_p\mathcal{M} \longmapsto T_p\mathcal{M}, \tag{1.1.14}$$

such that

$$v^\mu \longmapsto J_\mu{}^\nu v^\nu. \tag{1.1.15}$$

A question we may ask is: can this transformation on the tangent space be diagonalized? If J is indeed diagonalizable, then the eigenvalues should satisfy the same identity $J^2 = -\mathbb{1}$, implying it has eigenvalues i and $-i$. However, if the tangent space has real coefficients, i.e $v^\mu \in \mathbb{R}$ and the components of J are also real, then we cannot solve the equations:

$$Jv = iv \tag{1.1.16}$$

$$Jv' = -iv'. \tag{1.1.17}$$

Hence, we need to perform a complexification of the tangent space such that v^μ can take on complex numbers as well - doing so will allow us to solve the above equations. We denote the complexified tangent space as $T_p\mathcal{M}^{\mathbb{C}}$. This complex tangent space can be decomposed into an m dimensional space with eigenvalue i and an m dimensional space with eigenvalue $-i$:

$$T_p\mathcal{M}^{\mathbb{C}} = T_p\mathcal{M}^+ \oplus T_p\mathcal{M}^-.$$

We want to use this decomposition to guide us to a way of defining complex coordinates $z^i = (z^1 \ldots, z^m)$, allowing the associations :

$$T_p\mathcal{M}^+ \leftarrow \{\frac{\partial}{\partial z^i}\}, \tag{1.1.18}$$

$$T_p\mathcal{M}^- \leftarrow \{\frac{\partial}{\partial \bar{z}^i}\}, \tag{1.1.19}$$

$$\tag{1.1.20}$$

however this is not always possible. Only with certain conditions on J can the above be realised. J as it is defined, only gives us an "almost complex structure," it is necessary, but not complete. To obtain a complete complex structure on the manifold, we require $J_\mu{}^\nu$ to satisfy the following integrability condition:

$$0 = J_\mu{}^\nu \partial_\rho J_\sigma{}^\mu - J_\mu{}^\nu \partial_\sigma J_\rho{}^\mu - J_\sigma{}^\mu \partial_\mu J_\rho{}^\nu + J_\sigma{}^\mu \partial_\rho J_\mu{}^\nu. \tag{1.1.21}$$

It turns out if $J_\mu{}^\nu$ indeed satisfies the above differential equation, we can choose complex coordinates z^i such that:

$$J\left(\frac{\partial}{\partial z}\right) = i\left(\frac{\partial}{\partial z}\right), \tag{1.1.22}$$

$$J\left(\frac{\partial}{\partial \bar{z}}\right) = -i\left(\frac{\partial}{\partial \bar{z}}\right). \tag{1.1.23}$$

Writing $J_\mu{}^\nu$ in terms of these complex coordinates, we obtain:

$$J_i{}^j = i\ \delta_i{}^j \quad , \quad J_{\bar{i}}{}^{\bar{j}} = -i\ \delta_i{}^j \tag{1.1.24}$$

$$J_i{}^{\bar{j}} = 0 \quad , \quad J_{\bar{i}}{}^j = 0, \tag{1.1.25}$$

where the indices with and without the bars refer to the holomorphic and anti-holomorphic components. From this, we can now change from coordinates $(x^1, .., x^{2m})$ to complex coordinates $z^i = z^i(z^1, \ldots, z^{2m})$; $i : 1, \ldots, m$ using:

$$J_\mu{}^\nu \frac{\partial z^i}{\partial x^\nu}\frac{\partial x^m u}{\partial z^j} = i\ \delta_j{}^i, \tag{1.1.26}$$

$$J_\mu{}^\nu \frac{\partial \bar{z}^i}{\partial x^\nu}\frac{\partial x^m u}{\partial \bar{z}^j} = -i\ \delta_j{}^i, \tag{1.1.27}$$

$$J_\mu{}^\nu \frac{\partial z^i}{\partial x^\nu}\frac{\partial x^m u}{\partial \bar{z}^j} = 0, \tag{1.1.28}$$

$$J_\mu{}^\nu \frac{\partial \bar{z}^i}{\partial x^\nu}\frac{\partial x^m u}{\partial \bar{z}^j} = 0. \tag{1.1.29}$$

Solutions to these equations, which can only exist if $J_\mu{}^\nu$ satisfies (1.1.24), allow us to find complex coordinates which satisfy eqns. (1.1.22) and (1.1.23).

1.1.1.2 Kähler Manifolds

Typically in physics we deal with manifolds with both

1) $J_\mu{}^\nu$: **Complex structure**,

2) $g_{\mu\nu}$: **Riemannian metric**.

Manifolds which possess a compatibility condition between both their complex and Riemannian structure are called **Kähler Manifolds**. Essentially, Kähler Manifolds are just a special case of Hermitian manifolds. The compatibility conditions are as follows:

$$\nabla_\mu J_\rho{}^\nu = 0 \tag{1.1.30}$$

$$g_{\mu\nu}J^\mu{}_\rho J^\nu{}_\sigma = g_{\rho\sigma} \tag{1.1.31}$$

Assuming J satisfies the integrability condition given by eqn (1.1.21), we can write the compatibility conditions in terms of complex coordinates z^i ; $i - 1, .., m$. The metric $ds^2 = g_{\mu\nu}dx^\mu dx^\nu$ now looks like

$$ds^2 = 2g_{i\bar{j}}dz^i dz^{\bar{j}}, \tag{1.1.32}$$

with only mixed components being non zero, $g_{ij} = g_{\bar{i}\bar{j}} = 0$. It is convenient to introduce a 2-form, known as the **Kähler form** :

$$k = \frac{1}{2} g_{\mu\nu} J^{\mu}{}_{\rho} dx^{\rho} \wedge dx^{\nu} \tag{1.1.33}$$

$$= i g_{i\bar{j}} dz^{i} \wedge dz^{\bar{j}}. \tag{1.1.34}$$

It turns out this 2-form plays a central role in understanding properties of Kähler manifolds, hence its name. Using this Kähler form, we can rewrite the first compatibility condition as

$$dk = 0. \tag{1.1.35}$$

In component form this would be equivalent to

$$\partial_i g_{j\bar{k}} = \partial_j g_{i\bar{k}} \quad , \quad \partial_{\bar{j}} g_{i\bar{k}} = \partial_{\bar{k}} g_{i\bar{j}} \tag{1.1.36}$$

With these equations, we are able to obtain a very simple form of the metric which in turn simplifies many other formulas, like that of Riemann curvature. To understand what these equations mean. Consider a vector A_μ satisfying

$$\partial_\mu A_\nu - \partial_\nu A_\mu = 0. \tag{1.1.37}$$

We know that for a general manifold we can write $A_\mu = \partial_\mu \phi$, such that it satisfies (1.1.37) above. However, the converse is only true on a local coordinate patch, but not globally. The form of (1.1.36) is equivalent to that of (1.1.37), and so, locally one should be able to find some function $f_{\bar{k}}$, such that

$$g_{i\bar{k}} = \partial_i f_{\bar{k}}. \tag{1.1.38}$$

Because this holds for the complex conjugate case as well, we get that in each coordinate patch we can write

$$g_{i\bar{j}} = \partial_i \partial_{\bar{j}} K, \tag{1.1.39}$$

where K is called the **Kähler potential**. It is worthy to note that the Kähler potential is not actually a function on the manifold, otherwise the Kähler form would be exact implying that the Kähler form is actually trivial.

1.1.2 Cohomology

To start off the discussion, let's consider Maxwell's equations:

$$\nabla \cdot E = \frac{\rho}{\epsilon_0} \tag{1.1.40}$$

$$\nabla \cdot B = 0, \tag{1.1.41}$$

$$\nabla \times E = -\frac{\partial B}{dt}, \tag{1.1.42}$$

$$\nabla \times B = \mu_0 \left(J + \frac{\partial E}{dt} \right). \tag{1.1.43}$$

By introducing the antisymmetric four tensor, these can be written in a much more compact way:

$$F_{\mu\nu} = \begin{pmatrix} 0 & E_1 & E_2 & E_3 \\ E_1 & 0 & B_3 & -B_2 \\ E_2 & -B_3 & 0 & B_1 \\ E_3 & B_2 & -B_1 & 0 \end{pmatrix} \tag{1.1.44}$$

with

$$F_{\mu\nu} = -F_{\nu\mu}, \tag{1.1.45}$$

where $\mu, \nu = 0, 1, 2, 3$. Using this antisymmetric tensor, we can combine all the equations into two:

$$\partial_\mu F_{\nu\rho} - \partial_\nu F_{\mu\rho} = 0, \tag{1.1.46}$$

$$\partial^\mu F_{\mu\nu} = 4\pi j v. \tag{1.1.47}$$

In the language of differential forms, we can write Maxwell's equations in an even more compact way. Let us introduce the current $J = J_\mu dx^\mu$ and the 2-form F, which will be associated to the antisymmetric tensor in a natural way:

$$F = \frac{1}{2} F_{\mu\nu} dx^\mu \wedge dx^\nu, \tag{1.1.48}$$

then we can rewrite eqn (1.1.46) and eqn (1.1.47) as

$$dF = 0, \tag{1.1.49}$$

$$\delta F = 4\pi J. \tag{1.1.50}$$

We get $dF = 0$ since if we compute dF

$$dF = \partial_\mu F_{\nu\rho} dx^\mu \wedge dx^\nu \wedge dx^\rho, \tag{1.1.51}$$

the three wedge symbols guarantee that the three indices μ, ν, ρ are totally antisymmetrized and hence by virtue of (1.1.46) it vanishes.

From differential forms, we know that $d^2 = 0$, and so taking advantage of this, if $F = dA$, then of course $dF = 0$. This is similar to saying that since $\vec{\nabla} \cdot \vec{B} = 0$, we can have that $B = \vec{\nabla} \times \vec{A}$, where $\vec{A}$ is a vector

potential. In fact, by defining the 1- form

$$A = \phi dt + A_i dx^i \quad , i = 1, 2, 3, \tag{1.1.52}$$

we get that A_i is precisely this vector potential. Finally, we can then rewrite Maxwell's equations as

$$F = dA \tag{1.1.53}$$

$$\delta dA = 4\pi J. \tag{1.1.54}$$

There is however one redundancy in Maxwell's theory when using the vector potential as seen in (1.1.53); for a given A, we can always compute F, but for some F there is no unique A. To see this, just let

$$\widetilde{A} = A + d\lambda \tag{1.1.55}$$

then $d\widetilde{A} = A$ since $d^2\lambda = 0$ - this redundancy is known as a gauge symmetry of the theory.

It is important to note that only in Minkowski space do we have that $F = dA$. In general this is not true. How does one know when $F = dA$ holds on some general manifold? This is a question in cohomology. As the name suggests, cohomology is the dual to homology, which is in itself a more abstract concept better explained in the section following this one.

In summary, from the above, we learned that the first set of Maxwell's equations can be rewritten in the form given in eqn. (1.1.49) and (1.1.50). Furthermore, locally, these can always be solved by (1.1.53).
Using differential forms, we can generalize the above. Suppose the following :
ω is a closed k-form satisfying:

$$d\omega = 0.$$

From this, we can ask the question: if ω is a **closed from**, is it also an **exact from**? That is, can we write $\omega = d\lambda$, with λ being a $k-1$-form? Of course, if ω is already exact, then since $d^2 = 0$, ω is also closed. The converse question is, however not immediately as obvious. According to Poincare's Lemma, it turns out that on R^n a closed form is always exact. This also holds true on any manifold that can be continuously deformed to a point. For example, if we have a manifold, which we know to be covered by a family of U_i coordinates charts, then the image of each U_i being mapped into some subspace of $\mathbb{R}^n$ is always contractible. From this, with $d\omega$ being the differential form, it is always true that if we have a closed form, $d\omega = 0$ on a coordinate patch U_1 then it is also exact, $\omega = d\lambda$. Of course, some different coordinate patch U_2, $\omega = d\widetilde{\lambda}$, where λ and $\widetilde{\lambda}$ are not guaranteed to be the same on the overlapping region.
Ultimately, it is of great interest to know when a closed from is exact, and if it is not exact, to what degree of "non-exactness" it is. Cohomology thus enables us to distinguish which closed forms are not exact.

Let us introduce the space of closed forms Z^k as :

$$Z^k(\mathcal{M}) = \{\omega \in \mathbb{C}^k(\mathcal{M}) : d\omega = 0\}. \tag{1.1.56}$$

as well as

$$B^k(\mathcal{M}) = \{d\lambda : \lambda \in \mathbb{C}^{k-1}(\mathcal{M})\}. \tag{1.1.57}$$

these are both infinitely dimensional spaces, and for compact manifolds without a boundary, one finds that the difference of the two spaces is finite. So a definition of **cohomology** can be given as:

$$H^k(\mathcal{M}) = Z^k(\mathcal{M}) \Big/ B^k(\mathcal{M}). \tag{1.1.58}$$

Here, $H^k(\mathcal{M})$ consists of a closed differential form ω, however we can also have two differential forms ω, $\widetilde{\omega}$ which are equivalent if $\omega = \widetilde{\omega} + d\lambda$. In flat Minkowski space, such cohomology is trivial by Poincare's Lemma. Since $H^k(\mathcal{M})$ is a linear vector space, we can ask about its dimension b_k:

$$b_k = \dim H^k(\mathcal{M}). \tag{1.1.59}$$

These are also known as the Betti numbers. Under continuous deformations of a manifold $\mathcal{M}$, the Betti numbers remain topological invariants. In particular, the alternative sum of Betti numbers is called the Euler Characteristic:

$$\chi = b_0 - b_1 + b_2 - b_3 + ... \tag{1.1.60}$$

1.1.2.1 Representatives

Since cohomology can be considered as a set of equivalence classes, it is often useful to consider representatives of the class. By taking the quotient in (1.1.59) we divide $Z^k(\mathcal{M})$ into a set of subspaces. Each subspace consists of elements of Z^k which are related by B^k. Thus, we can consider equivalence classes of the differential form ω which are a subset of Z^k and are related to ω by the exact form:

$$[\omega] = \{\widetilde{\omega} : \widetilde{\omega} = \omega + d\lambda\}.$$

The question we can ask is: what is the representative of ω that represents all the k-forms which belong to equivalence class? It turns out, we can always choose a representative of the cohomology as a harmonic form.

Using the notation:

$$\Delta = d\delta + \delta d : C^k \to C^k,$$

if ω is closed, it is not necessarily true that $\Delta(d\omega) = 0$. However, we can always choose $\widetilde{\omega} = \omega + d\lambda$ such that $\widetilde{\omega}$ is harmonic, i.e. $\Delta\widetilde{\omega} = 0$. In other words if ω is closed then there exists an appropriate exact form such that we obtain an harmonic form. Conversely, if we require the harmonic condition, we find that we can fix the gauge degrees of freedom completely. That is, if $\omega + d\lambda$ and ω are both harmonic forms, we can show that the degrees of freedom become fixed by requiring $d\lambda = 0$[3].

Suppose we have compact and orientable manifold $\mathcal{M}$, a positive definite metric $g_{\mu\nu}$; then any $\omega \in C^k\mathcal{M}$

[3]Since this construction of harmonic forms requires a metric structure, in a Lorentzian space, such a construction would be very different.

can be written as:

$$\omega = d\lambda + \delta\widetilde{\lambda} + \omega_0, \tag{1.1.61}$$

where $d\lambda$ represents the closed form, $\delta\widetilde{\lambda}$ represents a co-closed form and ω_0 is just the harmonic form $\Delta\omega_0 = 0$. This decomposition of any form is known as the Hodge decomposition.

1.1.2.2 Hodge-de Rham cohomology

In de Rham cohomology we have that ω being a k-form is defined as:

$$C^k(\mathcal{M}) \ni \omega = \frac{1}{k!}\omega_{\mu_1,\ldots\mu_k} dx^{\mu_1} \wedge \ldots \wedge dx^{\mu_k}. \tag{1.1.62}$$

One can then consider space of closed forms modulo exact forms. In Hodge-de Rham cohomology we do a refinement of this structure. Where the basis $dx^{\mu_1} \wedge \ldots \wedge dx^{\mu_k}$ would be used to generate differential forms, now we have a basis made of complex coordinates dz^i and $dz^{\bar{i}}$. Important to note is that these coordinates do not mix under coordinate transformations. In other words, under a holomorphic coordinate transformation, a differential form $w_i dz^i$ will never mix with another differential from $\omega_{\bar{i}} dz^{\bar{i}}$. This means that we can decompose $k = p + q$, thus redefining C^k as:

$$C^{p,q}(\mathcal{M}). \tag{1.1.63}$$

Such a space will be generated by the basis $dz^{i_1} \wedge \ldots \wedge dz^{i_p} \ \wedge \ dz^{\bar{j}_1} \wedge \ldots \wedge dz^{\bar{j}_q}$. This creates what are called (p, q)-forms:

$$\omega = \frac{1}{p!q!}\omega_{\mu_{i_1\ldots i_p \bar{j}_1\ldots\bar{j}_q}} dz^{i_1} \wedge \ldots \wedge dz^{i_p} \ \wedge \ dz^{\bar{j}_1} \wedge \ldots \wedge dz^{\bar{j}_q}. \tag{1.1.64}$$

The important concept in cohomology is the exterior derivative operator

$$d = dx^\nu \frac{\partial}{\partial x^\mu}, \tag{1.1.65}$$

where together with it's conjugate the Hodge star $*$ and coderivative δ, we can map k-forms to either $(k+1)$-form, $(n-k)$-form or $(k-1)$-form respectively. In the context of complex manifolds, the natural decomposition of the two spaces extends to this definition of the exterior derivative

$$d = dz^i \frac{\partial}{\partial z^i} + dz^{\bar{i}} \frac{\partial}{\partial z^{\bar{i}}}, \tag{1.1.66}$$

$$d = \partial + \bar{\partial}. \tag{1.1.67}$$

With the mappings

$$\partial : C^{p,q} \longmapsto C^{p+1,q}, \tag{1.1.68}$$

$$\bar{\partial} : C^{p,q} \longmapsto C^{p,q+1} \tag{1.1.69}$$

$$\tag{1.1.70}$$

and

$$\partial^\dagger = - * \partial * : C^{p,q} \longmapsto C^{p-1,q}, \tag{1.1.71}$$

$$\bar{\partial}^\dagger = - * \bar{\partial} * : C^{p,q} \longmapsto C^{p,q-1}. \tag{1.1.72}$$

$$\tag{1.1.73}$$

The Laplace operator, previously defined as

$$\nabla = d\delta + \delta d \tag{1.1.74}$$

now becomes

$$\nabla = 2(\partial\partial^\dagger + \partial^\dagger\partial), \tag{1.1.75}$$

$$\text{or} \tag{1.1.76}$$

$$\nabla = 2(\bar{\partial}\bar{\partial}^\dagger + \bar{\partial}^\dagger\bar{\partial}). \tag{1.1.77}$$

With this Laplace operator on complex manifolds, we are able to find the representatives of the Hodge-de Rahm cohomology. Recall that in Section 1.1.2, the cohomology $H^k(\mathcal{M})$ was obtained by considering the space of solutions to $d\omega = 0$, where ω is a k-form, modulo $\omega \sim \omega + d\lambda$. In just the same manner, but using the new definition of d, we refine $H^k(\mathcal{M})$ to what is know as the Hodge-de Rahm cohomology

$$\bigoplus_{p+q=k} H^{p,q}(\mathcal{M}). \tag{1.1.78}$$

An example of a Hodge-de Rham cohomology element is an element of $C^{1,1}(\mathcal{M})$, say $\omega = \omega_{i\bar{j}} dz^i \wedge dz^j$. Then to get $H^{1,1}(\mathcal{M})$, all we look at is $d\omega = 0$. Such an example of ω is the Kähler form k as seen in eqn (1.1.34):

$$k = i g_{i\bar{j}} dz^i \wedge dz^j, \tag{1.1.79}$$

since k cannot be written as $k = d\Lambda$ - if the space is compact and without boundary then the volume form k^m of the space would be zero which is contradictory - we find that k has a non trivial element for $H^{1,1}(\mathcal{M})$.

1.1.3 Homology

Introducing an equivalence relation in the space of closed forms, namely the modulo exact form, allowed us to define a finite dimensional space $H^k(\mathcal{M})$ called cohomology. We will see that homologies are spaces which become dual to cohomology spaces.

Let K be a simplicial complex, where we can have **simplexes** σ of various dimensions. We want to decompose K into a p-simplex with $p = 1, ..., n = \dim(\mathcal{M})$. Each simplex can be introduced with some orientation and a given certain ordering - which for the examples below we assume clockwise. We can then denote $\sigma = \langle v_0, v_1, ..., v_p \rangle$. Putting a negative sign in front of σ switches the position of two vertices $\sigma = - \langle v_1, v_0, ..., v_p \rangle$. By considering all possible simplexes we obtain the space C_p, the vector space generated

by these simplexes. On the simplicial complex, the analogue of the exterior derivative is

$$\partial \ : \ \text{boundary opperator}, \tag{1.1.80}$$

defined when operating on p-simplex as

$$\partial \langle v_0, v_1, ..., v_p \rangle = \sum_{i=0}^{p} (-1)^i \langle v_0, ..\widehat{v_i}...v_p \rangle , \tag{1.1.81}$$

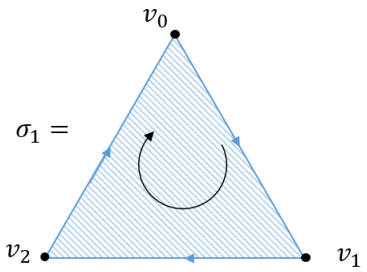
where the notation $\widehat{v_i}$ indicated we remove the ith vertex. This means

$$C_p \mapsto C_{p-1}. \tag{1.1.82}$$

To make this less abstract, consider first a single edge with two vertices

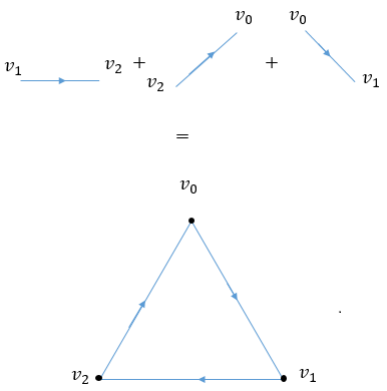


What we obtain from taking the boundary derivative of it is two points. They are however non zero, they are zero simplexes. Next, consider a triangle with some face:

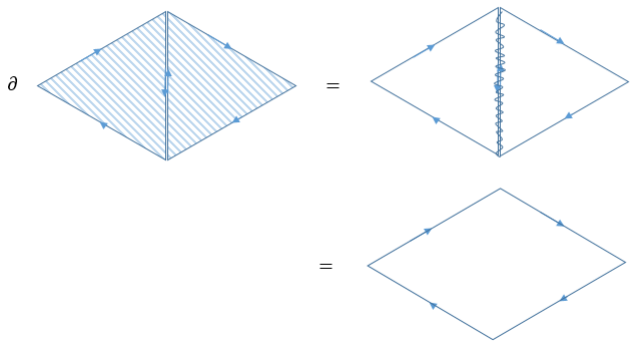


taking the boundary derivative of σ_1

$$\partial\sigma_1 = \langle v_1 v_2 \rangle - \langle v_0 v_2 \rangle + \langle v_0 v_1 \rangle \tag{1.1.83}$$



which leaves us with the boundary of the triangle only. Thus we see why ∂ in this context is called the boundary operator. A more complicated example is given by two of such triangles glued together, which diagrammatically looks like:



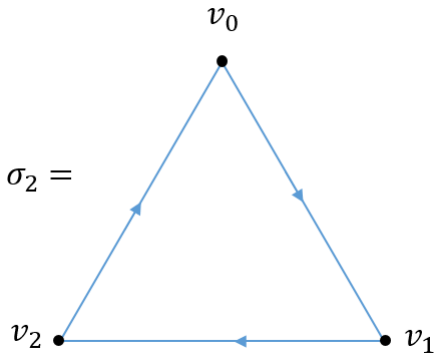
Since the two glued edges have opposing orientation, they cancel out, and we are left with a square boundary. One can show, that by acting on $\langle v_0, v_1, \ldots, v_p \rangle$ with ∂ twice and using it as defined in eqn. (1.1.81) the the boundary operator is nil-potent

$$\partial^2 = 0. \tag{1.1.84}$$

One can have edges with no face, and just a boundary. Such objects vanish with the boundary operator. We introduce the following

$$Z_p(K) = \{c \in C_p(K) : \partial c = 0\}, \tag{1.1.85}$$

which is a simplicial complex with no boundary - c vanishes when acting on it with ∂. Elements of $Z_p(K)$ are called cycles



We have

$$\partial\sigma_2 = \langle v_1 \rangle - \langle v_0 \rangle + \langle v_2 \rangle - \langle v_1 \rangle + \langle v_0 \rangle - \langle v_2 \rangle \tag{1.1.86}$$

$$= 0. \tag{1.1.87}$$

Here, all the end points cancel with each other resulting in the above cycle to have no boundary. There are some obvious cycles that one can think of, the space of such cycles is given by

$$B_{p(K)} = \{\partial C : C \in C_{p+1}\}. \tag{1.1.88}$$

This is obvious to some extent as when taking the boundary derivative of something with a boundary automatically results in something with no boundary. Here, $B_p(K)$ is a subspace of $Z_p(K)$. This is analogous to the discussion of de Rham Cohomology in section 1.1.2 where, there, we considered exact form and closed form and here, we consider cycles and boundaries. The homology is then defined to be

$$H_p(K) = Z_p(K) \setminus B_p(K). \tag{1.1.89}$$

One can then use triangulations of any topological space to find its homology. Sometimes, the distinction between homology with integer coefficients $H_p(M, \mathbb{Z})$ or real coefficients $H_p(M, \mathbb{R})$ is important as the former is better at "picking out topologies". Consider the group $SO(3)$, for example, which can also be thought of a S^3 sphere with the antipodal point identified. This means that as we pick a point in one hemisphere we automatically pick its antipodal point on the other hemisphere. Implying that only one of the hemispheres really needs to be considered. Such a space has the homology

$$H_1(SO(3), \mathbb{Z}) = \mathbb{Z}_2, \tag{1.1.90}$$

where $\mathbb{Z}_2 = \{0, 1\}$ is known as the torsion. It is the element of homology which corresponds to some finite group which, when looking looking at the real coefficient case, we get

$$H_1(SO(3), \mathbb{R}) = 0. \tag{1.1.91}$$

The non trivial element $\mathbb{Z}_2$ can only be seen with integer coefficients. By contrast, for H_0 one finds that

$$H_0(SO(3), \mathbb{Z}) = \mathbb{Z} \tag{1.1.92}$$

$$H_1(SO(3), \mathbb{R}) = \mathbb{R}. \tag{1.1.93}$$

1.1.4 Vector Bundles

One can define the tangent vector space as a space of vectors $v^\mu \frac{\partial}{\partial x^\mu}$ which lie tangent to a point p on the manifold. One can take this idea further by considering a collection of points p^i on the manifold. The group of all such tangent spaces will form what is called a vector bundle. Formally, this is written as

$$TM = \bigcup_{p \in \mathcal{M}} T_p M. \tag{1.1.94}$$

We can obtain a better understanding of the tangent bundle by introducing coordinates. To specify a point in the **tangent bundle**, we need a coordinate pair (x^μ, v^μ), where x^μ determines the location of point p, and the v^μ characterizes the vector in $T_p(\mathcal{M})$. In this construction, one sees that the tangent bundle is itself a special kind of manifold - with coordinates, (x^μ, v^ν). When specifying coordinates, one also specifies how coordinates transform from one patch to another. The coordinates on the tangent bundle are inherited

from coordinates on the base manifold. Suppose on this base manifold $\mathcal{M}$ two coordinate patches, U_i with coordinates x and U_j with coordinates $\widetilde{x}$, have an overlapping region. The transition functions then would be

$$\widetilde{x}^\mu = \widetilde{x}^\mu(x). \tag{1.1.95}$$

Since the tangent vector depends on the coordinate x^μ we have:

$$\widetilde{v}^\mu \frac{\partial}{\partial \widetilde{x}^\mu} = v^\nu \frac{\partial}{\partial x^\nu}. \tag{1.1.96}$$

From this follows that:

$$\widetilde{v}^\mu = \frac{\partial \widetilde{x}^\mu}{\partial x^\nu} v^\nu. \tag{1.1.97}$$

Thus, overlapping regions on the base manifold results in a pair of coordinates (x^μ, v^μ) and $(\widetilde{x}^\mu, \widetilde{v}^\mu)$ which themselves are overlapping - their tangent spaces are overlapping. We now have a well defined transition between these coordinates, namely eqns: (1.1.95) and (1.1.97). This notion can be generalized for not only tangent spaces, but also vector spaces. The resultant of such a generalization gives us the vector bundle E.

At each point p of the manifold $\mathcal{M}$ we have a vector space. Where in the case of tangent space, we have locally a direct product over each coordinate patch of the coordinate x of the base manifold and tangent space:

$$U_i \times \mathbb{R}^n. \tag{1.1.98}$$

Similarly, suppose we have coordinate patch U_i of $\mathcal{M}$, then the vector bundle E looks like:

$$U_i \times V, \tag{1.1.99}$$

where V is some vector space. In order to clearly express the notion of having a vector space at each point p we make use of the following definition:

E is a **vector bundle** if it satisfies the following;

- There is a projection map, $\pi : E \to \mathcal{M}$, so that for each point $p \in \mathcal{M}$ the inverse map $\pi^{-1}(p)$ is isomorphic to a vector space V
- We can choose an atlas of E so that for each local coordinate chart U, the coordinates of E is given by the pair (x, v) - where x are coordinates over U and $v \in V$.

Over each point p we have a vector space which is isomorphic to V, $p = \pi^{-1}(p)$. This vector space is called a **fiber** over p. The vector space can have either real coefficients - real vector bundle - or complex coefficients - complex vector bundle. In particular, a one-dimensional complex fiber is referred to as a **line bundle**.

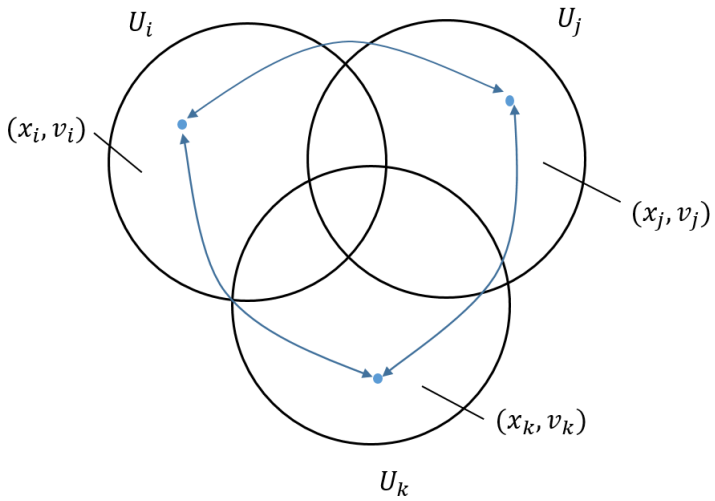
In the case of the tangent bundle, the way the coordinates on the base manifold transform, tells us how the coordinates on the tangent bundle transform. On the vector bundle, such information needs to be specified independently. Suppose we have a manifold $\mathcal{M}$, with coordinates (x, v) on U_i and $(\widetilde{x}, \widetilde{v})$ on U_j.

Just as before $\widetilde{x}^\mu = \widetilde{x}^\mu(x)$[4], however now we have to specify how the fiber coordinates transform. We do so by stipulating that it should depend on some linear transformation of v

$$\widetilde{v} = g(x)v, \tag{1.1.100}$$

where, in the case of a real vector bundle, $g(x) \in GL(N, \mathbb{R})$ with $N = \dim V$. In the case of tangent bundles, the linear transformation $g(x)$ was just $g = \frac{\partial \widetilde{x}^\mu}{\partial x^\nu}$. For vector bundles $g(x)$ will be something else in general. One needs to be careful however, as it is not always possible to choose a $g(x)$ in an arbitrary manner. To define a vector bundle consistently, it is necessary and sufficient to satisfy the following condition.

- Choose three overlapping coordinate patches U_i, U_j, U_k as seen below



  Then we have two different ways of comparing coordinates from say U_i with U_k. Either we go from U_i to U_k directly which results in

$$v_k = g_{k,i}(x)v_i \tag{1.1.101}$$

  or we can go via U_j giving:

$$v_k = g_{k,j}(x)v_j = g_{k,j}g_{j,i}(x)(x)v_i.$$

  All of these transformations have to be compatible in order to have a consistent coordinate system. This gives us the following consistency condition, or what is known as the **co-cycle condition**

$$g_{k,i} = g_{k,j}g_{j,i}. \tag{1.1.102}$$

For tangent bundles, we can easily check, for example, that indeed the transition function $g = \frac{\partial \widetilde{x}^\mu}{\partial x^\nu}$ obeys the co-cycle condition. In a more general vector bundle, there is no guarantee that this condition is always satisfied. Thus, the existence of a transition function $g(x)$ which satisfies the co-cycle condition defines a unique vector bundle on the manifold. We can go a step further in the generalization process and define a **fiber bundle**. Some common examples, which are important in the study of Calabi–Yaus are holomorphic

[4]If we are dealing with a differentiable manifold the transformation is a smooth function, for a complex manifold it is a holomorphic function.

vector bundles and holomorphic line bundles. If the total space E has the structure of a complex manifold, the projection map which we called π is a holomorphic map of complex manifolds and the map

$$\phi_U : \pi^{-1}(U) \to U \times \mathbb{C}, \tag{1.1.103}$$

is biholomorphic, then E can be considered to be a holomorphic vector bundles. An example of such is the **trivial bundle**, written as in eqn (1.1.98),

$$\mathcal{M} \times \mathbb{C}^k, \tag{1.1.104}$$

but with manifold $\mathcal{M}$. A holomorphic line bundle exists instead when the fiber of the holomorphic vector bundle is $\mathbb{C}$ with rank one. An important example is the **canonical bundle**.

More specifically it is the complex vector bundle $K_{\mathcal{M}} = \Lambda^{m,0}\mathcal{M}$, that is, its sections are $(m, 0)$-forms on a complex manifold which is called the canonical bundle, or also the holomorphic line bundle. We can also say that the canonical bundle is the determinant line bundle of the holomorphic cotangent bundle, in other words, it is the highest antisymmetric tensor product of the holomorphic cotangent bundle. See [21] for a more in depth review of holomorphic fiber bundles as well as other definitions.

1.1.5 Calabi–Yau manifolds

A Calabi-Yau manifold, $\mathcal{M}_{CY}$, is a manifold with a specific set of properties associated with it. Simply put, one can build a Calabi-Yau manifold by imposing certain restrictions:

1 **It is complex** -
With complex manifolds, by choosing *holomorphic* numbers as the coordinates, $\{\mathbb{C}^n(z_1, \ldots, z_n)|z_i \in \mathbb{C}\}$, the coordinate transformations can be carried out in a holomorphic fashion.

2 **It is Kähler** -
The Kähler part is (1), compatible with the aforementioned complex structure and (2), the holomorphic-holomorphic components of the metric vanish

$$g_{ij} = g_{\bar{i}\bar{j}} = 0, \tag{1.1.105}$$

where the bar represents the *anti-holomorphic* components. As a result all that remains are the mixed components of the metric $g_{i\bar{j}}$ such that:

$$g_{i\bar{j}} = \partial_i \bar{\partial}_j K. \tag{1.1.106}$$

Where K is called the Kähler potential[5]

3 **It has vanishing Ricci curvature** -
We can think of the zero Ricci curvature condition,

$$R_{i\bar{j}} = 0, \tag{1.1.107}$$

[5]In this definition, it is not globally defined. If it were, the volume of the *compact manifold* would become zero, rendering the manifold incompatible with the requirement that the *Riemannian metric* be *positive definite*. Due to this, the Kähler potential is only defined on *coordinate patches*.

as a sort of vacuum Einstein equation, with the Calabi-Yau manifold behaving like the solution to the Einstein vacuum equation, whereby the solution must adhere to the condition that the manifold be Kähler.

A result of $\mathcal{M}$ being Kähler is that the Ricci tensor has the form

$$R_{i\bar{j}} = \partial_i \partial_{\bar{j}} \log(\det g), \tag{1.1.108}$$

hence, if we further add that $\mathcal{M}$ is Calabi-Yau, then from condition 3:

$$\partial_i \partial_{\bar{j}} \log(\det g) = 0. \tag{1.1.109}$$

Whenever we have a function of the above structure - two derivatives equaling zero for any combination of coordinates - we are able to express the function as a sum of a holomorphic function and its complex conjugate

$$\log(\det g) = f(x) + \bar{f}(\bar{x}), \tag{1.1.110}$$

$$\det g = \Omega(x)\bar{\Omega}(\bar{x}), \tag{1.1.111}$$

where Ω is a locally defined function. The left hand side of equation (1.1.111) transforms like a determinate of a metric, and so a (n, n)-form - n - totally symmetric holomorphic indices and n totally antisymmetric anti-holomorphic indices. Under a coordinate transformation, if we have an n-form, it should transform properly - n holomorphic indices transform holomorphically and n anti-holomorphic indices transform anti-holomorphically. This implies $\Omega(x)$ should be holomorphic and $\bar{\Omega}(\bar{x})$ should be anti-holomorphic. If we require, for any coordinate patch, the holomorphic and anti-holomorphic properties be compatible with coordinate transformations, the holomorphic part of the transition functions must belong to the holomorphic part $\Omega(x)$. Likewise the anti-holomorphic part of the transition functions must belong to the anti-holomorphic part $\bar{\Omega}(\bar{x})$, otherwise, as stated above, $\Omega(x)\bar{\Omega}(\bar{x})$ will be incompatible with the coordinate transformations. This means that

$$\Omega(x) \text{ is a } (n, 0)\text{-form}, \tag{1.1.112}$$

$$\bar{\Omega}(\bar{x}) \text{ is a } (0, n)\text{-form}, \tag{1.1.113}$$

$$\tag{1.1.114}$$

furthermore, since it is equal to the determinate of the metric which is positive, Ω cannot be zero anywhere on the manifold $\mathcal{M}$. In summary, if $R_{i\bar{j}} = 0 \Rightarrow \exists\ \Omega$ an $(n, 0)$-form which satisfies two conditions:

- It is holomorphic, $\bar{\partial}\Omega = 0$,
- $\Omega \neq 0$ anywhere.

This then gives us another yet equivalent restriction:

4 **The first Chern class of a Calabi-Yau manifold** M **must vanish**. It was conjectured by Calabi and later proven by Yau, that the converse of the above result is also true, that is, if there exists a globally defined holomorphic $(n, 0)$-form which is everywhere non-zero, then there exists a Ricci flat Kähler metric.

The **Chern class** is defined as

$$\det\left(1+\frac{i}{2\pi}F\right), \tag{1.1.115}$$

where $F = dA + A \wedge A$. When X is a matrix one can use the relation $\det X = e^{\mathrm{tr}(\log X)}$, to expand (1.1.115) as

$$e^{\left(\mathrm{tr}(\log\left(1+\frac{i}{2\pi}F\right)F\right)} = c_0 + c_1 + c_2 + ... \tag{1.1.116}$$

where here, $c_i \in H^{2i}(\mathcal{M})$. These are called the Chern classes. More explicitly:

$$c_0 = 1 \tag{1.1.117}$$

$$c_1 = \frac{i}{2\pi}\mathrm{tr}F \tag{1.1.118}$$

$$c_2 = \frac{1}{2}\left(\frac{i}{2\pi}\right)^2 (\mathrm{tr}F \wedge \mathrm{tr}F - \mathrm{tr}(F \wedge F)) \tag{1.1.119}$$

$$\vdots$$

By requiring $c_1 = 0$, we require the vanishing of the first Chern class.

One more requirement, using the language of bundles is that

5 **The complex manifold $\mathcal{M}$ has a trivial canonical bundle** - The presence of a globally defined non-vanishing holomorphic $(n, 0)$-form Ω as seen in (1.1.112) means triviality of the canonical bundle is automatically satisfied.

And so, manifolds which satisfy all the above properties are called Calabi-Yau manifolds. In searching for Calabi-Yau manifolds, what we look for are solutions to the kinds of non-linear partial differential equations given by inserting $g_{i\bar{j}} = \partial_i \bar{\partial}_j K$ into equation (1.1.111). Yau showed that integrability of such differential equations and uniqueness of such solutions is guaranteed.

1.1.5.1 Complex 1 dimensional manifolds

To gain an intuitive understanding of these objects as well as to cover a few more concepts, we look at a few examples of Calabi-Yau manifolds.

1D Complex Torus

We begin by looking at a complex one dimensional - real two dimensional - torus parametrized by:

$$T^2 = \mathbb{C}/\mathbb{Z} + \tau\mathbb{Z} \tag{1.1.120}$$

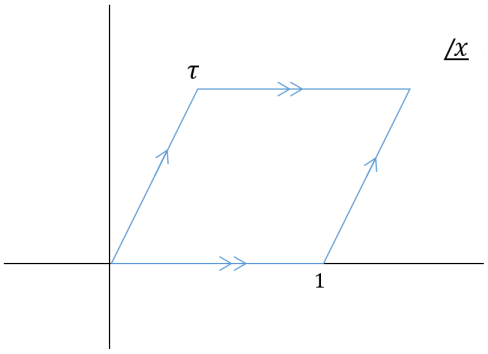


FIGURE 1.2: *Consider the coordinates* (x^1, x^2) *in the complex* x *plane, we can periodically identify them by allowing them to shift by some integer* m *and* k*, such that* $(x^1, x^2) \sim (x^1 + m, x^2 + k)$ *where* $m, k \in \mathbb{Z}$ *The coordinates* x^1, x^2 *are real, and so we can consider some complex combination* $x = x^1 + \tau x^2$*. This periodic identification turns out to be tangent to the periodic identification of* (1.1.120) *by shift of* $\mathbb{Z}$ *and by a shift of* $\tau\mathbb{Z}$*.*

From Figure 1.2, τ parametrizes the shape of torus, τ is called the **complex structure modulus**. In the context of Calabi–Yau manifolds, this complex structure moduli must have a holomorphic $(n, 0)$-form. In this case with $n = 1$, the holomorphic $(1, 0)$ - form Ω is dx:

$$\Omega = dx^1 + \tau dx^2. \tag{1.1.121}$$

It turns out we can extract the complex structure moduli by integrating dx over the homology cycles (Figure 1.3) of the Calabi–Yau manifold - in this case again, the torus.

$$\int_\alpha \Omega = 1 \quad , \quad \int_\beta \Omega = \tau. \tag{1.1.122}$$

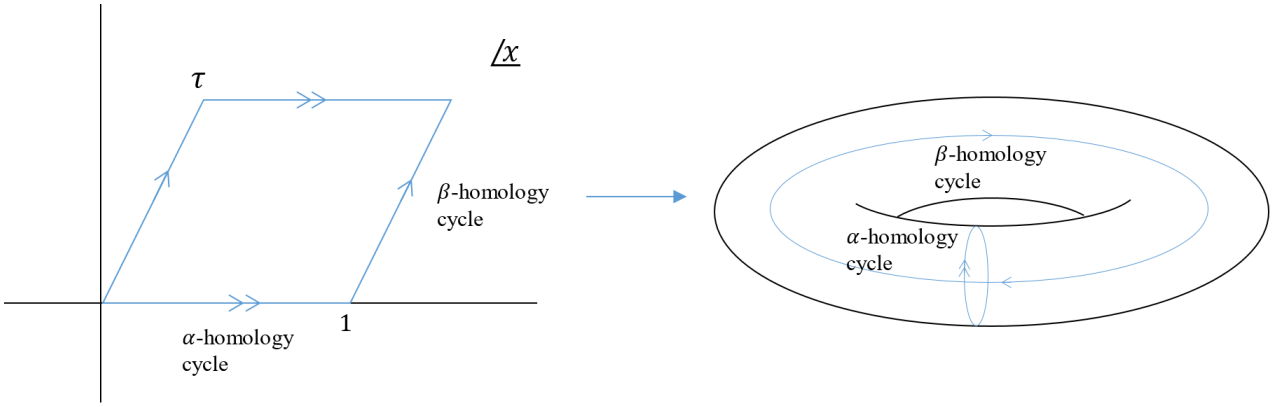


FIGURE 1.3: *We see the two positive* ***homology cycles*** α *and* β*. Integrating the holomorphic* $(1, 0)$*-form* Ω *over these two cycles, along the torus, enables us to find the complex structure moduli* τ*.*

Although, in this example it may seem trivial, extracting the complex structure moduli in this manner it is a general feature which can be applied to higher dimensional Calabi-Yau manifolds.

Since we are dealing with complex manifolds, one can make use of the Hodge-de Rham cohomology

$$H^{p,q} = \{w \in \Omega^{p,q} : dw = 0\} \diagup d\lambda, \tag{1.1.123}$$

where the dimension of the Hodge-de Rham cohomology $H^{p,q}$ is given by the **Hodge number** $h^{p,q}$. In our complex 1 dimensional torus example, there are only four Hodge numbers, as we are dealing with a $(1,0)$-form. Since for a torus, $H^{p,q}$ is spanned by $dx_{i_1} \wedge \cdots \wedge dx_{i_p} \wedge d\bar{x}_{j_1} \wedge \cdots \wedge d\bar{x}_{j_q}$

$$h^{p,q} = \binom{n}{p}\binom{n}{q}, \tag{1.1.124}$$

so that, we have

$$h^{0,0} = \binom{1}{0}\binom{1}{0} = 1 \tag{1.1.125}$$

$$h^{1,0} = \binom{1}{1}\binom{1}{0} = dx = 1 \tag{1.1.126}$$

$$h^{0,1} = \binom{1}{1}\binom{1}{0} = d\bar{x} = 1 \tag{1.1.127}$$

$$h^{1,1} = \binom{1}{1}\binom{1}{1} = dx \wedge d\bar{x} = 1 \quad \text{this is the volume of the one form} \tag{1.1.128}$$

$$\tag{1.1.129}$$

Typically the Hodge numbers are displayed simultaneously in what is called the Hodge diamond.

$$\begin{array}{ccccc} & & h^{0,0} & & \\ & h^{1,0} & & h^{0,1} & \\ & & h^{1,1} & & \end{array} = \begin{array}{ccccc} & & 1 & & \\ & 1 & & 1 & \\ & & 1 & & \end{array} \tag{1.1.130}$$

To paramterize the torus, in addition to the complex structure moduli τ, we need the area of the torus. Suppose we try a metric on the space

$$g_{i\bar{j}} = dx^i dx^{\bar{j}} = dx d\bar{x} \tag{1.1.131}$$

$$= dx^1 dx^1 + 2\mathrm{Re}(\tau dx^1 dx^2) + |\tau|^2 dx^2 dx^2, \tag{1.1.132}$$

where $x = x^1 + \tau x^2$. Next, one can rescale the metric by normalizing the area to one. To do this we multiply the metric by $\frac{r}{\mathrm{Im}(\tau)}$:

$$g_{i\bar{j}} = \frac{r}{\mathrm{Im}(\tau)} \left(dx^1 dx^1 + 2\mathrm{Re}(\tau dx^1 dx^2) + |\tau|^2 dx^2 dx^2 \right), \tag{1.1.133}$$

where r is now an additional parameter to measure the size of the manifold - here the torus. Substituting the form of the metric in (1.1.133) into the standard form of the Kähler form:

$$k = \frac{i}{2} g_{i\bar{j}} dx^i dx^{\bar{j}}, \tag{1.1.134}$$

$$= r dx^1 \wedge dx^2, \tag{1.1.135}$$

we see that r parametrizes the Kähler form. In general the Kähler form is a a linear combination of elements

of $h^{1,1}$. Here however, $h^{1,1}$ is one dimensional - another reason for the presence of only one parameter. And so, the parameter r is called the **Kähler class**.

We see that the geometry of the torus is thus parametrized by two parameters, the complex structure τ and the Kähler class r. This is not a unique feature of this one dimensional complex torus. In general, Calabi-Yau manifolds are parametrized by a complex structure and Kähler form. In fact, part of Yau's theorem says that if we specify complex structure moduli and Kähler class, then there is one and only one metric that is Kähler and satisfies the Ricci flatness condition. The moduli space of Calabi-Yau manifolds is thus referring to the various Kähler class and complex structure of Calabi-Yau manifolds.

It turns out that the torus has this moduli property that transforming τ by the following

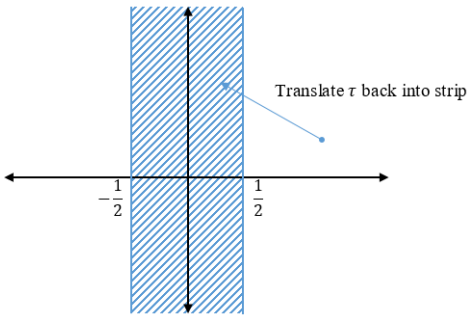
$$\tau \to \frac{a\tau + b}{c\tau + d} \; ; \; \begin{pmatrix} a & b \\ c & d \end{pmatrix} \in \mathrm{SL}(2, \mathbb{Z}), \tag{1.1.136}$$

we get the same complex structure. In particular the $SL(2, \mathbb{Z})$ structure is generated from two transformations

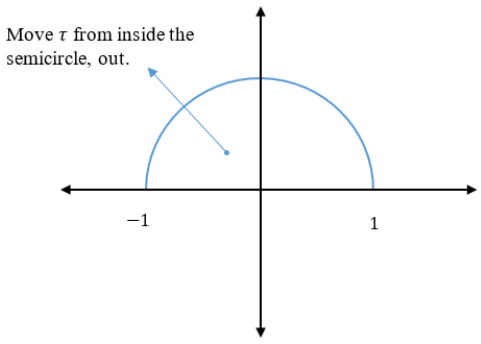
$$\tau \to \tau + 1, \tag{1.1.137}$$

$$\tau \to -\frac{1}{\tau} \tag{1.1.138}$$

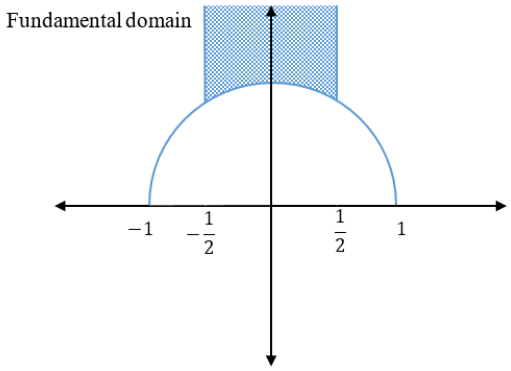
The first one means we can restrict between a band such that any τ outside the band can be translated back into it.



The second transformation means that any τ inside the semicircle of radius 1 can be moved outside.



The combined effect of these transformations allows us to restrict τ to what is called a **fundamental domain**.



We can use the combination of $\mathrm{SL}(2,\mathbb{Z})$ transformation to map points in the band, to any other point in the upper half complex plain - we can also show that this is a minimum space for which such transformations can be done, hence the term fundamental domain. The space of the complex structure moduli is given by the upper half complex plane (H), which one denotes as $\mathrm{H}\Big/\mathrm{SL}(2,\mathbb{Z})$. What about the space of Kähler moduli? It turns out that if we consider string theory, then the Kähler class is naturally complexified by introducing natural real parameters t, θ such that

$$t = ir + \theta. \tag{1.1.139}$$

The moduli space of r has exactly the same structure of that of the original τ, i.e. $\mathrm{H}\Big/\mathrm{SL}(2,\mathbb{Z})$. The total moduli space can thus be written as the tensor product between the two moduli spaces. in order to specify the geometry of the complex one dimensional torus, we have to specify τ and r.

$$\mathrm{H}\Big/\mathrm{SL}(2,\mathbb{Z}) \;\otimes\; \mathrm{H}\Big/\mathrm{SL}(2,\mathbb{Z}), \tag{1.1.140}$$

where, H is the same as the group $\mathrm{SL}(2,\mathbb{R})\Big/\mathrm{U}(1)$. As a group manifold, $\mathrm{SL}(2,\mathbb{R})$ does not have a positive metric. It is an indefinite metric space with one negative direction and two positive directions. By taking taking the quotient of $\mathrm{SL}(2,\mathbb{R})$ with the action of U(1), we achieve a positive definite space, thus making it equivalent to the upper half plane. Another observation to make is that $\mathrm{SL}(2,\mathbb{R}) \otimes \mathrm{SL}(2,\mathbb{R}) = O(2,2)$. $O(4)$ is the group of linear transformations which preserves the $4d$ euclidean space with euclidean signature flat metric

$$O(4) \Longleftarrow (dx^1)^2 + (dx^2)^2) + (dx^3)^2 + (dx^4)^2. \tag{1.1.141}$$

$O(2,2)$ is similar, but with two negative signs

$$O(2,2) \Longleftarrow (dx^1)^2 + (dx^2)^2) - (dx^3)^2 - (dx^4)^2. \tag{1.1.142}$$

Hence, $O(2,2)$ is the orthogonal group acting on the space with signature (2,2). Combining all the above, and noting that U(1) is the same as O(2), the total moduli space can be expressed as

$$\mathrm{H}\Big/\mathrm{SL}(2,\mathbb{Z}) \;\otimes\; \mathrm{H}\Big/\mathrm{SL}(2,\mathbb{Z}) \qquad = O(2,2:\mathbb{Z})\Big\backslash O(2,2:\mathbb{R})\Big/O(2)\times O(2).$$

What is interesting, is that this kind of structure actually persists for higher dimensional torus' as well as complex two dimensional Calabi-Yau manifolds.

1.1.5.2 Complex 2 dimensional manifolds

In the case of compact Calabi-Yau manifolds there are only two classes:

1. Two complex (4 real) dimensional torus T^4. In this case the Hodge diamond looks like

$$\begin{array}{ccccc} & & h^{0,0} & & \\ & h^{1,0} & & h^{0,1} & \\ h^{2,0} & & h^{1,1} & & h^{0,2} \\ & h^{2,1} & & h^{1,2} & \\ & & h^{2,2} & & \end{array} = \begin{array}{ccccc} & & 1 & & \\ & 2 & & 2 & \\ 1 & & 4 & & 1 \\ & 2 & & 2 & \\ & & 1 & & \end{array} \tag{1.1.143}$$

   One can also check that the Euler characteristic is zero as

$$\chi = \sum (1)^{p-q} h^{p,q} = 0. \tag{1.1.144}$$

   With regards to the moduli space, the Hodge number $h^{1,1}$ is of most interest as, in the complex $2d$ case, it gives both the number of complex and Kähler moduli parameters. For the T^4 there are thus in total 8 complex dimension moduli spaces parametrizing the size and shape of the torus. This forms the coset

$$O(4,4:\mathbb{Z}) \Big\backslash O(4,4:\mathbb{R}) \Big/ O(4) \times O(4) \,. \tag{1.1.145}$$

   In general for a D-dimensional torus T^D then the moduli space is

$$O(D,D:\mathbb{Z}) \Big\backslash O(D,D:\mathbb{R}) \Big/ O(D) \times O(D) \,. \tag{1.1.146}$$

2. The more interesting case comes from the non-flat Calabi-Yau manifold known as the $K3$ surface. This is in fact the only non-flat compact Calabi-Yau manifold in the 2 complex dimensional case. For the $K3$ surface the Hodge diamond is given by

$$h^{p,q} = \begin{array}{ccccc} & & 1 & & \\ & 0 & & 0 & \\ 1 & & 20 & & 1 \\ & 0 & & 0 & \\ & & 1 & & \end{array} \tag{1.1.147}$$

   From this we see that $\chi = 24$. Topologically all $K3$ surfaces belong to the same moduli space (mapable to each other via certain deformations of the Kähler class), this is why we say there is only one such case. Since $h^{1,0} = 0$, we say that it contains no isometries. In a classic mathematical context, we can consider the moduli space of $K3$ to be real, however with string theory, where we want to complexify

the moduli space, one then obtains the space of complex moduli together with the space of complexified Kähler moduli given by

$$O(20,4:\mathbb{Z})\Big\backslash O(20,4:\mathbb{R})\Big/O(20)\times O(4)\cdot$$

Here the dimension of the moduli space is $(20\times 2)+(20\times 2)=80$. One example of a $K3$ surface is to look at a polynomial equation on a generalized projective space - this reduces its dimension. $\mathbb{C}P^3$ is one such example. This is just the space of four complex numbers (z_1,z_2,z_3,z_4) then rescaled with $\lambda\in\mathbb{C}$ such that the quotient space is the same as $\mathbb{C}P^3$. Next, consider a homogeneous polynomial, $P(z)$ of degree d, i.e

$$P(\lambda z)=z^d P(z). \tag{1.1.148}$$

We require homogeneity since we want to impose the condition that

$$P(z)=0, \tag{1.1.149}$$

irrespective of the scaling λ. One can show that the first Chern class is given by:

$$C_1\sim(d-4)C_1(\mathbb{C}P^3). \tag{1.1.150}$$

In fact, for the space described by $P(z)=0$ to be Calabi-Yau, the first Chern class has to vanish, and thus $d=4$. Take as a simple example

$$P(z)=(z_1)^4+(z_2)^4+(z_3)^4+(z_4)^4. \tag{1.1.151}$$

The resultant space of solutions can be shown to be Ricci flat and Kähler. Of course, this is just one example, but as stated previously all other examples of $K3$ surfaces share the exact same moduli space.

1.1.5.3 Complex 3 dimensional manifolds

Of bigger interest, is the three complex dimensional example, or the Calabi-Yau three fold. In string theory one compactifies 10 dimensions to 4, thus requiring 6 real dimensions, or 3 complex dimensions. In such a case, the Hodge diamond is

$$h^{p,q}=\begin{array}{ccccccc} & & & 1 & & & \\ & & 0 & & 0 & & \\ & 0 & & h^{1,1} & & 0 & \\ 1 & & h^{2,1} & & h^{1,2} & & 1 \\ & 0 & & h^{2,2} & & 0 & \\ & & 0 & & 0 & & \\ & & & 1 & & & \end{array} \tag{1.1.152}$$

The zeros are there to ensure one is not dealing with a torus, or a product of torus with $K3$. From the Poincare duality, we also have

$$h^{1,1} = h^{2,2}, \tag{1.1.153}$$
$$h^{1,2} = h^{2,1}. \tag{1.1.154}$$

This gives only two independent Hodge numbers, $h^{1,1}$ and $h^{1,2}$. The Euler characteristic is given by

$$\chi = 2(h^{1,1} - h^{1,2}). \tag{1.1.155}$$

In general for Calabi-Yau n fold, CY_n, $h^{n-1,1}$ gives the complex structure and $h^{1,1}$ gives the Kähler class.

1.1.5.4 Complex Structure Moduli Space

In the same way as the CY_1, where we were used a $(1,0)$-form to describe the complex structure moduli space $\mathcal{M}_C$, we can use a holomorphic $(3,0)$-form Ω for the CY_3, with

$$\bar{\partial}\Omega = 0.$$

This holomorphic $(3,0)$-form is not unique. Multiplication of Ω by any complex number gives another holomorphic $(3,0)$-form which is also just as good a candidate to describe the complex structure moduli space. This means that for each point on a Calabi-Yau manifold, there exists a family of parameters of holomorphic $(3,0)$-forms. Thus, for each point in the moduli space of a specific Calabi-Yau manifold we have one complex parameter space. It is as if we have a complex line bundle. This gives a natural notion of metric on the line bundle

$$\|\Omega\|^2 = i\int_{\mathcal{M}_{CY}} \Omega \wedge \bar{\Omega}. \tag{1.1.156}$$

From (1.1.111) we saw that the above is just equal to the determinate of the metric - volume of the Calabi-Yau space. This allows us to define

$$K = \log\|\Omega\|^2. \tag{1.1.157}$$

It turns out this complex moduli space is itself a Kähler manifold, with the K above being its Kähler potential. This i, $\mathcal{M}_{CY}$ has a metric

$$G_{ab} = \partial_a\partial_{\bar{b}}K \ , a, b = 1, ..., h^{1,2}. \tag{1.1.158}$$

To paramaterize the complex structure moduli space, we use *flat coordinates* on $\mathcal{M}_{CY}$. We choose the basis $\{\alpha_I, \beta^I\}_{I=0,1,...,h^{1,2}}$ of the homology 3-cycle, $H_3(\mathcal{M}_{CY})$, with dimension

$$\dim H_3 = h^{3,0} + h^{2,1} + h^{1,2} + h^{3,0}, \tag{1.1.159}$$
$$= 2(1 + h^{2,1}), \tag{1.1.160}$$

since $h^{3,0} = h^{0,3} = 1$ and $h^{2,1} = h^{1,2}$. We choose the basis such that $\alpha_I \cap \alpha_J = 0$ and $\beta_I \cap \beta_J = 0$ but

$\alpha_I \cap \beta_J = \delta_I{}^J$. This is just a higher dimensional realization done in the complex 1 dimensional torus, where we can see the α and β cycles over the torus with α and β intersecting only once. These are known as a symplectic basis. We can now compute

$$X^I = \int_\alpha \Omega, \tag{1.1.161}$$

$$F^I = \int_\beta \Omega. \tag{1.1.162}$$

However, this gives us a redundant amount complex moduli. It should just be given by $h^{2,1}$ from $2(1+h^{2,1})$. To reduce this, we introduce

$$t^a = \frac{X^a}{X^0},\ a = 1, .., h^{2,1}, \tag{1.1.163}$$

where h^0 is just one of the directions of α_I and the ratio is to remove an ambiguity when rescaling Ω. It is these choice of t^a which are called flat coordinates. F_I is now also determined by X_I or these flat coordinates, in other words it is a homogeneous function of X:

$$F_I = F_I(X). \tag{1.1.164}$$

It can be shown that

$$F_I = \frac{\partial}{\partial X^I} F(X). \tag{1.1.165}$$

This single function $F(X)$ is one of the most important functions when understanding the structure of the complex moduli space of a Calabi–Yau space. If we know $F(X)$, not only will the relation between X^I and F_I be known, but also the metric can be computed. Typically, $F(X)$ is called the **pre-potential**. The exact relation between $F(X)$ and the metric G_{ab} can be seen by the following

$$\|\Omega\|^2 = i \int_{\mathcal{M}_{CY}} \Omega \wedge \bar{\Omega} \tag{1.1.166}$$

$$= \sum_I \int_{\alpha_I} \Omega \int_{\beta^I} \bar{\Omega} - \int_{\beta^I} \Omega \int_{\alpha_I} \bar{\Omega} \tag{1.1.167}$$

$$= \sum_I X^I \bar{F}_I - \bar{X}^I F_I, \tag{1.1.168}$$

$$\tag{1.1.169}$$

where the decomposition is given by the Riemann bi-linear identities. Since

$$G_{ab} = \partial_a \partial_{\bar{b}} \log \|\Omega\|^2, \tag{1.1.170}$$

we see how $F(X)$ can be used to determine the metric.

1.1.6 Reflexive Polytopes

When studying Calabi-Yau manifolds, there is a particular interest at looking at the complex and Kähler moduli of the Calabi–Yau manifold which is denoted $\mathcal{X}_6$. Reason being, there exists Calabi-Yau manifolds which arise in paired or mirror families with dual geometric properties to some other set of Calabi-Yau manifolds [25]. How complex structure is varied in one family should compare to how Kähler structure is varied in the other family. The concept of mirror symmetry stems from the fact that the geometrical properties of two families $\mathcal{X}_6$ and $\mathcal{X}_6^o$ yield two equivalent physical theories[26]. The study of the mathematical consequences of such a duality, is what we refer to as mirror symmetry. Consider a complex one dimensional torus (see Section 1.1.5.1), the geometry of the torus is parametrized by two parameters, the complex structure τ and the Kähler class r. This is not a unique feature of a one dimensional complex torus. As was shown, in general, Calabi-Yau manifolds are parametrized by a complex structure and Kähler form. The moduli space of Calabi-Yau manifolds is thus referring to the various Kähler class and complex structure of Calabi-Yau manifolds.

An insight by Baytrev was that mirror families of Calabi-Yau manifolds can be described using combinatorial objects called reflexive polytopes [20]. Consider a lattice polygon:

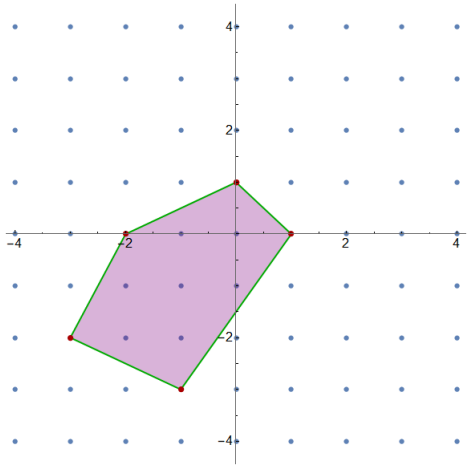


FIGURE 1.4: *We call the collection of integer coordinate points in the plane a lattice N. A lattice polygon is a polygon with vertices on these integer coordinate points.*

A polygon is reflexive if it contains if the single lattice point in its interior is the origin. We can describe a reflexive polygon by listing the vertices and equations of each edge line. Let M be another copy of the integer lattice. The dot product allows the pairing of points in N with points in M:

$$(n_1 \cdot n_2) \cdot (m_1 \cdot m_2) = n_1 m_2 + n_2 m_2. \tag{1.1.171}$$

If we call the lattice polygon in N which contains the point $(0, 0)$ Δ, then the polar polygon Δ^o, is the polygon in M that is given by:

$$\{(m_1, m_2) : (n_1 \cdot n_2) \cdot (m_1 \cdot m_2) \geq -1 \quad \forall \quad (n_1, n_2) \in \Delta\}. \tag{1.1.172}$$

For example, consider Figure 1.5 below:

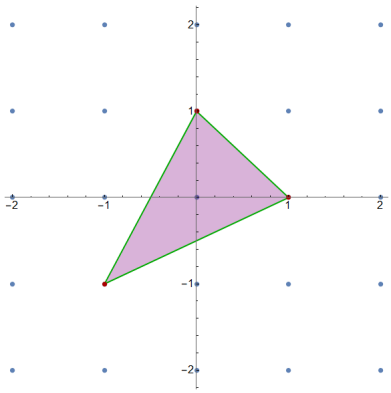


FIGURE 1.5: *Lattice polygon Δ with 3 lattice points on the boundary.*

by first finding the vertex coordinates, the equations of the edges become:

$$-x - y = -1, \tag{1.1.173}$$
$$2x - y = -1, \tag{1.1.174}$$
$$-x + 2y = -1. \tag{1.1.175}$$

To find the polar lattice polygon, we use (1.1.172). This then gives us:

$$(x \cdot y) \cdot (-1, -1) = -1, \tag{1.1.176}$$
$$(x \cdot y) \cdot (2, -1) = -1, \tag{1.1.177}$$
$$(x \cdot y) \cdot (-1, 2) = -1, \tag{1.1.178}$$

who's edge equations describe the new polar lattice polygon Δ^o in Figure 1.6 below

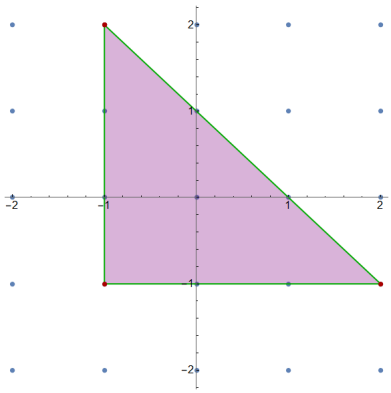


FIGURE 1.6: *Polar lattice polygon Δ^0 with 9 lattice points on the boundary.*

This is to show that if Δ is a reflexive polygon, then Δ^o is also reflexive,

$$(\Delta^o)^o = \Delta, \tag{1.1.179}$$

so Δ and Δ^o are said to be a mirror pair.

Extending this concept to higher dimensions, if we have a vector $\{\vec{v}_1, \vec{v}_2, \ldots, \vec{v}_q\}$ be a set of points in $\mathbb{R}^k$, the polytope with vertices $\{\vec{v}_1, \vec{v}_2, \ldots, \vec{v}_q\}$ is the convex hull of these points. If we let N be the lattice of points with integer coordinates in $\mathbb{R}^k$, a lattice polytope has vertices in N. Similarly, if we have the dual lattice M and a dot product

$$(n_1, \ldots, n_k) \cdot (m_1, \ldots, m_k) = n_1 m_2 + \ldots + n_k m_k, \tag{1.1.180}$$

then we can define the polar polytope Δ^o as:

$$\{(m_1, \ldots, m_k) : (n_1, \ldots, n_k) \cdot (m_1, \ldots, m_k) \geq -1 \quad \forall \quad (n_1, \ldots, n_k) \in \Delta\}. \tag{1.1.181}$$

This lattice polytope is said to be reflexive if Δ^o is also reflexive, in which case, Δ and Δ^o are mirror pairs.

It turns out that polytopes can be translated to polynomials [20, 27]. This can be done in the following manner:

- Associate the z_i^{th} complex variable with the ith standard basis vector in the lattice N;

$$(1, 0, \ldots, 0) \leftrightarrow z_1 \tag{1.1.182}$$
$$(0, 1, \ldots, 0) \leftrightarrow z_2 \tag{1.1.183}$$
$$\vdots$$
$$(0, 0, \ldots, 1) \leftrightarrow z_n. \tag{1.1.184}$$

- For each lattice point within the polar polytope Δ^o, one can define a monomial using

$$(m_1, \ldots, m_k) \leftrightarrow {}_{Z_1}(1, 0, \ldots, 0) \cdot (m_1, \ldots, m_k)_{Z_2}(0, 1, \ldots, 0) \cdot (m_1, \ldots, m_k) \ldots {}_{Z_k}(0, 0, \ldots, 1) \cdot (m_1, \ldots, m_k). \tag{1.1.185}$$

- Multiply each monomial by a complex parameter α_j, and add up the monomials. This gives us a family of polynomials parametrized by the α_j.

For continuation of the examples, the Laurent polynomials for the polygon shapes in Figure 1.6 are of the form given by:

$$\alpha_1 z_1^{-1} z_2^2 + \alpha_2 z_1^{-1} z_2 + \alpha_3 z_2 + \alpha_4 z_1^{-1} + \alpha_5 + \alpha_6 z_1 + \alpha_7 z_1^{-1} z_2^{-1} + \alpha_8 z_2^{-1} + \alpha_9 z_1 z_2^{-2} \alpha_1 + z_1^2 z_2^{-1},$$

and for Figure 1.5

$$\beta_1 w_1^{-1} w_2^{-1} + \beta_2 w_2 + \beta_3 + \beta_4 w_1.$$

Notice the number of terms are related to the number of lattice points in the polygons.

Solutions to the Laurent polynomials p_α constitute a geometric space. These geometric spaces, when compactified by using techniques from algebraic geometry, form spaces $\mathcal{X}_\alpha$ which are exactly the Calabi-Yau varieties of of dimension $d = k - 1$. For $k \geq 4$, the possible deformations of complex structure of $\mathcal{X}_\alpha$ for a complex vector space of dimension $h^{d-1,1}(\mathcal{X}_\alpha)$ are given by

$$h^{1,1}(\mathcal{X}_\alpha) = l(\Delta) - k - 1 - \sum_{\Gamma} l^*(\Gamma^o) + \sum_{\Theta} l^*(\Theta^o) l^*(\widehat{\Theta}^o), \tag{1.1.186}$$

$$h^{d-1,1}(\mathcal{X}_\alpha) = l(\Delta^o) - k - 1 - \sum_{\Gamma^o} l^*(\Gamma^o) + \sum_{\Theta^o} l^*(\Theta^o) l^*(\widehat{\Theta}^o), \tag{1.1.187}$$

where

- $l()$ = the number of lattice points.
- $l^*()$ = the number of lattice points in the relative interior of a polytope or face.
- Γ^o are the codimension 1 of faces of Δ^o.
- Θ^o are the codimensions 2 of faces of Θ^o.
- $\widehat{\Theta}^o$ is the face of Δ the dual to Θ^o.

When comparing this to the expressions for $\mathcal{X}^o_\alpha$ one finds the following relations

$$h^{1,1}(\mathcal{X}_\alpha) = h^{d-1,1}(\mathcal{X}^o_\alpha), \tag{1.1.188}$$

$$h^{d-1,1}(\mathcal{X}_\alpha) = h^{1,1}(\mathcal{X}^o_\alpha). \tag{1.1.189}$$

This represents the mirror families of Calabi-Yau varieties $\mathcal{X}_\alpha$ and $\mathcal{X}^o_\alpha$ of dimension $d = k - 1$. The classification of these Calabi–Yau manifolds thus amounts to that of reflexive polytopes in various dimensions, and the intense computer work of Kreuzer and Skarke was to combinatorially find such polytopes. For $n = 1$, there are 16 such polytopes in $\mathbb{R}^2$, and we have Calabi–Yau onefolds, or elliptic curves. For $n = 2$, there are 4319 such polytopes in $\mathbb{R}^3$, and we have Calabi–Yau twofolds, or K3 surfaces. For $n = 3$, there are $473,800,776$ such polytopes, and we have the Calabi–Yau threefolds. In principle, the same Calabi–Yau geometry can arise from different reflexive polytopes or triangulations of a given reflexive polytope. For the Calabi–Yau threefolds the Hodge number pairs $h^{1,1}$ and $h^{1,2}$ have become a topic of large interest, mainly as by looking at their distribution, "experimental evidence" of mirror symmetry was seen for the first time.

1.2 Background - Cosmological Inflation

The current observable Universe is in the order of 91 billion light years in diameter. On such scales, although one observes a definite structure - stars, moons and planets all clustered together within galaxies - they are spread throughout the Universe with no particular preference in direction. To all non-inertial observers, the observable Universe, on scales larger than 300 million light years, is thus said to be isotropic as well as homogeneous. Observations like these gave rise to important questions in cosmology, of which are detailed in the section below. Such properties can also be seen in the cosmic microwave background (up to one part in 10^{-5}). A natural question to ask is: how did the Universe come to this form? Working backwards through all the various phases of the Universe, one ultimately arrives at the Big Bang - an event[6] which occurred 13.7 billion years ago. From this, all matter, known and unknown, formed and interacted to create the Universe as it is.

Cosmology is thus the study of these interactions, of all matter in our Universe and how we got to where we are, as well as where we will eventually end up. According to Wilkinson Microwave Anisotropy Probe (WMAP) and Planck Satellite [28], our Universe is said to be composed of 71.4% dark energy, 24% dark matter, and a mere 4.6% ordinary matter. This large scale structure, which is responsible for the expansion of the Universe and for the formation of galaxies, was formed from gravitational instabilities of primodial density fluctuations originating from the smallest of quantum vacuum fluctuations, the description of which require tools in string theory and quantum field theory, but made significant due to an exponential expansion of the Universe known as inflation.

Inflation is thus a branch of cosmology which deals with the Universe at the earliest of times. There are aspects to inflation which are difficult to study in a purely analytic manner - it is thus our attempt to look at inflation, or more so the model generation problems for an inflationary theory, from a more statistical approach. Section 1.2.1 looks at explaining what inflation, in particular slow-roll inflation, actually is. This then leads us to random inflation in Section 1.2.2 where we discuss random potential models, both for single field and multi field cases. This gives us the set up for the work in Chapter 3 where we do an entire analysis on random polynomial potentials.

1.2.1 Inflation

Questioning why the Universe looks the way it does, has highlighted a few important problems. These are the horizon problem, flatness problem and monopole problem. Why these are of particular interest is because they give the necessary inspiration to the theory of inflation, even without the precise mechanism of how it occurred - which is the topic of current research. Firstly, when looking at the Universe from the perspective of the Cosmic Microwave Background (CMB), Figure 1.7 - we observes an homogeneous distribution of the background photon temperature.

[6] The term 'event' here is used somewhat loosely as in reality the Big Bang was more of the creation of time and space itself, in which events themselves can occur

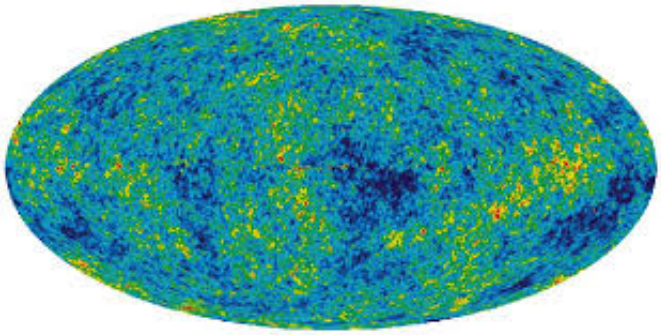


FIGURE 1.7: *Image [28] from the PLANCK satellite showing the temperature of the latest remnants of photons after the big bang. This shows the homogeneity of the photon temperature. Such a picture does not make sense as opposite points of the Universe are not causally connected.*

Photons, released after a phase of the Universe called recombination, were suddenly allowed to spread through the Universe, cooling down (wavelengths expanding) as the Universe itself expanded. This process of cooling has continued until current day, where the photon's wavelengths are now in the microwave region. How then, are two opposing sides of the Universe so uniform? It's as if two perfectly isolated systems of gases have the same temperature and are in equilibrium without having ever been in contact - in order to have equilibrium of two systems, there needs to be contact for heat transfer to occur. How could the CMB temperature across different sides of the Universe be the same if they were never causally connected? This is the horizon problem.

The flatness problem, which can also be stated as a 'fine tuning' problem, has to do with the very geometry of the Universe - it's just that, flat. This is a rather special geometric configuration of the Universe, with no apparent reason why it should have positive (spherical shape) or negative (saddle shape) curvature. The matter density Ω_0 of the Universe is what determines the curvature of the Universe. For a flat Universe, one requires $\Omega_0 = 1$. In fact, it has been calculated that the matter density of the Universe is indeed extremely close to critical density [29]. Moreover, for this to hold after billions of years of expansion, Ω_0 must have been to within 1 part in 10^{64} of the critical density. In other words, we require such a precise value, as, if it were even slightly outside that bound, the Universe would either have rapidly contracted again into a big crunch, or it would have expanded so much that we would not be able to see other galaxies. It indicates that we do not have a complete model and that something else is required to give us the initial conditions.

Lastly, the monopole problem arises as an anomalous problem of the Big Bang. Since at early times, the Universe can be described entirely in terms of particle physics, one deals with phase transition defects within the particles. Because the expansion of the Universe means the temperature of the Universe consequently decreases, these phase transitions arise naturally from particle models with symmetry breaking. Point defects are regarded as monopoles when they have a particular mass, and they cause fields to point radially away from them. It is the magnetic field configuration that these phase transition defects exhibit at infinity that makes them analogous to magnetic monopoles. Calculating the number of monopoles produced in events, such as electroweak symmetry breaking, reveals that magnetic monopoles should dominate the matter content within the Universe; this creates a contradiction, as we have never directly, or indirectly, observed monopoles in the Universe[7].

[7] The presence of monopoles would have a measurable effect on the curvature of the Universe and thus the Hubble parameter.

Inflationary scenarios dictate an extremely rapid expansion of the Universe. Such an expanding Universe introduces what is referred to as a scale factor $a(t) \sim \exp Ht$, where for inflation, $n > 1$ indicating a faster than light expansion of the Universe. Often assosciated with the scale factor is the **Hubble parameter** H which is a value that is time dependent and which can be expressed as

$$H \equiv \frac{d_t a(t)}{a(t)}. \tag{1.2.1}$$

The fundamental difference of inflation, as opposed to another contrasting model known as the DeSitter model, is to limit the amount of time that this rapid expansion occurs. Desitters model, based purely on solutions to Einsteins equations, failed to produce a Universe which looked like ours. Instead, it predicted an empty Universe with almost no radiation or matter. Guth, the pioneer of modern inflationary models, suggested that inflation was related to particle physics [30]. This suggested how cosmology could be united with particle physics in a phenomenological manner. By consequence of this, models for inflation suffer from the fact that they are essentially phenomenological. The potentials for the quantum fields that are responsible for inflation are generally introduced by hand. There are a lot of inflationary models currently circulating, from single field inflation to multifield inflation to large field inflation. Some models employ simple polynomial potentials for their fields, other models such as assisted inflation, consists of a series of exponential terms. The issue is that, there is no agreed method of looking for and studying certain inflationary potentials, and so a lot of the time studies are done ad-hoc. Any kind of potential can only be considered as a candidate for inflation if; it satisfies a certain set of slow-roll conditions, and the proposed inflation ends once those conditions are violated. Instead of scanning through particular kinds of potentials or models, there is something to be said about the general solution space of potentials which satisfy slow-roll conditions. By adopting some techniques and results from random algebraic geometry, one can then generate potentials for single scalar fields (inflatons) or even multifields, whose coefficients are randomly distributed and are of the order of the GUT scale. One can then ask something about the distribution of these potentials which satisfy slow-rolling. This then may elucidate the problem of which kind of potentials are preferred for inflation and if they are at all realistic.

How does string theory come into contact with cosmological inflation? The notion of what constitutes a natural inflationary model can be seen when generating effective theories in string theory. The moduli of compactifications is one geometric construction which involves the presence of many light scalar fields [31, 32, 33, 34]. It is these moduli which play a central role in the theory of inflation as they affect both the back evolution and perturbations. Of course from a pure inflation perspective the multitude of fields can seem unnecessary, however they are very common in string theory. Ultimately, inflation is the study of scalar fields. The most famous example of a scalar field with spontaneous symmetry breaking is that of Higgs field which breaks the electro-weak symmetry. The Higgs field was discovered, and verified, at the Large Hadron Collider at CERN. The association that scalar fields have with symmetry breaking is not limited to the Higgs fields, but also extends to GUT symmetries and supersymmetry.

Due to the phenomenological nature of inflation, it is not straight forward in choosing a suitable potential for the relevant scalar field. Fundamentally, inflation is characterized by a period of rapid expansion in the Universe for a certain period of time. This idea can be expressed in the following way. Consider the Friedman

equation in a flat Universe, written as

$$\dot{a} = \sqrt{\frac{8\pi G}{3} a\rho^{1/2}}, \tag{1.2.2}$$

here, ρ is the cosmological density which obeys the conservation equation

$$\dot{\rho} = -3\frac{\dot{a}}{a}(\rho + p), \tag{1.2.3}$$

where p is the pressure. Now, taking the time derivative eqn (1.2.2), and making use of the conservation equation, we have

$$\ddot{a} = -\frac{8\pi G}{3}\frac{\dot{a}}{2\rho^{1/2}}(\rho + 3p). \tag{1.2.4}$$

For as long as the Universe is expanding, $\dot{a}$ remains positive. Because of this, the condition for accelerated expansion is simply

$$\rho + 3p < 0. \tag{1.2.5}$$

One could state that a cosmological constant Λ with $p = -\frac{1}{3}\rho$ could allow for the above condition to hold. However, Λ does not decay and thus one would be left with an everlasting accelerating Universe. Requiring an end to inflation, implies "something must happen". By virtue of this statement we are able to postulate the existence of an "arrow of time". Therefore, the type of matter responsible for inflation cannot be exactly in equilibrium. To fix this, we introduce a scalar field (called the inflaton) which is slowly rolling down the valley of some potential. The length, number of *e-folds*, at which this rolling stage lasts is what determines if one has successful inflation - we are able to solve the various problems such as the flatness and horizon problems. It turns out that the number of e-folds required for successful inflation is between 60 and 100 e-folds. We can "test" for successful inflation by studying what are called slow-roll conditions. The simplest way of describing what these slow-roll conditions are, is by looking at a single scalar field.

The general action for a scalar field in curved space-time is

$$S = -\int d^4x\sqrt{|g|}(\mathcal{L}_g + \mathcal{L}_\varphi), \tag{1.2.6}$$

where typically, $\mathcal{L} = \frac{R}{16\pi G}$. For the scalar field

$$\mathcal{L}_\varphi = \frac{1}{2}g^{\mu\nu}\partial_\mu\varphi\partial_\nu\varphi - V(\varphi). \tag{1.2.7}$$

It turns out that the energy momentum density and pressure of such a homogeneous scalar field is

$$\rho_\varphi = \frac{1}{2}\dot{\varphi}^2 + V(\varphi), \tag{1.2.8}$$

$$p_\varphi = \frac{1}{2}\dot{\varphi}^2 - V(\varphi). \tag{1.2.9}$$

Taking $\frac{1}{2}\dot{\varphi}^2 \ll V(\varphi), \rho_\varphi \sim -P_\varphi$, the energy conservation then becomes

$$\ddot{\varphi} + 3H\dot{\varphi} + \frac{\partial V(\varphi)}{\partial \varphi} = 0, \tag{1.2.10}$$

which, together with Friedman equation, fully specifies the system. By taking the time derivative and squaring of

$$H = \sqrt{\frac{8\pi G}{3}(\frac{1}{2}\dot{\varphi}^2 + V(\varphi))}, \tag{1.2.11}$$

one derives another useful formula

$$2H\dot{H} = \frac{8\pi G}{3}\left(\dot{\varphi}\ddot{\varphi} + \frac{\partial V(\varphi)}{\partial \varphi}\dot{\varphi}\right), \tag{1.2.12}$$

$$= 8\pi G\dot{\varphi}^2, \tag{1.2.13}$$

$$\dot{H} = -4\pi G\dot{\varphi}^2. \tag{1.2.14}$$

Using the slow-roll approximations

$$\frac{1}{2}\dot{\varphi}^2 \ll V, \tag{1.2.15}$$

$$\ddot{\varphi} \ll 3H\dot{\varphi} \sim |V'|, \tag{1.2.16}$$

one obtains the **slow-roll parameters**

$$\epsilon = \frac{1}{16\pi G}\left(\frac{\partial V/\partial \varphi}{V}\right)^2 \quad ; \quad \eta = \frac{1}{8\pi G}\frac{\partial^2 V/\partial \varphi^2}{V} \tag{1.2.17}$$

such that the slow-roll conditions will read

$$\epsilon \ll 1 \quad ; \quad \eta \ll 1. \tag{1.2.18}$$

Unfortunately, although these are necessary conditions for the slow-roll approximation to hold, they are not sufficient, since even if the potential is very flat, it may be that the scalar field has a large velocity. Typically when choosing a potential, one checks to see if the slow-roll conditions are satisfied, in other words, one makes sure that the shape of the potential is flat enough such that the inflaton rolls down slowly enough. Once the rolling stops, inflation has ended, thus the potential needs to sustain slow-rolling long enough such that the slow-roll conditions are satisfied for approximately 60 e-folds. For a review of inflation as well as summary of observational results see [35, 36].

1.2.2 Random Slow-Roll Inflation - A Computational Approach

In the presence of a well-established and fundamental theory of inflation, there would exist a specific form of a potential $V(\phi)$, from which we could measure certain physical parameters. With the absence of such a theory, we settle with the task of choosing arbitrary forms of the inflationary potential, and work towards building a variety of models - all of which generate a multitude of possible inflationary theories. The ability to arbitrarily choose potentials for various models has brought with it a sense of disorder and

obscurity. How does one systematically explore different models and classify their relevance, when already a multitude of models have been presented? By constraining the inflationary scenario at a level matching the accuracy all current and new data, [37] presents a sort of encyclopedia of such models, presenting 74 different ones. It is in this context that random inflation can help out. In general, studying random inflation can have several meanings. For single field or a small number of fields, random inflation may imply scanning through randomly generated potentials and looking at how many satisfy the conditions for slow-roll inflation presented in the previous section. Alternatively we can study a specific potential, and randomly generate the initial conditions of the inflation, thereafter; within the random distribution of initial conditions, we study the landscape of initial conditions and study which ones favour inflation for a particular model. Such models are expanded in more detail in Section 1.2.2.1.

With multifield inflation, the need for random inflation is almost necessary. Considerable interest exists in fundamental particle physics theories, like supersymmetry or string theory often containing hundreds of scalar fields, which become relevant at energy scales near to that of the inflationary energy scale. Frazer and Liddle [38] mention that although it would be nice to understand what observables are specific to what models, in reality, due to the contrived nature of these models, this task is rather difficult. By introducing randomness to models and applying Monte Carlo techniques, it may be possible to understand the general features of such models. Another issue raised by them, is that multifield models have an almost infinite number of ways to inflate, the task of understanding how the potential energy driving inflation is distributed among all these fields becomes an incredibly difficult one. This problem is often referred to as the measure problem, and it deals with attempting to handle the infinite choices of initial conditions [38, 39, 40, 41].

In general, the approach that random multifield inflation adopts, is to study the dynamics of inflation in multifield models by creating an ensemble of random potentials - where the "randomness" is usually contained in the ability to construct such potentials[8]. Then, through a statistical analysis, one can make some comments on the inflationary landscape produced by their respective models.

1.2.2.1 Single Field inflation

There is no real pedagogical structure to random inflationary models - a consequence of the obscurity surrounding this particular sector of the field. And as mentioned earlier, such models are generally ruled out as real world inflationary theories. Thus, pedagogical explanations of how these models work cannot be separated by who developed the models. Some models are a lot more standard, and rely on mathematical distributions to determine their randomness, other models are more sophisticated or specialized as to suit their authors' task. What follows is a succinct recount of, what we may refer to as, "basis models". Many other models are, or have been, developed using these basis models as inspiration, as a point of reference or as reconfirmation of results obtained.

The work done in [43] constructs a large ensemble of potentials for single field inflation and looks at the dynamics statistically. In their Monte Carlo analysis, they looks closely at how the cosmological parameter probability distribution $f_p(p)$, predicted by inflation, depends on the inflation potential $V(\phi)$ and the

[8] The study of random potentials is not only limited to inflation. It is often useful to borrow techniques for the random generation of potentials from other aspects in physics, particular string theory and quantum field theory [42], and then adapt them to inflation.

measure. These potentials have the form:

$$V(\phi) = m_v^4 f\left(\frac{\phi}{m_h}\right), \tag{1.2.19}$$

where, m_v and m_h are constants which absorb the characteristic energy scales of $V(\phi)$, and f is a one dimensional Gaussian random field with unit variance, that is:

$$f(x) = \frac{a_0}{\sqrt{2}} + \sum_{k=1}^{n} a_k \cos\left(\frac{kx}{\sqrt{n}}\right) + a_{-k} \sin\left(\frac{kx}{\sqrt{n}}\right), \tag{1.2.20}$$

and the $(2n+1)$ Fourier coefficients $a_{-n}, \ldots, a_n$ are independent real-valued Gaussian random variables with zero mean and variance

$$\langle a_k^2 \rangle = A \sum q^\gamma e^{-\frac{q^2}{2}}, \tag{1.2.21}$$

with $q \equiv k/\sqrt{n}$, and the normalization constant A is chosen such that $\langle f(x)^2 \rangle = \frac{1}{2}\sum_{k=-n}^{n} \langle a_k^2 \rangle^2 = 1$. By choosing a variety of options for n and γ, they find that resulting parameter probability distribution $f_p(p)$ is rather insensitive to the detailed shape of f, but depends strongly on the energy scales m_h and m_v.

Slow-roll inflationary potentials, irrespective of their construction, fundamentally require that the inflaton "roll" down the potential towards a minimum, slowly enough such that the slow-roll conditions are met. Polynomial inflation models have the advantage of being able to include an arbitrary number of fields in the potential. These potentials will inherently contain many minima - one just needs to look for them.

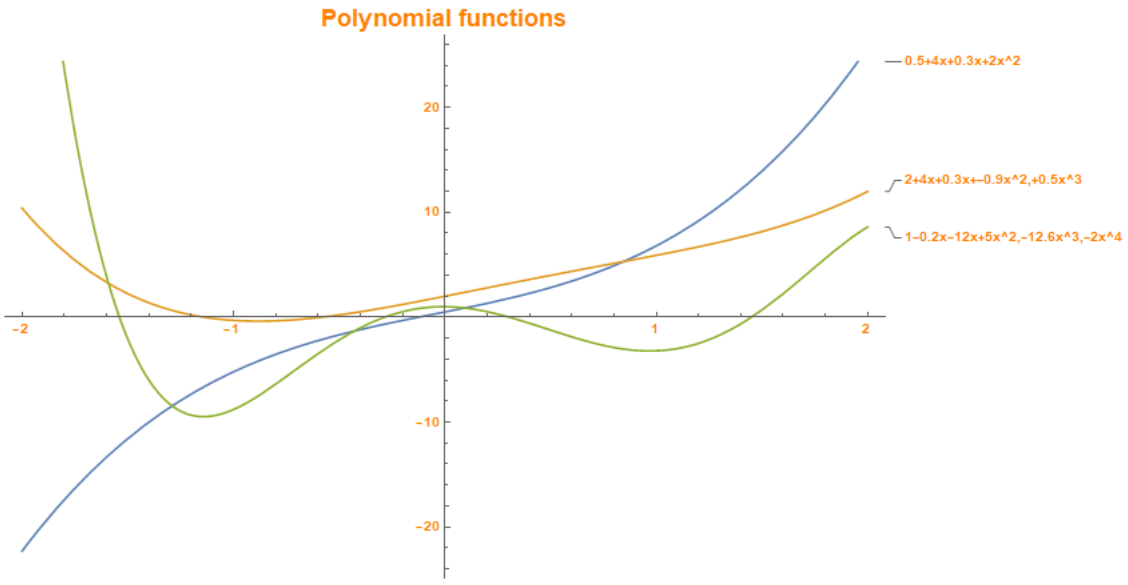


FIGURE 1.8: *An illustration of different first order polynomial functions of degree 3, 4, 5. which could all be used as example forms of a scalar field potential.*

The 1 dimensional polynomial function of various orders showcases this point - see Figure 1.8 above. The higher the order, the more one can fiddle with this polynomial function to achieve various shapes. This "fiddling" relates to the adjusting of the polynomial coefficients. Given a polynomial of a single variable with

various orders:

$$y_1(x_1) = a_1 + b_1 x_1 + c_1 x_1^2 + d_1 x_1^3, \tag{1.2.22}$$

$$y_2(x_2) = a_2 + b_2 x_2 + c_2 x_2^2 + d_2 x_2^3 + e_2 x_2^4, \tag{1.2.23}$$

$$y_3(x_3) = a_3 + b_3 x_3 + c_3 x_3^2 + d_3 x_3^3 + e_3 x_3^4 + f_3 x_3^5, \tag{1.2.24}$$

one can construct polynomials of different shapes depending purely on the coefficients. There is only one constraint on the coefficients, they need to give a function with minima. Since there are infinite ways of choosing the coefficients, and each choice leads to a potential which may have minima satisfying the slow-roll conditions, studying them all is not a simple task. The approach here is a random polynomial construction of a fixed order and field number. Thereafter, randomly choosing coefficients according to some distribution, we test each function looking for minima then testing the slow-roll conditions.

1.2.2.2 Multifield Inflation

Extending to multifields becomes more difficult. Increasing the dimensions to two introduces a problem not present in the $D = 1$ case. For $D = 1$, there are only two directions one needs to look. If one continuous along the curve, assuming all the polynomial coefficients obey minima conditions, one will eventually reach a minima. How do you choose this direction in multifield function? For example, consider the third order polynomial of degree 2, given by the form below:

$$f_1(x_1, z_1) = a_0 + a_1 x_1 + a_2 z_1 + a_3 x_1^2 + a_4 z_1^2 + a_5 x_1^3 + a_6 z_1^3 + a_7 x_1 z_1 + a_8 x_1 z_1^2 + a_9 x_1^2 z_1 \tag{1.2.25}$$

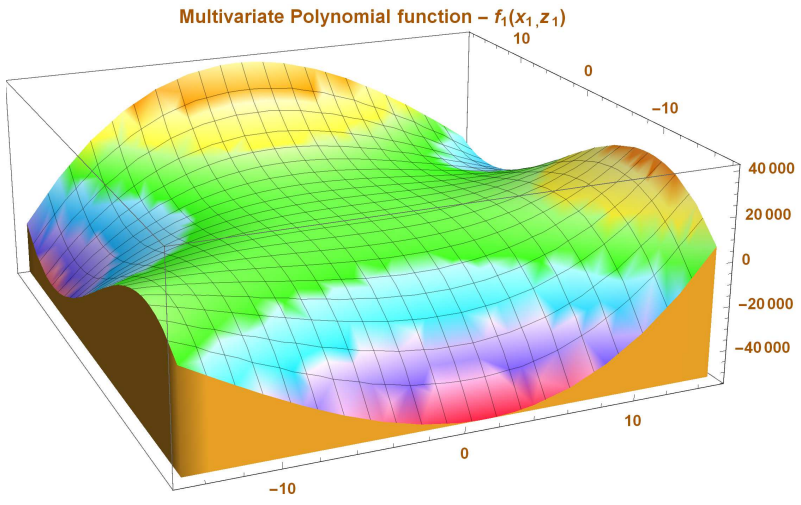


FIGURE 1.9: *An illustration of a third order multivariate polynomial functions. There are various directions in which an inflation may roll - each potentially satisfying the slow-roll conditions.*

Again, the choice of coefficients will determine the shape and the presence of minima. To find these one has to begin by first choosing a point on the surface, and then choose to move in some direction. On top of this, it is not so straight-forward to determine what relationship between coefficients will guarantee minima. This problem just intensifies with the number degree of the polynomial function. Although a

simple approach, due to computational speed restrictions, random polynomial potentials are limited to a small number of fields. It is however unknown how polynomial inflation depends on the choice of coefficients. And so, we can perform relevant computations to determine the inflationary landscape of such potentials determined by the random choosing of the coefficients. See Chapter 3 for a more detailed analysis of single and multifield polynomial potential models.

Typically, most random potentials are derived from a Fourier series expansion creating a global potential. How the models differ depend on the statistical distribution of coefficients, and other slight modification to the expansions. The standard approach is looking at a truncated Fourier series:

$$V = \sum_{J_1,\ldots,J_D=1}^{n} \left(a_{J_1\ldots J_D} \cos \sum_{i=1}^{D} J_i x_i + b_{J_1\ldots J_D} \sin \sum_{i=1}^{D} J_i x_i \right), \tag{1.2.26}$$

or in terms of wave vectors one could have a multifield generalization of eqn (1.2.20). One can apply different statistical constraints on the random potential and the distribution of the coefficients to obtain a model that will respect certain desired properties.

In slow-roll inflation, one of the requirements is that inflation needs to end close to a minima. Thus by scanning the potential for minimas, one can say something on the likelihood of inflation occurring. Of course, no minima signifies no inflation. However just the presence of a minima is not good enough. Further slow-roll conditions need to be satisfied in order to have successful inflation. The task of generating random potentials moves then to understanding the resultant structure of the Hessian matrix $\mathcal{H}$ which classifies the extrema. When V is a random potential, $\mathcal{H}$ becomes a random matrix[9](see [44, 45] for text on random matrices). This problem has been done in [46, 47] and extended in [48].

An issue surrounding the "static"[10] models mentioned previously, is the computational complexity of statistically analyzing large ensembles. One way to address this is by generating random potentials using Dyson Brownian motion [49]. More specifically, one requires that the Hessian matrix ($\mathcal{H}$) at some point in field space undergoes Dyson Brownian motion. Consider some arbitrary path in field space Γ, at some point p_0 along the path, the potential V_{p_0}, the derivative V'_{p_0} and the second derivative V''_{p_0} can all be defined. By requiring that

$$\mathcal{H}(p_1) = \mathcal{H}(p_0) + \delta\mathcal{H}. \tag{1.2.27}$$

We can, in theory, specify the Hessian matrix at point p_1. Performing such a process iteratively along Γ will build the potential along that path. The potential here is only defined locally, thus we cannot ask questions about the potential globally. According to [49], the perturbation matrix $\delta\mathcal{H}$ is constrained by certain symmetry arguments, such as statistical rotational invariance and statistical independence of the entries of the $\mathcal{H}$. The evolution process of $\delta\mathcal{H}$ is obtained by stipulating that each matrix element of $\mathcal{H}$ undergoes an independent Brownian motion between the nearby points p_0 and p_1. At the point p_0 where all the parameters are specified, the equations of motion will determine the inflationary trajectory for some

[9] Although $\mathcal{H}$ is random, what ever structure and constraints was imposed on the potential, will be manifest in the Hessian matrix.

[10] By static, one refers to the fact that the potential is defined everywhere globally, and does not change.

distance δ, at which point the Hessian undergoes Dyson Brownian motion. From this, the new potential is found at point $p_1 = p_0 + \delta$. This process then repeats itself until a metastable vacuum is met, which however, does not always happen.

This technique greatly benefits computing times. The authors in [49] claim that the number of terms required to study a given path in Dyson Brownian motion is some polynomial order in N, and the number of term required to define the potential - up to a second order expansion in some local charts - is at most $\mathcal{O}(N^3)$. Using this as a comparison to other constructions of random potentials, for example, using a super-position of a number of Fourier modes in a truncated Fourier series, where the coefficients belong to a statistical ensemble (for examples of such potentials see [43, 50, 38]), it turns out that at large N, the number of terms required for the potential in this basis, is of the order of the number of N-dimensional wavevectors, $\vec{k}$. After applying some UV and IR cut off limits, the total number of terms scales exponentially with the number of fields.

1.3 Background - Applied Conformal Field Theory

Advancement within the field of physics itself is ripe with situations where techniques borrowed from other fields have contributed to breakthroughs. Physics and mathematics have, in particular, a history of mutual information exchange. Advancements of topics within differential geometry and algebraic geometry, translate to advancements in general relativity and quantum field theory. Vice versa, advancements in particle physics and string theory enable breakthroughs in group theory etc. With physics, one develops problem solving tools, some more advanced than others, some less applicable than others. All of which, when used or adapted in the correct context can shed light, irrespective of the field.

Conformal field theory is one such topic in physics which makes use of very useful tools. Quantum field theory, at fixed points of renormalization group flows at second order phase transitions, is scale invariant [51, 52, 53]. Simply put, scale invariance implies "self-similarity" - zooming into an object which is scale invariant does not change the features of that object. Within physics, the interpretation of this invariance changes depending on the theory, for example in classical field theory, scale invariance means the theory does not depend on the length scale [54], whereas in quantum field theory, it implies particle strength interaction is not dependent on the energy of the particles [55]. From the perspective of statistical physics, it implies fluctuations of a phase transition at a critical point occur at all length scales [55]. At the critical point within a system, it is said that the Hamiltonian flows under the renormalization group into a critical fixed point. Thus, under such a flow, the coordinates of the system transform according to:

$$r- \longrightarrow b^{-1}r, \tag{1.3.1}$$

where b is a constant rescaling factor. Such a transformation is called a scale transformation. Once the Hamiltonian flows to the fixed point, its parameters no longer change, and it is said to be scale invariant. At this fixed point, invariances within the system, like rotational lattice invariance, have a Hamiltonian that will share the same rotational invariance. Under a general element of of the group formed by translation, rotation and dilatation, an arbitrary correlation function of scaling operators transforms as:

$$\langle \phi_1(r_1)\phi_2(r_2)\ldots\rangle = \prod_j b^{-x_j} \langle \phi_1(r_1')\phi_2(r_2')\ldots\rangle , \tag{1.3.2}$$

with x_j being the scaling dimension of ϕ_j. It turns out that in quantum field theory scale invariance is just a subset of the larger group of symmetries that is conformal symmetry. A powerful feature of conformal field theory, is that the symmetries which are often very restrictive problems can be solved for what would otherwise be intractable. As an example, conformal invariance fixes 2- and 3-point functions entirely. In an ordinary quantum field theory, especially one at strong coupling, these would be hard or impossible to calculate at all without making use of these methods.

Conformal field theories, are theories which admit a symmetry group larger than just the Poincaré spacetime, and Galilean symmetries. The added symmetries comes from the addition of invariance under scale transformations. In 2-dimensions, this symmetry is particularly powerful as it is infinitely dimensional - putting a powerful constraint on the structure of the Hilbert space as well as the operator algebra. Essentially,

it is the symmetries of these conformal transformations within a conformal field theory which make it so powerful and interesting. Conformal transformations are ones which preserve angles between vectors, but not necessarily distances. Thus a conformal transformation locally corresponds to the same group of translation, rotation and dilatation transformations.

1.3.1 Correlation functions

Since conformal field theory is incredibly vast, it is relevant to focus on correlations functions and how we can calculate them in 2D. This forms the basis of inspiration of how research in Chapter 4 was conducted. One simpler and perhaps more illuminating way of introducing correlations function in a sufficient manner, is by using a toy model known as the Ising model.

To describe physical systems, one needs the laws governing the fundamental properties of that system. Take the expansion of a solid for example; by knowing certain macroscopic properties of the solid one can describe its compressive/expansive behaviour. Such behaviour should be independent of the microscopic behaviour of the individual atoms and molecules which together comprise the solid. That is, you don't expect the macroscopic behaviour to change even if you halve the size of the object, while still maintaining all other variables constant of course. However, there is a limit to this argument. Eventually, if you continue to decrease the length scales of the macroscopic sample, we will encounter a situation where the microscopic properties will differ significantly from one sample to the next. The length scale at which this begins to happen is called the **correlation length**. This is the length over which degrees of freedom of an atom(in the case of materials) is correlated to another. Two collections of atoms in a particular sample separated by lengths longer than the correlations length are effectively disconnected, and so there is no appreciable difference in the macroscopic properties if the two samples are severed from each other. Typically what determines the correlation length are the external properties set by the state of the material. Points at which the macroscopic behviour changes abruptly is known as a critical point. Consider water at the critical point, where all three phases of matter exist simultaneously - properties of the material change in all the various phases, of which all coexist together at the same point. For certain systems whose phase transitions are continuous (Curie temperature in a ferromagnet, or liquid-gas critical point) have a correlation length which is effectively infinite - fluctuations in the material affect the material over all length scales. The 2D Ising model is a useful model to describe quantitatively this critical point behaviour.

The Ising model represents the magnetic dipole moments of atomic spins. Atomic spins σ_i can be in either one of two states $+1$ or -1 - often denoted with an arrow up or down respectively. These atomic spins are arranged in a 2D lattice structure. Variables such as external magnetic field β and temperature T affect the spin of each lattice site.

1.3.1.1 Two point functions

In an Ising model, one studies the spin-spin correlation functions. This tells us the 'amount of correlation' we expect between two spins for a given distance apart. Since each the spin at each lattice site affects it's nearest neighbour, the Ising model is said to have nearest neighbour interactions. The extent over which a

single lattice site can affect other lattice sites, depends on the correlation length. The correlation function can be calculated using the following:

$$f(r) = \frac{\langle \sigma_i \sigma_j \rangle - \langle \sigma_i \rangle \langle \sigma_j \rangle}{\langle \sigma_i \rangle \langle \sigma_j \rangle}, \tag{1.3.3}$$

where σ_i and σ_j are the spins sitting at different lattice sites separated by a distance r. The way we calculate $\langle \sigma_i \sigma_j \rangle$ is by simply multiplying the spin value of the two sites together. This means if $\sigma_i = \sigma_j$, $\sigma_i \sigma_j = 1$ else $\sigma_i \sigma_j = -1$. We sum these values over all possible pairings of two lattice site points which are all exactly the same distance r apart and take the average. This gives us a value between 0 (no information exchange) and 1 (maximal information exchange). $\langle \sigma_i \rangle \langle \sigma_j \rangle$ is just the average value of all the spins across all lattice sites. The resulting behavior of $f(r)$ has the following form:

$$f(r) \sim \frac{1}{r^\alpha} \exp\left[\frac{-r}{\xi}\right]. \tag{1.3.4}$$

Here, ξ is the correlation length of the system. It typically varies with the temperature and indicates the distance over which spins will respond to one another. Both at high and low temperatures, you have a very small correlation lengths - at high T, spins will fluctuate rapidly and independently of each other, whereas at low T, although the spins are mostly aligned, flipping σ_i will have hardly any effect another spin site σ_j. There is a critical point however, whereby the correlation length becomes infinite. This, as mentioned above, is signaling a phase transition. At the critical point you have that $\chi \to \infty$, thus $\exp\left[\frac{-r}{\xi}\right] \to 1$ and

$$f(r) \sim \frac{1}{r^\alpha}, \tag{1.3.5}$$

with $\alpha = 0.25$ for the Ising model.

1.3.1.2 Three point functions

There is also a three point correlation function which takes into account three spin sites $\sigma_i, \sigma_j, \sigma_k$, not two. Similar to above, it is defined as:

$$f(R) = \frac{\langle \sigma_i \sigma_j \sigma_k \rangle - \langle \sigma_i \rangle \langle \sigma_j \rangle \langle \sigma_k \rangle}{\langle \sigma_i \rangle \langle \sigma_j \rangle \langle \sigma_k \rangle}. \tag{1.3.6}$$

We obtain correlations in very much a similar manner. The resultant behaviour of the average correlation also follows a power law:

$$f(R) \sim \frac{1}{R^\eta} \exp\left[\frac{-R}{\chi}\right], \tag{1.3.7}$$

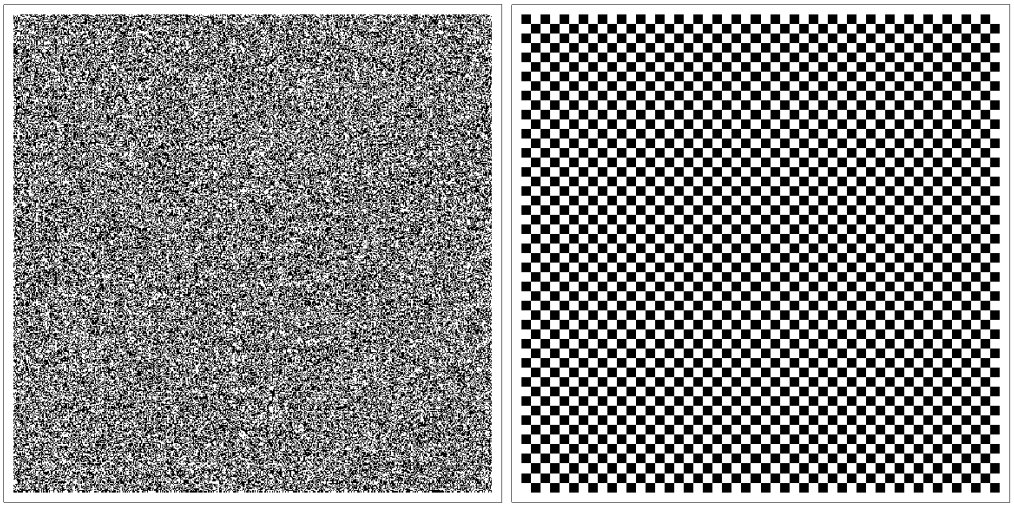
where $R = r_{ij} r_{ik} r_{jk}$.

1.3.1.3 Understanding what correlations show

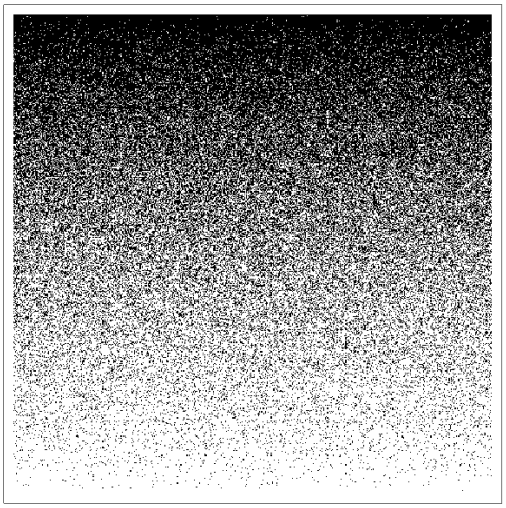
By construction, n-point correlations give us an indication of how related points are to each other. Knowing information about the state of one point gives us a probabilistic description of states of the other points in the correlation. Typically there is an underlying mechanism which gives rise to these relations. If we are

dealing with points in space, the distance between points, at which these relations break down, is associated with the range of influence points have with one another. In the context of physical systems this has direct consequences to the properties of matter. This behavior between points, can be studied just by analyzing these n-point correlations.

Consider a 2D grid whereby every element has two possible states, either $1/0$ or $1/-1$. To get an intuitive feel for what these correlation functions show, consider just the two points correlation function on the following three 2D grid setup:



(A) *Random distribution* (B) *Checkered distribution*

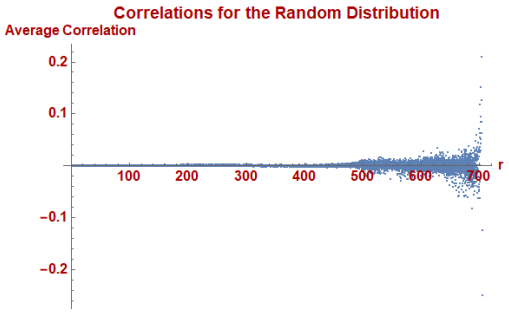


(C) *Inverse distribution*

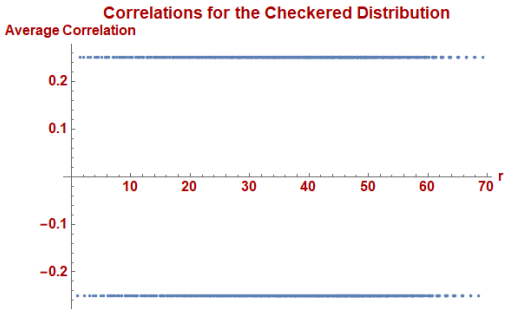
FIGURE 1.10: 500×500 *grids of points with different distributions. White and black blocks are represented by 1 and -1 respectively. For the purposes of clarity of illustration, the checkered grid is shown using an* 80×80 *grid.*

In this setup, the two point correlation function is the sum of all products of two element entries separated by a distance r and averaged over that particular distance. In other words, if say points $p_1 = -1$ which is 2 units away from $p_2 = 1$ then the correlation is $-1 \times 1 = -1$. Clearly, only when two elements are equal is the correlation 1 and when they are opposite the correlation is -1. Thus, in this particular setup, when considering many points, the closer the average correlation is to 1, for a given separation, the more likely that all those points are correlated to one another, or in other words, the more likely that the state of one

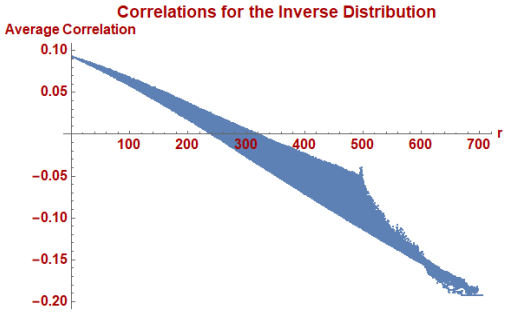
element will affect the state of another element. Similarly, the closer the correlation is to -1, the more likely points are anti-correlated - in of itself a form of correlation. Points that have an average correlation of -1 mean that you if a point is one of the two states, there is a strong likelihood that the other point is the other of the two states. The average correlations for the distributions can be seen in Fig. 1.11



(A) *Correlation of random distribution.*



(B) *Correlation of checkered distribution.*



(C) *Correlation of Inverse distribution.*

FIGURE 1.11: *The plots of average correlation for a given separation distance r. The large variation that occurs in (A) at $r = 500$ are artifacts given by the dimension of the grid. Over these distance, the correlations are biased as only certain diagonal directions can be considered, thus they are never considered in the analysis.*

As expected, for a random distribution, the average correlation is zero, since there is no relationship between states of each element. For the checkered distribution, each alternating distance has a correlation of exactly 1 or -1, this is due to the geometry of the setup. For a given white block, each block exactly one unit away is always black, and two units is always white again. Consider the first few entries in the correlation list:

$$(r, \text{correlation}) = \big((1,-1),(\sqrt{2},1),(2,-1),(\sqrt{5},1),(\sqrt{8},-1),(3,1),(\sqrt{10},-1)...)\big). \tag{1.3.8}$$

The two point correlations encode, that every alternating element is opposite to it's nearest neighbour. Lastly, the inverse distribution was generated by randomizing with a weighted condition:

$$P(1,-1) = \left(\frac{500}{500-i+1}, \frac{500}{500-i+1} - 1\right), \tag{1.3.9}$$

where, $i = 1, 2, ...500$ indicates the row number. As we see at small i. the probability that an element has the state of 1 is much higher than that of -1, then as i increases, this gets less and less. The average correlation plots shows this by having a positive average correlation at small r which then decreases as r increases - points become more and more anti-correlated at larger distances.

For certain systems, the correlation function - which generates the plots - has specific forms. These forms

are an indicator of how elements in the system communicate which each other, as well as how strongly they communicate with each other.

Chapter 2

Patterns in Calabi–Yau Distributions

This chapter was published in collaboration with Yang-Hui He and Vishnu Jejjala as:

Author : Y.H. He and V. Jejjala and L. Pontiggia

Title : Patterns in Calabi–Yau Distributions

Journal : Commun. Math. Phys.

Volume : 354

Year : 2017

Number : 2

Pages : 477-524

DOI : 10.1007/s00220-017-2907-9

2.1 Introduction

A Calabi–Yau n-fold is a Kähler manifold of n complex dimensions with a trivial canonical bundle. In superstring theory, it serves as a compactification manifold wherein a ten dimensional theory at high energies reduces to an effective theory in four spacetime dimensions. In particular, global $SU(n)$ holonomy ensures that 2^{1-n} of the original supersymmetry is preserved. Thus, confronted by the vacuum selection problem, Calabi–Yau compactifications present an avenue for Standard Model building especially in the context of the heterotic string [56, 57, 58, 59]. Indeed, the basis of the landscape is to consider flux compactifications on these geometries [60, 61].

To facilitate this approach to a low-energy phenomenology derived from string theory, mathematicians and physicists have constructed large datasets of Calabi–Yau threefolds [62, 63, 64, 65, 66, 67, 68, 69, 70, 71, 72, 73, 74, 75] as well as various refined analyses of properties thereof [76, 77, 78, 79, 80, 81, 82, 83].

By far the largest database was constructed in a *tour de force* of algebraic geometry, combinatorics, physics, and computer algorithms by Kreuzer and Skarke based on the theorems of Batyrev and Borisov [63, 64, 65, 73, 74, 75, 84, 85]. In short, these Calabi–Yau n-manifolds X_n are realized as a smooth hypersurface embedded in a toric variety A_{n+1} of complex dimension $n+1$; the Calabi–Yau condition simply translates to the requirement that the polytope defining A_{n+1} be **reflexive**. We will henceforth consider only such Calabi–Yau manifolds, of which there are a plethora.

Let us briefly recollect what all this means. The (possibly singular) toric variety A_{n+1} is specified by an integer polytope Δ in $\mathbb{R}^{n+1}$, which is a collection of vertices (dimension 0) each of which is an $(n+1)$-vector with integer entries and such that each pair of neighboring vertices defines an edge (dimension 1), each pair of edges defines a face (dimension 2), etc., all the way up to a facet (dimension n). Alternatively, Δ can be defined by a set of integer linear inequalities, each of which slices a facet. The polytope is then the convex body in $\mathbb{R}^{n+1}$ enclosed by these facets. We will always include the origin as being contained in Δ. Using the usual dot product $\langle\ ,\ \rangle$ inherited from $\mathbb{R}^{n+1}$, the dual polytope is defined by

$$\Delta^\circ := \left\{v \in \mathbb{R}^{n+1} | \langle m, v\rangle \geq -1, \forall\ m \in \Delta\right\}\ . \tag{2.1.1}$$

The polytope Δ is *reflexive* if all the vertices of Δ° are integer vectors. In this case, we can define the Calabi–Yau hypersurface X_n explicitly as the polynomial equation

$$\sum_{m\in\Delta} c_m \prod_{r=1}^{k} x_r^{\langle m, v_r\rangle + 1} = 0\ , \tag{2.1.2}$$

where $v_{r=1,\ldots,k}$ are the vertices of Δ° with k being the number of vertices of Δ° (or equivalently the number of facets of Δ), x_r are the coordinates of A_{n+1}, and c_m are numerical coefficients parameterizing the complex structure of X_n. Indeed, the reflexivity of Δ ensures that the exponents are integral whereby making the hypersurface polynomial as required.

The classification of these Calabi–Yau manifolds thus amounts to that of reflexive polytopes in various dimensions, and the intense computer work of Kreuzer and Skarke was to combinatorially find such polytopes. For $n = 1$, there are 16 such polytopes in $\mathbb{R}^2$, and we have Calabi–Yau onefolds, or elliptic curves. For $n = 2$, there are 4319 such polytopes in $\mathbb{R}^3$, and we have Calabi–Yau twofolds, or K3 surfaces. For $n = 3$, there are $473,800,776$ such polytopes (which was a formidable computer task!), and we have the Calabi–Yau threefolds. This sequence

$$\{1, 16, 4319, 473800776, \ldots\} \tag{2.1.3}$$

of remarkable growth rate, can be found in the Online Encyclopedia of Integer Sequences [86]. The numbers in higher dimension are still not known, nor has there been an asymptotic analysis of their growth. It should be emphasized that generically a reflexive polytope corresponds to a *singular* toric variety even though the hypersurface is chosen (by generic coefficients c_m) to miss the singularities and hence ensuring the smoothness of the Calabi–Yau X_n. For example, of the some half-billion reflexive polytopes in $\mathbb{R}^4$, only 136 A_4 are in fact smooth [87]. As we desingularize the toric variety by various star-triangulations of Δ, we are led to potentially *inequivalent* Calabi–Yau manifolds. In principle, the *same* Calabi–Yau geometry can arise from different reflexive polytopes or triangulations of a given reflexive polytope. Whereas K3 is essentially unique, we do not know how many Calabi–Yau threefolds there are. A systematic study to classify the desingularizations, to compute the necessary topological data, and to build an interactive

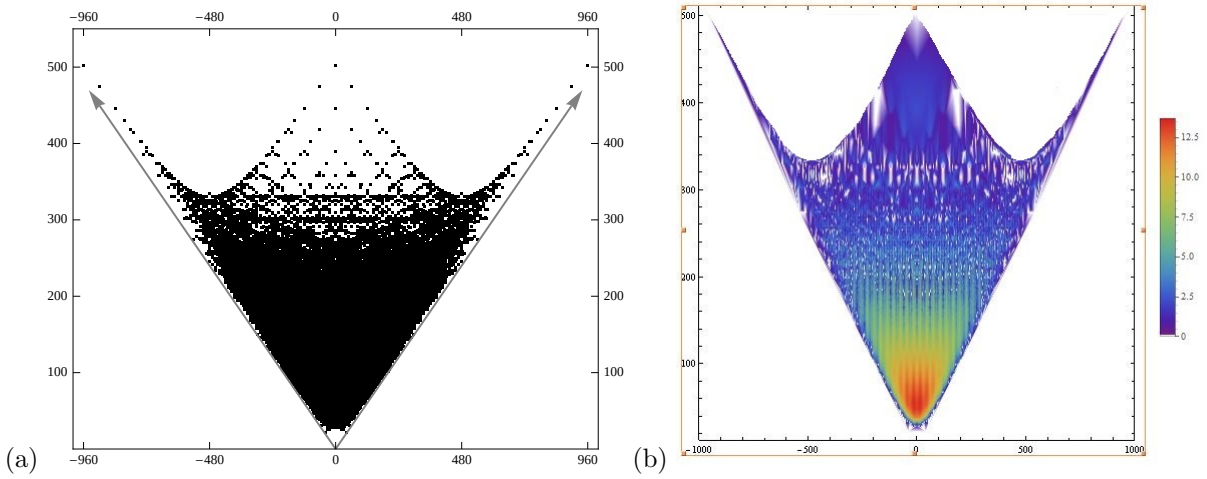


FIGURE 2.1: *(a) The cumulative plot of* $\chi = 2(h^{1,1} - h^{1,2})$ *on the abscissa versus* $h^{1,1} + h^{1,2}$ *on the ordinate for Calabi–Yau threefolds as hypersurfaces in toric fourfolds; (b) marking also the natural logarithm of the multiplicity of the Hodge pair with a color grading.*

online database [66] is under way. The moral is that there are almost certainly far more than half a billion Calabi–Yau threefolds!

Luckily, the Hodge numbers depend only on the polytope and not on the choice of desingularization. (The intersection numbers, however, do depend on the choice.) For Calabi–Yau threefolds, the pair of Hodge numbers $(h^{1,1}, h^{1,2})$ is a famous quantity. Indeed, the plot in Part (a) of Figure 2.1 has become iconic. Here, the sum $h^{1,1} + h^{1,2}$ is plotted against the Euler number $\chi = 2(h^{1,1} - h^{1,2})$, and the left-right symmetry supplies "experimental evidence" for *mirror symmetry*. There is enormous redundancy in this data: of the some half a billion reflexive polytopes, there are only $30,108$ distinct pairs of Hodge numbers and the pair $(27, 27)$ dominates the multiplicity, totaling almost one million. In Part (b) of Figure 2.1 we have attempted to visualize the distribution of the multiplicity by having a color density plot of the logarithm of the number over each Hodge pair.

Understanding this multiplicity forms the inspiration for the present work. While there have been analyses on the *shape* of the funnel-like plot [83, 81, 76], there has not been much work on its *density*, *i.e.*, the distribution of the multiplicity of Hodge data for the Calabi–Yau manifolds of various dimension. Of course, fundamentally, this is entirely due to the combinatorics of reflexive polytopes and might in principle be analytically determined. However, given the complexity of the problem it is expedient to analyze the available data which have been compiled over the years, observe intriguing patterns, and draw statistical inferences before turning to analytic treatments. This is what we achieve in this work.

The organization of the paper is as follows. We perform a detailed analysis on the structure and behavior of the threefold data in Section 2.2. This is motivated by looking for an exact function describing the relationship of the distribution of the Hodge pairs $(h^{1,1}, h^{1,2})$ with frequency.

In Section 2.2.1, we study the distribution of $(h^{1,1} - h^{1,2}, f)$. We find that this distribution is composed of a family of curves, for which each curve can be described using a modified pseudo-Voigt model. Although an approximation, the model is able to describe the general trend of the data, as well as some additional fine structure within each individual data point. Performing an analysis on the parameter relationships shows that three out of the five parameters can be expressed as a single variable, but conclude that additional modifications need to be introduced in the model to overcome certain shortfalls.

Subsequently, Section 2.2.2 performs an analysis on the structure of $(h^{1,1} + h^{1,2}, f)$. Similarly, this

distribution is composed of a family of curves for which each curve can be described using a Planckian profile. Combining the regression analysis for each curve within the distribution, we construct a single function able to approximately model the entire distribution of $(h^{1,1}+h^{1,2}, f)$ with only two variables. Section 2.2.3 uses the model developed in Section 2.2.1 to describe the distribution of the Euler number χ.

Section 2.2.4 is dedicated to the description of model validation in our context, as the usual statistical tests are inadequate. Section 2.2.5 discusses possible implications to physics by referencing recent advancements in F theory and further investigations of structures within the Kreuzer–Skarke database. In Section 2.3 and Section 2.4, we perform primary analyses of Calabi–Yau twofolds (Picard number and multiplicity) and Calabi–Yau fourfolds. Due to the lack of a complete data set, we are unable to provide a thorough analysis of the fourfolds as with threefolds. Finally the Appendix presents many supplementary plots and figures for the various sections. We conclude with a summary and outlook in Section 2.5.

2.2 Calabi–Yau Threefolds

As advertised in the Introduction, we will begin with the analysis of threefolds and identify patterns within this rich distribution of Hodge numbers and their frequency as plotted in Figure 2.1. It turns out striking patterns do exist, pointing to a definite structure within the threefold data, which consists of the triple $(h^{1,1}, h^{1,2}, f)$, where f is the number of reflexive polytopes in the Kreuzer–Skarke database with the given Hodge pair. Here, $h^{1,1}$ and $h^{1,2}$ respectively count the Kähler and complex structure moduli of the Calabi–Yau obtained from the reflexive polytope. More precisely [88], we have that

$$\begin{aligned} h^{1,1}(X) &= \ell(\Delta^*) - \sum_{\mathrm{codim}\theta^*=1} \ell^*(\theta^*) + \sum_{\mathrm{codim}\theta^*=2} \ell^*(\theta^*)\ell^*(\theta) - 5; \\ h^{1,2}(X) &= \ell(\Delta) - \sum_{\mathrm{codim}\theta=1} \ell^*(\theta) + \sum_{\mathrm{codim}\theta=2} \ell^*(\theta)\ell^*(\theta^*) - 5 \ . \end{aligned} \tag{2.2.1}$$

In the above, Δ is the defining polytope for the Calabi–Yau threefold X and Δ^* is its dual. Moreover, θ and θ^* are the faces of specified codimension of these polytopes respectively; $\ell(\ )$ is the number of integer points of the polytope while $\ell^*(\ )$ is the number of interior integer points. Indeed, our analysis of the distribution of Hodge numbers ultimately reduces to counting these integer points.

To facilitate the analysis, we plot $(h^{1,1}-h^{1,2}, f)$ and $(h^{1,1}+h^{1,2}, f)$ as shown in (a) and (b) of Figure 2.2, respectively. Recall that the Euler number $\chi = 2(h^{1,1} - h^{1,2})$. We will use the difference $h^{1,1} - h^{1,2}$ rather than the Euler number. In the simplest heterotic constructions, $|h^{1,1} - h^{1,2}|$ corresponds to the index of the Dirac operator and gives the number of generations of particles in the low-energy spectrum [56].

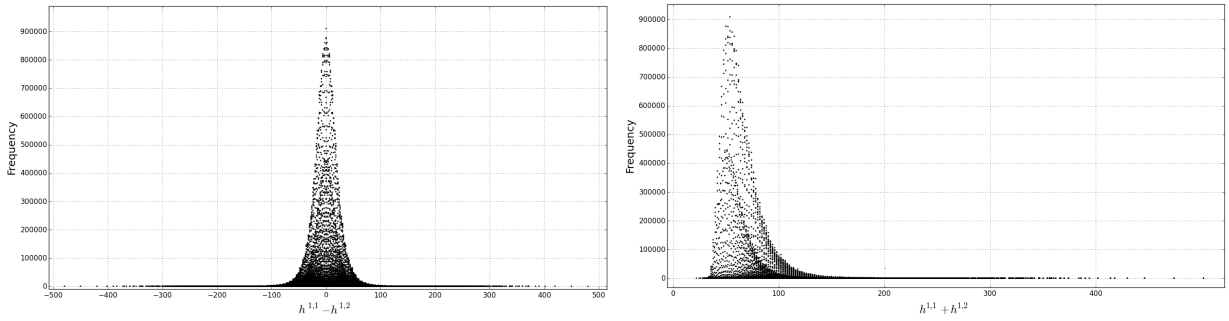


FIGURE 2.2: *(a) Frequency f plotted against $\frac{1}{2}\chi = h^{1,1} - h^{1,2}$; (b) Frequency f plotted against the sum of Hodge numbers $h^{1,1} + h^{1,2}$.*

By inspection, these plots already exhibit two patterns. Firstly, in both the $h^{1,1} - h^{1,2}$ and $h^{1,1} + h^{1,2}$ plots, there appears to be an inner distribution contained within the outer distribution. We find that these inner and outer distributions are related to the parity of $h^{1,1} \pm h^{1,2}$. Figure 2.3 elucidates this point by having the odd and even values in different colors. Though this parity structure may be a result of the Kreuzer–Skarke algorithm, its consistent appearance means we need to treat the distributions of even and odd distinctly for now.

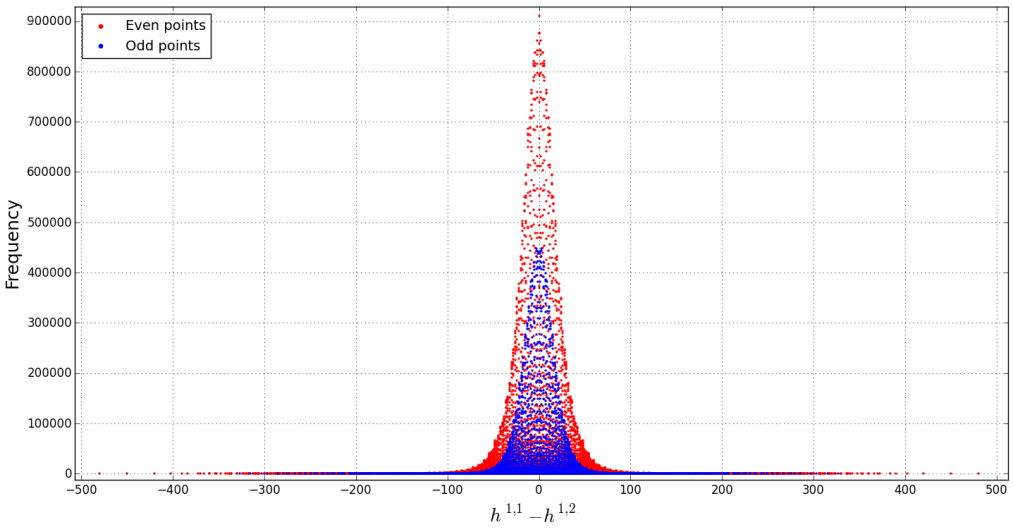
The second evident structure which can been seen by inspection, is that the outer edge of the distribution of $h^{1,1} - h^{1,2}$ (Figure 2.3(a)) appears to follow a normal like curve, whereas the edge of $h^{1,1} + h^{1,2}$ (Figure 2.3(b)) follows a Planck like curve. It is through the analysis of these distributions that we deduce their characteristic behavior and underlying structure. In the main body of this paper, we outline the results and analysis of only the even distributions for $h^{1,1} - h^{1,2}$ and $h^{1,1} + h^{1,2}$, except where it is important to present both. It turns out that any structure and patterns which are found in the even distributions for $h^{1,1} - h^{1,2}$ and $h^{1,1} + h^{1,2}$ are found identically in the odd distribution (see Appendix for various plots).

2.2.1 Analysis of $h^{1,1} - h^{1,2}$

Before we can present the results, it is important to explain some notation. When working with the distribution of $h^{1,1} - h^{1,2}$, we find that it is composed of many curves, whose individual structure is the same as the "edge" or boundary of the distribution mentioned earlier. As a consequence of this, we refer to $h^{1,1} - h^{1,2}$ as being composed of a "family of curves." Each curve is then classified by its r**-value**, where $r = h^{1,1} + h^{1,2}$. It is important to be clear that in this analysis, although $h^{1,1} - h^{1,2}$ is just half the Euler number, we are not summing over all the possible values of $h^{1,1} + h^{1,2}$. We are keeping these values distinct: hence, the r-curves we obtain. Later on in Section 2.2.3 we sum over all possible values of $h^{1,1} + h^{1,2}$ to get two plots representing the full Euler number distribution.

Consider the example in Figure 2.4(a). By ordering the data in terms of $h^{1,1} + h^{1,2}$, one can classify data sets within $h^{1,1} - h^{1,2}$ by an r-value. Holding r fixed, we can plot the frequency f versus the difference $h^{1,1} - h^{1,2}$. We call each value of r a curve, which we can overlay on the same plot. In this example, we tabulate data for curves identified by $r = 28$ and $r = 29$. As a further illustration, we show explicitly the curves of the even distribution within $h^{1,1} - h^{1,2}$ for $r = 42, 54, 66$ in Figure 2.4(b). By mirror symmetry, the curve is symmetric about the vertical axis, where $h^{1,1} - h^{1,2} = 0$.

(a)



(b)

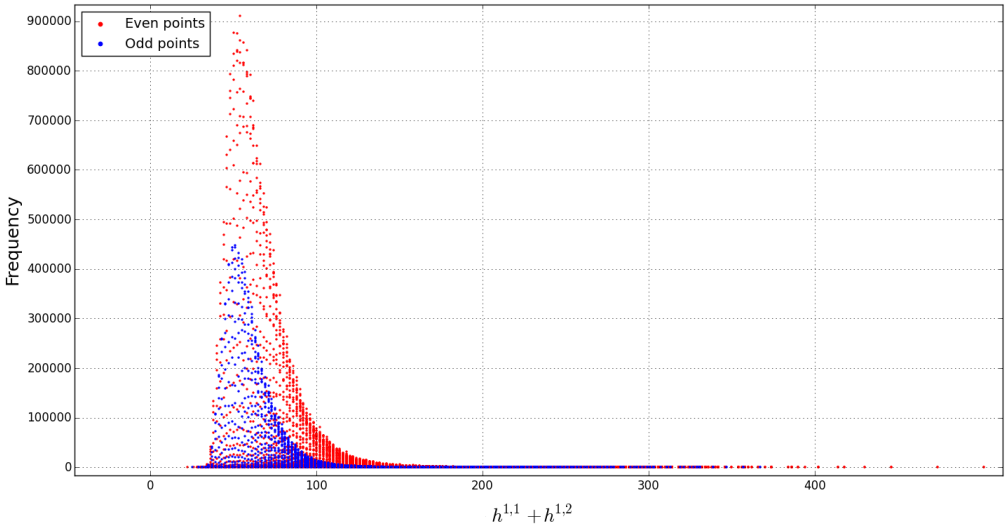


FIGURE 2.3: *(a) The $h^{1,1} - h^{1,2}$ distribution for threefolds, highlighting the two sub-distributions, where red and blue data points correspond to even and odd values of $h^{1,1} - h^{1,2}$, respectively; (b) The same, but for $h^{1,1} + h^{1,2}$.*

(a)

$h^{1,1}$	$h^{1,2}$	$h^{1,1} + h^{1,2}$	$h^{1,1} - h^{1,2}$	f
9	19	28	-10	1
10	18	28	-8	2
12	16	28	-4	1
14	14	28	0	3
16	12	28	4	1
18	10	28	8	2
19	9	28	10	1
11	18	29	-7	2
12	17	29	-5	1
13	16	29	-3	3
16	13	29	3	3
17	12	29	5	1
18	11	29	7	2

(b)

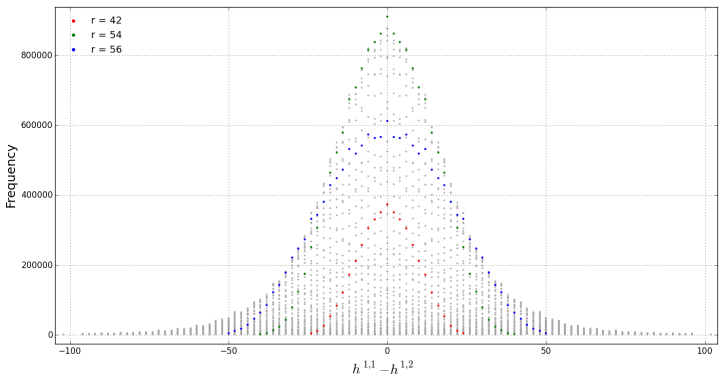


FIGURE 2.4: *(a) Example of repeated values of the sum $h^{1,1} + h^{1,2}$ being 28 and 29; (b) Three highlighted curves ($r = 42, 54, 66$) within the even $h^{1,1} - h^{1,2}$ distribution. The transparent grey data dots are all the data plots for the distribution. Refer to Figure 2.24 for the corresponding odd plot.*

We can now perform a regression analysis for each individual curve, in the quest of obtaining a function describing the distribution. In the analysis, we indeed find an approximate function predicting the fine structure of the data. We operate with one caveat: we ignore data points which have a frequency lower than 2000. At large r, the data, whose frequency is below 2000, begins to deviate from our model. The reason for such deviations, comes down to the fact that our model, though remarkably accurate, is still an approximation. We suspect that with further modifications, such deviations can be accounted for and that consequently, it may be possible to find an exact function to map the frequency distribution of $h^{1,1} - h^{1,2}$. Such statements also apply to the distribution of $h^{1,1} + h^{1,2}$.

2.2.1.1 A Pseudo-Voigt Fit

Due to the normally-distributed, peak-like nature of these curves, we performed a regression analysis using the following models: Gaussian; Cauchy (Lorenztian); Pearson7; Breit–Wigner; Voigt; and Pseudo-Voigt. In the Appendix 2.6.2.2, we perform a side by side comparison. It turns out that both the Voigt model (2.26e) as well as the pseudo-Voigt model (2.26f) give excellent fits.

We focus on the **pseudo-Voigt model** as it gives the best fits. This is a linear combination of a Gaussian and Lorentzian (Cauchy) distribution:

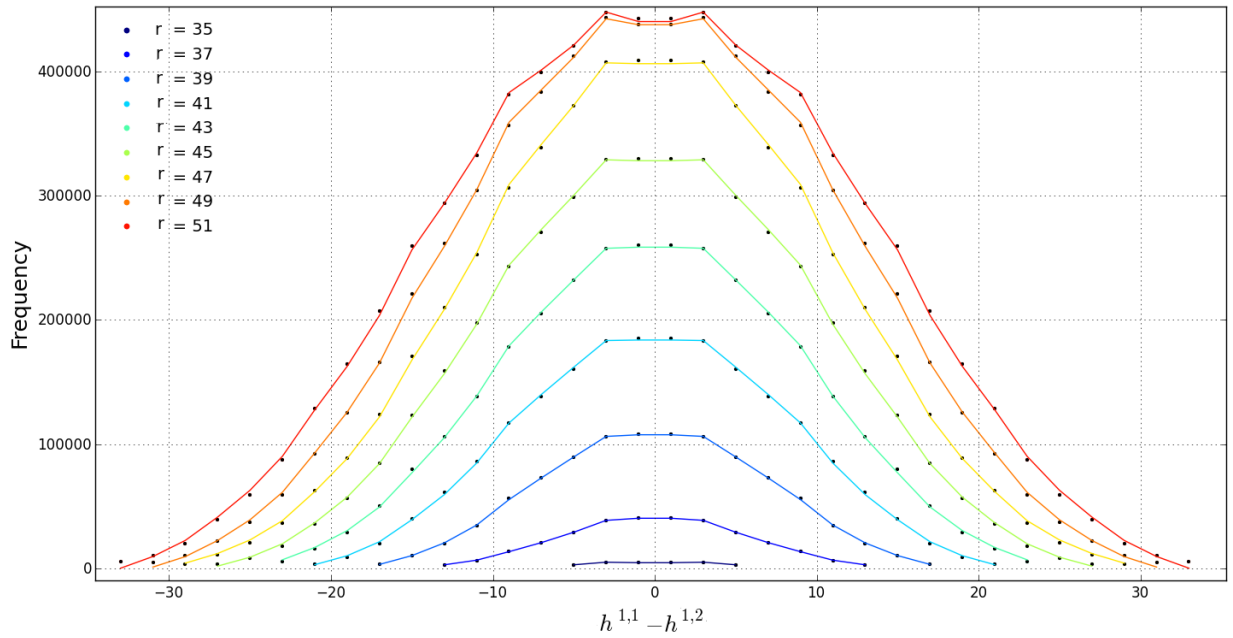
$$f(x, A, \mu, \sigma, \alpha) = (1-\alpha)\frac{A}{\sigma\sqrt{2\pi}} e^{\frac{-(x-\mu)^2}{2\sigma^2}} + \alpha\frac{A}{\pi}\left[\frac{\sigma^2}{(x-\mu)^2+\sigma^2}\right] , \tag{2.2.2}$$

with amplitude (A), center (μ), Gaussian width (σ), and fractional parameter alpha (α). However, we can modify the above distribution slightly so that the amplitude A of the distribution has an oscillating component

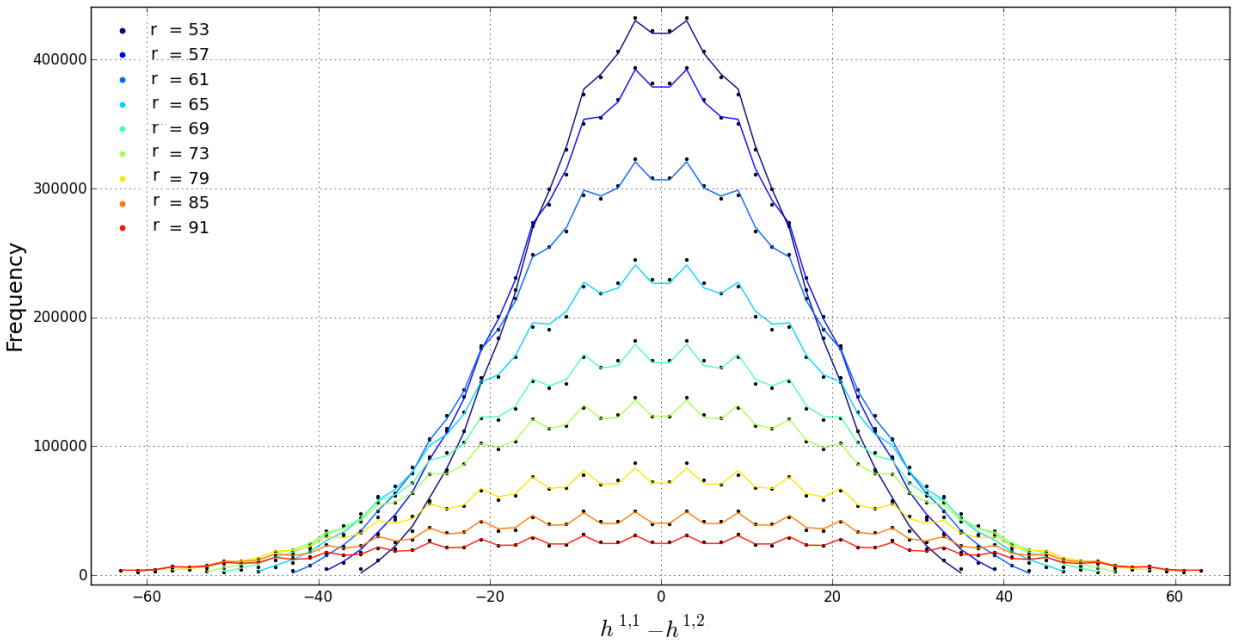
$$A(x, A_0, a, b) = A_0 + a\cos(2\pi b \cdot x) , \tag{2.2.3}$$

where A_0 is the original amplitude of a particular curve described by the pseudo-Voigt distribution, a is the amplitude of oscillations, and b represents the period. By doing a regression analysis one curve at a time using this modified pseudo-Voigt model, we are almost able to replicate not just the basic structure of each curve, but even the individual behavior of each data point in the entire distribution. (See Appendix 2.6.2.3 for a comparative plot of the all the regression curves using the standard, unmodified, pseudo-Voigt model.)

We plot the frequency against $h^{1,1} - h^{1,2}$ for various values of r (odd and even). Figures 2.5 and 2.6 are striking in their accuracy.

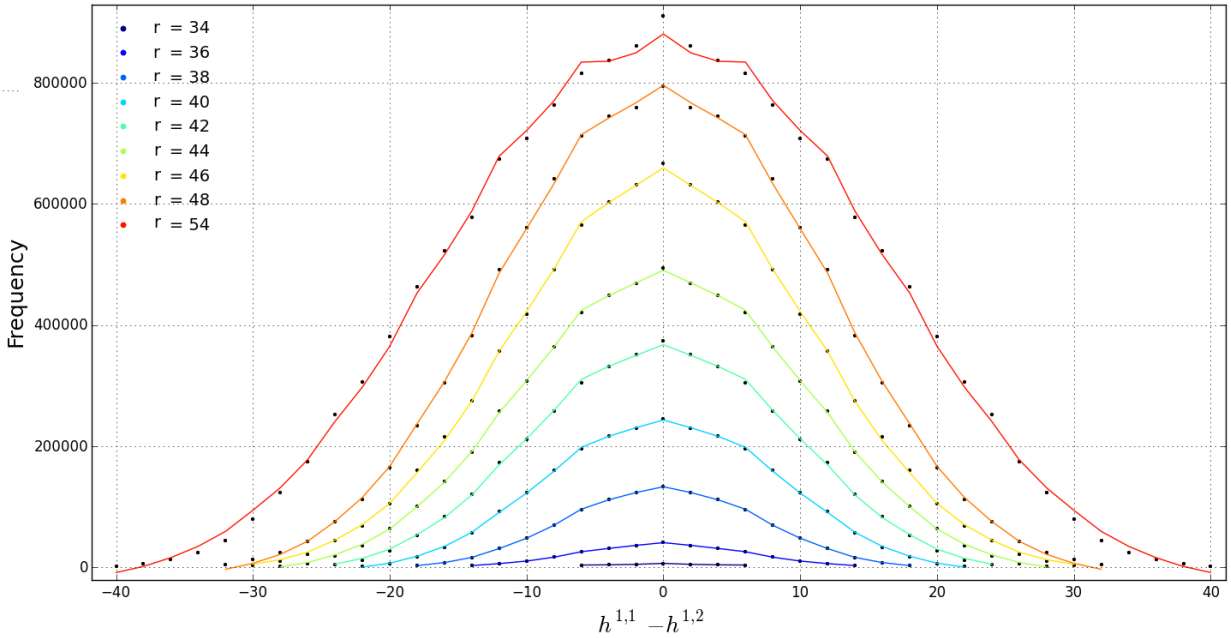


(A) Regression lines for all odd r valued curves, with $r \in [35, 51]$.

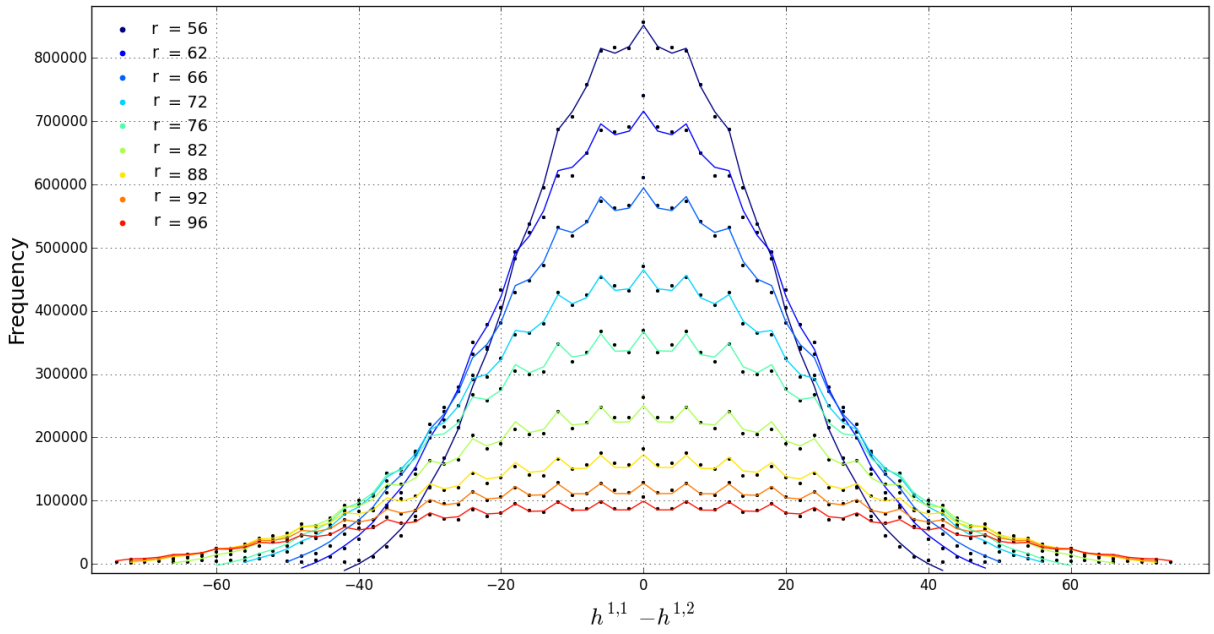


(B) Regression lines for few select odd r values, with $r > 51$.

FIGURE 2.5: *Plots of frequency against $h^{1,1} - h^{1,2}$ for various odd values of r. Each line represent a modified pseudo-Voigt profile based on the regression analysis for each curve. See 2.29a and for a plot of all even curves.*



(A) Regression lines for few select even r values, with $r \leq 54$.



(B) Regression lines for few select even r values, with $r > 54$.

FIGURE 2.6: *Plots of frequency against $h^{1,1} - h^{1,2}$ for various even values of r. Each line represent a modified pseudo-Voigt profile based on the regression analysis for each curve. See 2.29b for a plot of all odd curves.*

As these figures illustrate, each curve follows a pseudo-Voigt profile, however the individual data points seem to "jump" up and down, as if oscillating. It is this behavior of the data points which can be accounted for by the modified pseudo-Voigt model. To do the regression analysis, we used Python *lmfit* with a custom model which is just the modified pseudo-Voigt model. The parameters that were fitted are $(A_0, a, b, \sigma, \alpha)$. Due to mirror symmetry, $\mu = 0$. In Appendix 2.6.2.4, one can find a table with the value of every parameter for every curve as well as their reduced χ^2 values.

A few comments explicate the regression lines and the behavior of the distributions.

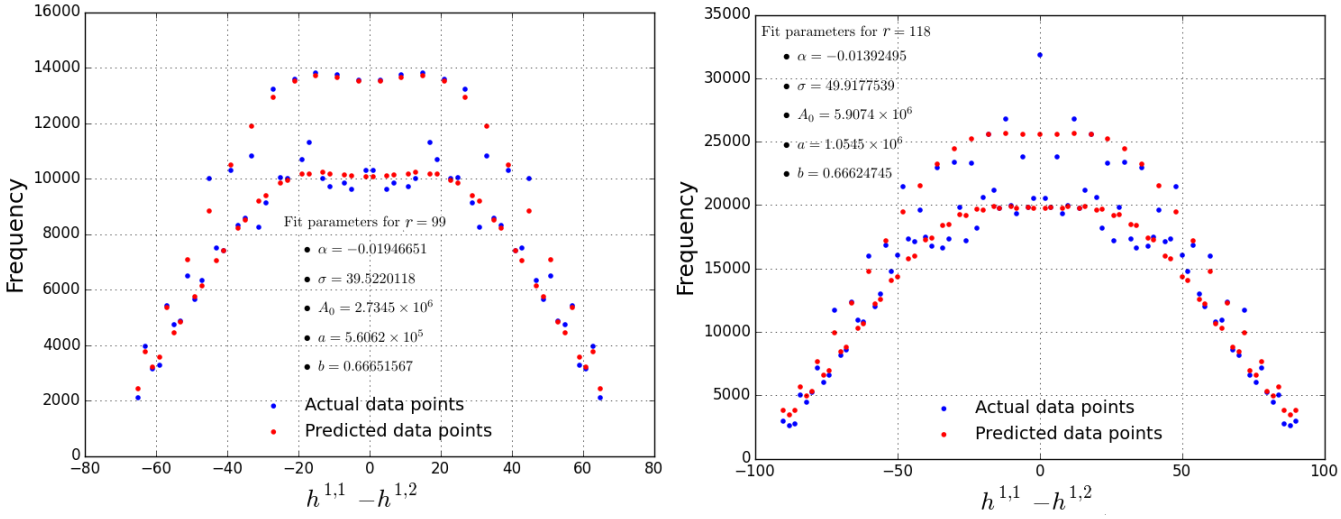


FIGURE 2.7: *These two plots serve two purposes. The first is to show how the modeled data should really look by using data points (red points) instead of the (perhaps misleading) lines (refer to Comment 1 below). The second purpose is to illustrate that as r becomes large (left plot has $r = 99$, right plot has $r = 118$), the actual data points deviate more and more from the modeled data, implying that there is a missing function in the modified pseudo-Voigt model which would allow one to describe the data at much lower frequencies.*

1. When we refer to the model as being an "excellent fit," it is principally a statement made by inspection of the curves and the data. If one inspects the reduced χ^2 values (Figure 2.30), the numbers are large, which statistically does not refer to a good fit. This is misleading however. Firstly, we need to consider that the number of parameters used in the model is five. This allows for a larger χ^2_R value. Secondly, the distribution is based on a discrete set of data. When doing a regression analysis using the modified pseudo-Voigt model, one obtains an equation which describes a continuous curve. Lastly, the frequency values span over several orders of magnitude. The tiniest deviation from a parametric model — in this case, the modified pseudo-Voigt profile — will be detected in cases where there is such a huge sample size. Typically the predicted model gives data points which are in the range of 0.02% to 3% accuracy from the actual data point. The tail behavior of the model is less accurate however, here the predicted values can be off from between 60% and 80%. For cases with a very poor fit, the last data point (large value of $h^{1,1} - h^{1,2}$) can have an error of up to 300% — this is another example of the model being less accurate at lower frequency. When one is dealing with such sample sizes, even a 1% error can give a difference of up to a couple of thousand. This difference summed over all the data points for a particular curve result in a large χ^2_R value. Due to the discussion in Section 2.2.4 we from now on ignore the χ^2_R as a test for model validation. Instead we opt for probability plots — which can also be seen in Section 2.2.4.

2. One obtains a continuous model to describe the discrete data, in reality, we should not be plotting fitted curves, but rather fitted data points — as can be seen in Figure 2.7. It is just illustratively more clear to display the curves. One could in principal work out out what the discrete approximation is to our continuous model.

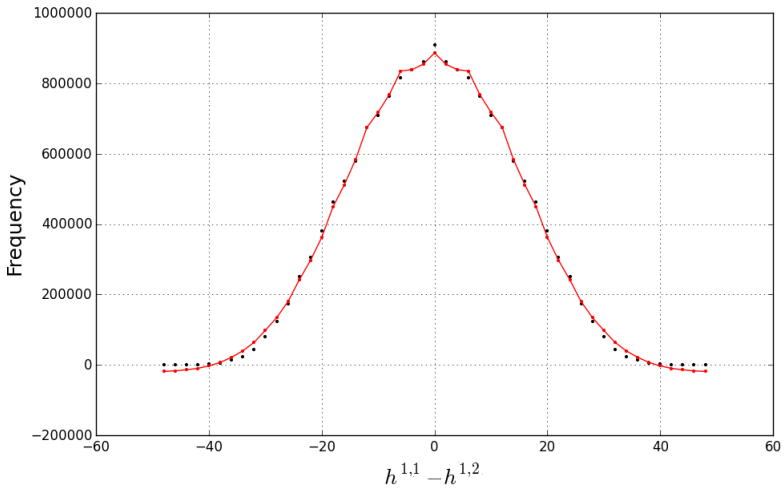


FIGURE 2.8: *By considering the entire frequency range, the model is not able to adequately describe the tail behavior. The model goes into the negative frequency range instead of tapering off to 0.*

3. Although the modified pseudo-Voigt distribution does a good job to model the behavior of the data, one still needs to address the problems experienced with our model at low frequency. A problem which is hidden, by virtue of our cut-off frequency, is that the tail of our models predicts negative values, Figure 2.8. There is a possibility that by having different variances σ_g, σ_c for the mixing of the two distributions (Gaussian, Cauchy), one could adjust the tail behavior. Introducing more and more parameters however does not always resolve the problem, as it is possible to over-fit the data. Yes, the model may be more accurate, but one loses physical significance. In a situation like ours, where one does not have any physical backing for choice in models, this line between fitting and over fitting is not so clear.

4. The odd distribution's behavior is more regular. In comparison to the even distribution, as one increases in r value, the behavior of the individual data points remain somewhat constant relative to the fitted curve. The even distribution becomes more and more irregular as one increases the r value. This suggests that there is an added parameter which seems as if it should be function of r. By regular and irregular we are referring to how well the data point is described by the model.

5. Both distributions become very irregular as the value of r becomes large ($r > 100$ and $r > 120$ for odd and even distributions respectively — see Figure 2.7). A large r value refers to curves which have a relatively low frequency. Again this suggests that the pseudo-Voigt model needs to some how have some function of r which "distorts" the behavior of the curves as r increases (by the looks of how the real data deviates from the modeled one, it seems that the missing functions is also oscillating in nature).

There exist, however, certain cases where the model is exact. In other words predicted values are the same as the actual values. This happens when one adjusts the frequency cutoff for each r curve individually. That is to say, we only examine data points with at least f_0 reflexive polytopes with a given value of r and $h^{1,1} - h^{1,2}$. If there are fewer than f_0 cases, the data is ignored.

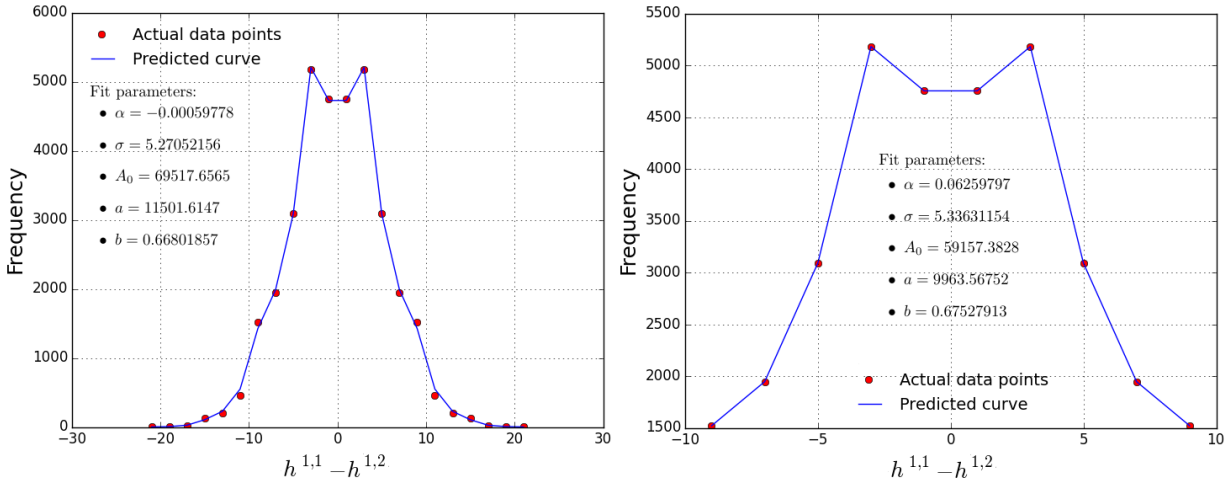


FIGURE 2.9: *Left plot shows the modeled line according to the modified pseudo-Voigt distribution with no cutoff frequency. We obtain a good fit to the data. The right plot has a cutoff frequency of* 460*, which is equivalent to a percentage cut off of* 9.68% *(calculated relative to the peak frequency for that r-curve). This curve is exact.*

This trend persists for all values of r, however what becomes apparent is that it's not the percentage cutoff frequency that determines whether or not one gets an exact fit, but rather, the number of data points that remains after the percentage cut of has been effected. Figure 2.31 gives a table of how many data points remain after an appropriate cut off percentage has been chosen to achieve a perfect fit. From this table we see that for even curves, one almost always requires 7 data points to achieve a perfect fit; for the odd curves, the number of data points is 10. The reason for this constant number throughout all the curves is that the centers of all the distributions for the various curves are all similar. As soon as one includes a larger number of data points we cannot achieve exact fits, and the model becomes approximate. At very low r values the number of data points remaining after cutoff are not too different to the total number of points. As r increase, the total number of points increase — the fact that we can achieve exact fits becomes less meaningful. The other models — even when including an oscillatory component were unable to give exact fits.

The model is thus much more accurate at low r values, and as r increases the actual data deviates more and more from the fit. This reinforces the statements from the comments that the pseudo-Voigt model can be modified further with some function $f(r, x)$ such that it will greatly improve the accuracy of the fit, and perhaps even become exact.

After the above analysis, we return to our goal of finding a single function describing the distributions. It is clear from the above that the function has to be a function of at least two variable, $f = f(x, r)$. We thus continue the analysis by plotting all the parameters vs r, in search for any relationships. We find that three parameters σ,b and α can be expressed in terms of r, the other parameters, while they show trends, do not give a precise relationship with r. For the even distribution of $h^{1,1} - h^{1,2}$, the r values range from 36 to 110, whereas for the odd distribution (see Figures 2.25a, 2.25b) the r values range from 37 to 99. By looking at Figure 2.10(a), it turns out that:

$$\alpha(r) = c_\alpha \ , \quad b(r) = c_b \ , \quad \sigma(r) = c_{\sigma_1} r + c_{\sigma_2} \ . \tag{2.2.4}$$

Our model of $h^{1,1} - h^{1,2}$ now looks as follows:

$$f(x, r, A_0, a) = (1 - c_\alpha)\frac{A_0(r) + a(r)\cos(2\pi c_b \cdot x)}{\sqrt{2\pi}(c_{\sigma_1} r + c_{\sigma_2})} e^{\frac{-(x)^2}{2(c_{\sigma_1} r + c_{\sigma_2})^2}} + c_\alpha \frac{A_0(r) + a(r)\cos(2\pi c_b \cdot x)}{\pi}\left[\frac{(c_{\sigma_1} r + c_{\sigma_2})^2}{x^2 + (c_{\sigma_1} r + c_{\sigma_2})^2}\right], \tag{2.2.5}$$

where $A_0(r)$ and $a(r)$ are two unknown functions yet to be determined (see Figure 2.10(b) for relationship plots). For replicating the plots as precisely as possible, one would need to keep the parameters, as they are, up to their 17 decimal values, without excluding terms as we have done. If one wants to reproduce the data from the model, one has to use the exact expressions. Making an approximation from an already approximate model leads to large errors.

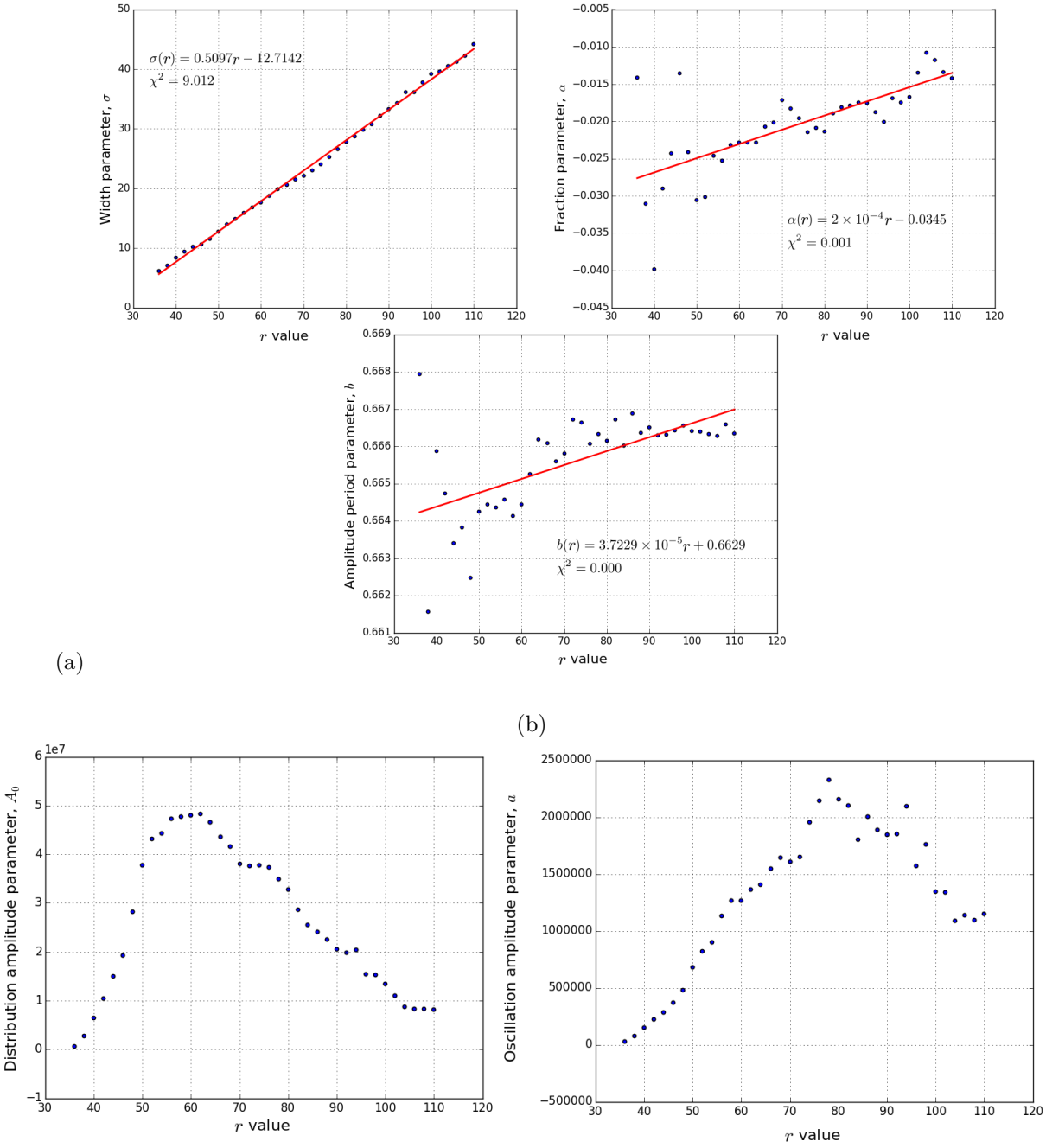


FIGURE 2.10: *For the even distribution of $h^{1,1} - h^{1,2}$. (a)The width parameter σ has a linear relationship with r such that $\sigma(r) = 0.5097r - 12.7142$. The amplitude period parameter, b, also has a linear relationship, however, since r is at most order 3 in magnitude, we can regard it as a constant such that $b(r) = 0.6629 \sim 2/3$. The same goes for the fraction parameter,α; we can regard it as a constant such that $\alpha(r) = -0.0345$. For odd parameter fit statistics see Figure 2.25a; (b) Plots of A_0 vs r (left) and a vs r (right). Both exhibit a similar pattern, however it is difficult to discern any nice relationships. For odd parameter plots see Figure 2.25b.*

The first plot in Figure 2.10.(a) in particular evinces a sinusoidal fluctuation about the mean. This again indicates the possibility of refining the plots by adding an extra function.

2.2.2 Analysis of $h^{1,1} + h^{1,2}$

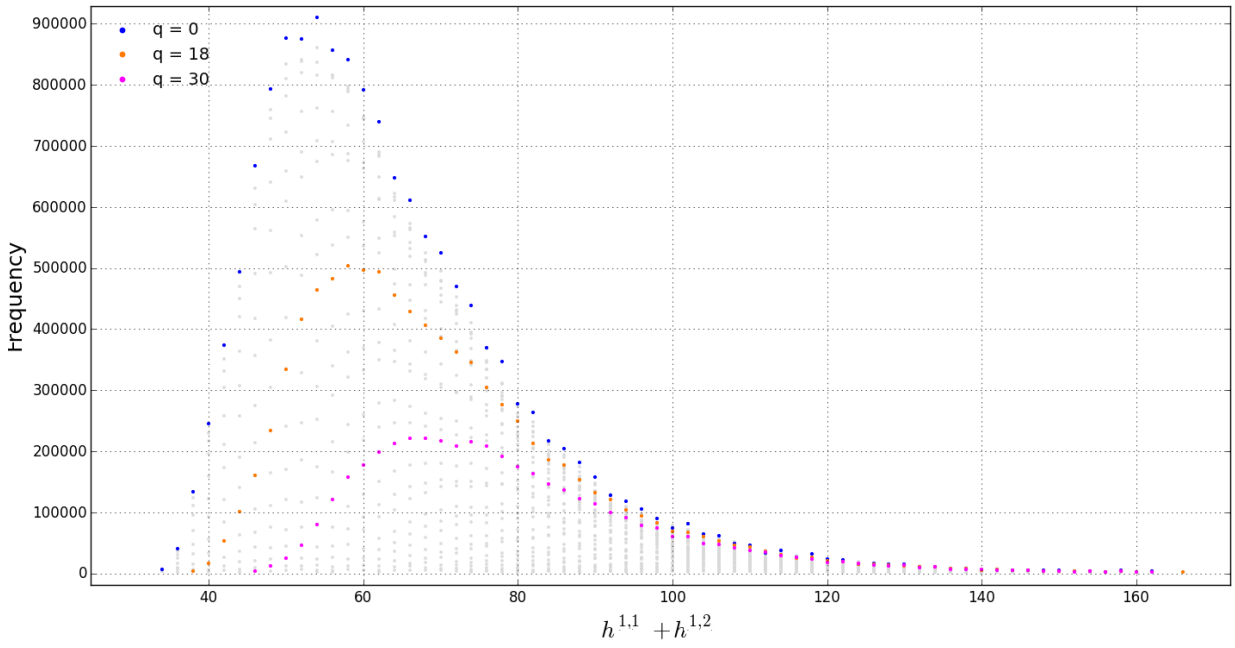


FIGURE 2.11:
Three curves ($q = 0, 18, 30$) within the even $h^{1,1} + h^{1,2}$ distribution. The transparent grey data dots are all the data plots for the distribution. Refer to Figure 2.32 to see the same example for the classification of odd curves within the odd distribution.

We begin by classifying the curves within the $h^{1,1} + h^{1,2}$ distribution (Figure 2.2) in an analogous way to how it was explained before. This time, we order the data by $h^{1,1} - h^{1,2}$ such that a single curve within $h^{1,1} + h^{1,2}$ can be identified by its q-value, where $q = h^{1,1} - h^{1,2}$. Due to mirror symmetry, the curve for $q = -a$ is the same curve as $q = a$, thus within our two-dimensional plots will only have $q > 0$. In continuation to the analysis on $h^{1,1} - h^{1,2}$, we use a cutoff frequency of 2000 and only present results from the even distribution within $h^{1,1} + h^{1,2}$, unless stated otherwise. As an example, illustrating the classification of curves within $h^{1,1} + h^{1,2}$, consider the curves $q = 0, 18, 30$ in Figure 2.11.

2.2.2.1 A Planckian Fit

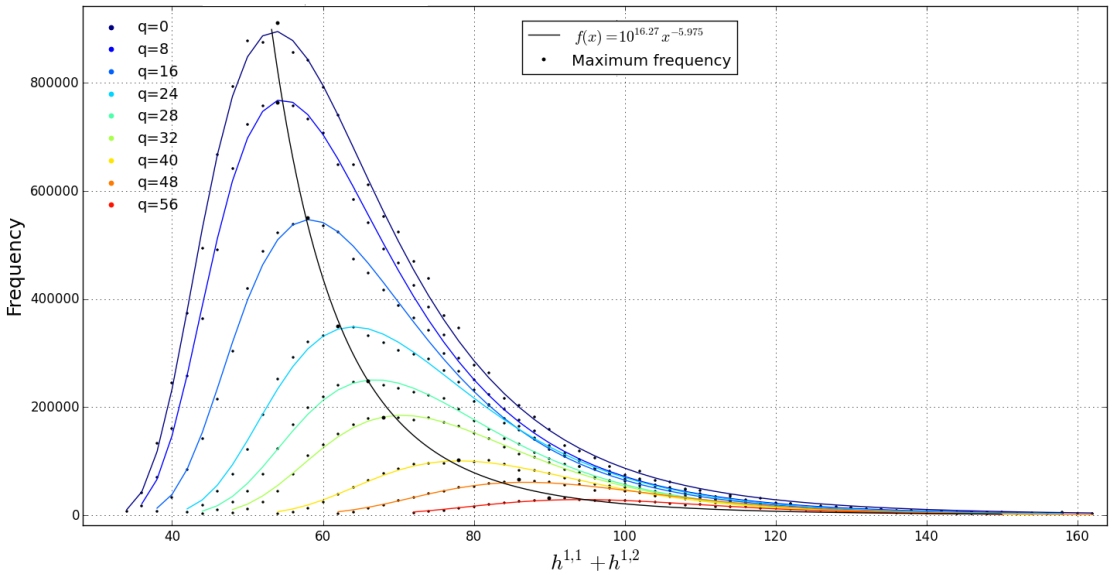
Each curve within the $h^{1,1} + h^{1,2}$ distribution behaves the same. Just like in the $h^{1,1} - h^{1,2}$ distribution, we do a regression analysis for each curve within the distribution independently, in the quest to describe the entire $h^{1,1} + h^{1,2}$ with a single function. The model we chose to describe $h^{1,1} + h^{1,2}$ is the simplest possible Planckian model

$$f(x, A, n, b) = \frac{A}{x^n} \frac{1}{e^{b/(x-22)} - 1} \tag{2.2.6}$$

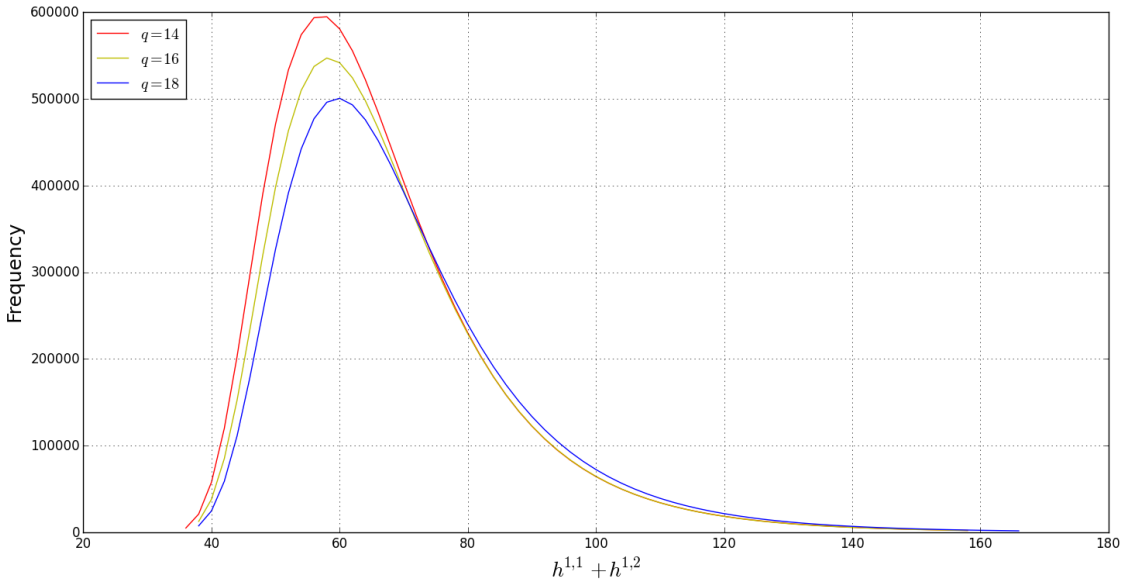
The parameter names in the fit results are the amplitude A, the power n, and some real constant b. The shift in x-axis is so that the distribution begins at 0 as the smallest $h^{1,1} + h^{1,2}$ above the cutoff is 22. The choice of a Planckian model in the above form is greatly motivated by the blackbody distribution $f(T, \lambda)$. The q curves within $h^{1,1} + h^{1,2}$ appear to behave in a manner analogous to the curves of constant T within the blackbody distribution. This is an initial trial. Later, we will discover additional structure in the distribution by trying

to mimic the blackbody distribution exactly. It turns out that the general behavior of the distribution is modeled very well, *cf.* Figure 2.12a.

Consider the maximum of each of the curves. As indicated in Figure 2.12a, we can fit the maxima to a curve as indicated using the data plotted for the given values of q. From the above analysis, the $h^{1,1} + h^{1,2}$ distribution behaves analogously to a blackbody spectrum — except for one small subtlety. It is in this subtlety that the added structure within $h^{1,1} + h^{1,2}$ is observed.



(A) *Lines of best fit from a regression analysis for a few select curves. The black data points represent the maximum frequency for that particular q-curve. the Black line is a line of best fit to describe the points of maximum frequency — this is analogous to a blackbody spectrum. See Figure 2.33a for the curves within the odd distribution.*



(B) *The curves segregate into three classes determined by the value of the even integer modulo* 6. *A similar pattern occurs in the odd distribution; see Figure 2.33b.*

FIGURE 2.12: *In the attempt to describe the data analogously to a blackbody distribution (a), we discover some subtle structure (b).*

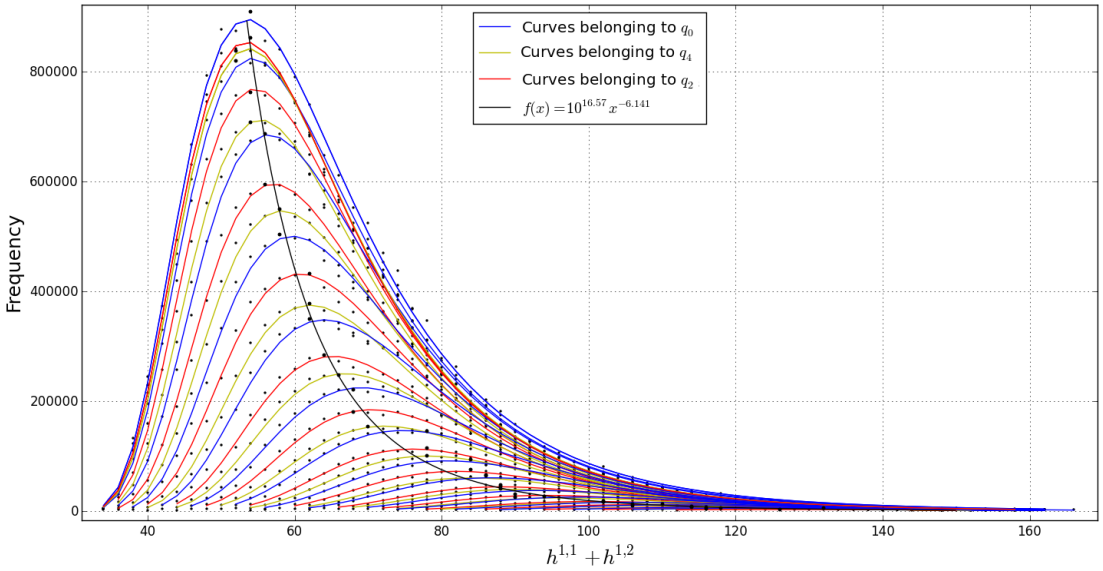
Just as was seen in Figure 2.2, $h^{1,1} + h^{1,2}$ appears to split up into two smaller distributions based on the

parity of $h^{1,1} + h^{1,2}$. One can then further break up both the even and odd distributions into three further sets. The manner we observed this added fine structure is again motivated by a blackbody spectrum. In a true blackbody distribution, the curves of constant T never overlap. However, if you consider the lines of best fit only, when looking at our distribution one sees an overlap of certain curves. For example, observe the following plot of curves which clearly cross in Figure 2.12b.

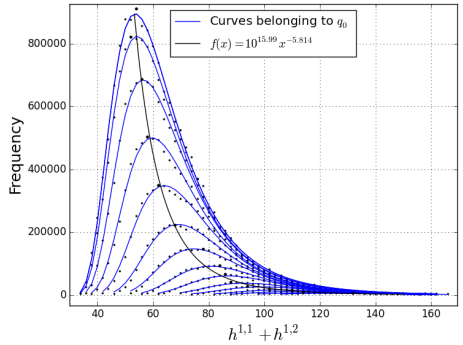
It turns out that this overlapping occurs consistently to the point where one can classify the curves (defined by their q value) into residue classes q_n distinguished by n mod 6. On the left hand side of the $h^{1,1} + h^{1,2}$ axis, the curves are ordered with red (residue class q_2) above yellow (residue class q_4) above blue (residue class q_0), whereas on the right hand side of the axis, the order is reversed. Similar behavior is observed in the odd distribution of $h^{1,1} + h^{1,2}$ with the curves in the residue classes q_1, q_3, and q_5 (see Figure 2.33b).

The clusters of curves constitute an entire set of mod 6 residue classes. These classes now define a set of curves which belong to very "nice" distributions that behave exactly like a blackbody distribution.[1] Compare, for example, a plot of the all the curves for even distribution of $h^{1,1} + h^{1,2}$, separated into their residue classes, Figure 2.13

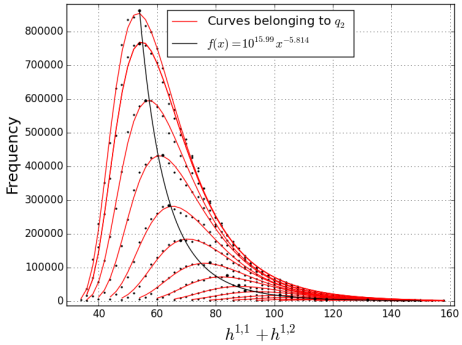
[1] Of course $h^{1,1} + h^{1,2}$ is not continuous. It is discrete. However, the structure of the best fit curve to the data points appears very similar to that of a continuous blackbody distribution.



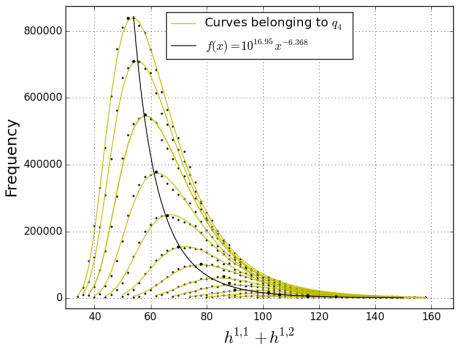
(A) *All the curves color coded according to what residue class their curves q_n belongs to.*



(B) *Family of curves all belonging to q_0.*



(C) *Family of curves all belonging to q_2.*



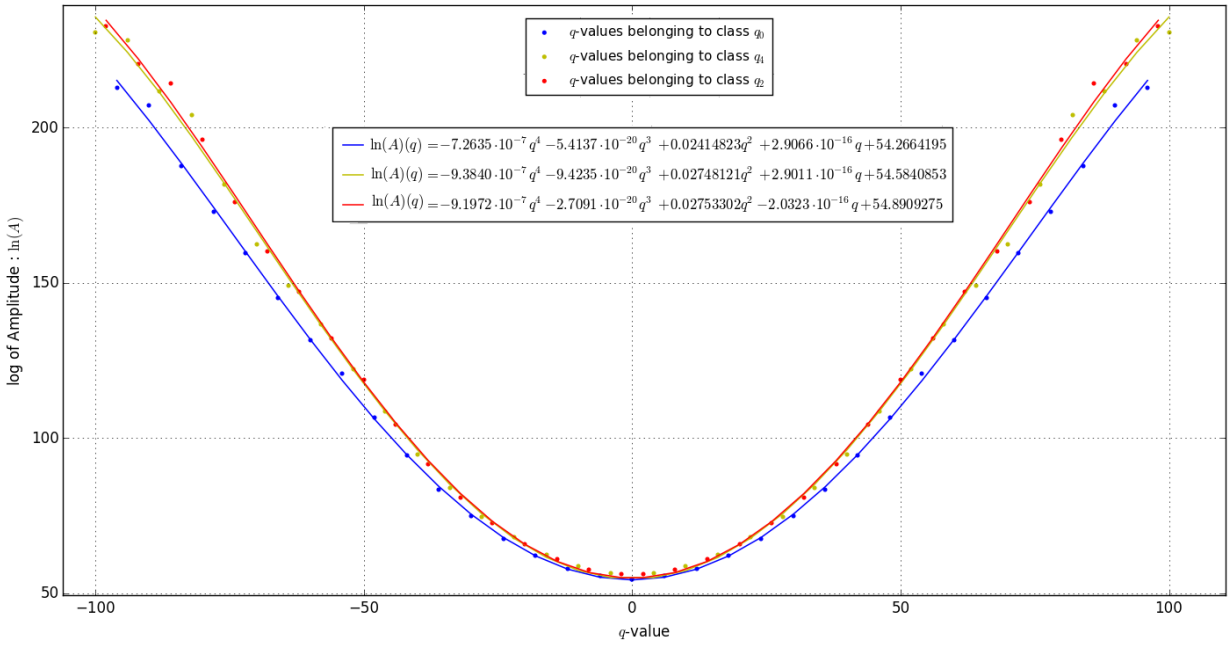
(D) *Family of curves all belonging to q_4.*

FIGURE 2.13: *We illustrate the added structure for even $h^{1,1} + h^{1,2}$ data, by displaying how the regression curves can be divided into residue classes. For the list of odd curves, refer to Figure 2.34.*

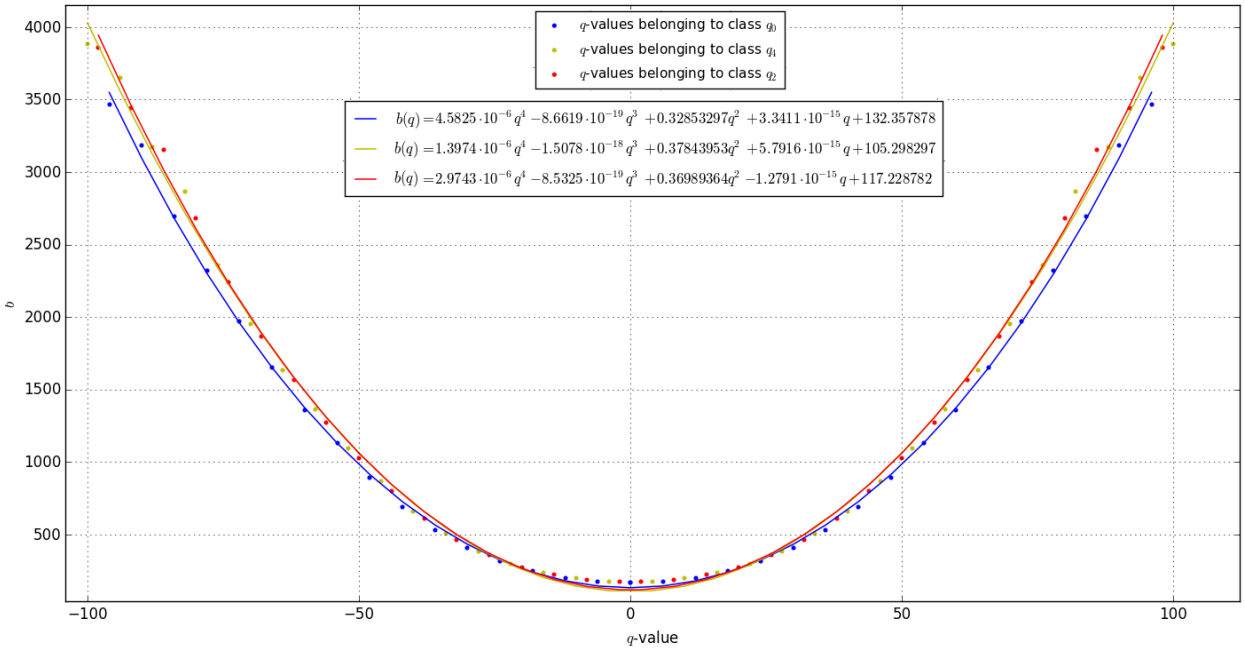
As a first approximation we have successfully modeled the general trend of the data. There is, however, a fine structure to the individual data points that we would like to model. Introducing an oscillating term in the amplitude, as seen in the analysis of $h^{1,1} - h^{1,2}$, unfortunately did not seem to improve the fits. Again, it appears that the least number of variables our functions can have is two, $f = f(x, q)$. This function will be slightly different in the values of coefficients, depending on which residue class one is modeling. Just as for $h^{1,1} - h^{1,2}$, we wish to express the parameters for the $h^{1,1} + h^{1,2}$ model (2.2.6) in terms of q. We

therefore write $A = A(q)$, $b = b(q)$, $n = n(q)$ and seek to find expressions for the coefficients.

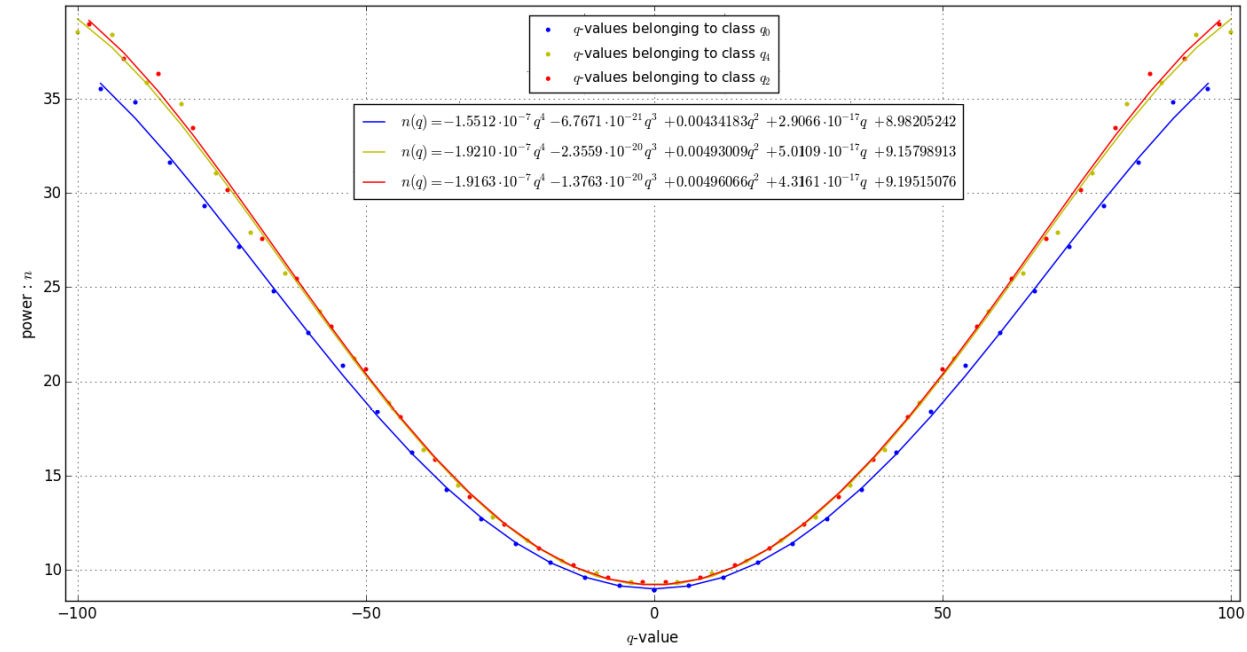
While the x-axis of $h^{1,1} + h^{1,2}$ has only positive q values — due to the fact the data points will overlap — when plotting them against the parameter values, we also have to consider the negative values of q. We present the various relationships (see Figure 2.35 for the plots for the odd distribution of $h^{1,1} + h^{1,2}$ analogous to Figure 2.14).



(A) *Plotting the q- value parameter vs the* $\log(A)$ *parameter.*



(B) *Plotting the q- value parameter vs the b parameter.*



(C) *Plotting the q- value parameter vs the power n parameter.*

FIGURE 2.14: *The parameter plots are color coded according to what residue class their q value belong to.*

Each distribution has an equation with different parameter values. However, the fact that we can express all the parameters in terms of q means we are able to get a generalized formula to describe the entire $h^{1,1} + h^{1,2}$ distribution — as long as the frequency is above 2000. For succinctness we use the following notation for the coefficients

$$A_{k,i}, \quad n_{k,i}, \quad b_{k,i} \ , \tag{2.2.7}$$

where the subscript $k = 0, 1, 2, 3, 4, 5$ refers to residue class q_k, and $i = 0, 1, 2, 3, 4$ refers to the coefficient of the i^{th} power of q. Thus, we have:

$$A_k(q) = \exp(\sum_{i=0}^{4} A_{k,i} q^i) \ , \quad n_k(q) = \sum_{i=0}^{4} n_{k,i} q^i \ , \quad b_k(q) = \sum_{i=0}^{4} b_{k,i} q^i \ , \tag{2.2.8}$$

where the matrix of coefficient values for $A_{k,i}, n_{k,i}$ and $b_{k,i}$ can be found in Appendix 2.6.3.2.[2] Our function (2.2.6) now is able to approximately describe the entire $h^{1,1} + h^{1,2}$ distribution:

$$f_k(x, q) = \frac{e^{\sum_{i=0}^{4} A_{k,i} q^i}}{x^{\sum_{i=0}^{4} n_{k,i} q^i}} \frac{1}{\left(e^{\frac{\sum_{i=0}^{4} b_{k,i} q^i}{(x-22)}} - 1 \right)}, \tag{2.2.9}$$

Of course there are certain constraints on the values of q. For a given k, q has to be an integer which falls within the residue class q_k. For even values of k, $x = 2m$, and for odd k, $x = 2m + 1$. We have $m > 12$.

A few comments about the analysis on the $h^{1,1} + h^{1,2}$ distribution are in order.

1. The Planckian model used in (2.2.6) could be modified in some manner such that there is some oscillating behavior in the amplitude. Any kind of oscillatory term we introduce, only has a mild effect on the model's behavior. As the q values exceed 100, the model is not able to describe the data very well.

2. Assuming one adds an oscillatory component to the model, the module used in python to do the regression analysis called *lmfit* is sensitive to the initial conditions set by the user. Since the model is a custom model, it is difficult to find the correct initial conditions such that the best fit line oscillates close to every point (as with $h^{1,1} - h^{1,2}$).

3. It is possible that the model used does not have the features required to describe the oscillatory "up and down" behavior of the data points. The Planckian model was chosen in that the $h^{1,1} + h^{1,2}$ distribution resembled a blackbody distribution.

4. In choosing a polynomial model for Figures 2.14a,2.14b,2.14c, we picked the lowest order polynomial that gave the best fit. Choosing the order to be four for all the plots appeared to be convenient. However, it is apparent that the parameter relationship plot in Figure 2.14b would be better described by a polynomial of order 6. One could use an order 6 polynomial for all the other relationships plots too, but doing so might not have any physical significance. One can achieve an arbitrarily good fit the larger the order of the polynomial used, but that does not necessarily mean the chosen model is the correct model.

2.2.3 The Distribution of the Euler Number

The Euler number for Calabi–Yau threefolds is

$$\chi = 2(h^{1,1} - h^{1,2}) \ . \tag{2.2.10}$$

[2] Perhaps it is important to state explicitly — due to potential confusion — that the coefficients $A_{k,i}$ refers to the natural logarithm of the amplitude values while A_k is the actual amplitude seen in the model.

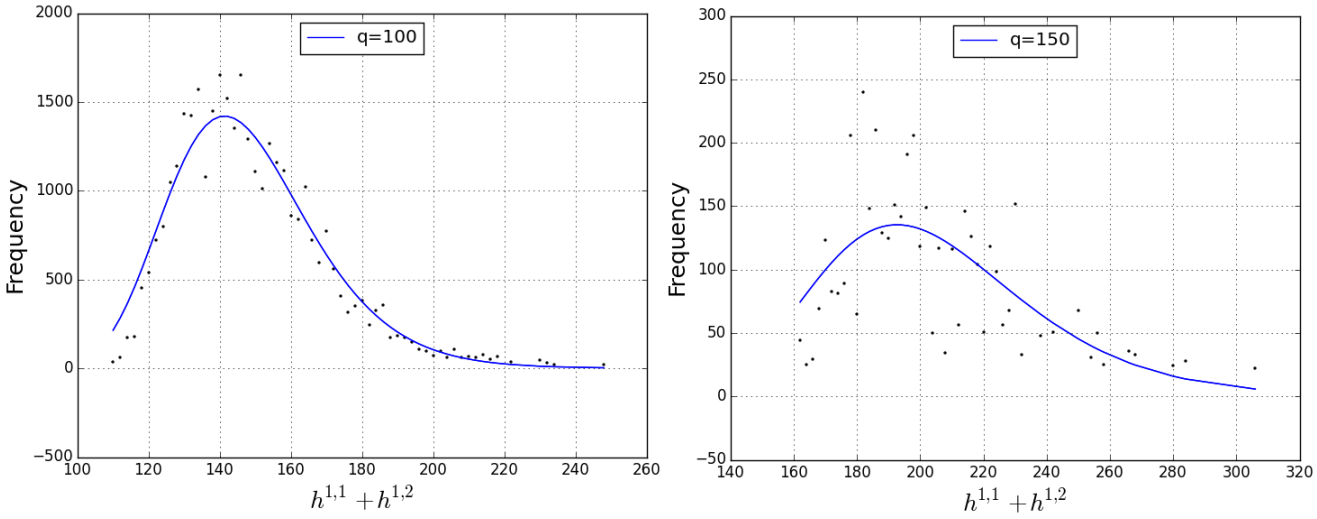


FIGURE 2.15: *Left figure is the fitted model(blue line) for a q value of 100 and right has a q value of 150. As the q-value increases, the scattering of the data points within* $h^{1,1}+h^{1,2}$ *increases to the point where the model works no longer. For an example of how the model begins to break down at large q, see Figure 2.36.*

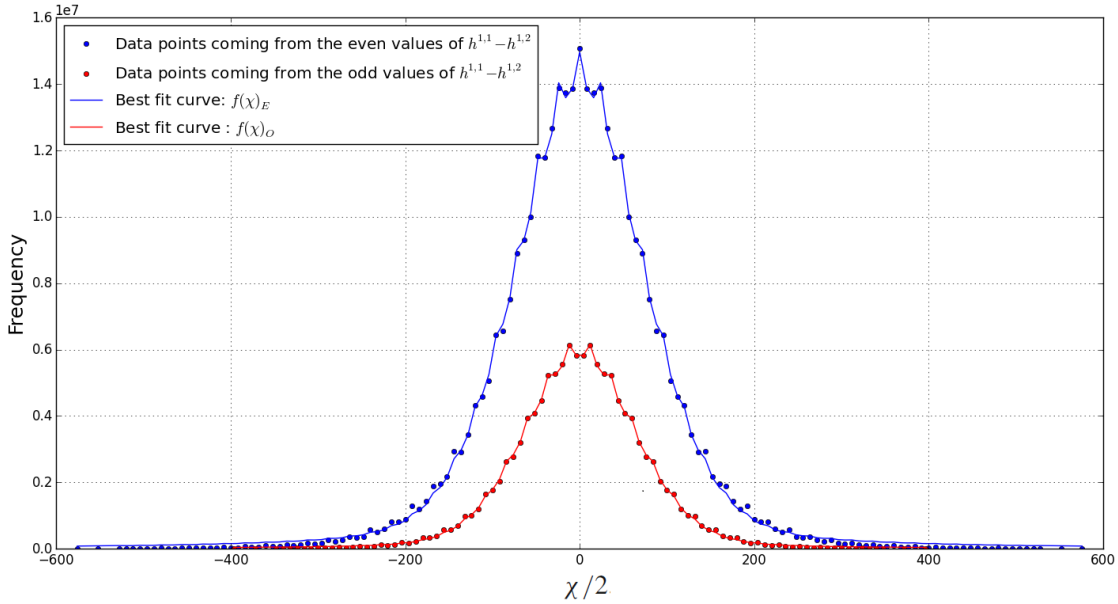
As mentioned previously, we are summing over all the various r-curves to obtained the full-Euler number distribution. A plot of χ versus frequency yields the pseudo-Voigt distribution. In particular, we can model the behavior of the distribution almost perfectly using the modified pseudo-Voigt curve (2.2.5) and (2.2.3), which is repeated here for convenience:

$$f(x, A, \sigma, \alpha) = (1-\alpha)\frac{A}{\sigma\sqrt{2\pi}}e^{\frac{-(x)^2}{2\sigma^2}} + \alpha\frac{A}{\pi}\left[\frac{\sigma^2}{x^2+\sigma^2}\right] , \tag{2.2.11}$$

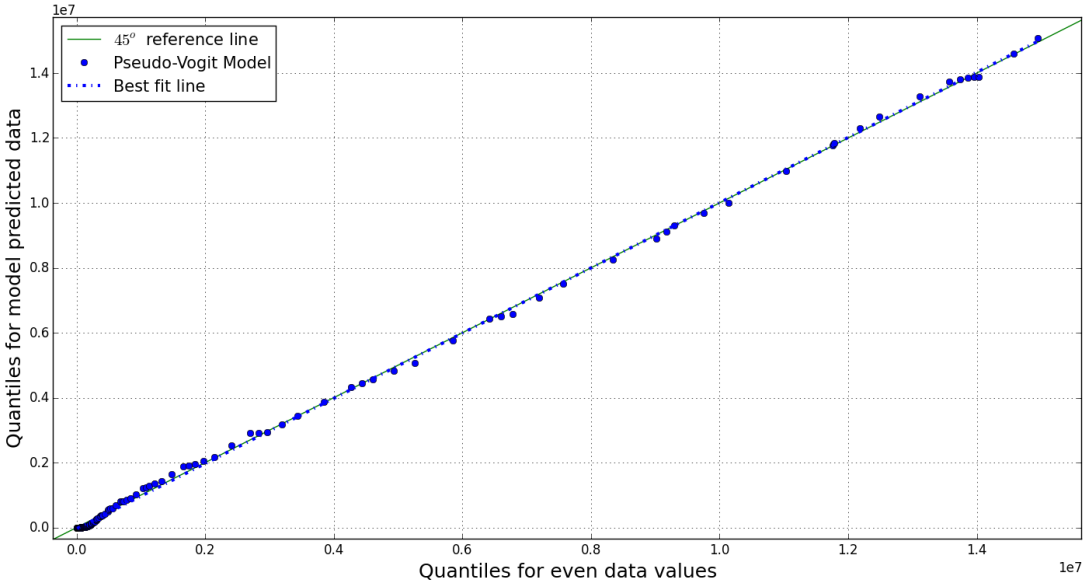
where

$$A(x, A_0, a, b) = A_0 + a\cos(2\pi b \cdot x) . \tag{2.2.12}$$

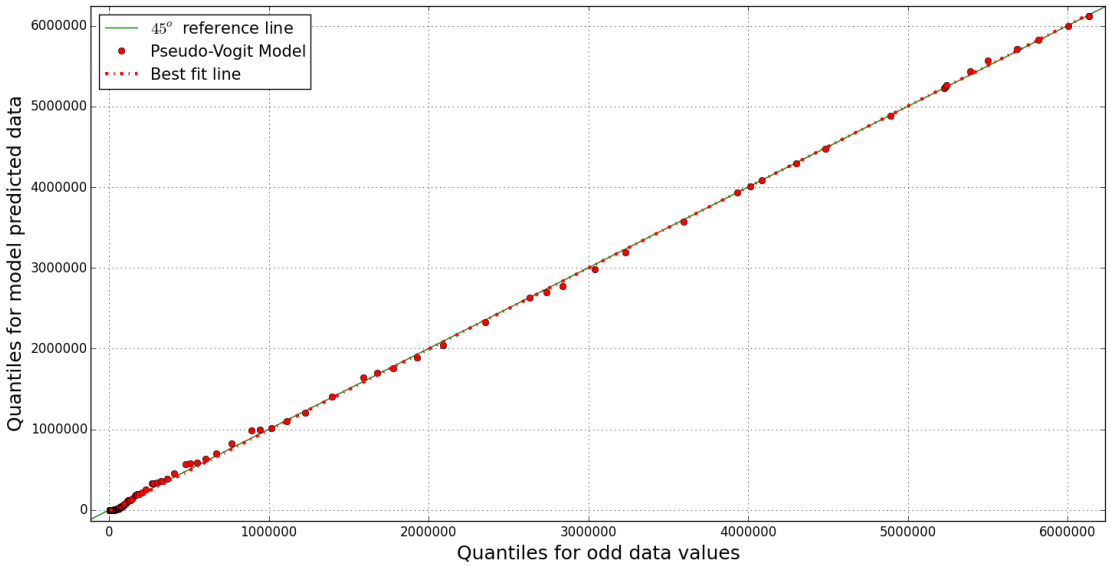
The results of the regression analysis for the Euler number distribution is presented in Figure 2.16a.



(A) *The distribution of Euler numbers fitted to a modified pseudo-Voigt curve. The blue curve* $f(\chi)_E$ *represents even values of* $\chi/2$*. The red curve* $f(\chi)_O$ *represents odd values.*



(B) *Probability plot for the even values of* $\chi/2$*. The model fits the data with* $R^2 = 0.99944$.



(c) *Probability plot for the odd values of $\chi/2$. The model fits the data with $R^2 = 0.99965$.*

FIGURE 2.16: *Various plots illustrating the actual fit of the modified pseudo-Voigt model. We can tell we have a good fit by looking at the probability plots for the quantiles of the standard pseudo-Voigt distribution vs quantiles for the actual data. The. The R^2 values in (b) and (c) are given relative to the line $y = x$.*

The fitted parameter values for $f(\chi)_E$ corresponding to even values of $h^{1,1} - h^{1,2}$ are:

$$(A_0, \sigma, \alpha, b, a) = (1.9032 \times 10^9, 75.8305889, 0.00718459, 0.58347826, 8.7427 \times 10^7) \ . \tag{2.2.13}$$

Likewise, the fitted parameter values for $f(\chi)_O$ corresponding to odd values of $h^{1,1} - h^{1,2}$ are:

$$(A_0, \sigma, \alpha, b, a) = (7.6043 \times 10^8, 64.9735680, 0.00549425, 0.83357720, 3.6881 \times 10^7) \ . \tag{2.2.14}$$

Although χ is only even, the two curves originate from the fact that if you take $\chi/2$ you get even and odd values. The two curves arise from the parity of $\chi/2$ and are presented in Figures 2.16a.

2.2.4 Goodness-of-fit

A goodness-of-fit test is implemented as a means of testing how well a given model describes some given data. Typically the model validation process consists of only quoting a single statistically generated number like the R^2, χ^2 or p values. Based on the size of this number, one then makes inferences on how well the chosen model fits the observation. One needs to be careful however of misusing such indicators as an absolute measure for assessing goodness-of-fit.

For a structural equation model (SEM) — in our case, the modified pseudo-Voigt and Planckian models — this assessment is not so straight forward as it would be for a simple regression analysis. To quantify the predictive power of an SEM, a single statistical test does not suffice - in fact, there is no single test. According to [89], the best one can do is assess three different aspects of what it means to have a good fit, these are: overall fit, comparative fits to a test model and model parsimony.[3] The only real test available

[3]Parsimony refers to the ability of a model to give a certain degree of fit whilst having the least required number of predictor variables.

is the chi-squared (χ^2) test, when it comes to overall fit, this χ^2 statistic is the most popular test. The χ^2 test compares observed and predicted correlation matrices with each other, and so, statistical significance is evaluated based on the value of χ^2. A large χ^2 value signifies a considerable difference between the correlation matrices. A low value indicates there is little statistical difference between matrices. Since the χ^2 test is between actual and predicted matrices only, when looking for overall fit, one searches for non-significant differences between the correlation matrices. Often, rather than presenting the χ^2 or χ^2_R (the chi-squared value relative to the degrees of freedom for the model) value, a p value is given instead. The p value, in a way, informs us whether one should reject a null hypothesis or not. A small p-value suggests that the differences in observed vs. predicted are too large to be consistent with the null-hypothesised model i.e. assuming the null-hypothesised model, the probability of observing what we did is relatively small, suggesting either an absolutely fluke experimental outcome or an incorrect model null-hypothesis. The p-values can be determined by a p-value calculator by inputting the χ^2_R value. There is no standard way of choosing a significance level for the p-value, but typically $p < 0.05$ is considered statistically significant.

In general, statistical non-significance given by appropriate values of the χ^2 fit statistics is adequate. However, one must be careful of drawing similar conclusions for structural equation modeling. The fit statistic makes a statement of the correlation matrices only, not about whether or not the correct model is identified. This is largely due to the sensitivity to sample size of the χ^2 test. In our analysis, the sample size (number of reflexive polytopes) is enormous — almost one billion! For large samples (> 200) the χ^2 test will give significant differences for any model used. This sensitivity to a sample size, together with an *effect size* and *alpha value*, is related to what one calls the power of a test - the probability of not incorrectly accepting a null hypothesis that is actually false.

Without worrying too much about what an effect size and alpha value is; for any alpha value, the greater the sample size, the greater the power of the statistical test. However, increasing the sample size beyond a certain amount, can result in the test having “too much" power[4]. Perceived effects in very large sample sizes, will always become significant[5]. Observe how in tables 2.30 and 2.37 the χ^2_R values for all the different curves is extremely large, naively indicating that we have a horrible fit — which would be an incorrect conclusion.

It is clear from the above discussion that we cannot use the χ^2 or p values in validating our choice in model. What is not so clear, is the additional subtlety in using purely statistical means to asses goodness-of-fit for our data. This subtlety lies at the heart of almost all statistical tests — the construction of a null hypothesis. The term frequency, as used in the statistical sense, refers to the number of outcomes for a certain event. The measurement of this outcome will often have certain known or unknown factors affecting it. These tests check for the probability that the errors found are too significant to be solely do to random variations in the data. For example, assume that statistical tests give non-significant results. If the residuals are small enough to be considered random errors in the measurement of the frequency, we could say that the model is appropriate. If however, the residuals are too large or present additional structure, we could say the model is good, but not quite the correct one as the residual errors are not “random enough". In our case, there is no notion of measured frequency and error in measurement of frequencies. Our frequencies are generated as a result of a combinatoric calculation. Statistical tests assume that the input is from measurement and observations (obeying some null-hypothesis), thus they are inherently constructed with this notion in mind. By inputting our data, the tests are trying to calculate something from a data set which

[4]Power is the probability that you do detect deviations from your null-hypothesised model, when the null-hypothesised model is, in fact, incorrect

[5]Conversely is also true, for extremely small sample sizes, any effect which should be significant, becomes insignificant

does not obey the very assumption they use in their calculations. We are not exactly clear how much this affects statistical outcomes, but it is important to keep in mind.

How do we validate then, that our chosen models are a good fit, or that our model is the best one at describing the data? We implement graphical methods. The first graphical method is obviously through pure inspection — this is not quite statistically quantifiable. There is a statistically based graphical method to asses goodness-of-fit called probability plots, Q-Q plots or P-P[6] plots. These plots were initially constructed to test the "normality" of a data set when the sample size is too large too depend on the χ^2 and p values. In principle, a standard probability plot tells you the likelihood that the a sample's distribution of data obeys a normal distribution — hence checking for normality. The answer to the question is not given by a statistical value, but rather by a graphical representation — from which one can extract statistical numbers. If the plotted data on this probability plot is a straight line, then we can determine that the sample set is normally distributed.

We can extend this concept further: we can take two different samples, and take a probability plot to determine if two data sets come from populations with a common distribution. Such a probability plot is referred to as a Q-Q (quantile-quantile) plot. Extending this concept one more time — as for our use — we will take the quantiles of our theoretical distribution (the modified pseudo-Voigt and Planckian profiles) as our "first sample" and plot them against the quantiles of our data as our "second sample", this will give us our probability plot. In all the probability plots, it is the quantiles of the respective data sets which are plotted against each other.

Quantiles are basically just a generalization of quartiles. For example, the k^{th} percentile of a set of values divides them, such that the number of values which lie below is $k\%$, and the number of values which lie above is $(100-k)\%$. The 25th percentile is the lower quartile or the $\frac{1}{4}$ quantile. Quantiles are the same as percentiles, but indexed by sample fractions rather than by sample percentages. Suppose that $p \in [0,1]$, the aim is to find the value that is the fraction p of the way through the ordered data set. As an example, if $p = \frac{1}{2} = 0.5$, we want to know what is the value that sits at $p = 0.5$ of the way through i.e. half way. The value that sits there (this value may have to be interpolated) will be called the quantile for the fraction $p = 0.5$. There are many different algorithms for generating the quantiles for a given data set, we use python to generate the quantiles in a manner similar to that discussed above. For an ordered data set, $x_1 \leq x_2 \leq x_1 \ldots \leq x_{n-1} \leq x_n$, the most common way of calculating quantiles is to first compute the empirical distribution function:

$$F(x) = \frac{1}{n}\sum_{i=1}^{n} = 1(x_i \leq x), \quad x \in \mathcal{R}, \tag{2.2.15}$$

and then define the quantile function to be the inverse of $F(x)$:

$$F^{-1}(p) = min\{x \in \mathcal{R} : F(x) \geq p,\ p \in (0,1)\}. \tag{2.2.16}$$

By generating the quantiles of some theoretical model and comparing them to the quantiles of a given data set of equal length, one can determine if the data set belongs to the same distribution as the data set belonging to the theoretical model — *i.e.*, does the data fit the model. If the quantiles are roughly equal the plots will all be more or less on a straight line.

[6] A P-P plot is the plot of the cumulative distribution frequency of the one data set against the CDF of the other. P-P plots are not as useful as Q-Q plots, thus are seldom used.

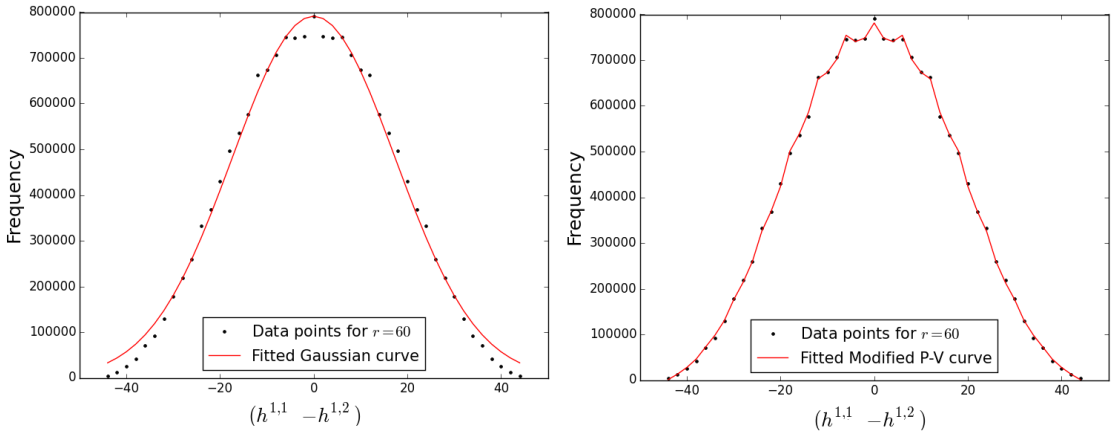
In probability plots :

1. The length of data set needs to be equal. For unequal lengths, one must perform an interpolation of data.

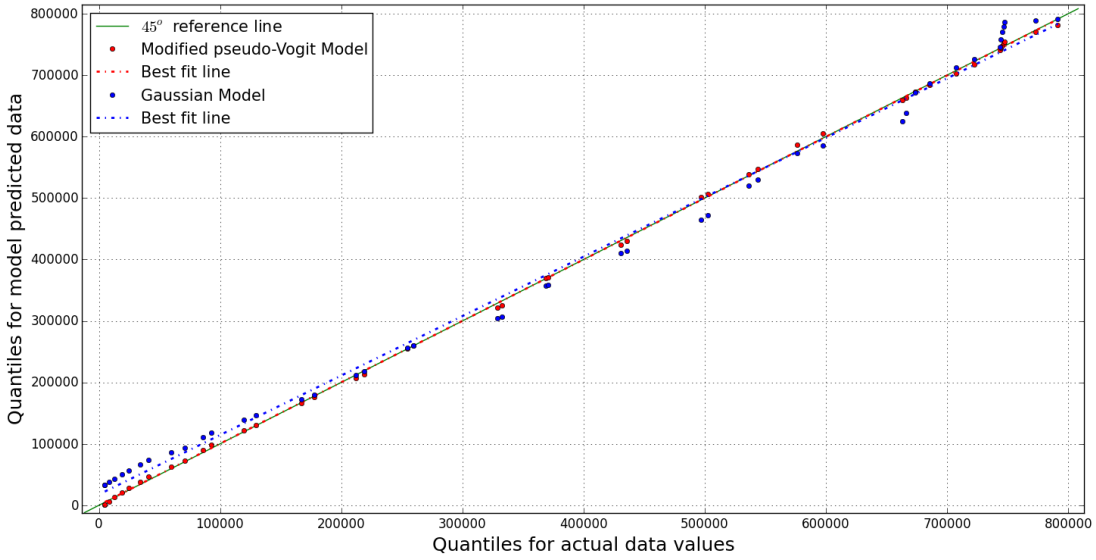
2. If two identical data sets were compared to one another, the points would lie exactly on a 45 degree line. Thus, for two different data sets, the deviation from this reference line determines the likelihood that the sets belong to similar distributions. To quantify this likelihood, one can calculate the R^2-value of the data, relative to the $y = x$ reference line.

3. Q-Q plots are not only limited to determining similarity in data sets. By analyzing the deviations which occur, one can determine how the scale and location of the data is shifted - the data would follow some line $y = mx + c$, where m, c would be the estimates of these shifts in scale and location. Also, from the distribution of points above or below the reference line, one can infer aspects of the tails and skewness in the data.

Consider the following curves for the $h^{1,1} - h^{1,2}$ distribution with $r = 60$ in Figures 2.17a and 2.17b.



(A) *Best fit curve for $r = 60$ based on the left: Gaussian model, right: modified pseudo-Voigt model.*



(B) *Probability plot for Figure 2.17a. The x-axis represents the quantiles for the actual data, the y-axis represents the theoretically predicted quantiles — dependent on the model chosen (red: modified pseudo-Voigt model ($R^2 = 0.99974$); blue: Gaussian model ($R^2 = 0.99334$). The R^2 values are not relative to the best fit lines, but are relative to the 45° reference line $y = x$. The closer the R^2 value is to 1, the more similar the predicted quantiles are to the actual ones, thus, the better the model describes the data.*

FIGURE 2.17: *Using probability plots, we are able to statistically see which model provides the better fit. We employ such graphical methods as standard goodness-of-fit tests such as the χ^2 fail to give meaningful results.*

For the $h^{1,1} + h^{1,2}$ distribution we just plot the data of $q = 2$ together with the corresponding probability plot in Figure 2.18.

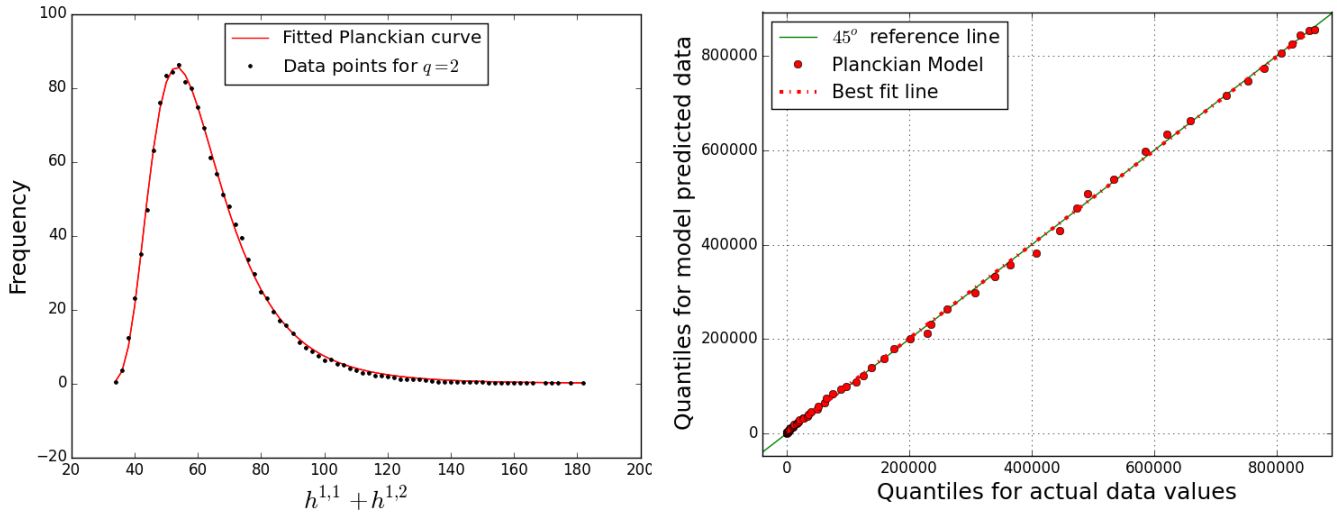


FIGURE 2.18: *Left: best fit curve of $h^{1,1} - h^{1,2}$ distribution for curve $q = 2$ based on the Planckian model. Right: probability plots of our fitted theoretical Planck model vs the $q = 2$, $h^{1,1} - h^{1,2}$ distribution.*

In its current form, the probability plots do not allow us to calculate p-values of the various models. This due to the same issue encountered previously. If one however standardizes the data according to the Z-standardization:

$$Z = \frac{X - \mu}{\sigma}, \tag{2.2.17}$$

where μ and σ are the mean and standard deviation, it is possible to calculate the p- values since the magnitude of each sample gets rescaled. The probability plot of all the models is displayed in the Appendix, with the relative p-values for each model — Figure 2.26g and Figure 2.26h. What we see is that the modified pseudo-Voigt is statistically the model which provides the best fit.

2.2.5 Implications for Physics

Calabi–Yau threefold compactifications of string theory have been the traditional approach to obtaining interesting phenomenological models. The plethora of geometries and configurations, ranging from heterotic strings on Calabi–Yau threefolds endowed with stable bundles, to D-brane probes on local Calabi–Yau varieties, to F-theory compactification on elliptic fibrations, has over the years justified the landscape and inspired various statistical analyses of the space of vacua.

Of particular interest have been the investigation of further structures in the Kreuzer–Skarke database, including identification of "the tip" where Hodge numbers are small [83, 71, 90], the top bounding curves where Hodge numbers are large [91], identifying elliptically fibered threefolds [92, 76, 77, 93], finding further fibrations such as K3-fibers [81, 94], or a step-by-step construction of all possible smooth Calabi–Yau hypersurfaces from the reflexive polytope data [66], etc. Now, it should be emphasized that each of the some 473 million reflexive polytopes admits, as an ambient toric variety, many[7] so-called maximal projective crepant

[7] The actual numbers are not yet known, but even up to $h^{1,1} = 7$, we already see from tens to thousands and with the number increasing potentially exponentially as we go up in Hodge number [66].

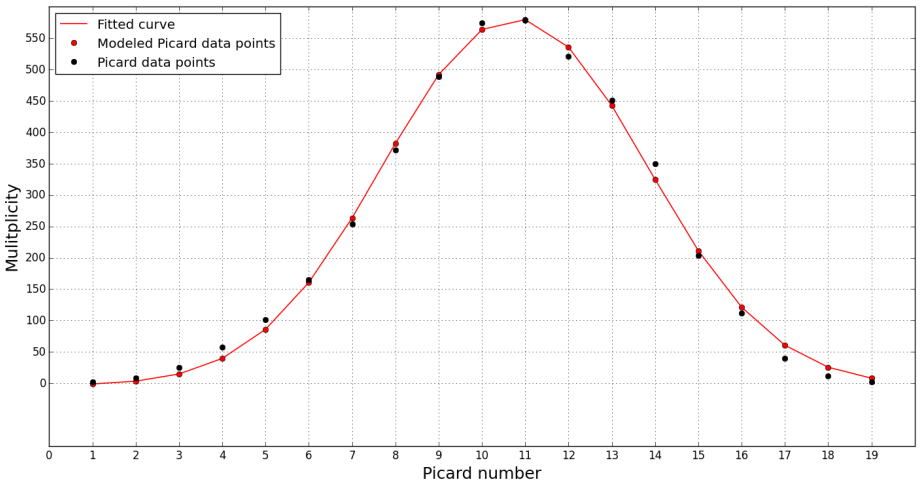
partial (MPCP) desingularization, each of which gives rise to a different Calabi–Yau threefold. Therefore, the actually number of Calabi–Yau threefolds from the Kreuzer–Skarke database is many orders of magnitude larger than 10^{10}. While manifolds coming from the same reflexive polytope have different geometrical data such as triple intersection numbers, which in the standard embedding in heterotic compactification correspond to Yukawa couplings, they do share the same Hodge numbers because these, by virtue of (2.2.1), depend only on the combinatorics of the polytope. We need to wait for significant theoretical and/or computational advances to have the full data of the Hodge pairs in view of the Calabi–Yau manifolds themselves, which might give new statistics. It would be perhaps even more interesting if the statistic remain largely the same, thereby hinting at some universality in the distribution of such topological data.

In the context of the recent works on F-theory, it is an important fact the vast majority of the Kreuzer–Skarke threefolds are elliptic fibrations over some complex surface, and in fact birational to [92, 93, 94] a Weierstrass model. For example, some 10^6 alone [92] come from elliptic fibrations over $\mathbb{P}^2$. Therefore the Kreuzer–Skarke dataset is directly relevant to F-theory. In the more classical context of heterotic strings, the Hodge numbers dictate the number of (anti-)generations in the standard embedding. In our above plots, the Euler number ± 6 indicate the three generation models. The generic paucity of $\chi = \pm 6$ manifolds led to the industry of non-standard embedding where extra vector bundle and Wilson line information is needed. The advantage of F-theory models is that the compactification data comes only from the Calabi–Yau manifold. In particular, the intersection theory of the cycles and fiber-degeneration structure determine the gauge group, anomaly cancellation, matter content, and Yukawa couplings. Much of this can be extracted from the polytope data.

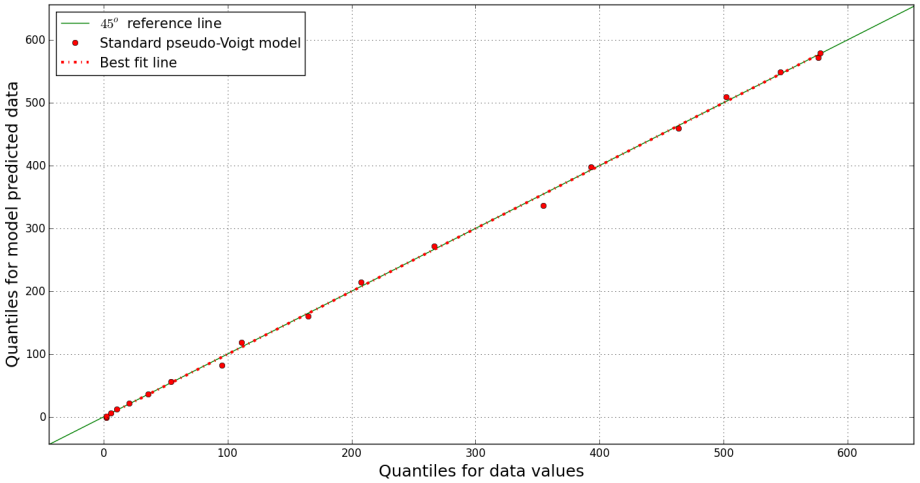
F-theory compactifications on threefolds, resulting in six dimensional gauge theories have been considered from the point of view of systematically classifying the base complex surfaces [93] and the statistics have been performed therein. Non-toric bases were considered and a number of Calabi–Yau threefolds beyond the Kreuzer–Skarke data were found. It is remarkable that the overall distribution of Hodge numbers remains largely unchanged. Indeed, in unpublished work of Kreuzer–Skarke, where they extended the hypersurface in toric fourfolds to double hypersurfaces in fivefolds, obtaining some 10^{10} more manifolds and the shape of Figure 2.1 persists. All these point to the Kreuzer–Skarke data being a robust representative in the space of Calabi–Yau threefolds. Our distribution subsequently seems a representative a sample, and we speculate that analyses of string vacua, in any context, should be thus weighted. For example, in study of the "typical" number of generations in four dimensional heterotic compatification, or of charged matter in six dimensional F-theory compactification, one should superpose our pseudo-Voigt profile.

2.3 Calabi–Yau Twofolds: K3 Surfaces

As noted in the Introduction, there are 4319 data points, corresponding to hypersurfaces as Calabi–Yau twofolds, *i.e.*, K3 surfaces, in reflexive three dimensional polytopes. Being algebraic K3 surfaces, there is only one relevant topological invariant, the Hodge number, $h^{1,1} = 19$. However, there is a further refined algebraic quantity for the K3 surface X, the rank of the Neron–Severi lattice $H^2(X;\mathbb{Z}) \cap H^{1,1}(X)$, which is the **Picard Number** $\rho(X)$ and which enumerates the number of divisors on the surface up to algebraic equivalence. The Picard numbers of the 4319 K3 surfaces were computed in [74]. We present the distribution thereof in Figure 2.19a.



(A) *For K3 surfaces, the multiplicity is plotted against Picard number with a pseudo-Voigt fit.*



(B) *Probability plot for the multiplicity quantiles vs the fitted standard pseudo-Voigt quantiles. The R^2 value is* 0.99908.

FIGURE 2.19: *Using probability plots, we are able to statistically see which model provides the better fit. We employ such graphical methods as standard goodness-of-fit tests, such as the χ^2 test, fail to give meaningful results.*

We only used the standard pseudo-Voigt profile as the modified one did not change the fit significantly. Here are the fit statistics for best fit curve: $(A, \mu, \sigma, \alpha) = (4517.45, 10.76, 2.97, -0.031)$, as shown in Figure 2.19.

What is interesting about Figure 2.19a is that the “oscillations" of the actual data points above and below the modeled curve is very apparent, yet modifying the pseudo-Voigt profile is unable to give any significant improvement. This leads to two potential conclusions: (a) The pseudo-Voigt profile is not the best profile to use in combination with an oscillatory component; (b) The manner in which the oscillations occur is not so straight forward as introducing simple cosine function. An interesting exercise would be to superimpose a cosine function along the distribution, by rotating it as one traverses the profile. As long as the wavelength, amplitude and angle of rotation are all small enough, the continuously rotated cosine function should remain a function everywhere along the profile.

2.4 Calabi–Yau Fourfolds

The analysis of the four fold data is performed in the same spirit as the threefold data. We aim to look for patterns in the frequency plots. Due to complex conjugation and Poincaré duality, the only topological invariants of fourfolds that vary are $h^{1,1}$, $h^{1,2}$, $h^{1,3}$, and $h^{2,2}$. Three of these are independent [68]:

$$h^{2,2} = 44 + 4h^{1,1} - 2h^{1,2} + 4h^{1,3} \ . \tag{2.4.1}$$

We compiled a database for the frequency of the triplets $(h^{1,1}, h^{1,2}, h^{1,3})$ to then obtain the following data structure

$$(h^{1,1}, h^{1,2}, h^{1,3}, f) \ .$$

Since one expects mirror symmetry within the invariants $(h^{1,1} \pm h^{1,3})$ [95], a plot of $h^{1,1} - h^{1,3}$ against $h^{1,1} + h^{1,3}$ (Figure 2.20) should be symmetric about the line $h^{1,1} - h^{1,3} = 0$.

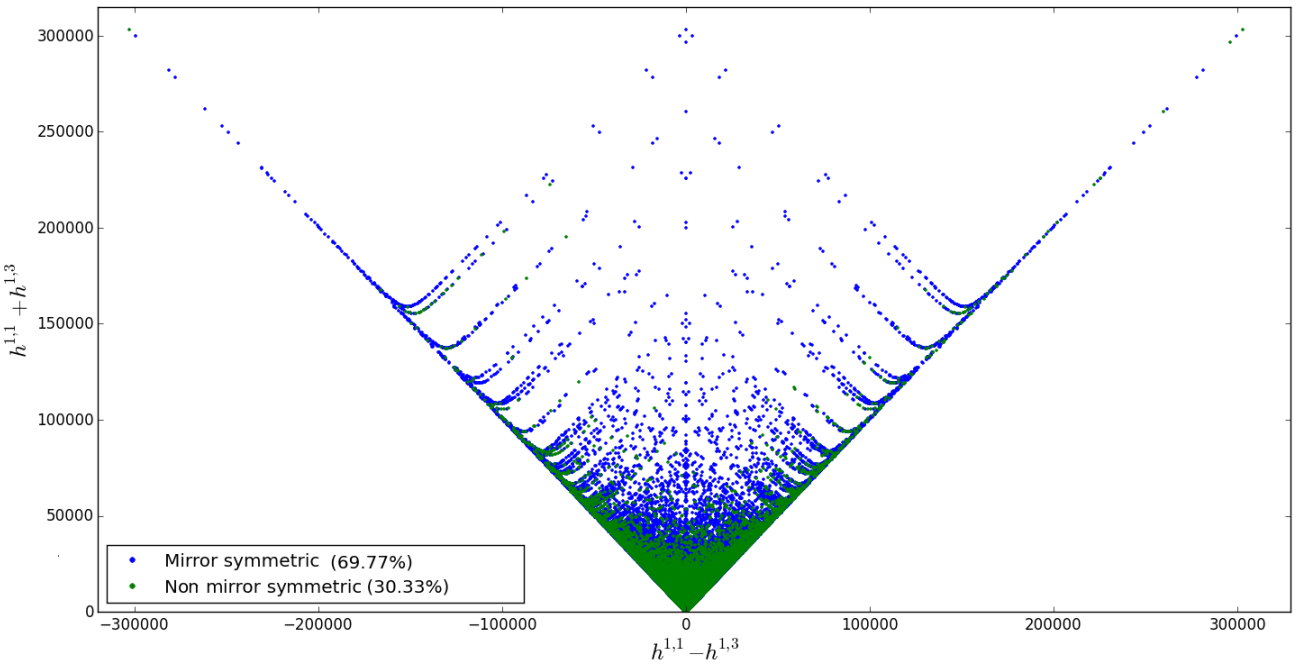


FIGURE 2.20: *The blue points correspond to manifolds with a mirror symmetric counterpart in the data set.*

Doing a quick analysis of the data yields the following observations: only partial mirror symmetry is found. For 69.77% of data points, the point $(h^{1,1} - h^{1,3}, h^{1,1} + h^{1,3})$ is accompanied by the point $(-h^{1,1} + h^{1,3}, h^{1,1} + h^{1,3})$. Taking frequency into account, the percentage drops to 27.35% — see Figure 2.38 in the Appendix. This is most likely due to an incomplete data base.

For now, we have performed a primary analysis on the Euler distribution only. The Euler number for

fourfolds is [68]:

$$\chi = 6(8 + h^{1,1} - h^{1,2} + h^{1,3}) \ . \tag{2.4.2}$$

Interestingly enough, the distinction between even and odd distributions persist in the fourfold data base. For illustrative purposes, we show the distribution of $\chi/6$ against frequency.

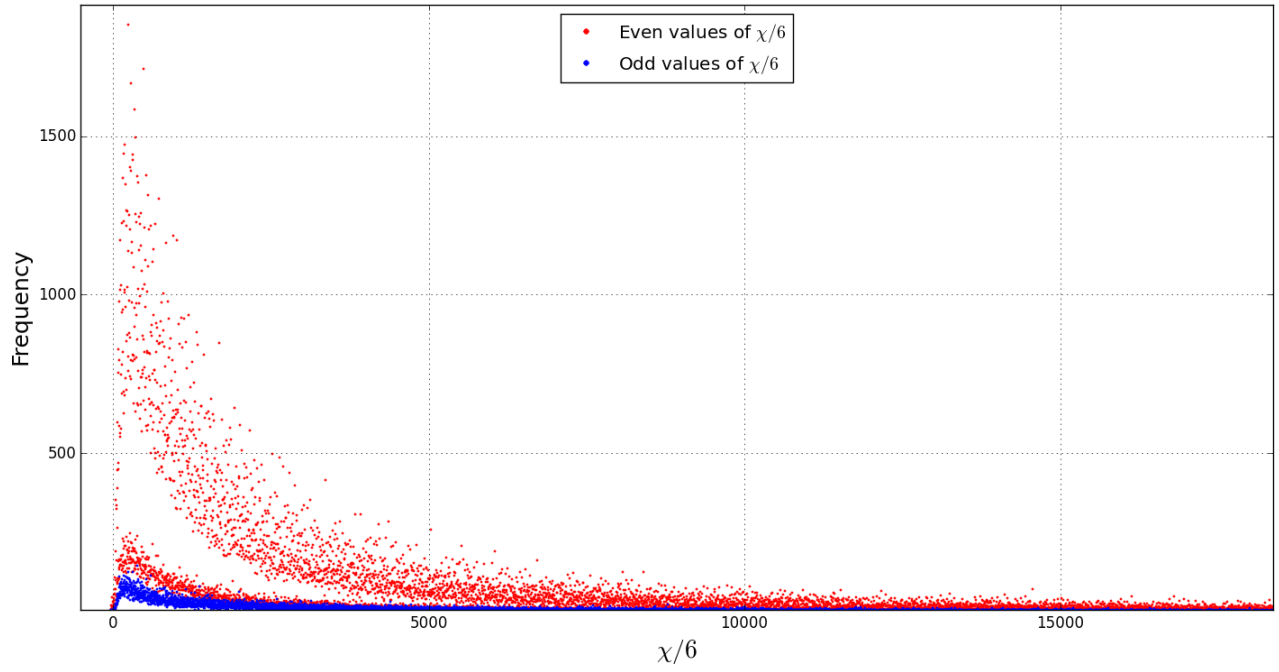
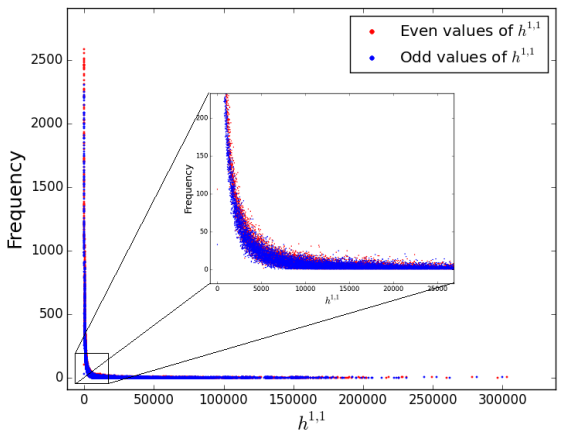
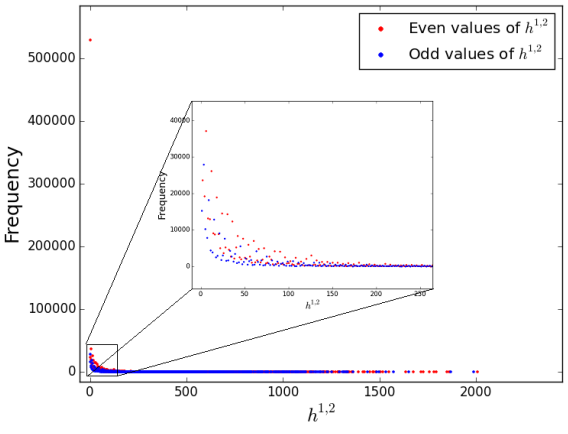


FIGURE 2.21: *Frequency of Calabi–Yau fourfolds with a given Euler number.*

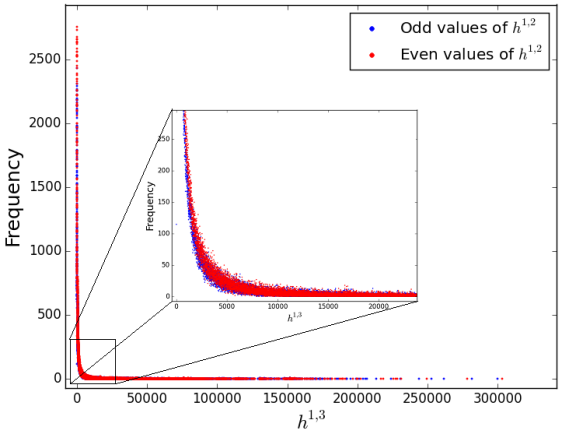
It is not immediately clear what is the reason for the gap, presumably it could be a cluster of data points which is missing from the data base. Until one obtains the complete fourfold data base of Hodge numbers, one can't say much else. We also preset plots of the individual Hodge numbers $h^{i,j}$ vs. frequency.



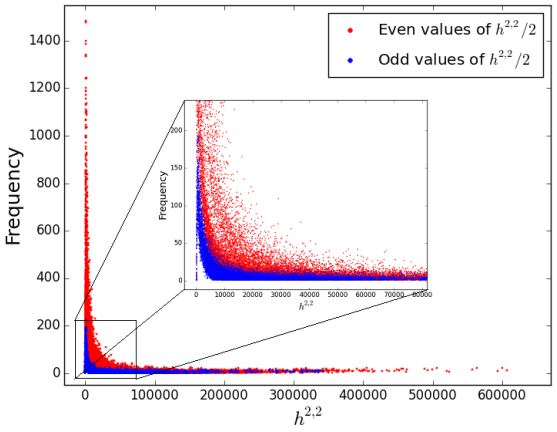
(A) $h^{1,1}$ *vs. frequency.*



(B) $h^{1,2}$ *vs. frequency.*



(c) $h^{1,3}$ *vs. frequency.*



(d) $h^{2,2}$ *vs. frequency.*

FIGURE 2.22: *The frequency for all the Hodge $h^{i,j}$ numbers. Red points and blue are odd and even points respectively for the various Hodge numbers. The data points are very dense close to the origin making it difficult to properly illustrate the mixing of odd and even Hodge numbers. Only $h^{2,2}$ (c) has a clear separation between of an even values.*

2.5 Conclusions and Outlook

By examining the distribution of Hodge numbers of Calabi–Yau manifolds of complex dimension two, three and four, realized as hypersurfaces in toric varieties of one higher dimension as constructed by Kreuzer and Skarke based on the results of Batyrev and Borisov, we have found many hithertofore undiscovered patterns. We summarize our key points as follows.

- For threefolds, there are 30108 distinct pairs of Hodge numbers $(h^{1,1}, h^{1,2})$ from 473800776 reflexive polytopes, the frequency of both the half-Euler number $h^{1,1}-h^{1,2}$ and the sum $h^{1,1}+h^{1,2}$ are distributed according to whether the value is odd or even;

  – The half-Euler number $h^{1,1} - h^{1,2}$ follows a modified pseudo-Voigt distribution

$$f(x) = (1-\alpha)\frac{A'}{\sigma\sqrt{2\pi}}e^{\frac{-(x)^2}{2\sigma^2}} + \alpha\frac{A'}{\pi}\left[\frac{\sigma^2}{x^2+\sigma^2}\right] .$$

  where the modification is made in the amplitude A of the distribution, such that

$$A' = A_0 + b\cos(2\pi\cdot b) .$$

  There is fine periodic substructure in terms of curves indexed by an integer r. Our model is accurate for low r-values ($r \in [36, 110]$ and $r \in [37, 99]$); using probability plots as test for goodness of fit, this modified pseudo-Voigt model is indeed the best one out of several standard candidates (cf. Figure 2.30 for all the R^2 and p values).

Among A, σ, α, b, a, the parameters σ, b, α have a strong linear relationship with r:

$$\begin{array}{lll} & \text{Even } r & \text{Odd } r \\ \sigma(r) = & 0.5097r - 12.7142 & 0.51379r - 13.2494 \\ \alpha(r) = & 2 \times 10^{-4} r - 0.0345 & 2.25 \times 10^{-4} r - 0.0388, \\ b(r) = & 3.7299 \times 10^{-5} r + 0.6629 & 7.9101 \times 10^{-5} r + 0.65956 \end{array}$$

For a small subset of curves with a low r-value and an appropriate cut-off frequency, it is extraordinary that the model *exactly fits the data*. That is, it appears that the number of data points for each curve required, such that the model will result in a perfect fit is: 7 for even r-valued curves and 10 for the odd valued r-curves, see Figure 2.31.

– The quantity $h^{1,1} + h^{1,2}$ follows a Planckian distribution

$$f(x) = \frac{A}{x^n} \frac{1}{e^{b/(x-22)} - 1}$$

There is a substructure of curves, indexed by an integer q, each Planckian and with some periodic behavior. The curves q_n appear clustered into groups of residue classes distinguished by n mod 6, and the parameters $\log(A), n, b$ all have extremely strong relationships with the q value.
By substituting this relationship into the model, we have a function $f_k(x, q)$ that approximately describes the entire $h^{1,1} + h^{1,2}$ distribution up to a q value of $69,100$:

$$f_k(x,q) = \frac{e^{\sum_{i=0}^{4} A_{k,i} q^i}}{x^{\sum_{i=0}^{4} n_{k,i} q^i}} \frac{1}{\left(e^{\frac{\sum_{i=0}^{4} b_{k,i} q^i}{(x-22)}} - 1 \right)}, \tag{2.5.1}$$

with $k = 0, 1, \ldots 5$ and the coefficients given in (2.6.9),(2.6.10),(2.6.11).

– The Euler number $\chi = 2(h^{1,1} - h^{1,2})$ follows the modified pseudo-Voigt distribution composed with a sinusoidal $A + A_0 + a\cos(2\pi b \cdot x)$ which is almost an exact fit, with the coefficients given by $(A_0, \sigma, \alpha, b, a) = (1.9032 \times 10^9, 75.8305889, 0.00718459, 0.58347826, 8.7427 \times 10^7)$, at $R^2 = 0.99944$ for even χ and
$(1.9032 \times 10^9, 75.8305889, 0.00718459, 0.58347826, 8.7427 \times 10^7)$ at $R^2 = 0.99965$ for odd χ,
The modified pseudo-Voigt distribution is remarkably accurate in predicting the overall and fine sub-structure of the Euler number distribution.

- For K3 surfaces, we have looked at the distribution of the multiplicity with Picard number. We find that this distribution follows a standard pseudo-Voigt profile. Adding in the sinusoidal modification does not significantly increase the overall fit. The parameters are given by $(a, \mu, \sigma, \alpha) = (4517.45, 10.76, 2.97, -0.031)$ with $R^2 = 0.99908$.

- For Calabi–Yau fourfolds, there is no exact mirror symmetry, due to incompleteness of available data. Nevertheless, by breaking up the data into three groups, we have

  – Mirror symmetric partners with the same frequency: 27.35%

  – Mirror symmetric partners without the same frequency: 42.22%

– Non mirror symmetric partners: 30.33%

By plotting the various $h^{i,j}$ vs frequency we see there is no distinction between even and odd data values for $h^{i,j}$, expect for $h^{2,2}/2$. This distinction is carried out further in the Euler number distribution where odd points are clustered on a band with much lower frequencies. The even values of $\chi/6$ appear to be distributed along to separate bands.

It is remarkable how well the pseudo-Voigt distribution, modified with a sinusoidal component, fits the distribution of topological numbers of toric Calabi–Yau manifolds, often giving an exact fit. Of course, what we are studying at heart is the number of integer points inside (*cf.* (2.2.1)) reflexive polytopes. This is a highly non-trivial counting problem whose answer will ultimately give full analytic results for our distributions and we suspect that the answer should be some generalized pseudo-Voigt function.

Now, in addition of Calabi–Yau manifolds, stable vector bundles over various such manifolds in a variety of construction beyond Kreuzer–Skarke have also been studied algorithmically over the years in the context of heterotic compactification (*cf. e.g.*, [96, 97, 98, 99]). One can see a somewhat pseudo-Voigt profile in these as well, even though there is no underlying polytope and the counting problem is dictated by certain Diophantine system. It would be interesting to see why this shape is universal in such classifications.

Here we include all additional plots to supplement the main body. This includes the relevant plots for the odd distributions — since in the main text we only presented the plots for even distributions — as well as the regression analysis statistics and parameter values for both distributions.

2.6 Appendix

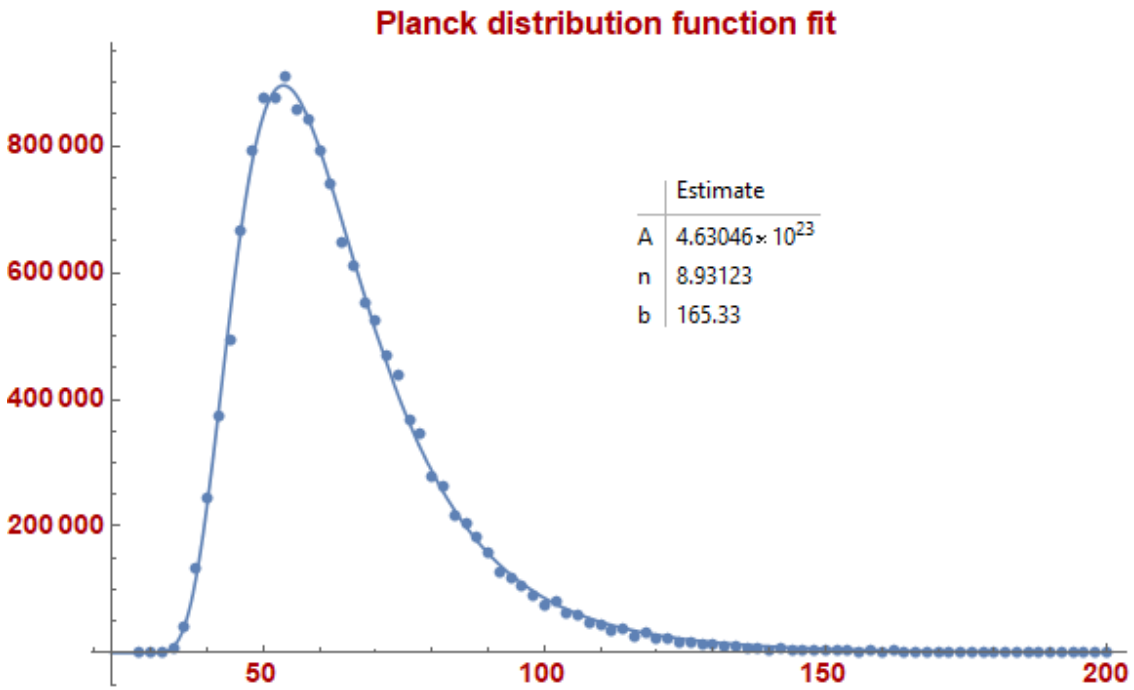
2.6.1 Gamma distribution

The following page is added after the publication of this paper. We decided to investigate the Gamma distribution as a viable model for the $h^{1,1} + h^{1,2}$ data as an alternative to the Planck distribution, which was already studied.

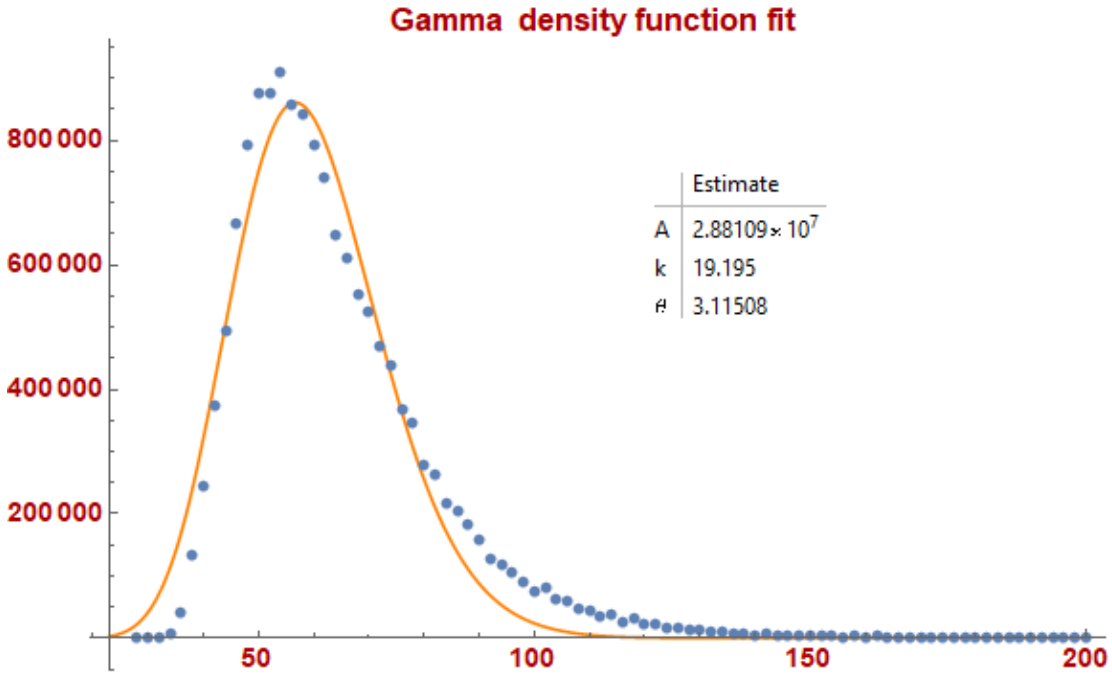
The three variable Gamma probability density function is given by

$$\Gamma(A, k, \theta) = \frac{Ax^{k-1}}{\theta^k \Gamma(k)} e^{\frac{-x}{\theta}}, \tag{2.6.1}$$

where k is the shape parameter, θ is the scale parameter and A is the amplitude. The gamma function is important in maths and physics as it is a extension to the factorial function. Where the factorial function is defined for non-negative integers, the gamma function is defined for all positive real numbers. By choosing suitable values of k and θ one is able to find a shape that resembles the data of the $h^{1,1}+h^{1,2}$. It is of interest to then do a regression fit of the data using the gamma function as our model. The fact that the gamma function is the canonical distributions of positive numbers could potentially give a stronger interpretation to why such a distribution can be used to mode data, as the data is generated by a counting procedure of positive numbers. Below is a plot of the fit statistics for $q_0 = 0$:



(A) *Sample fit using the already tested distribution as a reference distribution*



(B) *Sample fit using the Gamma density distribution*

FIGURE 2.23: *A comparison of the new Gamma distribution with the previous Planck distribution*

Without needing to give further examples, we immediately see that the gamma distribution, although able to describe the general shape, is much worse than the Planck distribution. This is the same for all values even and odd values of q_0. It appears that the Planck distribution is still the best suited for the description of the data within the $h^{1,1} + h^{1,2}$ distribution.

2.6.2 Supplementary plots for the $h^{1,1} - h^{1,2}$ distribution

All even plot counterparts will be referenced in the figures. The plots appear in the same order as in the main body, with descriptions only if necessary.

2.6.2.1 Plots for the odd distribution as counterparts to the even ones

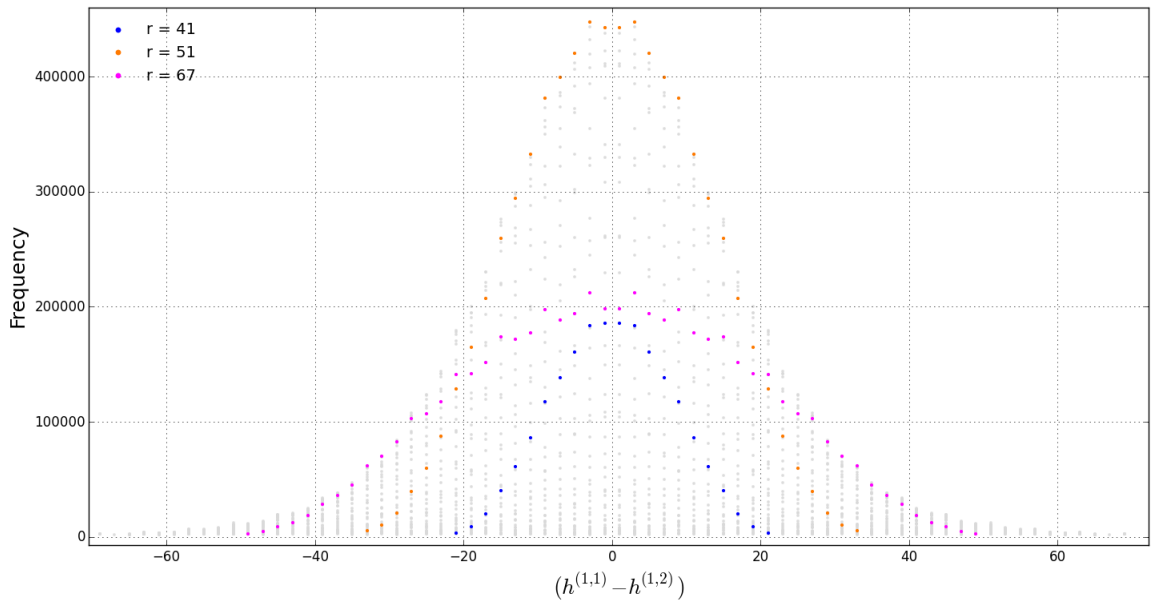
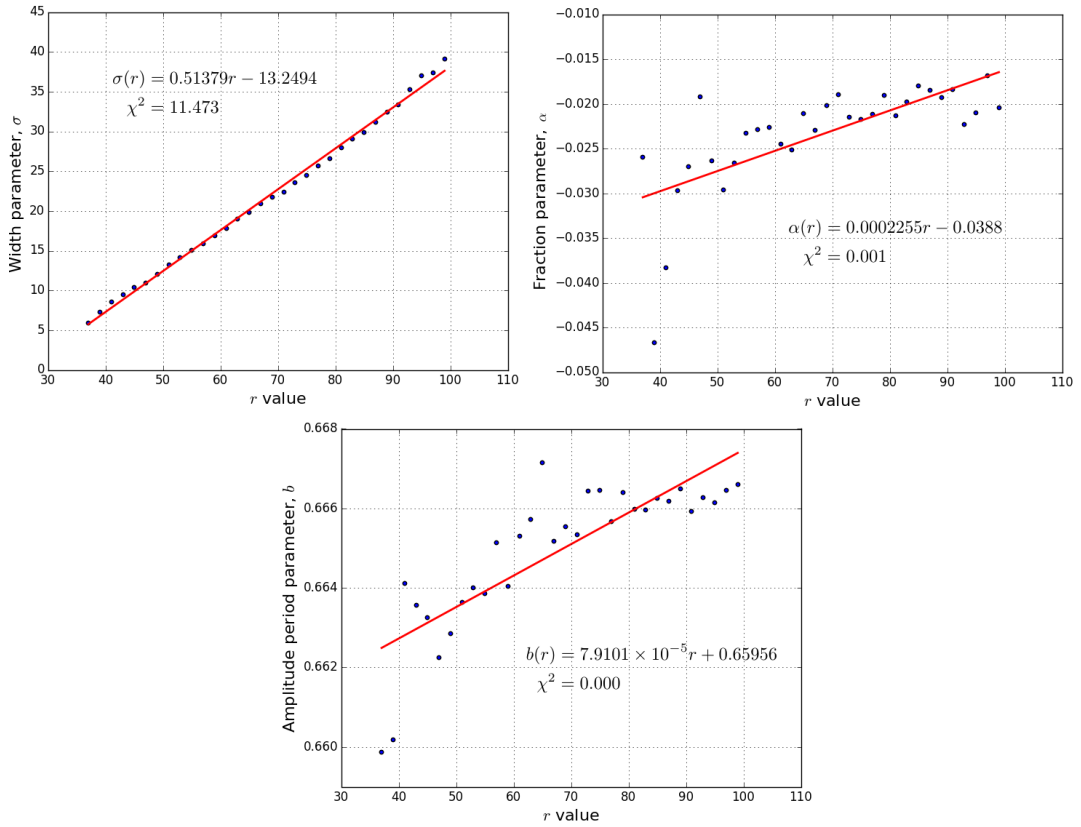
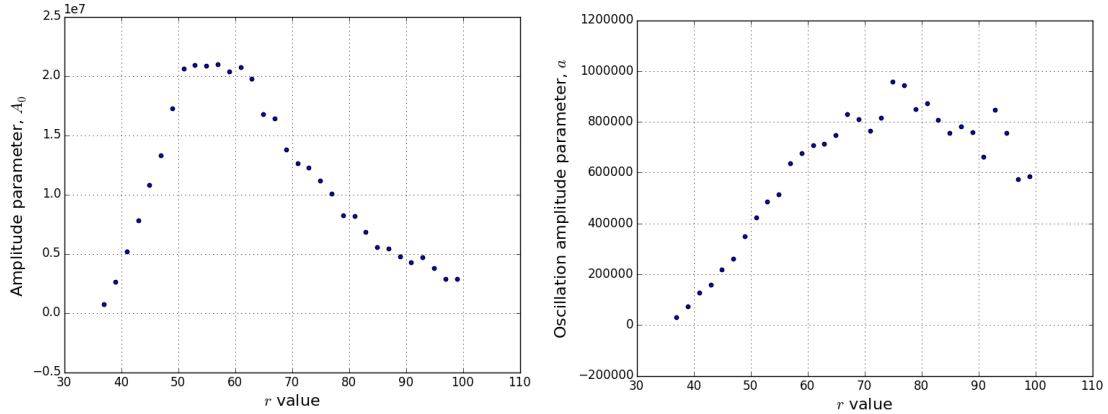


FIGURE 2.24: *Three highlighted curves ($r = 41, 51, 67$) within the odd $h^{1,1} - h^{1,2}$ distribution. The transparent grey data dots is the rest of the distribution. Refer to Figure 2.4 for the even plot.*



(A) *The width parameter σ has a linear relationship with r such that $\sigma(r) = 0.51379r - 13.2494$. The amplitude period parameter,b, also has a linear relationship, however, since r is at most order 3 in magnitude, we can regard it approximately as a constant such that $b(r) = 0.65956 \sim 2/3$. The same goes for the fraction parameter,α, we can regard it as a constant such that $\alpha(r) = -0.0388$. For even parameter fit statistics see Figure 2.10.*



(B) *Plots of A_0 vs r (left) and a vs r (right). Both exhibit a similar pattern, however it is difficult to find any nice relationships. For even parameter plots see Figure 2.10.*

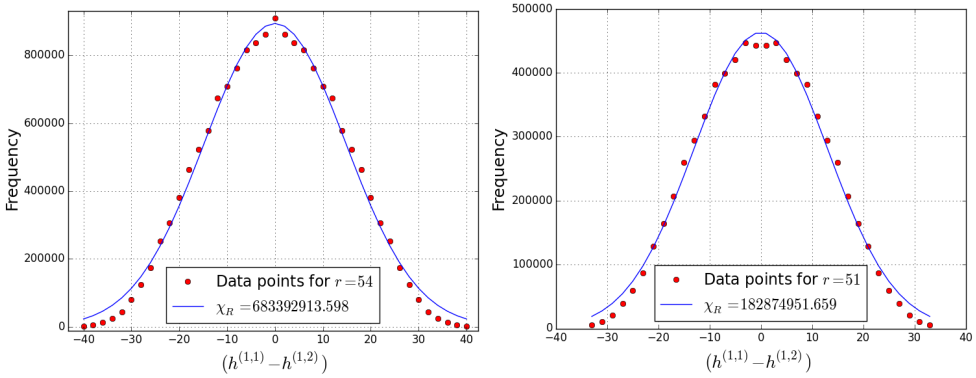
FIGURE 2.25: *The plots of the various parameters A, σ, α, b, a versus r for odd values of r.*

2.6.2.2 Comparative plots

Here we present a comparison of various models we used, by plotting them side by side with the relevant fit-statistics. We choose a single even curve, $r = 54$, and odd curve, $r = 51$, to illustrate the difference between models.

Gaussian Model

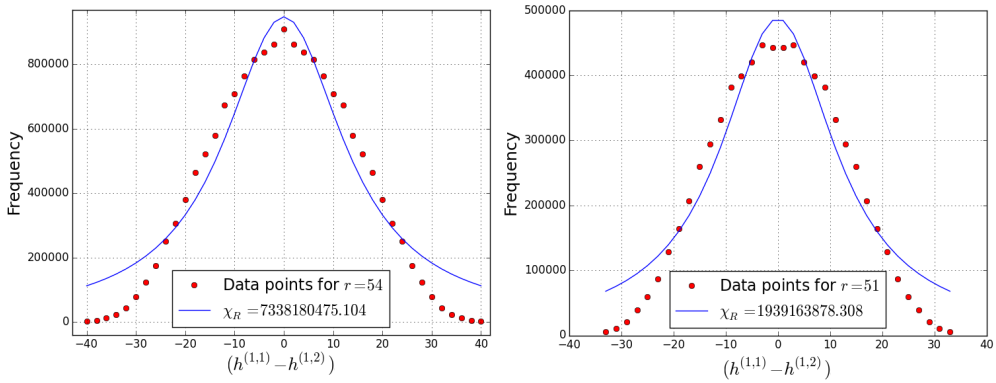
$$f(x, A, \mu, \sigma) = \frac{A}{\sigma\sqrt{2\pi}} e^{-(x-\mu)^2/2\sigma^2} \tag{2.6.2}$$



(A) *Gaussian model.*

Lorentzian Model

$$f(x, A, \mu, \sigma) = \frac{A}{\pi}\left[\frac{\sigma}{(x-\mu)^2 + \sigma^2}\right] \tag{2.6.3}$$

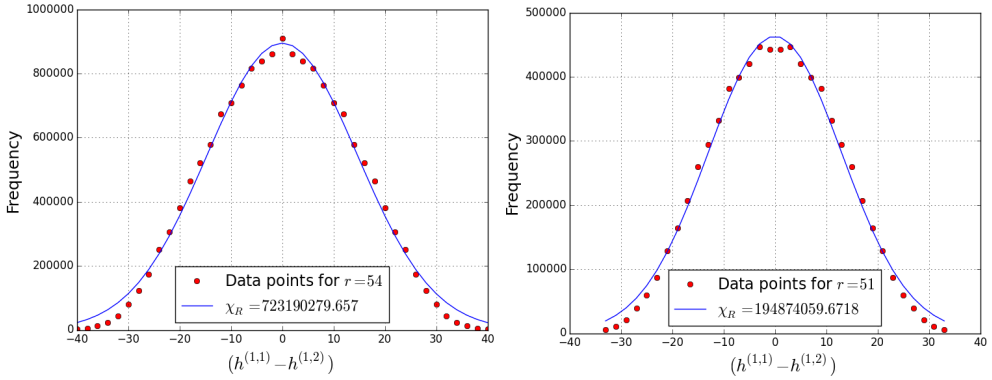


(B) *Lorentzian (Cauchy) model.*

Pearson7 Model

$$f(x, A, \mu, \sigma, m) = \frac{A}{\sigma\beta(m - \frac{1}{2}, \frac{1}{2})}\left[1 + \frac{(x-\mu)^2}{\sigma^2}\right]^{-m}, \tag{2.6.4}$$

where β is the Beta function.

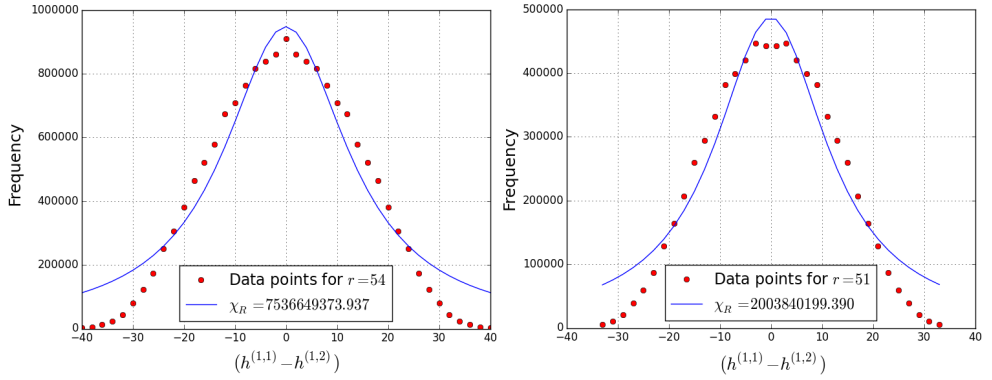


(C) *Pearson7 model.*

Breit-Wigner Model

This model is based on the Breit-Wigner function.

$$f(x, A, \mu, \sigma, t) = \frac{A(t\sigma/2 + x - \mu)^2}{(\sigma/2)^2 + (x - \mu)^2} \tag{2.6.5}$$



(D) *Breit–Wigner model.*

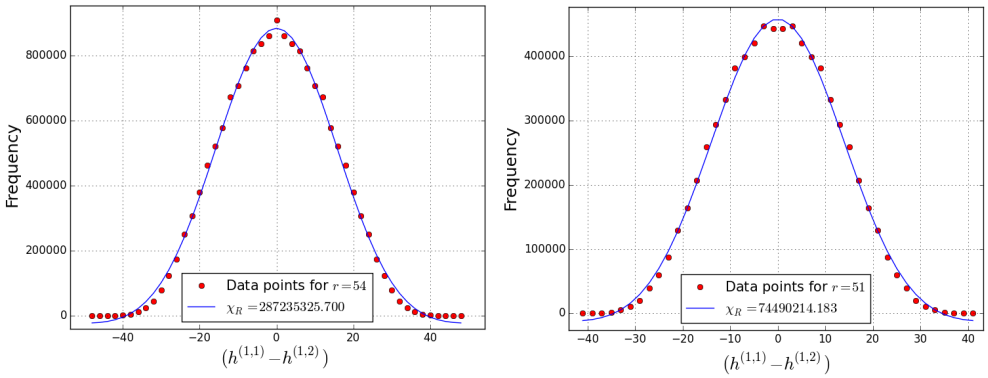
Voigt Model

$$f(x, A, \mu, \sigma, \gamma) = \frac{a\mathrm{Re}[(z)]}{\sigma\sqrt{2\pi}} \tag{2.6.6}$$

where

$$z = \frac{x - \mu + i\gamma}{\sigma\sqrt{2}}\ , \quad w(z) = e^{-z^2}\mathrm{erfc}(-iz) \tag{2.6.7}$$

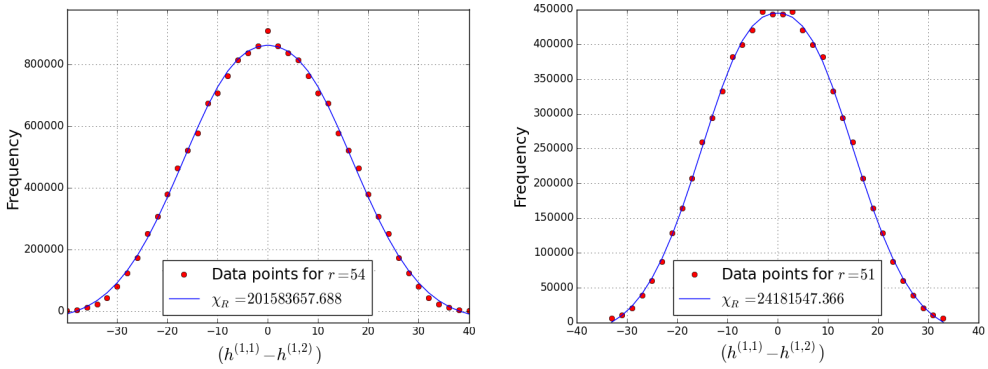
The Voigt model is a convolution of the Gaussian and Lorentzian models.



(E) *Voigt model.*

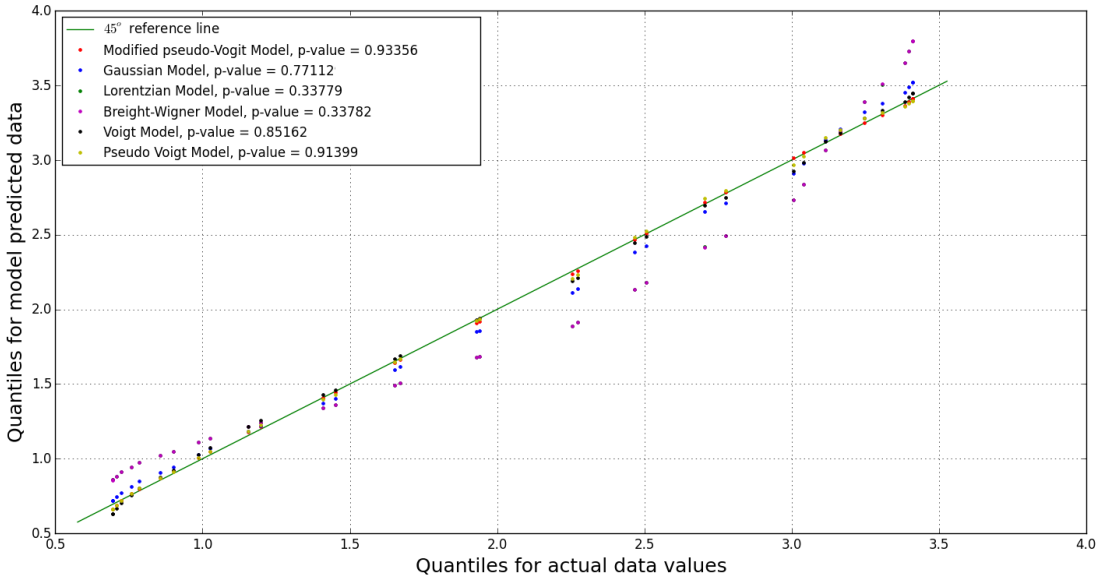
pseudo-Voigt Model

$$f(x,A,\mu,\sigma,\alpha)=(1-\alpha)\frac{A}{\sigma\sqrt{2\pi}}e^{\frac{-(x-\mu)^2}{2\sigma^2}}+\alpha\frac{A}{\pi}\left[\frac{\sigma^2}{(x-\mu)^2+\sigma^2}\right] \tag{2.6.8}$$

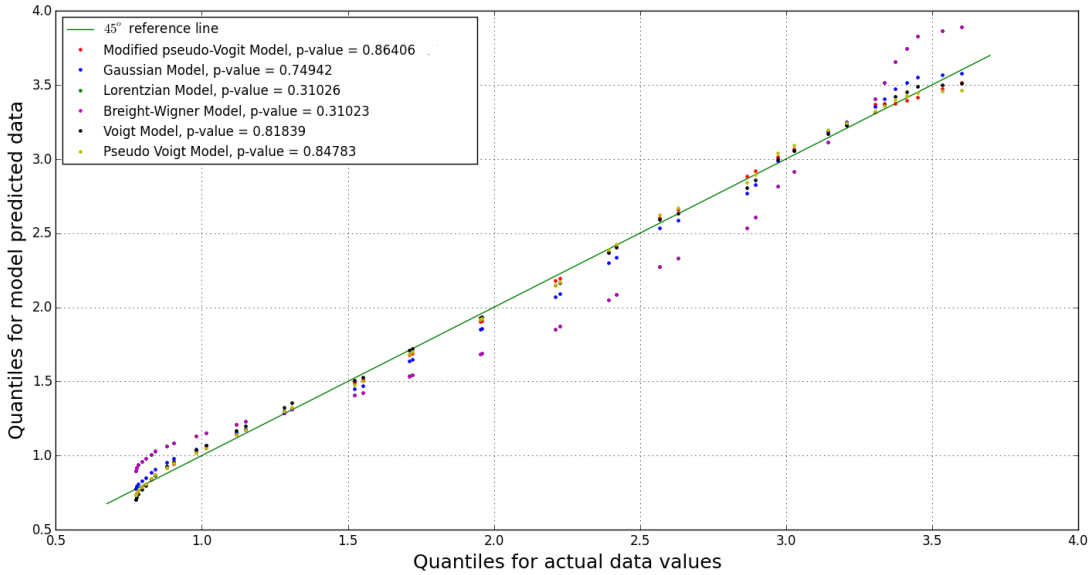


(F) *Pseudo-Voigt model.*

We present the standardized and shifted probability plots for the above comparisons:



(G) *The probability plot for* $r = 51$.

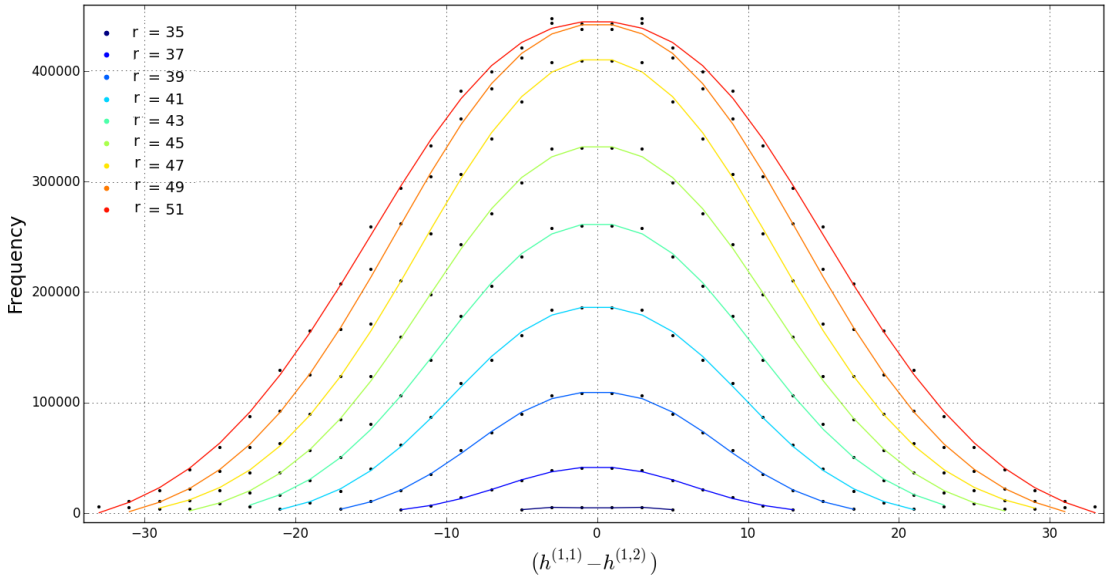


(H) *The probability plot for $r = 54$.*

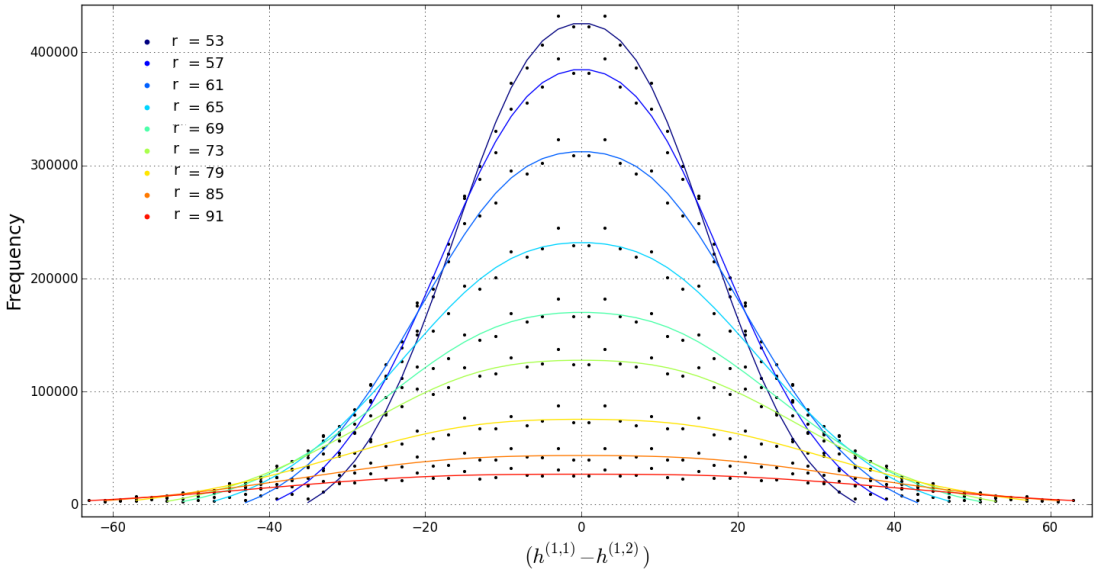
FIGURE 2.26: *For all models, the left hand graph is for $r = 54$ and the right is for $r = 51$. The probability plot presents all the models together. All the above mentioned modeled are included to compare their resemblance with the actual data. The larger the p value the better the line $y = x$ fits the data, implying the better the model is at describing the data.*

2.6.2.3 A first approximation to the data

The overall behavior of the data across each curve is modeled extremely well using the pseudo-Voigt model. Here we present a few plots illustrating a first approximation to the data. A second approximation can be made by introducing an oscillating amplitude as described in Section 2.2.1

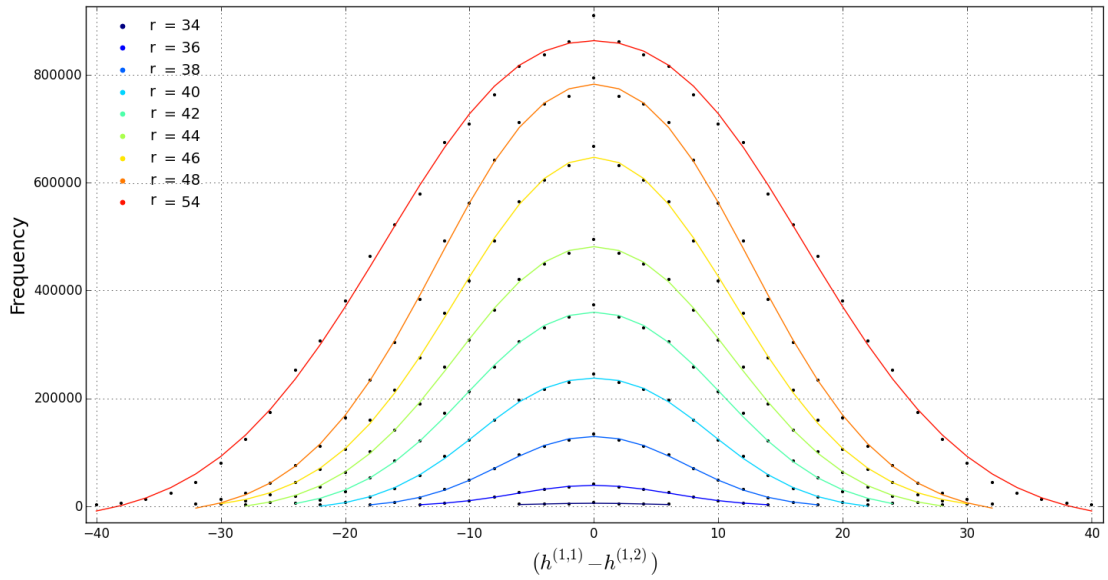


(A) *Regression lines for few select odd r values, with $r \in [35, 51]$.*

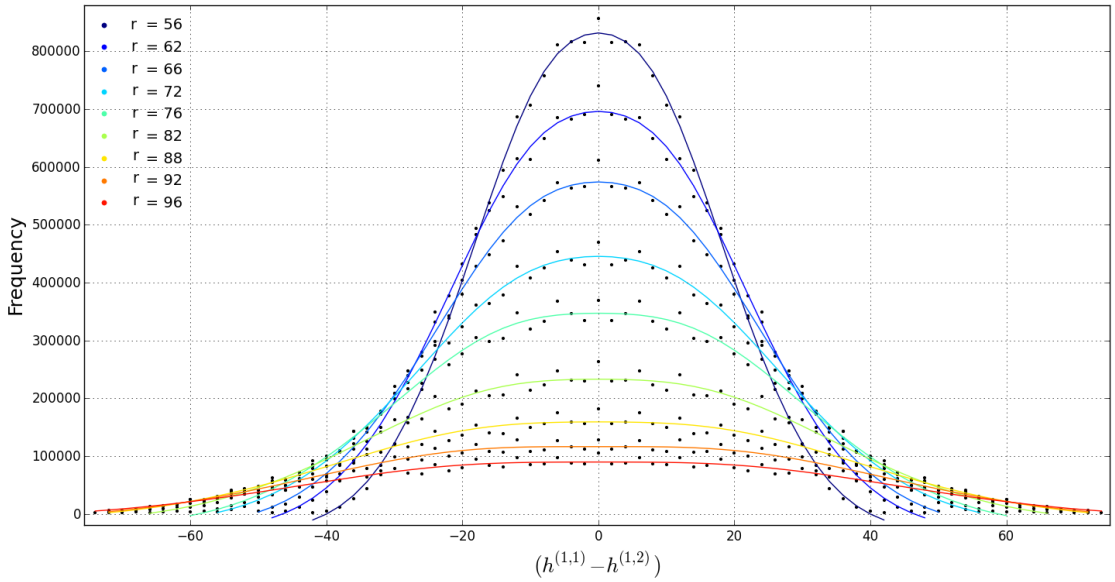


(B) *Regression lines for few select even r values, with $r > 51$.*

FIGURE 2.27: *Best fit curve based on the pseudo-Voigt model for the same sets of curves as seen in Figure 2.5.*



(A) *Regression lines for few select even r values, with $r \leq 54$.*

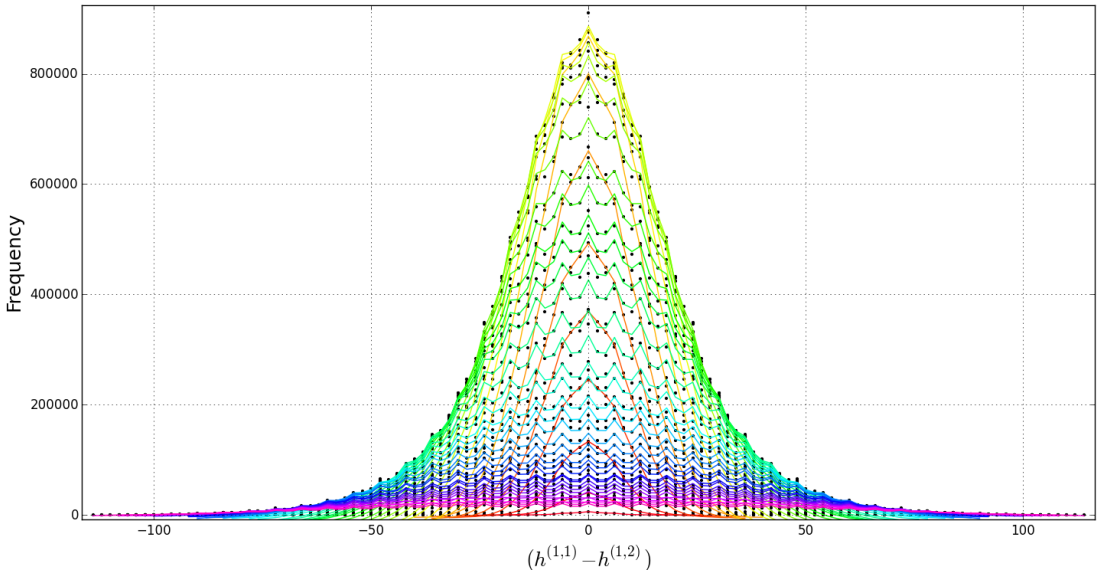


(B) *Regression lines for few select even r values, with $r > 54$.*

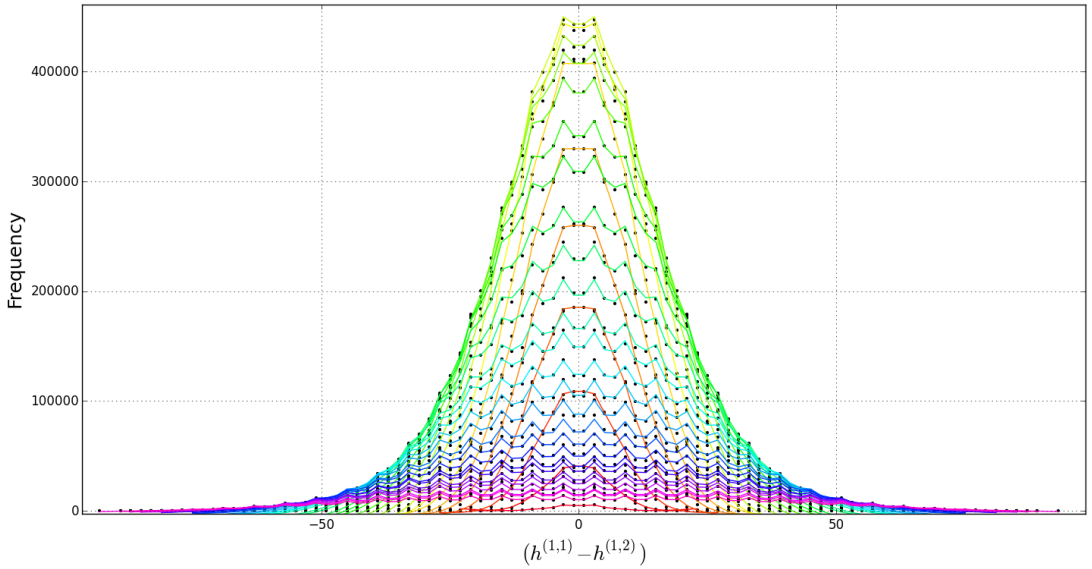
FIGURE 2.28: *Best fit curve based on the pseudo-Voigt model for the same sets of curves as seen in Figure 2.6.*

2.6.2.4 Table of parameter values and statistics

Here we present the parameter values as well as the reduced χ value, χ_R, in a tabular format for all even r curves — $r \in [34, 120]$ — and for all odd r curves — $r \in [35, 99]$.



(A) *Every fitted even curve from* $r = 34$ *until* $r = 120$.



(B) *Every fitted even odd from* $r = 35$ *until* $r = 99$.

FIGURE 2.29: *This is what the entire distribution looks like using our modified pseudo-Voigt model. See Figure 2.30 for the fitted coefficients as well as the fits for every curve given by the probability plots.*

r	A_0	σ	α	b	a	χ^2_R	R^2	p
34	74808.00828	5.61029	0.003766498	0.671247693	11882.85554	1913.323108	1	1
36	621112.5048	6.14542	-0.009876003	0.667458363	28438.58633	40004.88553	0.99902292	0.917177648
38	2545950.513	7.04214	-0.021320726	0.661106908	70029.4258	775992.3274	0.99989369	0.967870386
40	5997498.444	8.38473	-0.027896601	0.664313042	135241.8977	7016236.151	0.999812973	0.954767302
42	10051959.39	9.39476	-0.023578526	0.664331865	214365.7566	11248381.6	0.999606558	0.944633818
44	14383706.27	10.1952	-0.019800045	0.663363561	275921.3615	10356248.68	0.999910944	0.970052621
46	18900236.24	10.6388	-0.011402813	0.663897086	363905.1143	12630489.6	0.999822533	0.958642702
48	26936446.43	11.52	-0.019075394	0.662588045	456942.6269	48618344.01	0.99980274	0.948813265
50	35415476.39	12.7568	-0.02505046	0.663930639	634805.0051	159409130.3	0.999167385	0.888518617
52	40513641.09	13.9486	-0.025150833	0.663741398	770677.2752	156093179.3	0.999322987	0.887202979
54	42054878.16	14.9145	-0.020889662	0.664242039	851781.3562	177830377.5	0.998742804	0.864062454
56	45318925.17	15.9308	-0.022451431	0.664639342	1081188.801	91014311.13	0.999616346	0.901628544
58	45777655.84	16.8075	-0.020439012	0.66390829	1216222.825	79515308.6	0.999550544	0.915805654
60	45383436.12	17.6159	-0.019455309	0.664461299	1195317.789	67324781.93	0.99975046	0.937493846
62	45890243.65	18.7829	-0.020089061	0.664969685	1299727.161	95590289.64	0.999225833	0.885179311
64	44629202.3	19.8429	-0.020615871	0.665932096	1347466.72	78628169.68	0.998988401	0.871831349
66	41517968.02	20.5755	-0.018305682	0.666138254	1468293.568	54603587.95	0.999239136	0.882676184
68	39712672.75	21.4871	-0.017963577	0.66544129	1569245.184	40212010.61	0.999379453	0.892005972
70	36807367.68	22.0999	-0.015684425	0.665873362	1557320.642	33793439.97	0.999174607	0.878072158
72	36162771.81	23.0026	-0.016476545	0.666763067	1581985.228	21554913.66	0.999683961	0.917179602
74	36144785.21	24.0403	-0.017822108	0.666499021	1872368.976	28640120.59	0.999322336	0.875539384
76	34490648.35	25.2339	-0.018605896	0.666121761	1980563.649	44636083.29	0.998671434	0.824721608
78	32892619.57	26.6155	-0.018823052	0.666381088	2189453.136	33663175.17	0.998301995	0.828346496
80	30667295.71	27.8144	-0.019346889	0.665996548	2025935.144	27318925.61	0.998478381	0.808972237
82	27351655.4	28.6931	-0.017490104	0.666752586	2011512.915	26284425.4	0.99726603	0.770596127
84	24566921.31	29.8261	-0.016927049	0.666024732	1732875.478	23309744.54	0.996555935	0.706834711
86	22906614.56	30.8169	-0.016442317	0.666905358	1911979.009	14429329.24	0.997492504	0.744338007
88	21528402.71	32.153	-0.016214982	0.666381087	1804104.196	18088956.91	0.995744097	0.678346825
90	19886629.72	33.3369	-0.016681365	0.666516895	1783587.312	11527968.91	0.996471494	0.693352255
92	18648959.11	34.3926	-0.017242388	0.66632638	1741577.927	5377588.556	0.998485737	0.769625304
94	18809829.16	36.3033	-0.018365807	0.666336104	1925176.842	8355841.233	0.987709685	0.561674719
96	14889894.87	36.1253	-0.016184316	0.666464019	1520828.275	4989263.018	0.996861999	0.711953875
98	14740741.19	37.7735	-0.016677525	0.666516294	1693173.472	4104162.131	0.996716296	0.711028368
100	13273455.92	39.1882	-0.016641154	0.666363484	1333642.914	3437131.53	0.994423193	0.5603671
102	11130677.16	39.4973	-0.013892005	0.66646458	1359292.476	4680926.074	0.990953211	0.499880801
104	9339364.392	40.191	-0.01257178	0.666411434	1159602.308	3377262.44	0.993594806	0.438020147
106	8684918.797	41.0922	-0.012755565	0.666256708	1185946.732	2646190.089	0.993791084	0.560243553
108	8380821.944	42.139	-0.013639004	0.666558606	1104233.414	1209490.828	0.996572623	0.62437074
110	8195376.057	44.0026	-0.014513112	0.666306562	1162489.945	922920.416	0.996020933	0.58859257
112	7991589.586	44.9151	-0.016013529	0.749095555	-170845.2098	5798070.695	0.99570584	0.646270602
114	7502725.304	47.0497	-0.015129142	0.666363214	1206184.755	1116881.881	0.993672141	0.622571007
116	6781922.133	48.3831	-0.015377227	0.714161497	-72768.74536	4292917.226	0.991182119	0.440649435
118	6003445.42	49.6367	-0.014286543	0.666241038	1072317.828	1327245.637	0.974412536	0.334997699
120	5081179.349	50.9995	-0.01397899	0.666354981	907092.9689	920853.6576	0.985746862	0.256871587

r	A_0	σ	α	b	a	χ^2_R	R^2	p
35	69517.6991	5.27052174	-0.00059798	0.66801823	11501.6207	2615.83922	0.98471088	0.83735891
37	666812.118	5.8927625	-0.01836059	0.66078722	27241.5063	53480.6329	0.99993762	0.97888572
39	2416867.36	7.26453848	-0.03399152	0.66024643	67114.7518	1572652.39	0.99986798	0.97276103
41	4946864.13	8.55598954	-0.03144232	0.66427804	118674.653	4114738.1	0.99969021	0.94841959
43	7433511.2	9.48971721	-0.02373655	0.66365772	149610.971	4400631.37	0.99983906	0.95857146
45	10410867.9	10.3532866	-0.02296192	0.66294576	209654.283	6625433.8	0.99987931	0.96407889
47	13000374.3	10.9406034	-0.01676022	0.66241434	254340.624	5703915.71	0.99985986	0.96200221
49	16632005.3	11.9906222	-0.02272541	0.66291891	334507.932	14172879.3	0.99988501	0.95711674
51	19624874.6	13.1819995	-0.02567549	0.66328796	402205.527	24721179.6	0.99977948	0.93356734
53	20046551.4	14.1510506	-0.02328543	0.66408311	465061.332	24857709	0.9997502	0.93661201
55	20316683.4	14.9970179	-0.02144823	0.66400324	497654.277	18227092.5	0.99954277	0.91633107
57	20461751.5	15.8792577	-0.02119817	0.66478694	618719.277	11819717.5	0.99975386	0.94214571
59	19628194.9	16.8390468	-0.02028947	0.66406865	650103.969	11914092.5	0.99976798	0.93883246
61	19631420.5	17.818317	-0.02146377	0.66501447	671348.429	12630471.7	0.99979416	0.94184719
63	18811815.6	18.9977095	-0.02268492	0.66582044	679837.657	16391189.7	0.99935615	0.88866674
65	16183229.9	19.7772633	-0.01933318	0.66722014	721485.873	11360773.2	0.99896912	0.86475537
67	15604477.1	20.8972797	-0.02064514	0.66500765	789587.968	8036678.17	0.99923827	0.88131905
69	13104503.1	21.6694017	-0.01784441	0.66555933	767710.979	6136325	0.99891504	0.85442783
71	12181331.7	22.3450186	-0.01735848	0.66535239	737223.294	2981281.47	0.99934345	0.88305521
73	11688172.2	23.5912589	-0.01959154	0.66631585	778331.602	2642181.63	0.9995577	0.90136661
75	10374775.4	24.4411893	-0.0189423	0.66649826	888710.412	2623581.62	0.99959387	0.92108108
77	9517481.18	25.6570194	-0.01932509	0.66566431	893712.308	2823201.59	0.99845812	0.84029783
79	7885048.98	26.6109387	-0.01774641	0.66650459	817061.631	2805786.84	0.99643597	0.75771938
81	7552444.81	27.9445846	-0.01901739	0.6660062	808353.444	1400649.06	0.99864589	0.82824688
83	6530766.47	29.1128891	-0.01843932	0.66597173	771351.758	1574872.99	0.99621037	0.69960965
85	5276286.62	29.9134628	-0.01668256	0.6662315	721999.658	1012336.36	0.99647231	0.68125485
87	5180484.66	31.1360788	-0.0174236	0.66615796	749182.031	769658.124	0.99744609	0.72808704
89	4543976.97	32.482801	-0.01819782	0.66650101	724406.102	470757.434	0.99655444	0.64638776
91	4114525.48	33.329044	-0.01782562	0.66591614	645509.413	430237.138	0.99581489	0.6910904
93	4317572.14	35.4965215	-0.02067125	0.66630679	783101.682	408316.122	0.99672503	0.77503965
95	3525255.74	37.183235	-0.01980839	0.66614479	708403.91	531215.258	0.9881393	0.507914
97	2748721.76	37.3626861	-0.01640557	0.66642785	558435.856	533865.612	0.98187428	0.35676676
99	2721520.91	39.2526357	-0.01960972	0.66656673	558530.974	196164.967	0.99611455	0.0092328

FIGURE 2.30: *Left : list of best fit coefficients for all even curves $r \in [34, 120]$. Right: List of best fit coefficients for all odd curves $r \in [35, 99]$. In both tables, the last two columns represent the R^2 and p values for the probability plot for each curve. The p-values were obtained by first performing a Z-Standardization on the data.*

Even					Odd				
r-value	Max F	% Cut off	Number of data points		r-value	Max F	% Cut off	Number of data points	
			Total	At cut off				Total	At cut off
28	3	0	7	7	29	3	0	6	6
30	99	13.13	11	9	31	22	9.09	12	8
32	768	9.6	23	9	33	553	4.88	20	10
34	6258	15.1	25	9	35	5180	19.3	22	10
36	40739	24.35	27	9	37	40607	16.25	24	10
38	133355	35.99	31	9	39	108236	32.34	28	10
40	244716	50.26	35	9	41	185481	46.9	30	10
42	373126	69.68	33	7	43	259859	53.49	34	10
44	494185	76.89	37	7	45	330009	59.99	36	10
46	666992	73.76	41	7	47	408797	61.89	38	10
48	793852	80.74	43	7	49	443162	69.95	40	10
50	877191	82.42	43	7	51	447109	74.45	42	10
52	875275	86.6	45	7	53	432081	76.37	46	10
54	910113	84.6	49	7	55	419456	77.24	46	10
56	816288	92.86	49	7	57	393842	86.33	48	10
58	793170	92.54	51	7	59	354495	81.52	52	10
60	791325	89.72	55	7	61	322535	89.91	54	10
70	495068	94.53	65	7	71	164257	84.63	64	10
80	278120	89.89	75	7	81	69757	86.01	76	10
90	278120	48.5	85	7	91	31675	82.08	82	10
100	78244	88.18	93	7	99	13812	86.88	90	10
110	45370	88.16	105	7					
120	22840	87.56	113	9					

FIGURE 2.31: *A list showing the number of data points left after increasing the cut off frequency to achieve a perfect fit. Conversely, one may state is as, the number of data points for each curve required such that the model will result in a perfect fit.*

2.6.3 Supplementary plots for the $h^{1,1} + h^{1,2}$ distribution

2.6.3.1 Plots for the odd distribution as counterparts to the even ones

All even plot counterparts will be referenced in the figures. The plots appear in the same order as in the main body, with descriptions only if necessary.

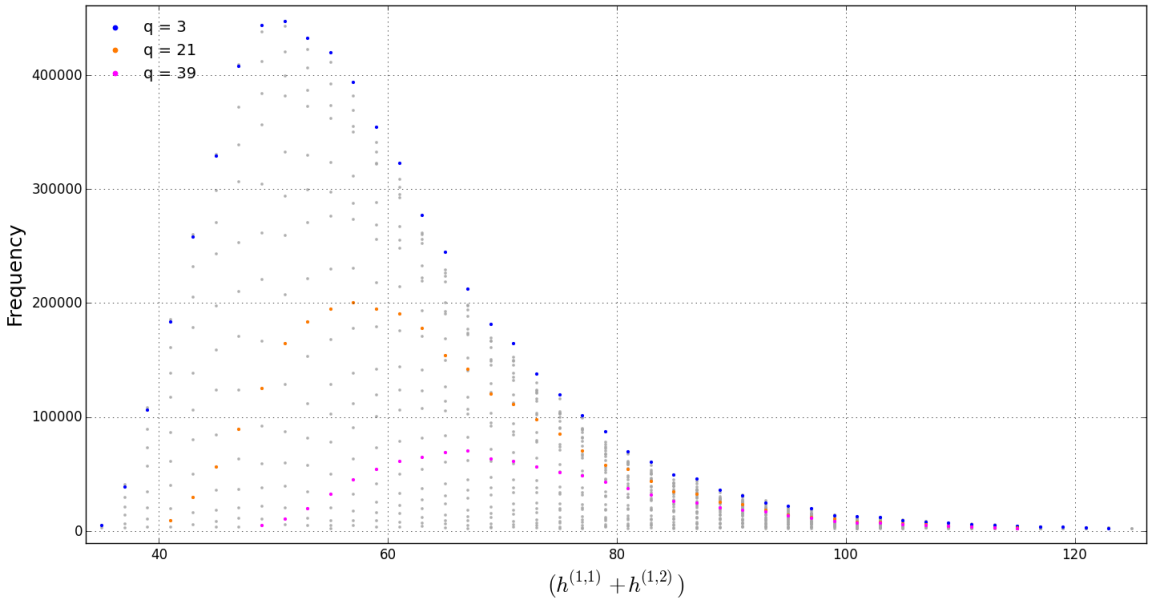
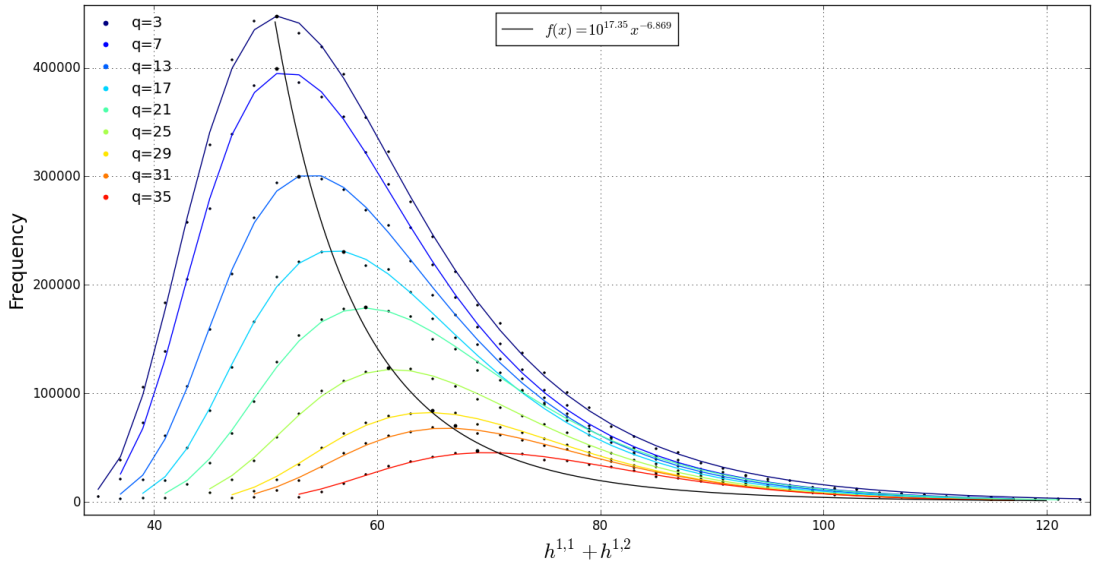
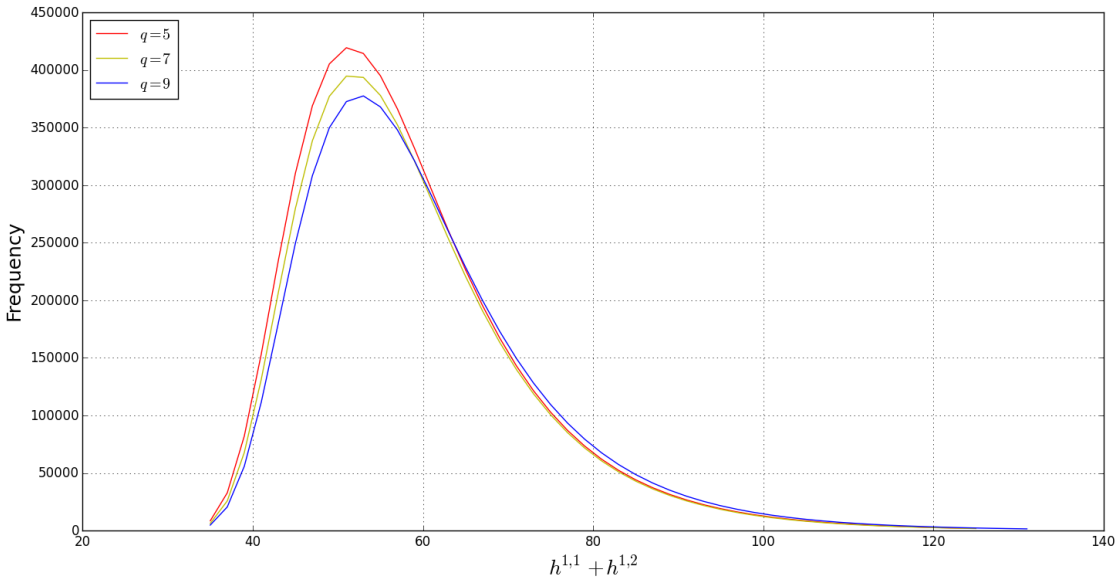


FIGURE 2.32: *Three highlighted curves ($q = 3, 19, 31$) within the odd $h^{1,1} + h^{1,2}$ distribution. The transparent grey data dots are all the data plots for the distribution. Refer to Figure 2.11 for the even plot.*

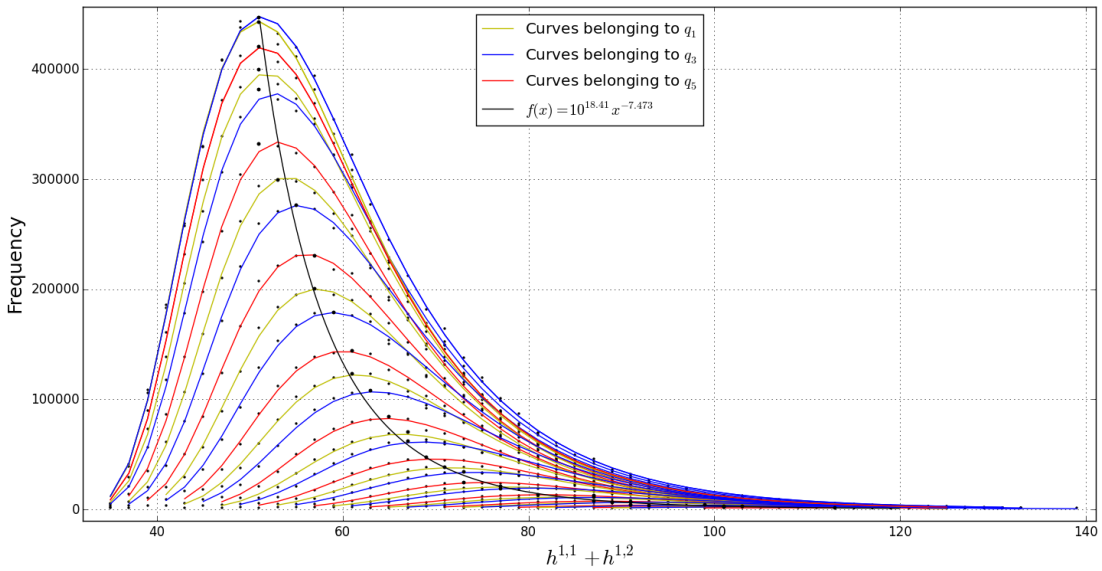


(A) *Lines of best fit from a regression analysis for a few select curves. The black data points represent the maximum frequency for that particular $q-curve$. the black line is a line of best fit to describe the points of maximum frequency — this is analogous to a blackbody spectrum. See Figure 2.12a for the curves within the even distribution.*

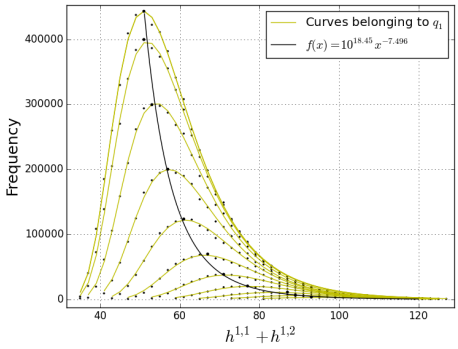


(B) *The curves segregate into three classes determined by the value of the even integer modulo* 6. *A similar pattern occurs in the even distribution; see Figure 2.12b.*

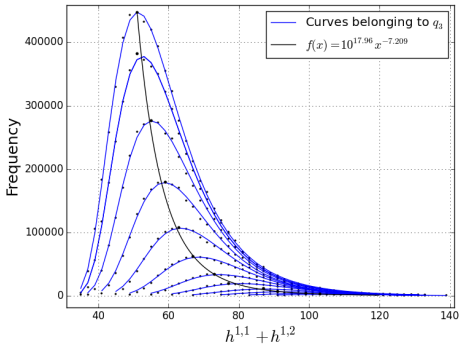
FIGURE 2.33: *In the attempt to describe the data analogously to a blackbody distribution (a), we discover some subtle structure, (b). These are the odd counterparts to Figure 2.12.*



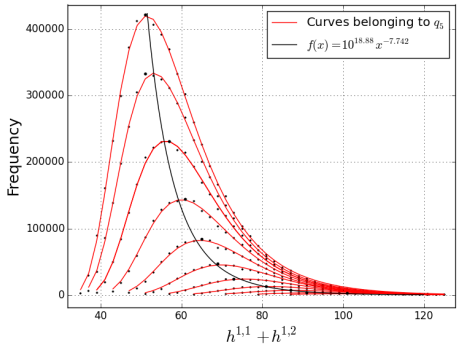
(A) *All the curves color coded according to what residue class their curves q_n belongs to.*



(B) *Family of curves all belonging to* q_1.

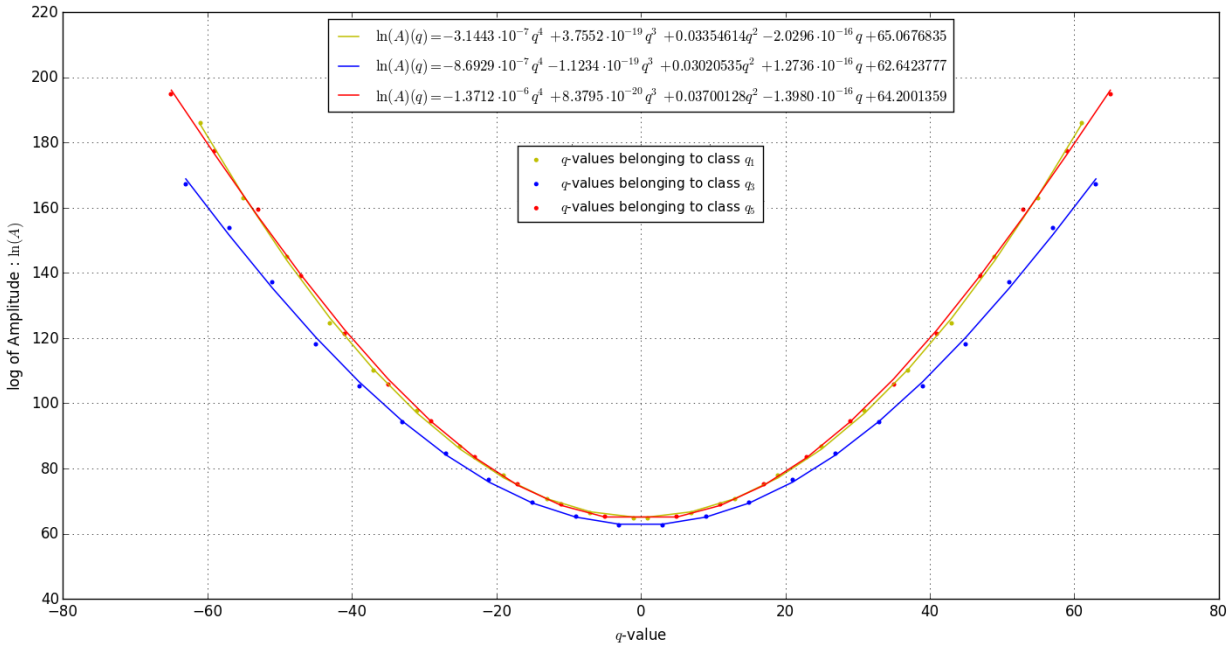


(C) *Family of curves all belonging to* q_3.

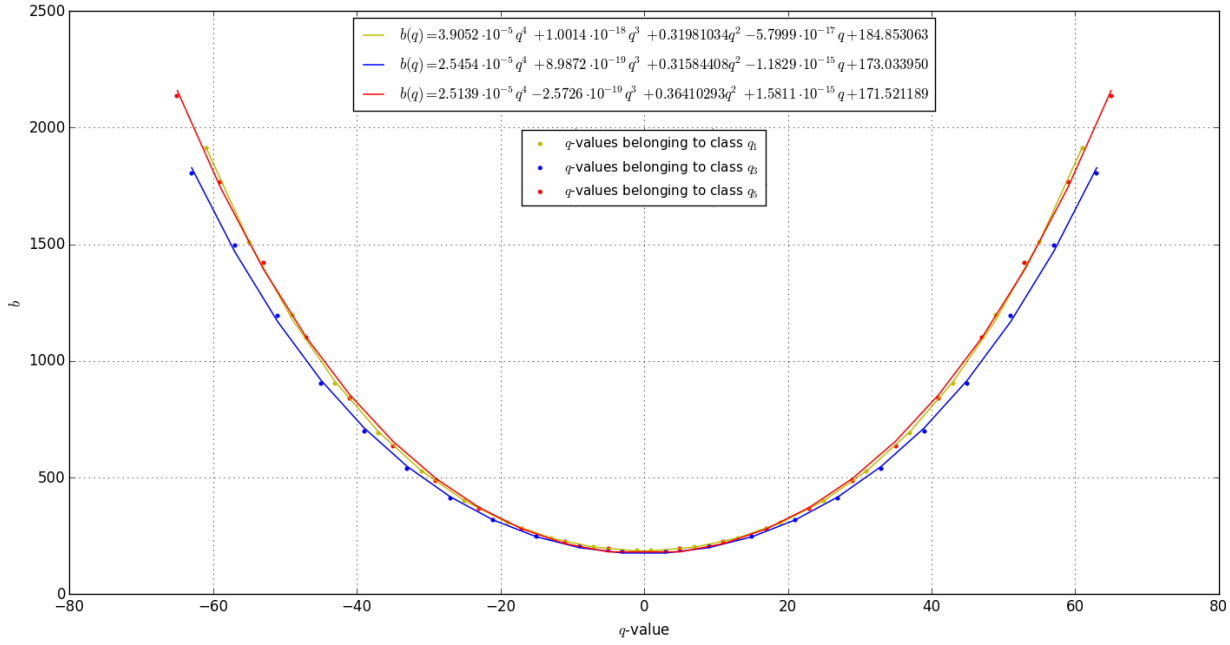


(D) *Family of curves all belonging to* q_5.

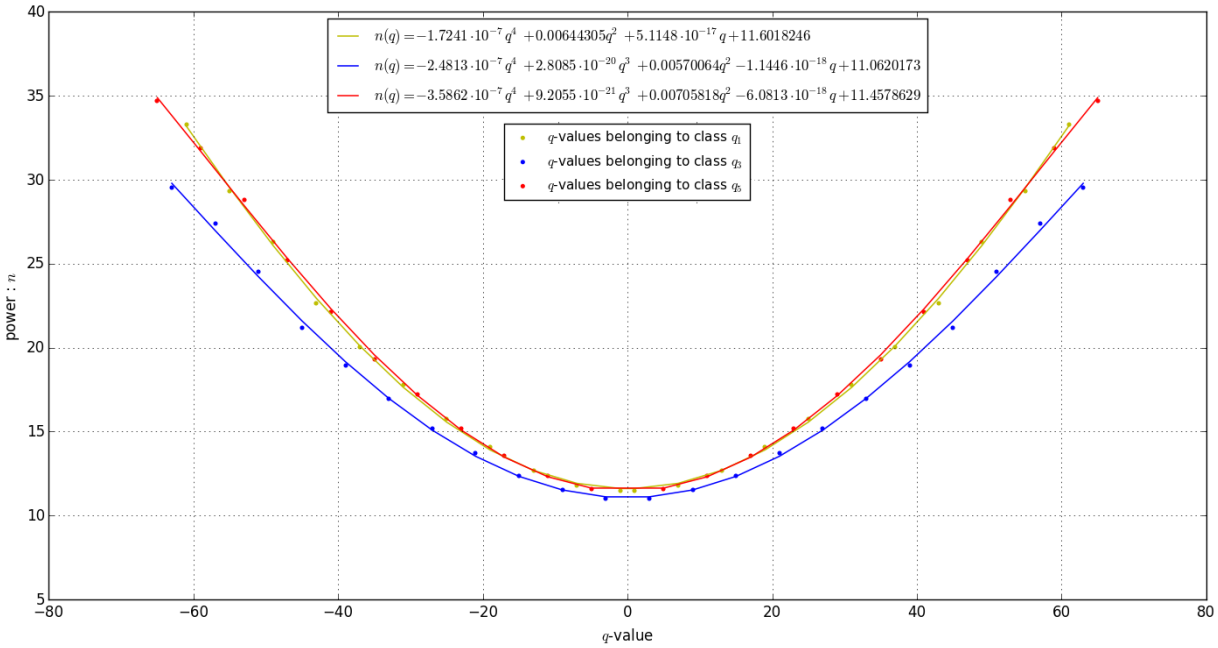
FIGURE 2.34: *We illustrate the added structure for odd* $h^{1,1} + h^{1,2}$ *data, by displaying how the regression curves can be divided into residue classes. For the list of even curves, refer to Figure 2.13.*



(A) *Plotting the q- value parameter vs the* $\log(A)$ *parameter.*



(B) *Plotting the q- value parameter vs the b parameter.*



(c) *Plotting the q- value parameter vs the power n parameter.*

FIGURE 2.35: *The parameter plots are color coded according to what residue class their q value belong to. For the relationships in the even distribution, see Figure 2.14.*

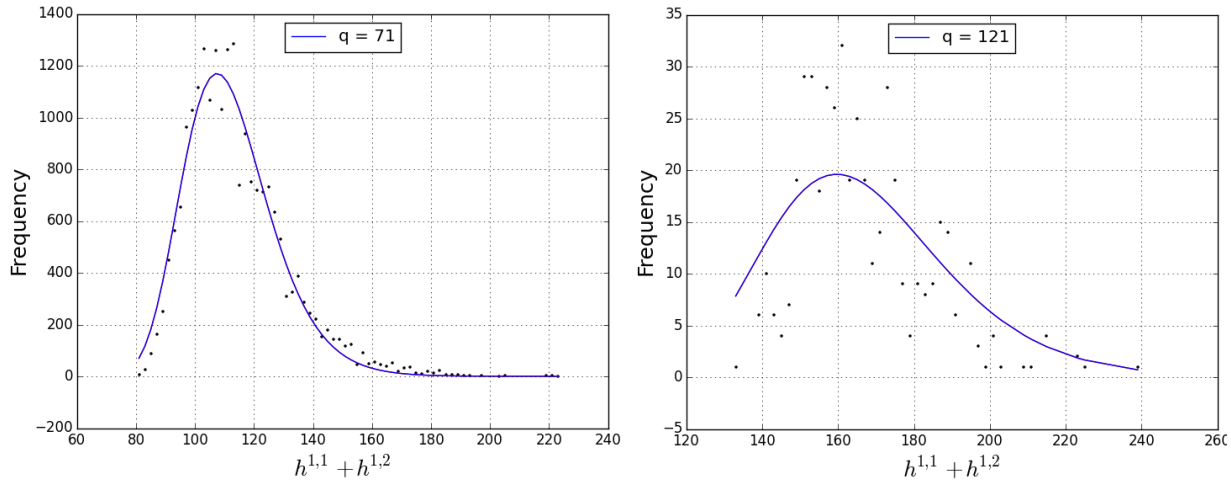


FIGURE 2.36: *Left figure is the fitted model(blue line) for a q value of 71 and right has a q value of 121. As the q-value increases, the scattering of the data points within $h^{1,1} + h^{1,2}$ increases to the point where the model works no longer. For an example of how the model begins to break down at large q, see Figure 2.15.*

2.6.3.2 Table of parameter values, coefficient values and statistics

q	n	b	$\ln(A)$	χ^2_R	R^2	p
0	8.93083135	165.322244	54.4902667	115338787.4	0.99943456	0.90355933
2	9.33100737	171.619423	56.2365529	86744223.38	0.99941661	0.90313829
4	9.35921323	174.243364	56.4183799	79636074.26	0.99945988	0.90804824
6	9.15714724	174.698696	55.6051245	78159100.89	0.99945177	0.90431738
8	9.57462978	186.106521	57.5571629	79812235.5	0.99940322	0.90539217
10	9.79154152	195.73856	58.6438354	72485389.34	0.99948539	0.91392681
12	9.5880961	200.712867	57.9336132	75534737.26	0.99963771	0.92346571
14	10.2491103	220.819009	61.0432495	64077134.03	0.9995487	0.91817024
16	10.4914929	236.074532	62.3685732	58709554.85	0.99957486	0.92151757
18	10.3760463	246.531143	62.0927375	58119944.17	0.99956689	0.91632693
20	11.1218075	274.956303	65.7459807	48854280.37	0.99919898	0.8906012
22	11.5532872	298.881967	67.9886289	42481778.28	0.99917848	0.8912926
24	11.3663725	313.307475	67.4918064	39237109.23	0.9989311	0.87061057
26	12.4166129	355.560944	72.6497069	28759082.5	0.99882732	0.87228524
28	12.7691656	384.581954	74.6674572	22243686.17	0.99924448	0.89325445
30	12.6894483	406.767631	74.7062602	17629876.3	0.9993154	0.88949423
32	13.8815504	462.687499	80.7409756	12509194.76	0.99927066	0.89163831
34	14.4765595	505.577447	83.9731435	9337609.09	0.99925081	0.89116175
36	14.2413274	529.387648	83.3720102	8819647.781	0.99942056	0.90231328
38	15.8169165	608.625248	91.4047442	5569077.245	0.99923201	0.88967633
40	16.349038	658.037252	94.4944182	4878474.443	0.99919338	0.88154018
42	16.1912135	691.261106	94.2923259	4679157.964	0.99906349	0.88398659
44	18.1005802	796.219314	104.225499	3575959.582	0.99819891	0.84339097
46	18.8376152	864.069993	108.413983	3485429.849	0.99711189	0.80746862
48	18.3294437	886.994271	106.517192	3742836.478	0.99663247	0.80148621
50	20.6272191	1026.3688	118.604632	2550085.404	0.99492294	0.76918876
52	21.1759554	1091.79709	121.927527	2068604.81	0.99402921	0.75114473
54	20.7571875	1127.43808	120.497481	2213288.382	0.99518652	0.75834784
56	22.6875666	1257.21615	130.798265	1200845.969	0.99554623	0.77318115
58	23.6283802	1359.92622	136.312334	1171384.578	0.99609563	0.7765067
60	22.4580953	1352.48226	130.910755	1267334.281	0.9955536	0.76067776
62	25.3137153	1558.90413	146.324868	670967.8101	0.99500786	0.76027754
64	25.3244289	1603.12416	146.824885	647121.3779	0.99362734	0.71823791
66	24.6357215	1638.37623	144.068359	699238.179	0.99434629	0.73644239
68	27.1759004	1836.21188	157.949175	326820.4071	0.99439751	0.72455049
70	27.7560774	1938.97103	161.69022	342571.3033	0.99617755	0.76233335
72	26.960085	1955.18548	158.266959	642806.509	0.98968587	0.63615763
74	29.9433382	2222.22549	174.848859	202372.2104	0.99055632	0.63801974
76	30.7510953	2332.98771	179.797525	206551.4666	0.98750424	0.587467
78	28.9842496	2291.16584	171.036976	349357.371	0.98607809	0.53279776
80	32.2657369	2579.15523	189.320277	125882.0585	0.98870807	0.55363038
82	32.951907	2711.30509	193.774326	92385.52151	0.98586611	0.51710224
84	30.4719125	2585.82228	180.790451	161559.2102	0.98337638	0.52603608
86	33.2223315	2870.76888	196.32384	67083.31487	0.96310176	0.39162425
88	33.0152923	2905.88625	195.605348	54134.98199	0.97813256	0.56580301
90	32.452978	2953.68556	193.495666	128633.7698	0.96655373	0.46936396
92	32.2748776	2965.96548	192.249148	48845.94672	0.91956493	0.34423447
94	30.5994413	2867.18956	183.016328	60329.22018	0.79416806	0.22700301
96	30.5373576	2945.66088	183.699961	126777.4424	0.84637432	0.22130179
98	29.7580503	2914.9165	179.028421	43017.60215	0.64681657	0.28617484
100	28.0712553	2800.34637	169.674959	31972.1718	0.5910797	0.36058935

q	n	b	$\ln(A)$	χ^2_R	R^2	p
1	11.482689	188.26938	64.640695	10739914	0.9995146	0.9243267
3	11.008489	183.35228	62.616043	7073080	0.9996669	0.9315442
5	11.591629	194.73374	65.236556	6642755.4	0.9996168	0.9301414
7	11.792028	202.33355	66.226267	5782482.4	0.9996329	0.9327556
9	11.527199	204.98519	65.21877	5193239	0.9996321	0.9276872
11	12.358534	225.46685	69.057348	4660440.1	0.9996558	0.9336964
13	12.660932	240.0392	70.622858	4151006.2	0.9995703	0.9281643
15	12.383067	247.47068	69.650053	4053624.1	0.9995841	0.9234965
17	13.557861	280.96975	75.193111	3651657.8	0.9994172	0.9199323
19	14.076779	305.56615	77.850081	3174437	0.9995381	0.9254928
21	13.699439	316.40697	76.504985	3309447.5	0.9996719	0.9312652
23	15.159539	364.72264	83.541341	2224126.6	0.9994852	0.918997
25	15.729403	397.96698	86.578101	1902413.7	0.9994912	0.917291
27	15.200676	411.02099	84.580741	2064269.2	0.9992464	0.9002134
29	17.228911	483.68516	94.488372	1448892.8	0.9991714	0.8994929
31	17.798967	525.80198	97.650175	1162968.6	0.9986576	0.8730177
33	16.93601	535.78585	94.127709	980777.37	0.9988245	0.8660956
35	19.278601	632.70127	105.81339	691125.75	0.9984497	0.8745987
37	20.041628	689.78187	110.04235	513439.44	0.999073	0.900835
39	18.933939	698.72236	105.34806	364507.66	0.9983439	0.843742
41	22.107573	839.76313	121.39181	194299.88	0.9990818	0.8920139
43	22.637093	901.93577	124.64212	152134.88	0.9990143	0.8941551
45	21.162296	902.53125	118.15491	153776.51	0.9974057	0.8071796
47	25.2137	1101.0979	138.94099	67751.3	0.9985178	0.8710315
49	26.284397	1195.3354	145.03946	63294.618	0.99799	0.8479883
51	24.525682	1192.442	137.14593	92767.708	0.9913448	0.7268201
53	28.790335	1421.5498	159.33483	39928.21	0.9936578	0.7553077
55	29.323074	1510.0419	162.8653	37196.452	0.9936361	0.7295352
57	27.365459	1494.7997	153.84324	40851.635	0.9935716	0.7339095
59	31.8577	1765.7928	177.4976	20519.768	0.9908882	0.6964478
61	33.291403	1910.9736	185.87455	16184.565	0.9911659	0.7134993
63	29.515581	1805.3579	167.28047	24047.013	0.9884544	0.6685204
65	34.683819	2134.8346	194.79778	7495.1455	0.9866505	0.675547

FIGURE 2.37: *Left : list of best fit coefficients for all even curves $q \in [0, 100]$. Right: List of best fit coefficients for all odd curves $q \in [1, 65]$.*

Coefficient values for the description of the entire $h^{1,1} + h^{1,2}$ distribution

$$A_{k,i} = \begin{pmatrix} 54.2664195 & 2.9066 \times 10^{-16} & 0.02414823 & -5.4137 \times 10^{-20} & -7.2635 \times 10^{-7} \\ 65.0676835 & -2.0296 \times 10^{-16} & 0.03354614 & 3.7552 \times 10^{-19} & -3.1443 \times 10^{-7} \\ 54.8909275 & -2.0323 \times 10^{-16} & 0.02753302 & -2.7091 \times 10^{-20} & -9.1972 \times 10^{-7} \\ 62.6423777 & 1.2736 \times 10^{-16} & 0.03020535 & -1.1234 \times 10^{-19} & -8.6929 \times 10^{-7} \\ 54.5840853 & 2.9011 \times 10^{-16} & 0.02748121 & -9.4235 \times 10^{-20} & -9.3840 \times 10^{-7} \\ 64.2001359 & -1.3980 \times 10^{-16} & 0.03700128 & 8.3795 \times 10^{-20} & -1.3712 \times 10^{-7} \end{pmatrix} \tag{2.6.9}$$

$$b_{k,i} = \begin{pmatrix} 132.357878 & 3.3411 \times 10^{-15} & 0.32753297 & -8.6619 \times 10^{-19} & 4.5825 \times 10^{-6} \\ 184.853063 & -5.7999 \times 10^{-17} & 0.31981034 & 1.0014 \times 10^{-18} & 3.9052 \times 10^{-5} \\ 117.228782 & -1.2791 \times 10^{-15} & 0.36989364 & -8.5325 \times 10^{-20} & 2.9743 \times 10^{-6} \\ 173.033950 & -1.1829 \times 10^{-15} & 0.31584408 & 8.9872 \times 10^{-19} & 2.5454 \times 10^{-5} \\ 105.298297 & 5.7916 \times 10^{-15} & 0.37843953 & -1.5078 \times 10^{-18} & 1.3974 \times 10^{-6} \\ 171.521189 & 1.5811 \times 10^{-15} & 0.36410293 & -2.5726 \times 10^{-19} & 2.5139 \times 10^{-5} \end{pmatrix} \tag{2.6.10}$$

$$n_{k,i} = \begin{pmatrix} 8.98205242 & 2.9066 \times 10^{-17} & 0.00434183 & -6.7671 \times 10^{-21} & -1.5512 \times 10^{-7} \\ 11.6018246 & 5.1148 \times 10^{-17} & 0.00644305 & 0 & -1.7241 \times 10^{-7} \\ 9.19515076 & 4.3161 \times 10^{-17} & 0.00496066 & -1.3763 \times 10^{-20} & -1.9163 \times 10^{-7} \\ 11.0620173 & -1.1446 \times 10^{-18} & 0.00570064 & 2.8085 \times 10^{-20} & -2.4813 \times 10^{-7} \\ 9.15798913 & 5.0109 \times 10^{-17} & 0.00493009 & -2.3559 \times 10^{-20} & -1.9210 \times 10^{-7} \\ 11.4578629 & -6.0813 \times 10^{-18} & 0.00705818 & 9.2055 \times 10^{-21} & -3.5862 \times 10^{-7} \end{pmatrix} \tag{2.6.11}$$

2.6.4 Supplementary plots for the fourfold data.

When looking for mirror symmetry in the fourfold data, we only observed partial mirror symmetry. Below is the full break down of the data set.

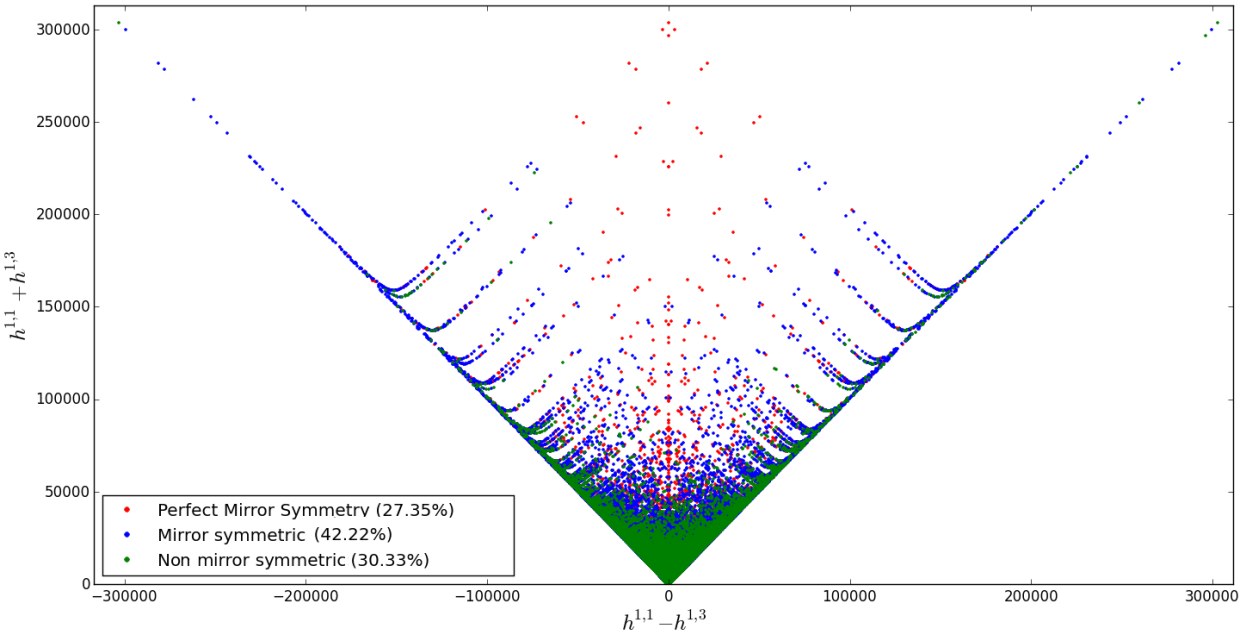


FIGURE 2.38: *Mirror symmetry is incomplete in the fourfold data set.*

Chapter 3

Flatness of Minima in Random Inflationary Landscapes

This chapter has appeared in a preprint with collaborators Yang-Hui He, Vishnu Jejjala, Yan Xiao and Da Zhou as:

Author : Y.H. He, V. Jejjala, L. Pontiggia, Y. Xiao and D. Zhou

Title : Flatness of Minima in Random Inflationary Landscapes

Year : 2017

E-print : 1704.08351

Archive prefix : arXiv

Primary class : hep-th

3.1 Introduction

In order to solve the well known horizon and flatness problems, cosmological inflation [100, 30, 101, 102] posits that the Universe underwent a period of exponential expansion early in its history. To date, there is no uniquely compelling realization of how inflation transpired. The literature abounds with numerous and varied proposed mechanisms [103, 37]. Paradigmatic models involve scalar fields which dynamically roll until arriving at the (relative) minimum of some potential.

While a model of physics that purports to approximate our world must correctly trace out the cosmological history of the Universe, these are not the only considerations in selecting a theory. The Standard Model of particle physics establishes that at low energies the particles in Nature organize themselves into three generations of chiral fields that transform in representations of the $SU(3) \times SU(2)_L \times U(1)_Y$ gauge group. Top down realizations of low energy gauge theories from a fundamental theory such as string theory typically

augment the symmetries of the S-matrix with supersymmetry. The simplest scenario for preserving $\mathcal{N} = 1$ supersymmetry in four dimensions involves the compactification of the heterotic string in ten dimensions on a Calabi–Yau threefold [56]. This effort has led to a number of constructions that reproduce the matter spectrum and Yukawa interactions observed in the Standard Model [99, 104, 105, 106, 107, 108, 109, 110, 111, 112, 113]. Again, we have an abundance of models that are *a priori* indistinguishable on the basis of experiments.

As we do not have a *sui generis* path to the real world, we propose to study a large class of models at once and incorporate inputs of both cosmology and particle physics. The most important characterization of a Calabi–Yau threefold is a pair of topological invariants $h^{1,1}$ and $h^{2,1}$. There are $h^{1,1}$ Kähler and $h^{2,1}$ complex structure parameters that describe the size and the shape of the geometry. In the most naïve setup, these deformation parameters supply candidates for the scalar fields in inflation. The largest available catalog of Calabi–Yau threefolds is derived from the Kreuzer–Skarke database of reflexive polytopes [63]. Using the methods of Batyrev and Borisov [88, 63], each consistent triangulation of a reflexive polytope yields a toric Calabi–Yau manifold. In [66, 114], topological and geometric data are tabulated for the Calabi–Yau threefolds thus obtained for low values of $h^{1,1}$. Heterotic Standard Model constructions in string theory typically employ Calabi–Yau geometries with small values of the Hodge numbers. For example, [104] uses a manifold with $(h^{1,1}, h^{2,1}) = (3, 3)$. Where there are explicit candidates for particle physics from string theory, we expect only a small number of moduli to appear in the low energy effective action. Motivated by this fact, these are the models that we investigate in this article.

We aim to provide statistics for how many (possibly metastable) vacua support slow-roll constraints on inflation. Working in effective field theory, we examine random polynomial potentials for inflation with a small number of scalar fields. The justification for examining these models derives from string constructions of de Sitter like metastable vacua, *e.g.*, the KKLT [115] and Large Volume Scenarios [116]. In the latter class of models, the number of flat directions in the low energy effective potential is given by the number of parametrically large four cycles. (In fact, the number of flat directions is one less than the number of large cycles [116].) There are 69 explicit Calabi–Yau geometries with two large cycles and one known Calabi–Yau geometry with three large cycles [117]. These are candidate manifolds for bona fide cosmological model building in string theory that correspond to one field and two field inflation. In light of this, we study random potentials relevant to these cases in particular.

The potentials we study are sums of monomials in the scalar fields. We truncate the expansion to focus on the interactions that are relevant or marginal from the perspective of a four dimensional low energy effective action. As higher order monomials in the fields are irrelevant operators, we expect these to be mass suppressed and neglect them for the purposes of our investigations. We will study models where the time scale for inflation if $t_{\rm GUT}$. Correspondingly, the energy scale in the problem is $M_{\rm GUT}$. Invoking naturalness [118], we choose coefficients in the potential to be order one with respect to this scale. (It is not always required that we choose $t_{\rm GUT}$ as the natural time scale in the problem; in fact, certain models [103, 37] employ energy scales which are lower than $M_{\rm GUT}$.) In discussing single field models with order one coefficients, our work is analytic. In multi-field models, we construct random potentials whose coefficients are selected from distributions.

At the outset, we should note that the cases we analyze where there are few moduli may well represent an atypical class of string compactifications. While there are 473 800 776 reflexive polyhedra in four dimensions, there are only 30 108 pairs of Hodge numbers that appear in the threefold dataset. The number of reflexive polytopes in the Kreuzer–Skarke list peaks at the Hodge numbers $(h^{1,1}, h^{2,1}) = (27, 27)$.

There are 910 113 such polytopes. Indeed, there are significant and surprising patterns in the distribution of Calabi–Yau geometries close to this maximum [119]. Reflexive polytopes with low Hodge numbers are sparse in the Kreuzer–Skarke database. Flux compactifications on Calabi–Yau threefolds yield, in principle, an enormously large number of potential vacua for string theory [120, 121]. There are, however, to date no explicit constructions of the Standard Model on a geometry with Hodge numbers that correspond to those of a typical Calabi–Yau manifold. As there are good reasons to be skeptical about anthropic resolutions to the cosmological constant problem and there are potential issues regarding the stability of the flux vacua [122, 123, 124], we adopt an agnostic attitude. We simply note that if a construction is stable in this context, a generic compactification on a typical Calabi–Yau manifold will most likely involve a large number of moduli fields. As we review below, the large-N limit of inflaton fields is studied in complementary work.

The organization of the paper is as follows. In Section 3.2, we discuss the setup for random inflation. In Section 3.3, we investigate the case of single field inflation with $O(1)$ coefficients. This analysis is a completely analytic study of polynomial equations. In Section 3.4, we examine the case of two scalar fields with couplings up to quartic order. Again, the coefficients are $O(1)$. We choose coefficients using a uniform distribution and a Gaussian distributions for coefficients of indefinite sign and a gamma distribution for coefficients that are positive. In Section 3.5, we remark on future investigations in the context of semi-realistic string models.

3.2 Random potentials for inflation

The action we consider assumes the form

$$I = -\int d^4x\sqrt{-g}\,\left(\frac{R}{16\pi G} + \frac{1}{2}g^{\mu\nu}\partial_\mu\boldsymbol{\phi}\cdot\partial_\nu\boldsymbol{\phi} - V(\boldsymbol{\phi})\right)\,, \tag{3.2.1}$$

where the Einstein–Hilbert term is supplemented by a matter sector that consists of k scalar fields,

$$\boldsymbol{\phi} = (\phi^1, \phi^2, \cdots, \phi^k)\,. \tag{3.2.2}$$

For simplicity, we assume that the metric in field space is the identity matrix, *i.e.*,

$$\partial_\mu\boldsymbol{\phi}\cdot\partial_\nu\boldsymbol{\phi} = \delta_{ij}\partial_\mu\phi^i\partial_\nu\phi^j\,. \tag{3.2.3}$$

The scalar potential $V(\boldsymbol{\phi})$ determines the model and can be expanded as a polynomial in the fields ϕ^i.

This setup lets us examine cosmological inflation. Deducing the form of the potential is a long standing problem; many scenarios present attractive phenomenological features, and to date observation has provided only limited guidance in selecting $V(\boldsymbol{\phi})$. In models with a single inflation field, famously the WMAP [125] and Planck [126] observations disfavor the simplest quadratic potential. Other scenarios are variously consistent with the data. See, for example, [127] for a recent review.

One of the simplest multi-field models, hybrid inflation [128], involves coupling two fields according to the potential

$$V(\phi,\psi) = \frac{1}{4\lambda}(\lambda\psi^2 - M^2)^2 + \frac{1}{2}m^2\phi^2 + \frac{\lambda'}{2}\phi^2\psi^2\,. \tag{3.2.4}$$

Here, λ and λ' are couplings and M and m are the masses of ψ and ϕ, respectively. We require that $V(\phi) = \frac{1}{2}m^2\phi^2 \ll \frac{M^4}{4\lambda}$. This guarantees that the inflationary energy density of the false vacuum associated to the symmetry breaking potential $V(\psi) = \frac{\lambda}{4}(\psi^2 - M^2)^2$ dominates. The effective mass for the ψ field is $M_{\rm eff}^2 = -M^2 + \lambda'\phi^2$, which vanishes at $\phi_*^2 = M^2/\lambda'$. Starting from $\phi^2 \gg M^2$, the minimum is at $\psi = 0$. This is morally a single field model with an effective potential of the form

$$V_{\rm eff} = \frac{\lambda}{4}M^4 + \frac{1}{2}m^2\phi^2 \ . \tag{3.2.5}$$

The field rolls until it reaches ϕ_*. The $\psi = 0$ locus is then unstable, and the field rolls again into the true minima at $\phi = 0$, $\psi = \pm M$. Interest in the model stems from its versatility and success in predicting certain features of inflation, such as the power law behavior of the perturbation spectrum. By tweaking the model in various ways, one can deal with inflation with or without first order phase transitions. While this is a prototype multi-field model, there is a built-in hierarchy to the coefficients. (See also [129].)

By constraining the inflationary scenario at a level matching the accuracy of current experimental data, [37] presents an encyclopedia of 74 satisfactory models. In our work, we adopt a slightly different approach and address the question of how generic or specific the models should be in order to satisfy experimental constraints. For this purpose, we consider randomly generated multi-field models (with the inflationary potential being given by polynomials with random coefficients) and verify whether the models can satisfy a certain set of conditions. In particular, we demand that the scalar potential has a parameter window such that slow-roll conditions are satisfied.

Suppose there are some minima that satisfy the slow-roll conditions. What are the global features of the potentials that accommodate this? Turning the question around, given a large set of potentials (which may have some distribution in the function space), how likely is it that the potential has regions that satisfy slow-roll conditions? How often can slow-roll inflation be accommodated with $O(1)$ coefficients? These are the issues we aim to address below.

In an analysis of multi-field inflation, the need to establish the behavior of random potentials is almost compulsory. Generic compacticiations, can have hundreds of scalar fields [61, 130, 131, 132]. Since these theories describe physics at energy scales close to the inflationary scale, there is considerable interest in analyzing their dynamics. Considering random potentials with large-N fields has a considerable history [46, 133, 134, 50, 135, 48, 35, 36, 136, 49, 137, 138, 139]. As multi-field models have an almost infinite number of ways to inflate, the task of understanding how the potential energy driving inflation is distributed among all these fields becomes an incredibly difficult one. This problem is often referred to as the measure problem, and it deals with attempting to handle the possible initial conditions [41, 38, 40, 39]. Multidimensional landscapes may also be afflicted by instabilities [140, 141, 142]. In general, the approach that random multi-field inflation adopts, is to study the dynamics of inflation by creating an ensemble of random potentials. Then, through a statistical analysis, one can comment on the inflationary landscape produced by the respective models. Related studies have recently appeared in the context of Gaussian models [143, 144] and non-minimal kinetic terms [145].[1] The study of random potentials is of course not limited to inflation. It is useful to borrow techniques for the generation of random potentials from other fields in physics, in particular string theory and quantum field theory [147, 148], and adapt these ideas to the cosmological context.

[1] As we were completing this work, a similarly themed investigation appeared in [146]. This work examines inflationary landscapes corresponding to one dimensional potentials.

In Section 3.3, we analyze the single field case analytically. In Section 3.4, we investigate the statistics of random inflation by examining a large set of sample potentials for two field inflation. In each potential, the coefficients are random numbers that fall within a particular range. For each sample potential, we examine whether it has slow-roll regions. We calculate the fraction of potentials that do have slow-roll regions and examine what features they have in common. For succinctness, in the following we will use the term "*slow-roll potentials*" to refer to those potentials that satisfy the slow-roll conditions in some region of the field space. We assume the potential term $V(\boldsymbol{\phi})$ is a polynomial in ϕ^i up to degree four and is bounded below. In this paper, we only consider single field and two field inflation models. In the former case, we shall denote $\boldsymbol{\phi} = \widetilde{\varphi}$, and in the latter, $\boldsymbol{\phi} = (\widetilde{\varphi}, \widetilde{\psi})$. Both cases are developed in the following sections.

3.3 Single field models

The polynomial potential up to degree four for single field inflationary models has the form

$$V_{a,b}(\widetilde{\varphi}) = \frac{\widetilde{\varphi}^2}{2}(M^2 - aM\widetilde{\varphi} + b\widetilde{\varphi}^2) \ , \tag{3.3.1}$$

where $M \lesssim 10^{16}$ GeV is the mass of the inflaton $\widetilde{\varphi}$, and a and b are two dimensionless random numbers. Note that in order for the potential to be bounded from below, the quartic term must be positive, which means we presume b is positive. Another feature about this potential is the symmetry

$$V_{-a,b}(\widetilde{\varphi}) = V_{a,b}(-\widetilde{\varphi}) \ , \tag{3.3.2}$$

which indicates if $V_{a,b}$ is a slow-roll potential, $V_{-a,b}$ must also be slow-roll. So again we only need to assume that a is positive.

Now, to factor out the parameter M, we perform a rescaling, $\widetilde{\varphi} = M\varphi$, which also makes φ dimensionless. Then the potential can be recast as

$$V(\varphi) = \frac{M^4}{2}\varphi^2(1 - a\varphi + b\varphi^2) \ , \tag{3.3.3}$$

where we have omitted the two subscripts a and b on V.[2] Consequently, the two slow-roll parameters are

$$\begin{aligned} \epsilon &= \frac{M_{\rm Pl}^2}{2}\left(\frac{V'(\widetilde{\varphi})}{V(\widetilde{\varphi})}\right)^2 = \frac{1}{2\mu}\left(\frac{V'(\varphi)}{V(\varphi)}\right)^2 \ , \\ \eta &= M_{\rm Pl}^2\frac{V''(\widetilde{\varphi})}{V(\widetilde{\varphi})} = \frac{1}{\mu}\frac{V''(\varphi)}{V(\varphi)} \ , \end{aligned} \tag{3.3.4}$$

where $M_{\rm Pl}$ is the Planck mass and $\mu = M^2/M_{\rm Pl}^2$ is the square of the ratio between the mass of the inflaton and the Planck mass. The Planck 2015 [127] data tells us that the scalar spectral index is measured to be $n_s = 0.9655 \pm 0.0062$ and the slow-roll parameters are deduced to satisfy

$$\epsilon < 0.012 \ , \qquad \eta = -0.0080^{+0.0088}_{-0.0146} \ . \tag{3.3.5}$$

[2] Adding a zeroth order term to the potential will shift the energy of the relative minimum. Though the potential appears in the denominator of the slow-roll conditions, we assume constant terms in the potential do not greatly affect flatness and therefore neglect such a term in writing the potential.

Noting that $n_s - 1 = 2\eta - 6\epsilon$, in our analysis we demand that the slow-roll parameters are $O(10^{-2})$:

$$\epsilon < 0.01 \ , \qquad |\eta| < 0.01 \ . \tag{3.3.6}$$

Given the definition of μ, the two slow-roll parameters are actually independent of the specific value of inflaton mass M because the M^4 term in (3.3.3) appears in both the numerator and denominator of (3.3.4) and therefore cancels.

If we define a new variable $y = a\varphi$, the whole analysis will only depend on the ratio of b to a^2, which shall be dubbed β, instead of the explicit values of a and b. So we can define an auxiliary potential,

$$v(y) = \frac{2a^2}{M^4} V(\varphi) = y^2(1 - y + \beta y^2) \ , \qquad \beta = \frac{b}{a^2} > 0 \ , \tag{3.3.7}$$

and two new slow-roll parameters which only depend on one parameter β,

$$\bar{\epsilon} = \frac{1}{2}\left(\frac{v'}{v}\right)^2 = \frac{\nu}{0.01}\epsilon \ , \qquad \bar{\eta} = \frac{v''}{v} = \frac{\nu}{0.01}\eta \ , \tag{3.3.8}$$

where

$$v' \equiv \frac{dv}{dy}, \qquad v'' \equiv \frac{d^2v}{dy^2} \ , \qquad \nu \equiv \frac{0.01\mu}{a^2} = \frac{0.01}{a^2}\frac{M^2}{M_{\rm Pl}^2} \ . \tag{3.3.9}$$

The slow-roll conditions become

$$\bar{\epsilon} < \nu \ , \qquad |\bar{\eta}| < \nu \ . \tag{3.3.10}$$

Of course, we have assumed $a \neq 0$ in (3.3.7) and (3.3.10), and the special $a = 0$ case can be approximated by setting a to be an extremely small nonzero number, then $a \to 0$ corresponds to the $\beta \to \infty$ case, which is a special situation that will be discussed in Section 3.3.1.1.

From (3.3.7) one can see that as $y \to \pm\infty$, $v \sim y^4$ while $v' \sim y^3$ and $v'' \sim y^2$, so (3.3.6) is always satisfied. That means, there exists a $y_0 > 0$ and a $y_0' < 0$ such that (3.3.6) holds true for all $y > y_0$ or all $y < y_0'$. In other words, in any cases there are always at least two trivial slow-roll regions, $(-\infty, y_0')$ and (y_0, ∞). Our search for an inflationary scenario excludes these regions where the (3.3.6) is satisfied simply due to the largeness of the potential v.[3] We aim to isolate other, perhaps more realistic scenarios which satisfy the slow-roll conditions with a flat v (*i.e.*, small v' and v'') region of finite length.

From (3.3.8) we have

$$\frac{d\bar{\epsilon}}{dy} = \frac{v'}{v^3}(v''v - v'^2) = -\frac{y^2}{v^3}v'\left[2 - 4y + (3 + 2\beta)y^2 - 6by^3 + 4\beta^2 y^4\right]. \tag{3.3.11}$$

For $y < 0$, we have $v > 0$, $v' < 0$, and the expression within the brackets is positive, so $\frac{d\bar{\epsilon}}{dy} > 0$. This means, if we find a $y_0' < 0$ such that $\bar{\epsilon}(y_0') = 0.01$, then $(-\infty, y_0')$ is a trivial slow-roll region and $(y_0', 0)$ does not contain a non-trivial slow-roll region. Hereafter, we are only interested in the region with $y > 0$.

In deducing the regions that satisfy the slow-roll conditions in single field inflation, we do not need to perform a Monte Carlo analysis or scan over potentials with random coefficients. It suffices to analytically examine a system of polynomial equations. We look for the true minimum of the potential. Complementary

[3] This is not to say that regions where inflation transpires by virtue of a large denominator v must always be disregarded. Models such as chaotic inflation can use these trivial regions of the potential.

investigations (see, for example, [146]) examines relative minima in random landscapes. In the following subsection, we will see that different intervals for β exhibit characteristic behavior.

3.3.1 Behavior of slow-roll parameters

Graphically, we can draw the slow-roll parameters, which are functions of y given a specific value of β, on the plane and use the horizontal lines $\bar{\epsilon} = \nu$ and $\bar{\eta} = \pm\nu$ to intercept curves of the slow-roll parameters $\bar{\epsilon}$ and $\bar{\eta}$ respectively, then from the interception one can easily read off whether there are slow-roll regions for the corresponding potential. The classification of different behaviors of $\bar{\epsilon}$ and $\bar{\eta}$ will be represented below.

To determine the behavior of slow-roll parameters $\bar{\epsilon}$ and $\bar{\eta}$, we compute their partial derivatives with respect to y,

$$\frac{\partial\bar{\epsilon}}{\partial y} = \frac{y^2 v'}{v^3} f(y,\beta)\ , \qquad \frac{\partial\bar{\eta}}{\partial y} = \frac{2y}{v^2} g(y,\beta), \tag{3.3.12}$$

where

$$\begin{aligned} v' &:= 2y - 3y^2 + 4\beta y^3, \\ f(y,\beta) &:= -2 + 4y - (3+2\beta)y^2 + 6\beta y^3 - 4\beta^2 y^4, \\ g(y,\beta) &:= -2 + 6y - (6+4\beta)y^2 + 15\beta y^3 - 12\beta^2 y^4. \end{aligned} \tag{3.3.13}$$

For $\beta > 9/32$ we have $v > 0$ and $v' > 0$, so the signature of $\frac{\partial\bar{\epsilon}}{\partial y}$ or $\frac{\partial\bar{\eta}}{\partial y}$ depends on the signature of $f(y,\beta)$ or $g(y,\beta)$. In order to determine the signature of f and g, we differentiate them with respect to y,

$$\begin{aligned} \frac{\partial f}{\partial y} &= 4 - 2(3+2\beta)y + 18\beta y^2 - 16\beta^2 y^3, \\ \frac{\partial^2 f}{\partial y^2} &= -48(\beta y - 3/8)^2 - (4\beta - 3/4) < 0, \\ \frac{\partial g}{\partial y} &= 6 - 2(6+4\beta)y + 45\beta y^2 - 48\beta^2 y^3, \\ \frac{\partial^2 g}{\partial y^2} &= -144(\beta y - 5/6)^2 - (8\beta - 33/16) < 0. \end{aligned} \tag{3.3.14}$$

Since $\frac{\partial^2 f}{\partial y^2} < 0$ and $\frac{\partial^2 g}{\partial y^2} < 0$, $\frac{\partial f}{\partial y}$ and $\frac{\partial g}{\partial y}$ are monotonically decreasing functions of y. In addition, $\frac{\partial f}{\partial y}(y = 0) > 0$ and $\frac{\partial f}{\partial y}(y = \infty) < 0$, so $\frac{\partial f}{\partial y}$ has one root in $(0,\infty)$. By the same token, $\frac{\partial g}{\partial y}$ also has one root in $(0,\infty)$. We illustrate the previous analysis in Figure 3.1. From Figure 3.1 we can see that both functions f and g have one and only one maximum which is $\bar{y}$ (respectively $\bar{y}'$) in $(0,\infty)$. As $f(0,\beta) = g(0,\beta) = -2$ and $f(\infty,\beta)$ or $g(\infty,\beta) < 0$, we conclude, (1) if $f(\bar{y},\beta) < 0$ (respectively, $g(\bar{y}',\beta) < 0$), $\bar{\epsilon}$ (respectively, $\bar{\eta}$) is monotonically decreasing in $(0,\infty)$; (2) if $f(\bar{y},\beta) > 0$ (respectively, $g(\bar{y}',\beta) > 0$), $\bar{\epsilon}$ (respectively, $\bar{\eta}$) has one local minimum and one local maximum in $(0,\infty)$. Between these two cases, there is an intermediate stage which is $f(\bar{y},\beta) = 0$ or $g(\bar{y}',\beta) = 0$. As a result, we need to solve following two sets of equations,

$$\begin{cases} f(y,\beta) = 0 \\ \frac{\partial}{\partial y} f(y,\beta) = 0 \end{cases} \quad \text{and} \quad \begin{cases} g(y,\beta) = 0 \\ \frac{\partial}{\partial y} g(y,\beta) = 0 \end{cases}. \tag{3.3.15}$$

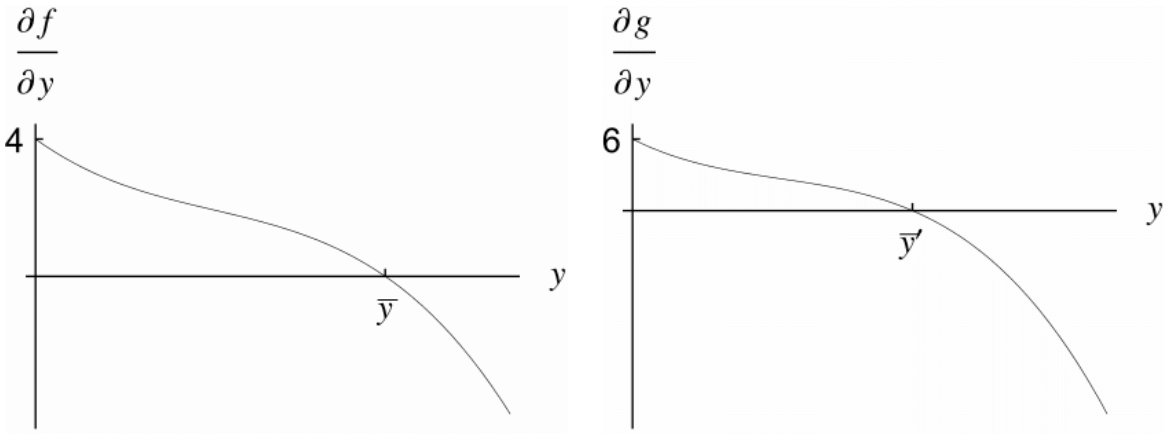


FIGURE 3.1: *Roots of* $\frac{\partial f}{\partial y}$ *and* $\frac{\partial g}{\partial y}$.

The two sets of equations are reduced, by a Groebner basis elimination, to

$$(784\beta^3 - 846\beta^2 + 270\beta - 27)(4\beta - 1) = 0 \tag{3.3.16}$$

and

$$(8192\beta^3 - 10368\beta^2 + 3591\beta - 378)(25\beta - 6) = 0 \tag{3.3.17}$$

respectively. Eq. (3.3.17) gives $\beta = 0.778890$, which supplies the bounds for the interval in Section 3.3.1.1, and (3.3.16) gives $\beta = 0.602103$, which then supplies the bounds for the interval in Section 3.3.1.2.

3.3.1.1 $\beta \geq 0.7789$

For $\beta \geq 0.7789$, both $\bar{\epsilon}$ and $\bar{\eta}$ are monotonically decreasing for $y \in (0, \infty)$, which is shown in Figure 3.2. From this graph it can be readily seen that given any ν there is only one trivial slow-roll region for $y > 0$

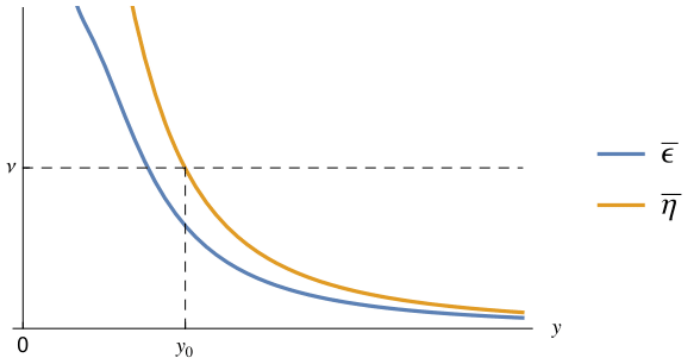


FIGURE 3.2: *Shapes of* $\bar{\epsilon}$ *and* $\bar{\eta}$ *for* $\beta \geq 0.7789$.

which in this graph is (y_0, ∞).

3.3.1.2 $0.6021 \leq \beta < 0.7789$

For β in this region, $\bar{\epsilon}$ is still a monotonically decreasing function for $y \in (0, \infty)$ while $\bar{\eta}$ is not any longer. The shape of these two slow-roll parameters are shown in Figure 3.3. From this graph one can easily read off, given that $\nu_{\min} < \nu < \nu_{\max}$, the two slow-roll regions, one of which is (y_0, ∞) which is trivial, and

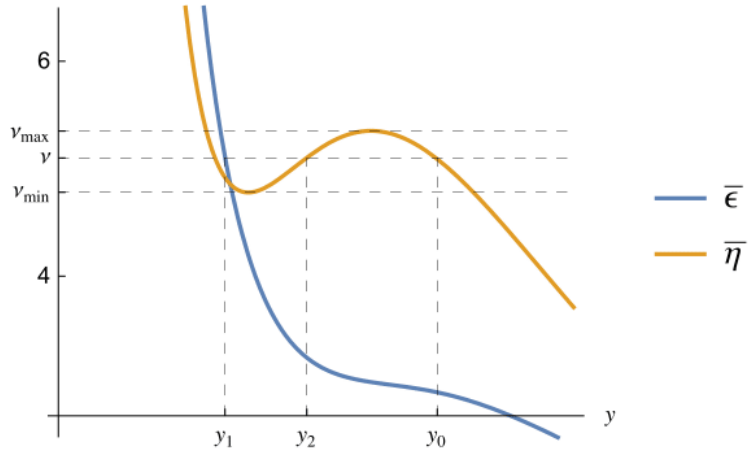


FIGURE 3.3: *Shapes of $\bar{\epsilon}$ and $\bar{\eta}$ for $0.6021 \leq \beta < 0.7789$.*

the other is (y_1, y_2) which has finite length and is thus the kind of slow-roll region we are searching for. From this graph we can also see that there are an upper bound and a lower bound for ν beyond which there is still only one trivial slow-roll region. In fact, this is a common feature, which will be justified in Sections 3.3.1.3, 3.3.1.4, and 3.3.1.5. Therefore, all these bounds of ν corresponding to different β render a window opening to non-trivial slow-roll regions, which shall be plotted in Section 3.3.2.

3.3.1.3 $9/32 \leq \beta < 0.6021$

For $\beta < 0.6021$, both $\bar{\epsilon}$ and $\bar{\eta}$ are not monotone functions of y in $(0, \infty)$, thus we should expect, on the whole, a wider range of ν that opens to non-trivial slow-roll regions. In particular, for $\beta \in [9/32, 0.6021)$, the potential v is still a monotonically increasing function for $y > 0$, which means there is no local minimum of v in $y \in (0, \infty)$ (the cases that v has a local minimum in $y \in (0, \infty)$ shall be dealt with in the following two subsections). The typical shapes of $\bar{\epsilon}$ and $\bar{\eta}$ are presented in Figure 3.4. From this figure, we can see that given $\nu \in (\nu_{\min}, \nu_{\max})$, there is a non-trivial slow-roll region, (y_1, y_2), apart from the trivial one, (y_0, ∞).

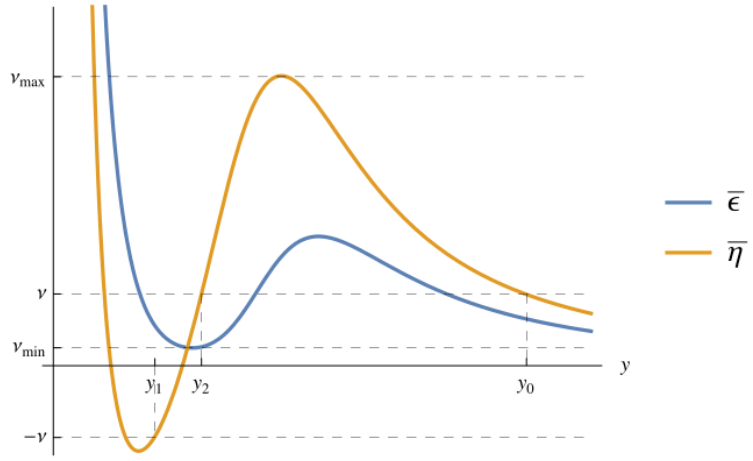


FIGURE 3.4: *Shapes of $\bar{\epsilon}$ and $\bar{\eta}$ for $9/32 \leq \beta < 0.6021$.*

3.3.1.4 $1/4 < \beta < 9/32$

In this interval, $v > 0$ still holds, but v' is not positive definite any longer. So $\frac{\partial \bar{\epsilon}}{\partial y}$ has two more roots which are the roots of v'. When $\beta < 9/32$, the potential $v(y)$ has a minimum on the right half $y - v$ plane. In

particular, for $\beta > 1/4$ this minimum is a local minimum (see the first graph of Figure 3.5). Physically, we

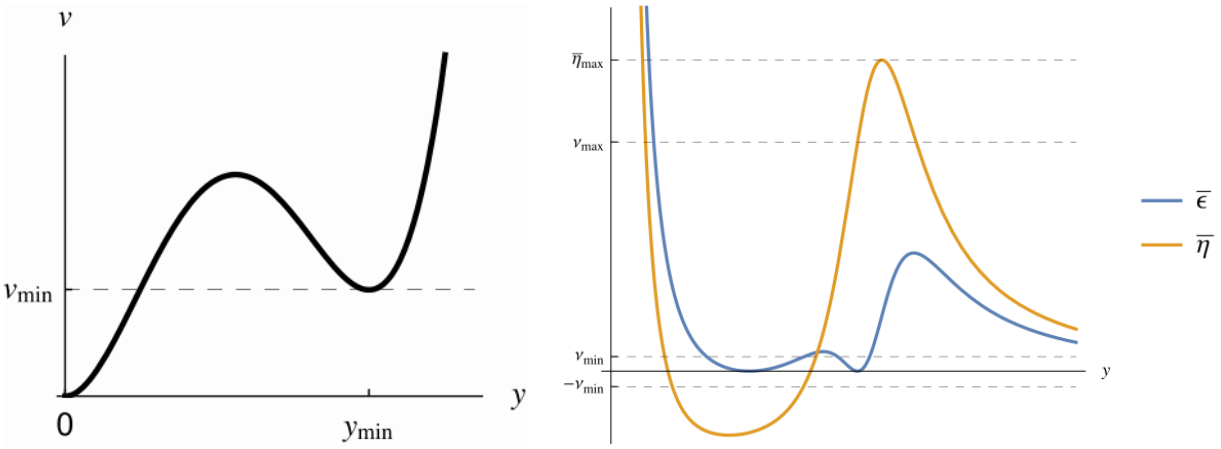


FIGURE 3.5: *The first graph shows the potential v has a local minimum at $y_{\min} > 0$. The second illustrates typical shapes of $\bar{\epsilon}$ and $\bar{\eta}$ for $1/4 < \beta < 9/32$.*

prefer the Universe to not being inflating at the minimum of the potential; the Universe should be reheating and the field should be oscillating. To ensure this, we look for $|\bar{\eta}(y_{\min})| > \nu$, where $y_{\min}$ is the local minimum point of v. Because of this extra filter, the upper bound of ν (*viz.*, $\nu_{\max}$) is not necessarily equal to the local maximum of $\bar{\eta}$ (*viz.*, $\bar{\eta}_{\max}$), which is illustrated in the second graph of Figure 3.5. In that graph, the lower bound of ν, namely $\nu_{\min}$, is also not at the minimum of $\bar{\epsilon}$ which is 0. This is the consequence of the restriction $\bar{\eta} > -\nu$.

3.3.1.5 $0 < \beta \leq 1/4$

Finally, when $\beta < 1/4$, v in the denominator of (3.3.12). This contributes two extra singularities. The potential v has a true vacuum in the right half $y - v$ plane, which is shown in the first graph of Figure 3.6. At this true vacuum, the potential is negative (or zero for $\beta = 1/4$) and thus potential $v(y)$ has two (or one

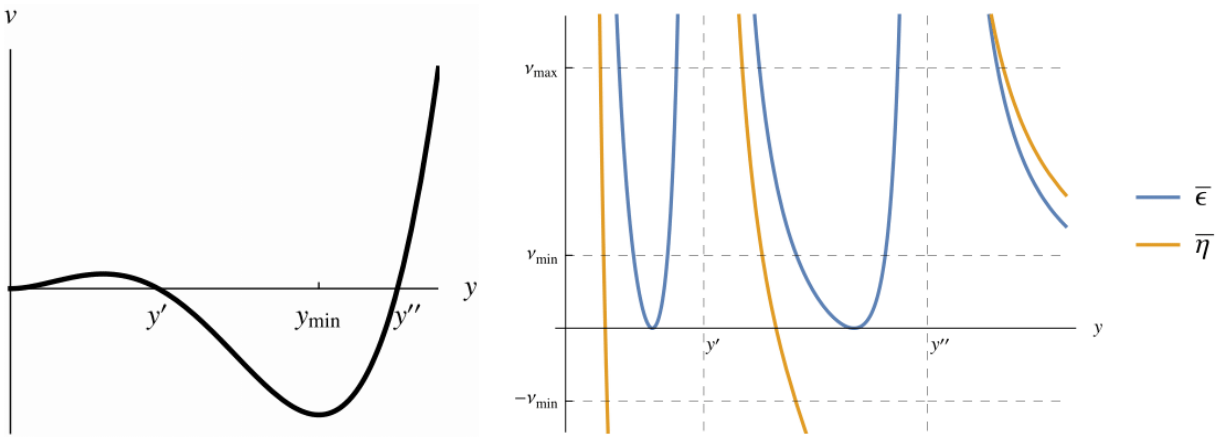


FIGURE 3.6: *The first graph shows the potential v has a global minimum at $y_{\min}$. The second illustrates typical shapes of $\bar{\epsilon}$ and $\bar{\eta}$ for $0 < \beta < 1/4$. The $\beta = 1/4$ case is a special case in which y' and y'' coincide.*

when $\beta = 1/4$) roots, dubbed y' and y'' respectively.

As a result, the slow-roll parameters $\bar{\epsilon}$ and $\bar{\eta}$ are singular at these two roots of v, which can be seen from the second graph of Figure 3.6. The bounds of ν, namely $\nu_{\min}$ and $\nu_{\max}$ are also denoted in that graph.

3.3.2 The window

Now that we have worked out all possible combinations of β and ν that opens a window to non-trivial slow-roll potentials whose procedure can be algorithmized by computer programs, we plot the numerical results in Figure 3.7. There are two salient features in this figure. First, at $\beta = 1/4$, the upper bound

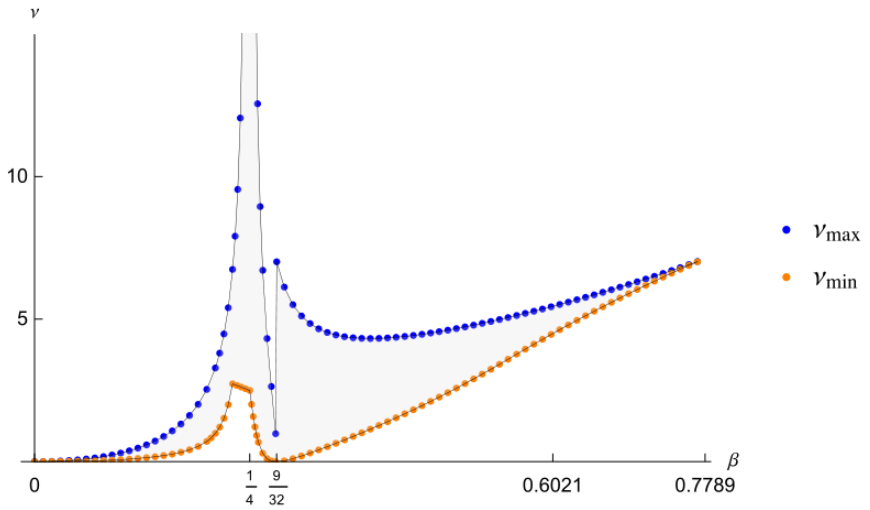


FIGURE 3.7: *The window that opens to non-trivial slow-roll potentials.*

of ν blows up, which means for any large enough ν the potential always has a non-trivial slow-roll region. Second, at $\beta = 9/32$, there is a discontinuity (jump) in the upper bound of ν. This is because, from $\beta > 9/32$ to $\beta < 9/32$, a local minimum $y_{\rm min}$ appears suddenly in the potential, and the subsequent introduction of the extra constraint $|\bar{\eta}(y_{\rm min})| > \nu$ which ensures that the Universe does not inflate at the minimum of the potential makes the bound for ν discontinuous.

3.4 Multi-field models

In this section, we investigate which potentials accommodate the slow-roll conditions for inflation with two fields. The form of the potentials we have is

$$\begin{aligned} V(\widetilde{\varphi},\widetilde{\chi}) &= \frac{\mu^2}{2}M^2\widetilde{\varphi}^2 + \frac{\rho^2}{2}M^2\widetilde{\chi}^2 + a_1 M\widetilde{\varphi}^3 + a_2 M\widetilde{\varphi}^2\widetilde{\chi} + a_3 M\widetilde{\varphi}\widetilde{\chi}^2 + a_4 M\widetilde{\chi}^3 \\ &\quad + b_1\widetilde{\varphi}^4 + b_2\widetilde{\varphi}^2\widetilde{\psi}^2 + b_3\widetilde{\chi}^4 \,, \end{aligned} \tag{3.4.1}$$

where the masses μM and ρM for the fields $\widetilde{\phi}$ and $\widetilde{\chi}$ are defined in terms of M, the GUT mass, the $a_i M$ are cubic couplings, and the b_i are quartic couplings. We will assume that the masses are around the GUT scale ($\sim 10^{16}$ GeV). We motivate the quartic potential from a Wilsonian perspective wherein higher order terms are suppressed by the energy scale at which new physics enters. We assume this is the string scale or Planck scale ($\sim 10^{19}$ GeV). Terms higher than quartic order, as they are suppressed by this higher energy scale, are neglected in the analysis. The coefficients a_i and b_i are order one numbers. The terms that appear in (3.4.1) are dictated by the fact that we demand all slow-roll potentials to be bounded from below. With this in mind, the a_i can be positive or negative and the b_i are positive. When both fields tend to $-\infty$, the

quartic terms should have no odd powers in any of the two variables. We can rescale (3.4.1) similarly to what we did in the single field case. With $\widetilde{\varphi} = M\varphi$ and $\widetilde{\chi} = M\chi$, we have

$$\begin{aligned} v(\varphi,\chi) &= \frac{\mu^2}{2}\varphi^2 + \frac{\rho^2}{2}\chi^2 + a_1\varphi^3 + a_2\varphi^2\chi + a_3\varphi\chi^2 + a_4\chi^3 \\ &\quad + b_1\varphi^4 + b_2\varphi^2\chi^2 + b_3\chi^4. \end{aligned} \tag{3.4.2}$$

Now all parameters and variables in potential v are dimensionless and it is sensible to talk about the magnitude of parameters. Note that $V = M^4 v$. These methods can readily be generalized to having more scalar fields. We simply require that the superpotential is renormalizable and bounded from below. As adding more scalars and studying the potentials explicitly in the finite field case is computationally more intensive, we do not extend the analysis beyond the two field level in this work. When searching for minima in the potential one will encounter both false and true vacua. We allow for slow-roll regions around false vacua (local minima) and not only the true vacua (global minima). The reason that we allow for both false and true vacua for slow-roll in two field case is based on computational and physical grounds. If we only look for global minima to test our slow-roll constraints, we firstly need to find global minima using methods such as steepest gradient descent subject to some arbitrary initial conditions. This will greatly increase the computational time and render the numerical test impossible in a reasonable time frame. Moreover, on physical grounds as long as the false vacuum is sufficiently long lived, the Universe may be in a metastable state. We do not analyze the lifetime to exclude short lived false vacua as this analysis depends on details of, say, particle physics and the presence of other nearby minima.

3.4.1 Slow-roll conditions for multi-field inflation

It is important to discuss the slow-roll conditions for multi-field inflation models as they are fundamentally different from those of single field case. The conditions are discussed in detail in [149]. We shall demand the following:

$$\begin{aligned} \epsilon &\equiv -\frac{\dot{H}}{H^2} = 3\left(\frac{\dot{\phi_i}^2}{V}\right) = \frac{M_{\rm Pl}^2(\partial_i V)^2}{2V^2} \ll 1 \ , \\ \xi &\equiv \sqrt{\widehat{V_1}\cdot\overleftrightarrow{V_2}\cdot\overleftrightarrow{V_2}\cdot\widehat{V_1}} \ll 1 \ , \end{aligned} \tag{3.4.3}$$

with

$$\widehat{V_1} \equiv \frac{\partial_i V}{|\partial_i V|} \ , \overleftrightarrow{V_2} \equiv \frac{M_{\rm Pl}^2(\partial_i\partial_j V)}{V} \ , \tag{3.4.4}$$

for fields $\boldsymbol{\phi} = (\varphi,\chi)$. Here the conditions are derived from the approximation $3H\dot{\phi}_i \approx -\partial_i V$, which is essentially the consistent second slow-roll condition. This comes down to neglecting $\ddot{\phi}_i$ compared to $\partial_i V$. But when comparing two vectors, it is sensible only to compare their norms. Therefore we have the *strong second slow-roll condition* $|\ddot{\phi}_i| \ll |\partial_i V|$. The reason it is called the strong second slow-roll condition is because its smallness implies

$$\eta \equiv \widehat{V_1}\cdot\overleftrightarrow{V_2}\cdot\widehat{V_1} \ll 1 \ , \tag{3.4.5}$$

where η is defined to be

$$\frac{1}{\epsilon H}\frac{d\epsilon}{dt} = 4\epsilon - 2\widehat{V_1}\cdot\overleftrightarrow{V_2}\cdot\widehat{V_1} = 4\epsilon - 2\eta \ll 1 \ . \tag{3.4.6}$$

Therefore the slow gradient flow by the fields defined in (3.4.3) is not the only way to get a slowly-varying quasi-de Sitter expanding phase.

3.4.2 Numerical tests

In this section, we numerically determine whether a potential of the form (3.4.4) satisfies the slow gradient flow condition in (3.4.3). Because we now have the free parameters $\vec{a}$ and $\vec{b}$, we will adopt the Monte Carlo paradigm to characterize the shapes of potentials and quantify the rate of success.

3.4.2.1 Setup for numerics

The experiment is set up as follows.

1. The coefficients $\vec{a}$ and $\vec{b}$ in cubic and quartic terms in (3.4.2) are first sampled from a uniform distribution within range $[-3, 3]$ and $[0, 5]$ respectively. In addition, we also sampled the $\vec{a}$ coefficients from a Gaussian distribution with mean 0 and variance 1, and $\vec{b}$ coefficients from a exponential distribution with $\lambda = 1$.

   Let us briefly justify these choices of parameters. The experiments with the uniform distribution are performed in the spirit of Monte Carlo simulations, where parameters are chosen essentially at random. The choice of the uniform distribution is further justified by the fact that we do not know the region where slow-roll solutions reside in the seven dimensional parameter space of the potential coefficients. On the other hand, the choice of normal distribution with particular mean and variance will center our data around that mean and therefore may miss possible slow-roll regions. The choice of uniform distribution reflects the fact that we have no knowledge on the region of slow-roll samples within the parameter space *a priori*. In addition, the parameters are chosen to be of $O(1)$ with respect to GUT scale. This comes from the fact that the higher order terms of the potential do not get corrections from quantum gravity effects, thereby, the potential is written in this particular quartic form. Note that this polynomial potential allows vertices that mix the two inflatons. This rules out the models such as assisted inflation where potential takes steep exponential [150] due to the fact that our potentials are polynomials.

   In the second set of experiments, the Gaussian distribution for $\vec{a}$ is motivated by the Central Limit Theorem. If we suppose our coefficients can be observed, the averages of n measurements of each coefficient then approach Gaussian distribution when $n \to \infty$. Meanwhile, the mean and variance are chosen on the grounds of naturalness. *A priori*, the coefficients should be order one numbers at the scale determined by the masses of the inflatons, which we set to GUT scale. Therefore, our choice of Gaussian distribution for $\vec{a}$ can be seen from previous arguments. On the other hand, we have $\vec{b}$ follow a Gamma distribution. We demand each of the elements of $\vec{b}$ to be positive in order to ensure that the potential is bounded from below. Just as the Gaussian distribution is a maximum entropy probability distribution for positive and negative real numbers, the Gamma distribution is the maximum entropy probability distribution for positive real numbers. The Gamma distribution therefore becomes the

natural candidate for selecting coefficients. In particular, we use an exponential distribution with $\lambda = 1$, which is a Gamma distribution with shape parameter $k = 1$ and scale parameter $\theta = \lambda$. Again, the choice of 1 is motivated on the grounds of naturalness. The Central Limit Theorem requires large n. It is not clear that this applies when only a small number of scalar fields participate in inflation, so the comparison between the two possibilities is useful.

2. For each set of random coeffcients $\vec{a}$ and $\vec{b}$, we search for a point that satisfies conditions (3.4.3) within a particular range for fields ϕ_i by using the MATHEMATICAfunction[4]

$$\textbf{FindInstance}[<\textit{slow-roll conditions}>, \{\varphi, \chi\}]. \tag{3.4.7}$$

The search region within field space is rectangular with origin in the middle. The size of both sides of this region is twice the maximum of distances between origin and any stationary points of the potential. [5] This is justified because we want a slow-roll region that is near a stationary point and the potential becomes steep far out from the origin in our potentials that are bounded from below. We do not want to falsely classify solutions as slow-roll simply by virtue of the fact the denominator, which is determined by the value of the potential, is large near infinity in field space.

3. For particular conditions in (3.4.3), we have observational constraints of

$$\epsilon < 0.01 \quad \text{and} \quad \xi < 0.01 \tag{3.4.8}$$

from measurements of scalar spectral index n_s that directly restricts slow-roll parameters. We also note that since the ξ condition implies η, the results from imposing ξ should be smaller than those from η.

4. The inflaton mass parameters are defined as $\mu = m_\varphi/M_{\rm GUT}$ and $\rho = m_\psi/M_{\rm GUT}$, where m_φ and m_ψ are the inflaton masses. Here, we set them both to be of GUT scale, so μ and ρ are of order $O(1)$. With the mass parameters fixed, we take $N = 314000$ uniformly distributed random coefficient samples, $(\vec{a}_1, \vec{b}_1), \ldots, (\vec{a}_N, \vec{b}_N)$. To be precise, we first of all generate 157000 samples using the MATHEMATICA function **RandomReal[{-3, 3}, 4]** for $\vec{a}$ and **RandomReal[{0, 5}, 3]** for $\vec{b}$. Then we apply the slow-roll conditions in (3.4.3) to these coefficients using the approach and constraint described in (3.4.7) and (3.4.8) to obtain instances[6] of relative minima that satisfy the necessary conditions. By noticing that the potential (3.4.2) is symmetric under the following transformation for $\mu = \rho$,

$$\varphi \leftrightarrow \chi, \quad a_1 \leftrightarrow a_4, \quad a_2 \leftrightarrow a_3, \quad b_1 \leftrightarrow b_3, \tag{3.4.9}$$

we apply this symmetry to the slow-roll coefficients found previously in the 157000 samples. That is equivalently getting all slow-roll coefficients in 314000 random samples. In addition, this is also done

[4] Of course, we wrote more code than just this one line function.

[5] To be precise, we used `GroebnerBasis[]` to solve for zeros of the gradients of the potentials to find the extrema. However, this method actually turns the cubic polynomials into higher power polynomials (sometimes as high as 9-th order) thus making numerical solution highly sensitive to small change of gradient. For future work, we suggest to use `NSolve[]` directly instead and this might change the results slightly.

[6] The **FindInstance** function in MATHEMATICA is not capable of finding all desired slow-roll instances due to the mathematical complications of the slow-roll conditions and the internal algorithms designed for this task in MATHEMATICA. Our experimental comparison of **FindInstance** with the more comprehensive but slower **NSolve** function indicate that results from using the two options are similar.

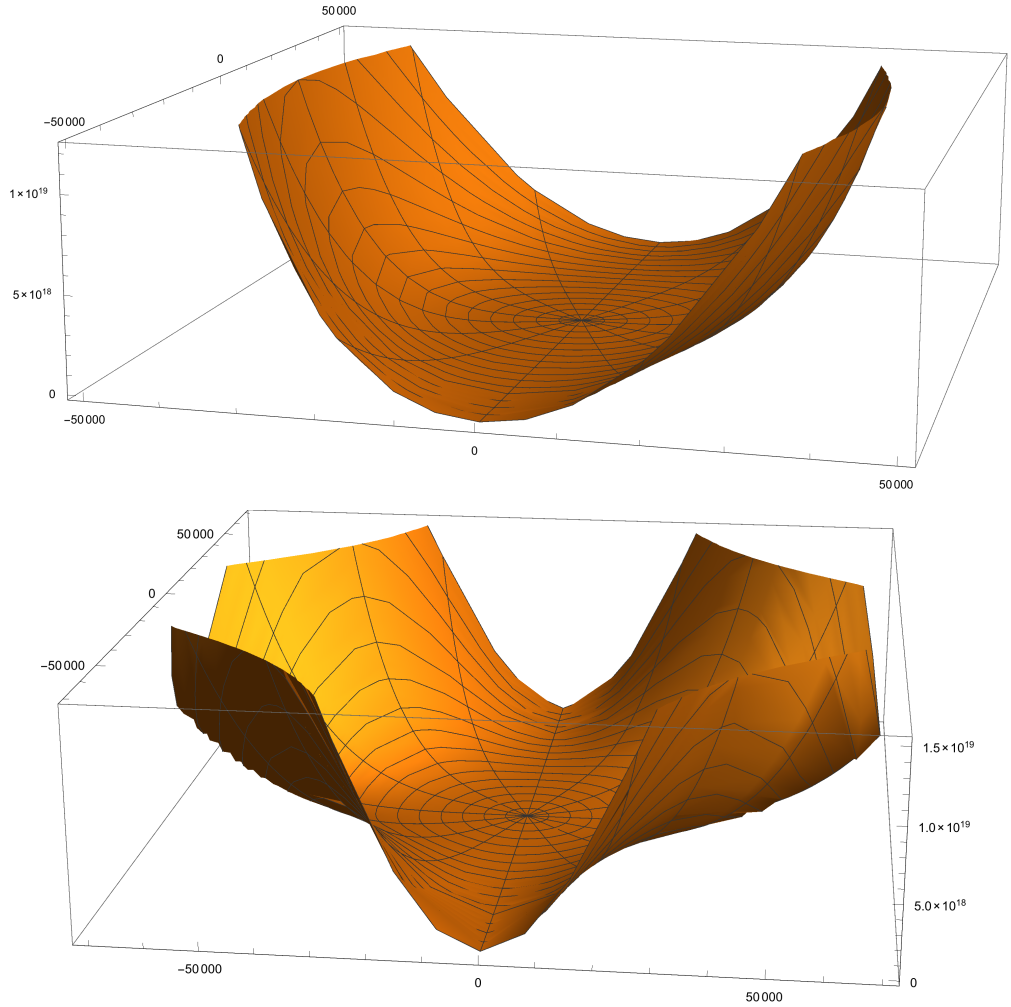


FIGURE 3.8: *Two of the 76 slow-roll potentials for the uniform distribution in Table 3.1. They have coefficients* $\boldsymbol{a} = (1.85634, -2.75233, 0.59967, 0.655031)$, $\boldsymbol{b} = (4.61147, 3.281, 0.00123865)$ *and* $\boldsymbol{a} = (0.675461, -0.286123, 2.6534, 1.6393)$, $\boldsymbol{b} = (0.294909, 4.25653, 0.00658533)$ *respectively. The point instances found in their slow-roll regions are at* $(-46745.5, -426)$ *and* $(-64074., -193.667)$*, and the potential values there are around* 2.2×10^{19} *and* 5×10^{18}*. However, the farthest stationary points are at* $(-0.091192, -396.138)$ *and* $(-0.311574, -186.663)$*.*

for 145000, or equivalently, 290000 samples drawn from Gaussian/Gamma distributions with means and shape parameters chosen as unity.

3.4.2.2 Numerical results

Of all the slow-roll potentials we obtained from choosing coefficients using both the uniform and Gaussian distributions, all of the slow-roll points found with function **FindInstance** have their distances from the origin greater than 30,000. The absolute values of potentials corresponding to these point instances have order of magnitude above $\mathcal{O}(10^{16})$. Figure 3.8 depicts two typical slow-roll potentials we have found for the uniform distribution.

$$\begin{aligned} v(\varphi,\chi) &= \frac{\varphi^2}{2} + \frac{\chi^2}{2} + 1.85634\varphi^3 - 2.75233\varphi^2\chi + 0.59967\varphi\chi^2 + 0.655031\chi^3 \\ &\quad +4.61147\varphi^4 + 3.281\varphi^2\chi^2 + 0.00123865\chi^4, \end{aligned} \tag{3.4.10}$$

Distribution	Range of $\boldsymbol{a}$	Range of $\boldsymbol{b}$	Samples	Slow-Roll	Percentage
Uniform	$[-3, 3]$	$[0, 5]$	157,000	76	0.05%
Gaussian Gamma	$[-\infty, \infty]$	$[0, \infty]$	145,000	131	0.1%

TABLE 3.1: *Slow-roll potentials found in random sample potentials of chosen distributions*

has three real stationary points,

$$(-0.091192, -396.138), \quad (-0.028419, -0.497133) \quad \text{and} \quad (0, 0), \tag{3.4.11}$$

the furthest of which is around 400 units of distance away from the origin. However, the slow-roll point we found is at $(-46745.5, -426)$, which is far beyond the region we expected. The potential at the slow-roll point is 2.2×10^{19}, and the gradient is -1.9×10^{15} and -6.1×10^{12} in φ and χ directions respectively. One can check that, the two slow-roll parameters,

$$\epsilon = 0.0037 \quad \text{and} \quad \xi = 0.0055, \tag{3.4.12}$$

satisfy the constraints in (3.4.8). However, from the careful inspection of this specific example, we can see that the slow-roll (and its adjacent region) satisfy the $\epsilon \ll 1$ and $\eta \ll 1$ conditions because the potential at this distance from the origin is large and the two slow-roll parameters are both roughly inversely proportional to some power of the potential. All the other slow-roll instances we found in our random samples are similar to this specific example. We stated in Section 3.3 that we wanted to exclude those regions where (3.3.6) was satisfied simply due to the largeness of the potential. However, now that these are the only slow-roll regions we have found for the two-field case, the best statistics we can get is from this kind of slow-roll potential.

To get a better idea about the slow-roll potential, we stack all the successful potentials in a single plot in Figure 3.9. As the figure shows, all the slow-roll potentials have a steep and a flat direction. This qualitative shape of the potentials recalls those found in models of hybrid inflation type [**hi**]. Generic initial conditions in the neighborhood of a minimum would first fix the field in the direction perpendicular to the valley (the steep direction), and then the field would roll along the valley to the minimum at the bottom. Unlike the potential for hybrid inflation discussed in the introduction, informed by our choices of random coefficients, the parameters that appear in the potentials here are all typically of order one with respect to the GUT scale.

The statistics of slow-roll potentials we found in potentials from the uniform and Gaussian/Gamma distribution are listed in Table 3.1. From Table 3.1, we can see that in all randomly generated coefficients, around 0.05% of them correspond to slow-roll potentials and 0.1% for Gaussian/Gamma distribution. This supplies a *lower bound* for the percentage of relative minima that accommodate the slow-roll conditions for inflation with two scalar fields.

We also draw distributions of values of coefficients $(\vec{a}, \vec{b})$ that correspond to slow-roll potentials in Figure 3.10. These figures show that in spite of the uniform distribution that we presume as priors for a_i and b_i, the slow-roll conditions pick the coefficients according to the mass distributions in these histograms. The distributions of all components of $\vec{a}$ and $\vec{b}$ deviate noticeably from the uniform distribution. This indicates that the slow-roll conditions set some constraints on the values of coefficients in a probabilistic sense. Deviations may also be a product of having a low number of slow-roll regions, only around 70, despite starting with a minimum of 150000 samples. A greater computational analysis would be required to obtain more concrete statistics for the distribution of slow-roll regions.

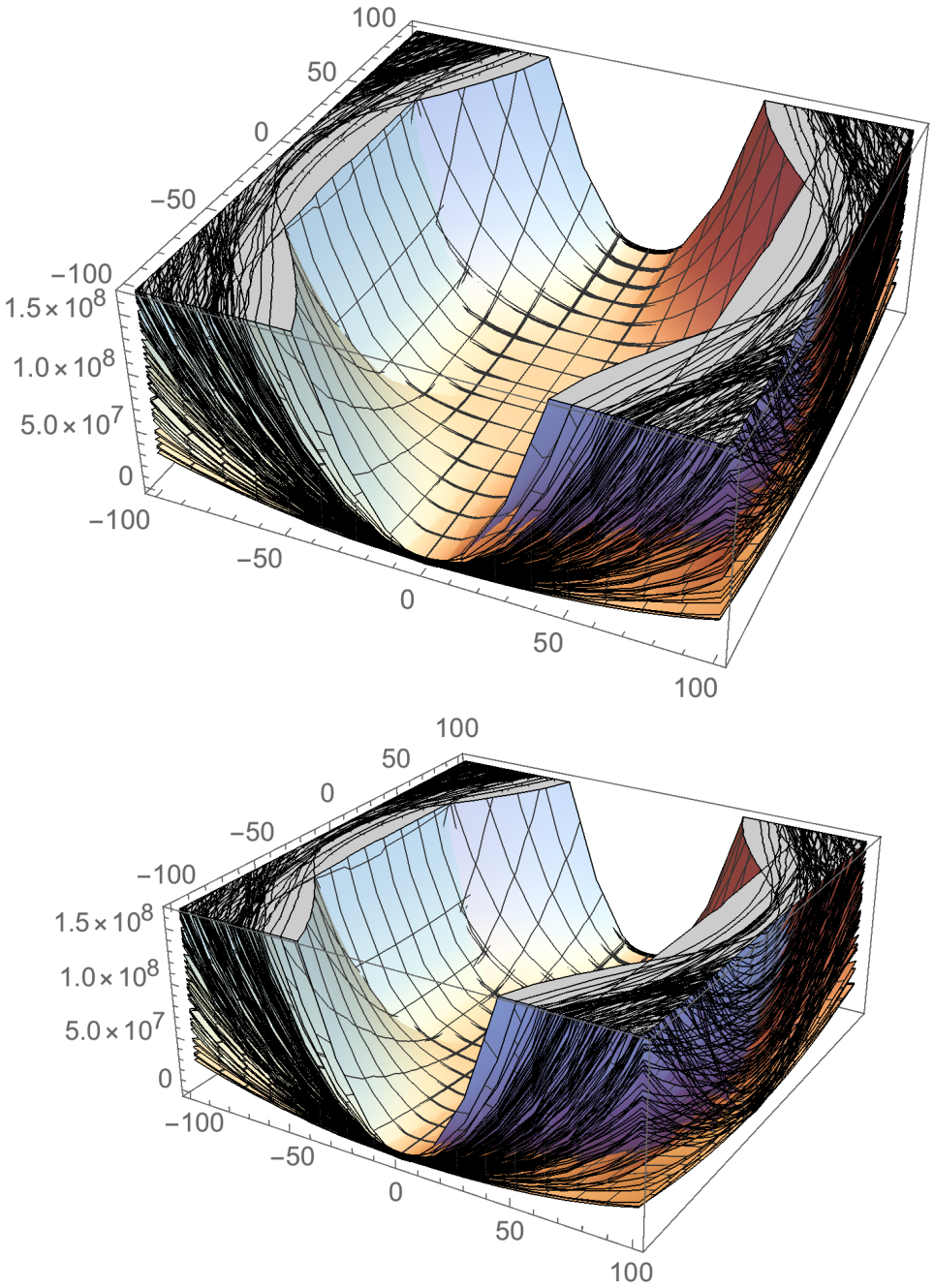
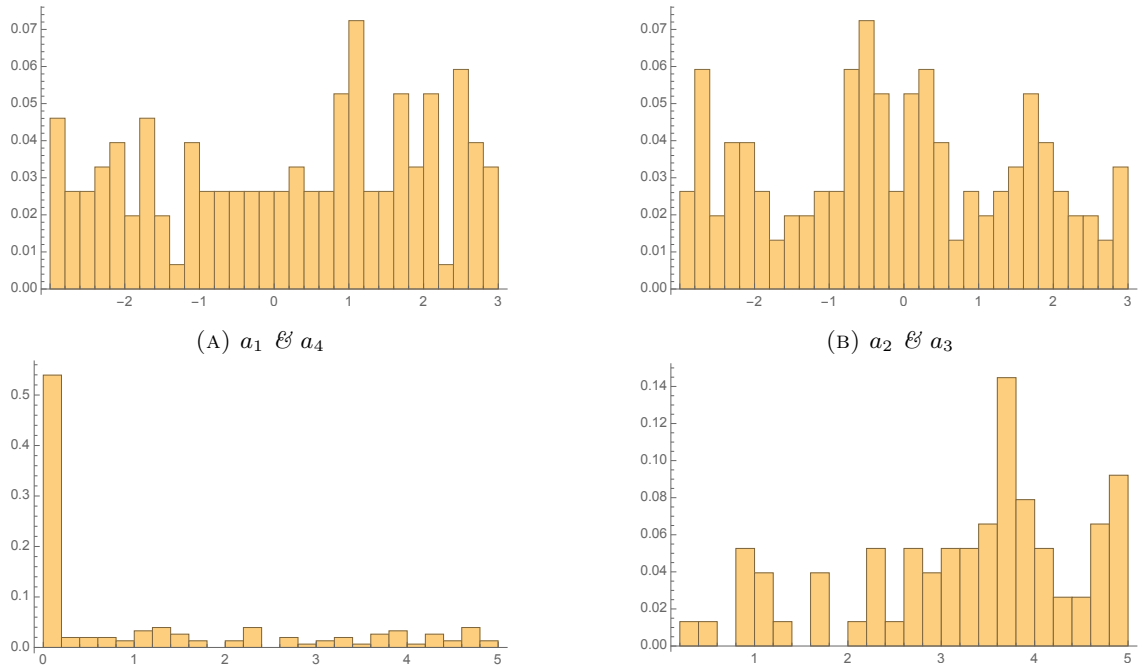


FIGURE 3.9: *The top figure gives the stack of all found potentials for uniform distribution and the bottom one gives that for Gaussian distribution.*



(A) a_1 & a_4 (B) a_2 & a_3

(C) b_1 & b_3 (D) b_2

FIGURE 3.10: *Distribution histogram for $\vec{a}$ and $\vec{b}$ coefficients drawn from uniform distribution. The x-axes are values for $\vec{a}$ and $\vec{b}$ and the y-axes are for probabilities for those values to occur.*

In addition to the results from uniform distribution, we also present the histogram plots for coefficients of slow-roll potentials for Gaussian/Gamma distribution in Figure 3.11. We can see from the plot that the Gaussian nature of the plot still is still present. This shows that the slow-roll conditions we choose respects the Gaussianity of initial samples.

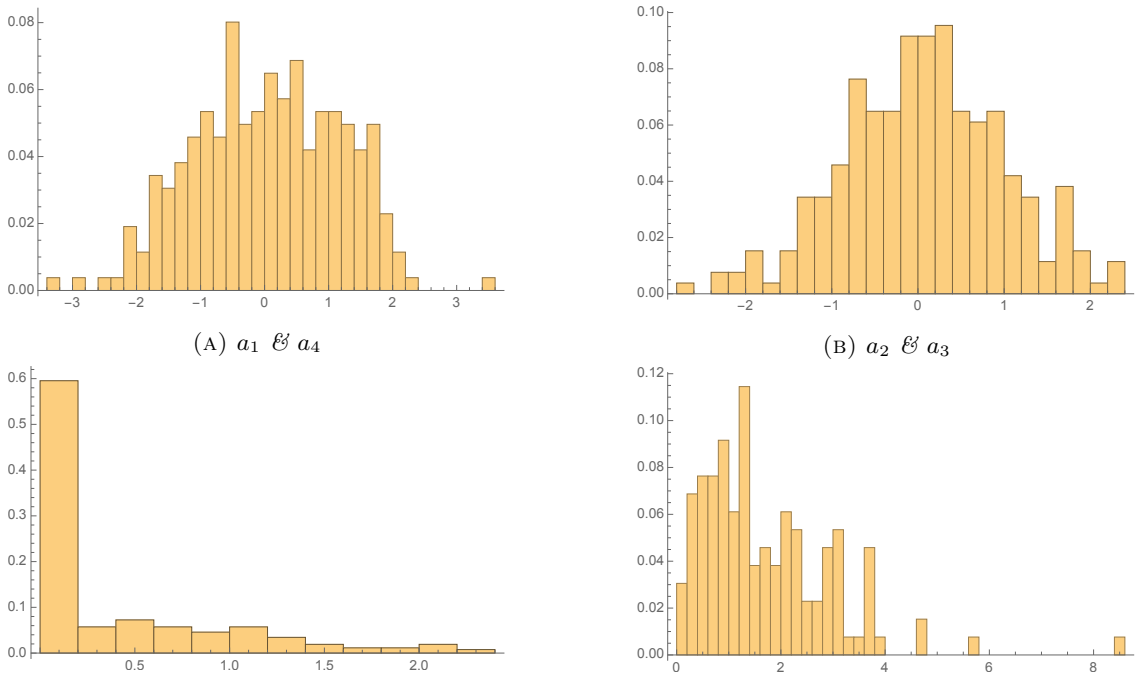
Preliminary experiments with varying the mass parameters for the scalar fields over several orders of magnitude do not significantly change the percentages of slow-roll solutions.

3.5 Discussion and outlook

With the advent of Big Data in theoretical physics and ever-increasing computational power, we are gaining further glimpses into the various landscapes of theories ranging from string vacua to cosmological scenarios. In this paper, we have been motivated by the question of the probability of having slow-roll inflation within the landscape of effective potentials for inflatons.

We started with the case of a single field with the most generic form of the potential up to degree four, subject to the constraints of slow-roll. Here, there are only two parameters, which we have dubbed β and ν, and which can be expressed in terms of the couplings. We can solve the problem numerically to arrive at Figure 3.7. The figure depicts a non-trivial region of parameter values which satisfy the slow-roll conditions.

With two inflatons, the situation is understandably more intricate. Here, up to degree four, there are seven parameters. The slow-roll conditions then translate to a polynomial system in the fields and in the parameters. This is then a problem in a potential landscape sculpted by these parameters. We find that the slow-roll conditions for multi-field are insensitive to the distribution we used, *i.e.*, we find that they



(A) a_1 & a_4 (B) a_2 & a_3

(C) b_1 & b_3 (D) b_2

FIGURE 3.11: *Distribution histogram for $\vec{a}$ and $\vec{b}$ coefficients drawn from Gaussian/Gamma distribution. The x-axes are values for $\vec{a}$ and $\vec{b}$ and the y-axes are for probabilities for those values to occur.*

give the same percentage of slow-roll instances. Moreover, initial experiments that change the mass scale yield similar results. The inflatons for slow-roll inflation traverse far into field space so that the slow-roll conditions are satisfied in part due to the largeness of V. The potential has a characteristic shape in which the fields would roll first down a steep direction and then follow a valley to the minimum.

In the single field case, the condition $V'\,V''' \ll V^2\,M_{\rm P}^{-4}$ accounts for constraints on the running of the spectral index. It would be reasonable to develop the equivalent third derivative condition for multi-field case and include this within the framework of random potentials. In addition, in this work we do not explicitly compute the number of e-foldings for each of the potentials that support slow-roll inflation. While we can exclude certain minima as being unable to support the necessary number of e-foldings, the suitability of other minima for this purpose depends critically on the choice of initial conditions for the inflaton fields. There is no obvious *a priori* selection criteria for this informed by realistic string constructions of the Standard Model. We defer a systematic analysis on this point for future work.

In general, with an arbitrary number of inflatons and a potential up to a specified degree, the slow-roll constraints will produce a large polynomial system with still larger number of parameters. For example, in the heterotic string Standard Models to which we alluded in the introduction, the contribution to the number of moduli fields come from the geometry — roughly the sum of the Hodge numbers — and from the bundle — roughly the number of endomorphisms [151]. For the $(3,3)$ Calabi–Yau threefold studied in [104, 105] the total number of moduli is $6+19=25$.

The usual Groebner basis [152] approach to analyzing such systems will soon become rather prohibitive and even numerical algebraic geometry [147] will find this challenge daunting. Our approach of randomization over parameters is thus the standard technique, and the statistics over the landscape is an enlightening overview of how special or generic our universe is. Aided by work done in [153, 154], one could find a relationship between the general statistics of successful inflation in random polynomial potentials with the

general statistics of stationary points in the same potentials. They note that the variance of positive real roots both increases with the degree of the polynomial and converges with sample size. Knowing this may give, for example, a convenient saturation limit of test samples, shifting a greater proportion of computational resource to just the search for relationships between minima and slow roll regions. Finding this would allow us to derive properties of the inflationary landscape from the statistics of the minima themselves. More work is needed hover in developing actual “search and test" techniques for inflation within these minima.

One should mention also that there is a branch of mathematics known as random algebraic geometry where the usual quantities such topological invariants and cohomology, which govern the physics, have their analogues in the stochastic sense. It will certainly be interesting to study polynomial systems arising from the potential landscape under this light.

Chapter 4

New Tools in the Analysis of Large Scale Wildfires

This chapter is work done in collaboration with Sally Archibald, Kevin Goldstein and Vishnu Jejjala. It is written with the intention to publish after the submission of this Ph.D.

4.1 Introduction

Global fire occurrences are of interest to scientists who study earth system modeling. Fires have crucial impact on vegetation and animal habitat. They burn down forests, but also enrich the soil with nutrients allowing for regrowth of plants and grass. Furthermore, as climates change, so do probabilities of fires increase or decrease - hot arid weather generates more bio fuel. Under specific conditions fires can grow incredibly big posing safety hazards to human, plant and animal populations. With the interplay between climate, fire and vegetation, the problem of distinguishing clear cause and effect relationships between these factors can be difficult. System modeling enables scientists to deal with the large space of self interacting variables, however, they suffer from generality or too high a specificity. The former doesn't possess any real world predictive power, and the latter becomes computationally unfeasible due to the number of required parameters.

The evolution of fire can be separated into three stages: the ignition occurrence of a fire, the spread dynamics and the stopping conditions. An important aspect in modeling these stages involves understanding the spatial distribution of vegetation in a particular landscape. Of course, knowing the population spread is also important as humans have direct impact on how and where vegetation grows. This however, only sets some initial conditions on the landscape, dictating how the fire will then evolve. Spatially representing the vegetation in computer models can be a tricky task as knowing the percentage distribution of certain fuel is not a representation of the complex landscapes that actually exist. Complex process simulations of how fire works do exist, such as the model from Rothermal[14] which take into consideration variables such

as fire height, convection currents and heat radiation effects. Although a very useful model to people like firefighters, on top of the extreme computational complexity it introduces when applying it at a global level, it fails to explain the last stage in the evolution of fires - their natural end. In most simulations the wildfires are put out artificially, they are not allowed to continue endlessly as they have no indication of when the fire will stop. This then limits the accurate simulation of fire spread over large distances, whereby in real life global fire spreads can span several thousand kilometers, simulations only show around tens of kilometers.

Percolation models offer a new angle to explain how fires can come to an end [155, 156]. This is because these models focus on threshold behaviour. Such behaviour exists in various fields such as infection theory - how infectious must a disease be before the entire population contracts it, or things like viralness of videos or posts in social media. They introduce a criticality condition; stating when a particular process will affect an entire population, or vice versa, at what point will a certain process cease to spread. Such epidemiological models have use in understanding the last stage in fires. In particular, they give a critical value for the percentage of flammable landscape [157, 158]. In other words, if a landscape contains more than 59.28% vegetation which is flammable, the fire will spread, if it is lower, the fire will self extinguish. In addition to this threshold value is also the probability of spread - for a fire in a given cell, what is the likelihood of it spreading to a neighboring cell. The question of thresholds can also be asking in the context of fire spread; is there a threshold of how far a fire will spread? Take for example a situation where there is a fire in a landscape that has a fuel above the percolation threshold, but now weather conditions change, such that temperatures decreases, dew on vegetation thus increases. What happens is that the spread probability of the fire dramatically decreases and this then also causes self extinguishing conditions for the fire.

What results from the models based on percolation threshold behaviour is an emergent property in fire simulations called scale invariance. Interstingly, the fractal pattern which is formed can be seen in both real world examples of fires which self extinguish and simulations. Scale invariance refers to a sense of self-similarity - structural patterns on large scales look the same as structural patterns when zoomed in. Scale invariance is studied further when looking at self-organized critical behaviour(SOC) [15, 159, 160], where it is suggested that fire size distributions follow power-laws (i.e. show scale invariance) but our ability to accurately quantify this, as well as what this means mechanistically for fire propagation in different ecosystems have not yet satisfactorily been resolved. There are at least three mechanisms by which power-law behavior might emerge in fire size distribution: a) self-organized criticality (intrinsic drivers), b) power-law behavior in the weather drivers of fire (extrinsic drivers), and c) scale invariance in the landscapes in which fires are spreading.

In physics, scale invariance is a property which is very well studied. Systems which exhibit scale invariance possess a particular type of symmetry which aids in solving equations or making assumptions about that system. Thus, the interpretation of scale invariance changes depending on the theory. For example, in classical field theory, scale invariance means the theory does not depend on the length scale, whereas in quantum field theory, it implies particle strength interaction is not dependent on the energy of the particles. There is a theorem, called Polchinski's theorem [161, 162], stating that a Lorentz invariant theory in two dimensions is also conformal invariant. Theories which have conformal invariance are very interesting as they fix what are called correlation functions. By fixing, we mean that we know what the function describing the correlations look like. The fixing of these correlations, allows a more rigorous way of quantifying to what

degree a system is scale invariant. Furthermore, they can provide tools of directional analysis, meaning one can, in the context of fires, quantifiably differentiate fire distribution in particular directions. This opens up the potential of investigating the affect of wind vs fuel in creating fire patches.

For our analysis, we use MODIS burned area data from two different regions globally which we expect to show variation in fire size distribution due to differences in their fire ecology. We chose homogeneous areas where the influence of landscape-features should be minimized so as to assess the role of weather and internal dynamics in driving the behaviour of the system. Over a 12 year period from 2002 to 2014, we investigated the variability between years and looked to relate this to changes in the drivers of large fires in these ecosystems, as well as quantify the transnational invariance and compare this to information on wind fields for the areas studied. Section 4.2 is used to introduce relevant concepts in conformal field theory, as well as expand on the tools we used for the analysis and how they work. In Section 4.3 we present a sample of a few plots highlighting the fitting procedure as well as a few tables showing all fitted variables. In addition we show possible relations of our modeled variables to variables like average temperature, rainfall and average wind speed. In Section 4.3.4 we discuss potential issues with regards to both the model as well as the data used in the model, which itself is often a limiting factor in the viability of a given model. Finally we summarize the efficacy in our proposed tools and discuss future work.

4.2 Conformal field theory basics

4.2.1 Two dimensional CFTs

Quantum field theories that are invariant under angle preserving transformations enjoy *conformal invariance*. Statistical systems acquire this symmetry near quantum critical points. In particular, at a conformal fixed point, the beta functions vanish and correlations extend to all scales. In two dimensions, conformal symmetry yields an infinite dimensional algebra of local conformal transformations. Under a conformal transformation, a quasi-primary field transforms as follows:

$$\begin{aligned} \mathbf{x} &\to \mathbf{x}' \\ \Phi(\mathbf{x}) &\mapsto \Phi'(\mathbf{x}') = \left|\frac{\partial \mathbf{x}'}{\partial \mathbf{x}}\right|^{-\Delta/2} \Phi(\mathbf{x}) \ , \end{aligned} \tag{4.2.1}$$

where Δ is the conformal dimension of the field $\phi(\mathbf{x})$. The two point and three point correlation functions of quasi-primary fields are as follows:

$$\langle \Phi_1(\mathbf{x}_1)\Phi_2(\mathbf{x}_2)\rangle = \begin{cases} \frac{C_{12}}{x_{12}^{2\Delta_1}} & \text{if} \quad \Delta_1 = \Delta_2 \\ 0 & \text{if} \quad \Delta_1 \neq \Delta_2 \end{cases} \ , \tag{4.2.2}$$

$$\langle \Phi_1(\mathbf{x}_1)\Phi_2(\mathbf{x}_2)\Phi_3(\mathbf{x}_3)\rangle = \frac{C_{123}}{x_{12}^{\Delta_1+\Delta_2-\Delta_3} x_{23}^{\Delta_2+\Delta_3-\Delta_1} x_{13}^{\Delta_3+\Delta_1-\Delta_2}} \ , \tag{4.2.3}$$

where $x_{ij} = |\mathbf{x}_i - \mathbf{x}_j|$ and Δ_i is the conformal dimension of $\Phi_i(\mathbf{x})$. In particular, when $\Phi_i(\mathbf{x}) = \Phi(\mathbf{x})$, we have

$$\langle \Phi(\mathbf{x}_1)\Phi(\mathbf{x}_2)\rangle = \frac{A}{x_{12}^{2\Delta}} , \qquad \langle \Phi(\mathbf{x}_1)\Phi(\mathbf{x}_2)\Phi(\mathbf{x}_3)\rangle = \frac{B}{(x_{12}x_{23}x_{13})^{\Delta}} . \tag{4.2.4}$$

See [163] for a review.

For unitary local quantum field theories, scale invariance in combination with Lorentz invariance implies conformal invariance [164]. In essence, this conclusion arises from showing that the trace of the stress tensor may be written as

$$T_{\mu}{}^{\mu} = \partial_\mu \partial^\mu L(x) , \tag{4.2.5}$$

where $L(x)$ is a local operator. The argument is extremely general and counterexamples such as elasticity involve circumventing axioms like reflection positivity [165]. In our current setting, we do not have *a priori* knowledge of the Lagrangian and therefore cannot define the stress tensor from variation of the action with respect to the metric:

$$\delta S = -\frac{1}{2}\int d^2x \; T^{\mu\nu}\delta g_{\mu\nu} . \tag{4.2.6}$$

Moreover, the systems we examine are classical. Because the relationship between the log of the number of fires of a given size versus the log of the size of the fire is linear, the systems exhibit approximate scale invariance. We adopt the techniques of conformal field theory to interrogate this behavior.

4.2.1.0.1 Fire propagation: To study fire propagation, we define a field

$$\psi(\mathbf{x},t) = \begin{cases} 1 & \text{if } \mathbf{x} \text{ on fire in year } t \\ 0 & \text{if } \mathbf{x} \text{ not on fire in year } t \end{cases} . \tag{4.2.7}$$

The one point function $\mathrm{E}[\psi(\mathbf{x},t)]$ tells us the density of fire in a year t. The expectation value denotes an average over the grid. We then compute two point functions and three point functions. Fixing t, these are, respectively,

$$f(x_{12},t) := \langle \psi(\mathbf{x}_1,t)\psi(\mathbf{x}_2,t)\rangle = \mathrm{E}[\psi(\mathbf{x}_1,t)\psi(\mathbf{x}_2,t)] - \mathrm{E}[\psi(\mathbf{x},t)]^2 , \tag{4.2.8}$$

$$g(x_{123},t) := \langle \psi(\mathbf{x}_1,t)\psi(\mathbf{x}_2,t)\phi(\mathbf{x}_3,t)\rangle = \mathrm{E}[\psi(\mathbf{x}_1,t)\psi(\mathbf{x}_2,t)\psi(\mathbf{x}_3,t)] - \mathrm{E}[\psi(\mathbf{x},t)]^3 , \tag{4.2.9}$$

where $x_{123} = (x_{12}x_{23}x_{13})^{\frac{1}{3}}$.

4.2.1.0.2 Fire geography: To study the geography of fire propagation, let us also define

$$\varphi(\mathbf{x},t) = 2\big(\psi(\mathbf{x},t) - \frac{1}{2}\big) \qquad \Longrightarrow \qquad \varphi(\mathbf{x},t) = \begin{cases} +1 & \text{if } \mathbf{x} \text{ on fire in year } t \\ -1 & \text{if } \mathbf{x} \text{ not on fire in year } t \end{cases} . \tag{4.2.10}$$

It is convenient to introduce an additional shift

$$\phi(\mathbf{x},t) = \varphi(\mathbf{x},t) - \overline{\varphi}(t) , \qquad \overline{\varphi}(t) := \mathrm{E}[\varphi(\mathbf{x},t)] , \tag{4.2.11}$$

so that, by construction, $\mathrm{E}[\phi(\mathbf{x},t)]=0$. The two point function and three point function are, respectively,

$$f(x_{12},t) := \langle \phi(\mathbf{x}_1,t)\phi(\mathbf{x}_2,t)\rangle = \mathrm{E}[\phi(\mathbf{x}_1,t)\phi(\mathbf{x}_2,t)] \ , \tag{4.2.12}$$

$$g(x_{123},t) := \langle \phi(\mathbf{x}_1,t)\phi(\mathbf{x}_2,t)\phi(\mathbf{x}_3,t)\rangle = \mathrm{E}[\phi(\mathbf{x}_1,t)\phi(\mathbf{x}_2,t)\phi(\mathbf{x}_3,t)] \ . \tag{4.2.13}$$

4.2.1.0.3 Fits: The two point function and three point function are fitted as follows:

$$f(x_{12},t) = \frac{Ae^{-x_{12}/\xi}}{x_{12}^{\alpha}} \ , \tag{4.2.14}$$

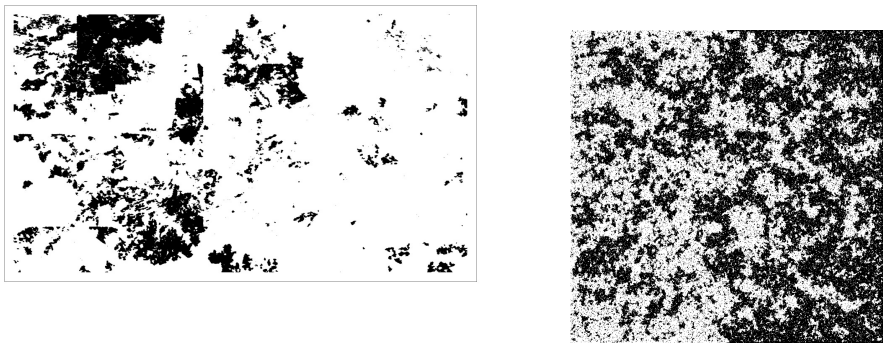
$$g(x_{123},t) = \frac{Be^{-x_{123}/\zeta}}{x_{123}^{\eta}} \ . \tag{4.2.15}$$

In (4.2.14) and (4.2.15), the parameters ξ and ζ are correlation lengths. In a conformal field theory, due to scale invariance, the correlation lengths go to infinity and, from comparison to (4.2.4),

$$\Delta = \frac{1}{2}\alpha = \frac{1}{3}\eta \ , \tag{4.2.16}$$

so the exponents in the denominators of the two and three point functions are not independent. The code for the analysis is checked against the Ising model, a well known two dimensional CFT. The failure of conformal invariance in fire arises as a consequence of the violation of transnational and rotational symmetry due to features such as wind and weather and the lack of unitarity as this is not an isolated quantum system and one cannot "unburn" a patch of land.

4.2.2 Correlation of Fire Occurrences



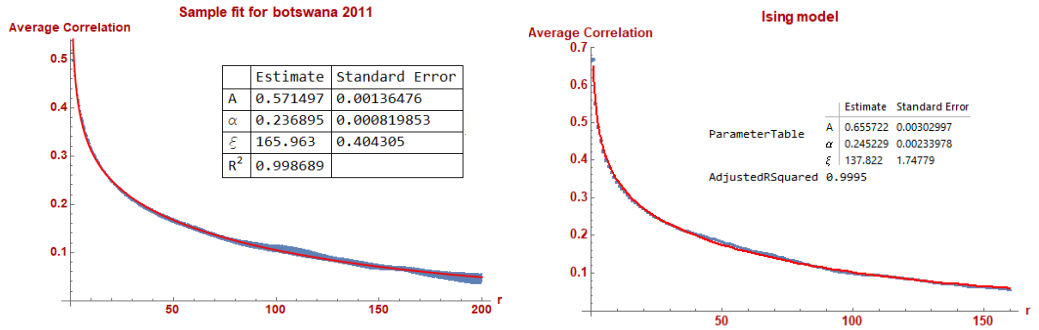
(A) *Fire occurrences in Botswana in the year 2011.*

(B) *Ising model near critical temperature.*

FIGURE 4.1: *Grid (A) is a representation of fire occurrences (black points) in a particular region near the river Delta in Botswana. Grid (B) represents the spins of an Ising model near the critical temperature. Black points indicate arrow/spin down and white points indicate arrow/spin up.*

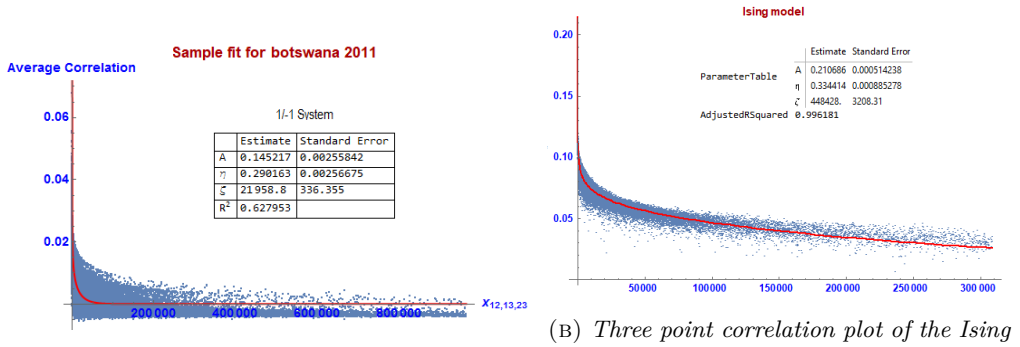
Satellites allow the monitoring of regions by spatially mapping out fire occurrences. If, in a given year, a certain patch within the region catches fire, a data point is captured by assigning the value of 1 to that patch of land. By gridding the region, one obtains a map of data points - each signaling whether or not a

fire has occurred in that year. A data point of 1, as mentioned, indicates fire, and 0 indicated no fire. Since fire spreads, due to various factors such as weather, fuel and geography, neighbouring patches of land are inevitably affected. At the end of each year, one then has a 2D grid of data, structured in such a way that it lends itself to a correlation analysis as outlined above. Merging the language of correlation function analysis and fire propagation, given a fire in one patch, what is the likelihood of that particular patch of fire having a causal influence to a different patch separated some distance away? There is a caveat here, and that is that all the gathered data of fire occurrences is averaged over a particular year. So our analysis would be insensitive to direct causal relations of a single fire event. It is difficult thus to say exactly over what time scale communication between fire patches occur, but by doing the correlation analysis, one can definitely say that there is some property within the overall mechanism of fire propagation which gives rise to a particular kind of "burning pattern" within these regions. Consider figure 4.1; the Ising model *(B)*, a 2 dimensional toy model in conformal field theory, is used to describe the critical point behaviour of spin lattice sites in a background magnetic field. Whereas *(A)* is a map of Botswana indicating all fire occurrences in 2011. The two point and three point function comparisons strongly suggest the same model using in the Ising model is suitable for wild fire occurrences



(A) *Two point correlation plot of fire occurrences.* (B) *Two point correlation plot of the Ising model.*

FIGURE 4.2: *The major difference between these two is that the Ising model is modeled over a torus, and thus requires periodic boundary conditions, whereas the analysis of the Botswana data was done on a flat grid. The presence of a correlation length for the Ising model is due to the fact that it is very difficult to generate an Ising model map at the critical temperature. Thus, we say "close to the critical temperature"*



(A) *Three point correlation plot of fire occurrences.* (B) *Three point correlation plot of the Ising model.*

FIGURE 4.3: *The three point correlations for the Ising model obey the expected relationship between* $\eta = 0.3314$ *and* $\alpha = 0.2452$ *given in eqn* (4.2.16)*, that is* $0.3314/3 \simeq 0.2452/2$*. For the fire in Botswana, there is no relationship between exponents, which is not too surprising since, as mentioned, we do not have a unitary system.*

The shape and parameters are remarkably similar - this gives weight to the motivation for performing a correlation analysis. The three point functions are not as clean as the two point functions, this is due to the random sampling approach used. Year by year, the parameters change, however they all fit very well every year as will be seen in the next section.

4.2.3 Directional Correlations

In addition to the standard average correlation analysis, for the two point functions, one can become more specific in the analysis and focus on correlations in particular directions. Consider the example grid below:

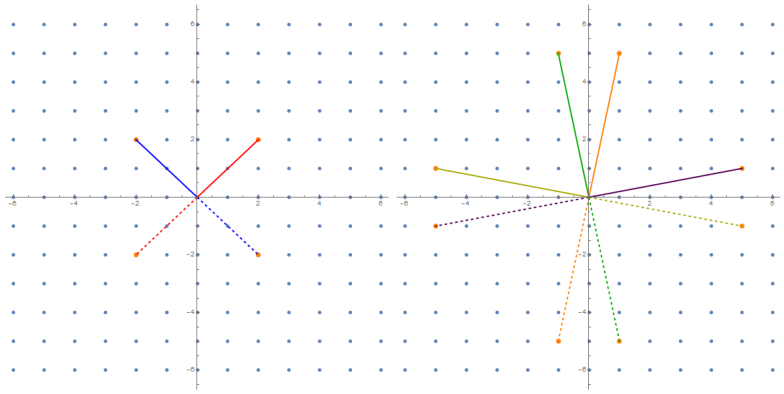


FIGURE 4.4: *Left: All possible lines joining two points separated by* $r^2 = 8$. *Right: All possible lines joining two points separated by* $r^2 = 26$.

Associated with all the lines are their respective angles. In reality, we only need to consider the thick lines, as the dashed lines are just translations of the solid lines. If we calculate the average correlation - distinct to points joined by a line of length r and a given angle, then we can calculate a directional correlation. If one direction has a stronger correlation than another, or there is a different type of correlation, the directional correlations will pick this up. Consider the same inverse random distribution from Figure 1.11c from Section 1.3, below is the result of doing a directional correlation analysis of two particular directions

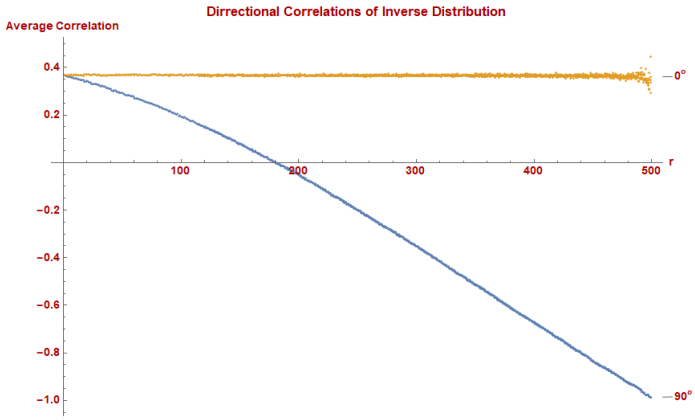
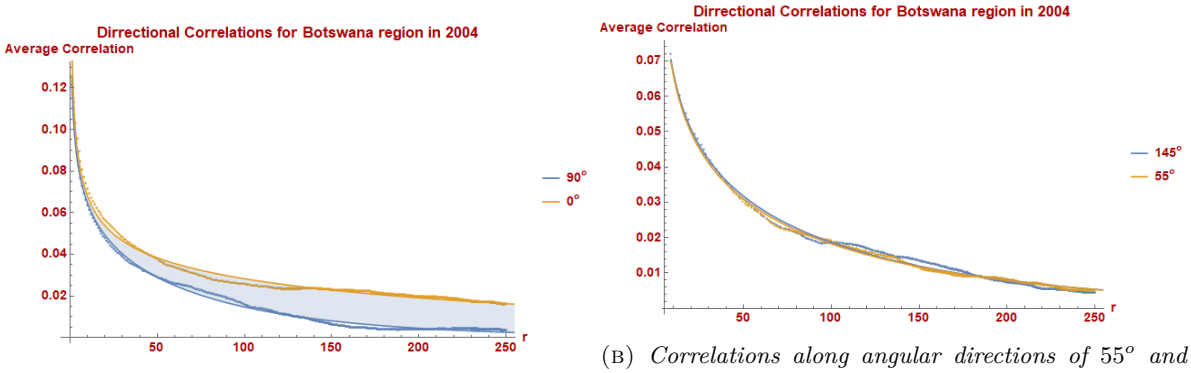


FIGURE 4.5: *Directional correlations highlight the different behaviours of the data at different angles.*

From this, we see that it is indeed the correlations along the vertical directions (90^o) which reflect the underlying distribution of the data - points become more and more anti-correlated as distances increase. However, along directions parallel to the horizontal we see a constant correlation of just below 0.4, Since the "spreading" of the data does not exist in this direction, the correlations of points that lie along lines at 0^o remain constant.

This is a very useful tool, as it allows a finer analysis in correlations of fire occurrences. Say for example there is a particular direction for which the wind over a certain region blows over a year. If this wind causes fires to spread in the same wind direction, then points along those directions should have a correlation which is different to directions perpendicular. By scanning every angle as well as its complement from 0^o to 89^o, one can identify which correlations differ the most. There are several ways one can use as the "identifier" which quantitatively says one correlation is different to the other. For our analysis, we opt to look at the area between the best-fit curves. The angle which has the largest area between two angles will be deemed the angles with the largest difference in correlation. For illustration, consider the Botswana data over the year 2004:



(A) *Correlations along angular directions of* 0^o *and* 90^o.

(B) *Correlations along angular directions of* 55^o *and* 145^o.

FIGURE 4.6: *There is a larger difference in correlations along directions parallel and perpendicular to* 0^o *than there is along directions parallel and perpendicular to* 55^o.

This method of using the area subtended between two best fit curves gives a quantitative description for the difference between correlations at various angles. By then plotting the area difference across all angles, one can see the variation in correlations with direction. If there is indeed directional preference in the occurrences of fire, this analysis will pick it up. Before this, it is also helpful to gain an understanding on how the function describing the model actually works, in terms of how each parameter affects the shape of the graph.

In the correlation function

$$f(r) = \frac{A}{r^{\alpha}} e^{-\frac{-r}{\xi}} \tag{4.2.17}$$

the three parameters affect the shape of the graph in the following ways:

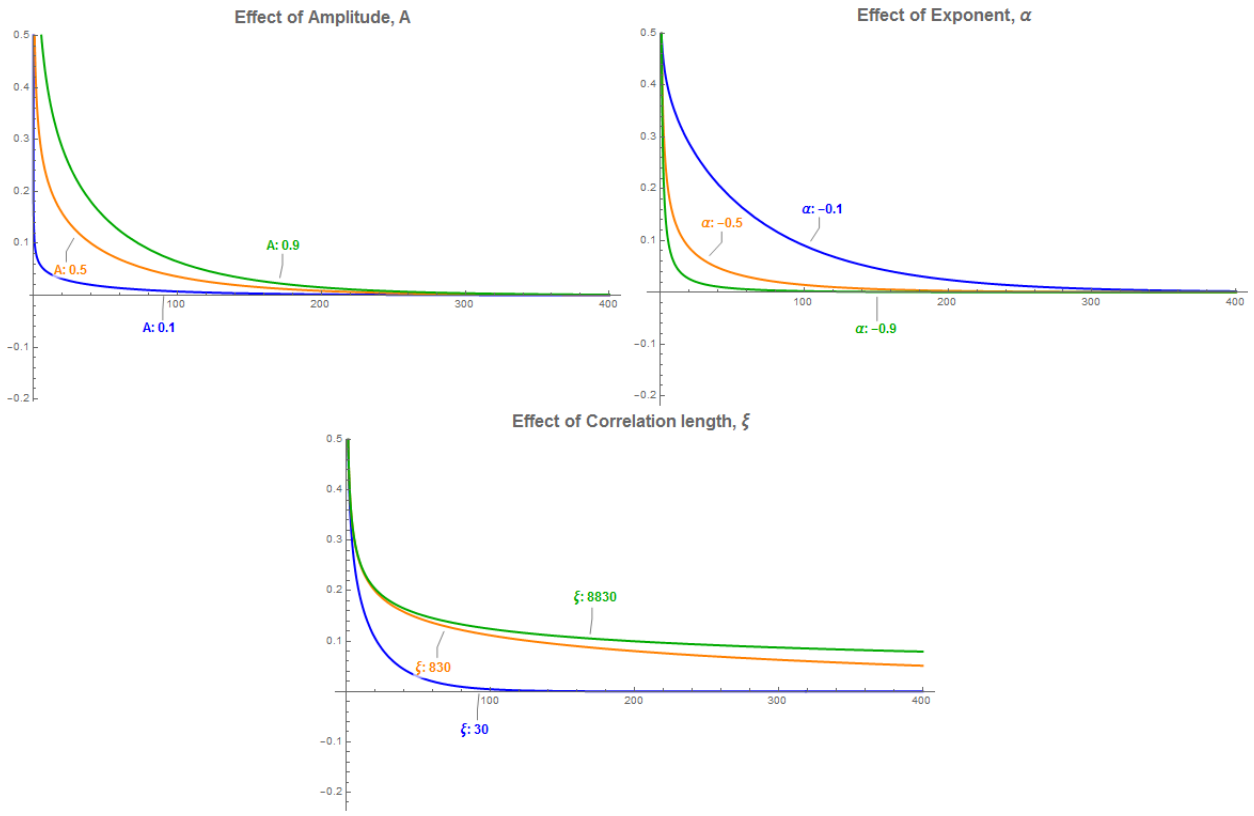


FIGURE 4.7: *Shape dependence on correlation function variables. In each different scenario, the other variables are kept constant.*

1. **Amplitude,** A : The amplitude affects the scaling. Although in the plots above, it appears that a lower amplitude pulls the curve towards the center, this is just an illusion given by the fact that the scale on the axis remains unchanged. Were we to zoom in say for the blue graph to a scale which goes from 0 - 0.1 instead of 0 - 0.5 on the y axis, the shape would look exactly the same.

2. **Exponent,** α: The exponent has the effect of making the curve steeper by symmetrically pulling in the inflection point towards the center (larger values of α) or further away (smaller values of α). Of course making α smaller means that the correlation falls off to zero slower and slower, implying the "correlation mechanism" of the system is stronger. In the case of fire, a lower α implies greater correlation from one point to another; in other words, if we have a fire at A, then there is a higher probability that it will have caused the fire at B (assuming the distance between A and B is within the correlation length). If the exponent was larger, than even if A and B are still separated by a distance within the correlation length, a fire at A will have had a much smaller role in causing a fire at B.

3. **Correlation Length,** ξ: The correlation length tells us what the maximum distance is that we can relate the cause of a fire at location B to a fire at location A. A larger correlation has the effect of lifting the bottom part of the graph. As ξ gets bigger and bigger, it converges since the factor $\exp(-r/\xi) \to 1$ as $\xi \to \infty$.

With this in mind, the results of the two point function, three point function and directional correlation analysis can be presented. Since we want to investigate two different setups of the grid by using a $1/0$, $1/-1$ for fire/no fire representation, we will first present the entire results for the $1/-1$ system and thereafter for the $0/1$ system. This will be done first for the region of Botswana, and then of Kazakhstan.

4.3 Results

Since there are quite a few plots as well as quite a few years, it is more instructive to illustrate a few cases detailing relevant details. Thereafter, a table detailing values for fitted variables are presented together with additional exploratory plots. Some plots do not fit as well as other, especially in the zones of Botswana. Reasons for these are explored in Section 4.3.4, while also discussing other shortfalls/strong points of the methodology applied.

4.3.1 Sample Plots

The original region studied is that of the greater Botswana[166] and Kazakhstan[167] and some surrounding areas. This is the rectangular region as shown in Figures 4.8 and 4.9 below. These smaller regions were chosen as to be as homogeneous of vegetation as possible so to highlight effects of external natural phenomena. Each grid point represents a plot of land which is $50m \times 50m$.

Botswana

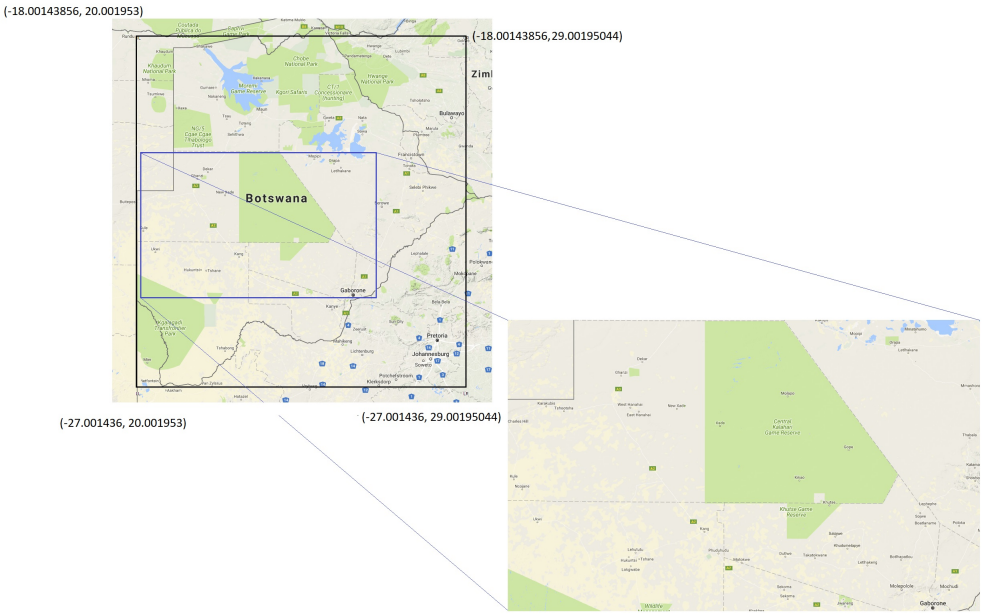


FIGURE 4.8: *Large region has dimensions of* 2048×2048 *units, with the smaller region having dimensions of* 1470×836 *resulting in a* $73km \times 41km$ *region.*

Kazakhstan

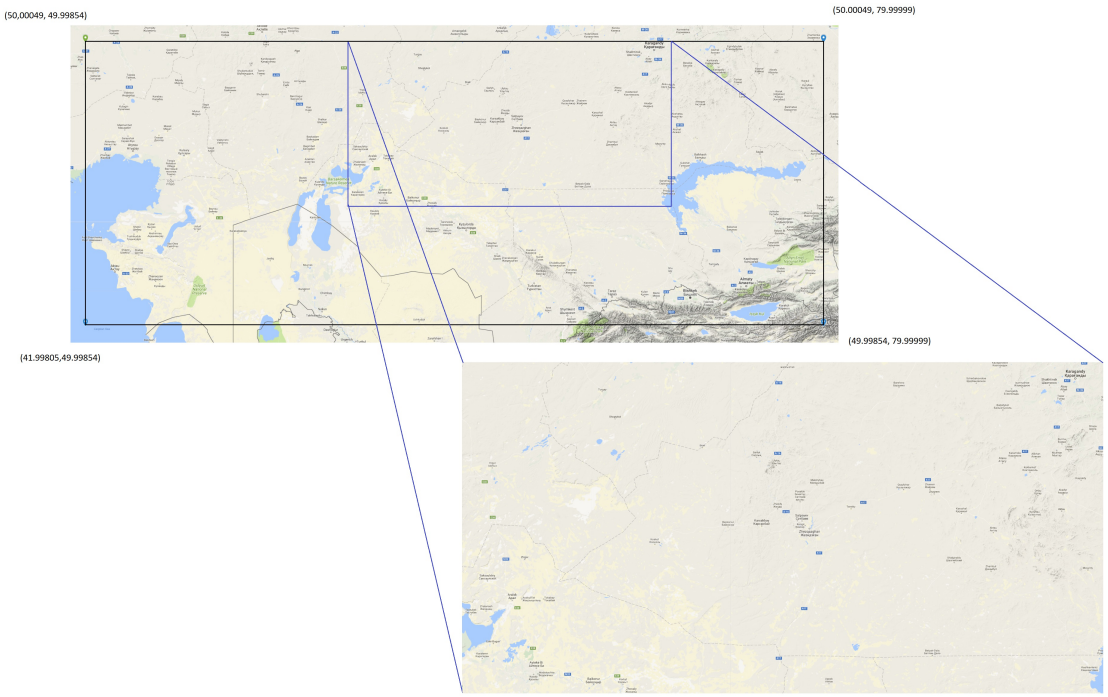


FIGURE 4.9: *Large region has dimensions of* 6827×1820 *units, with the smaller region have dimensions of* 2961×1025 *resulting in a* $148km \times 51.25km$ *region.*

Since Botswana has a few interesting features, we illustrate two different years: 2002 and 2008. Whereas for Kazakhstan which is a lot more regular we show the year 2003. In each year we show a plot of the two-point correlations, three-point correlation and direction correlation analysis. We illustrate two formats:

1. **Format of 1/-1**: If fire is represented by 1 and no fire by -1, then there are four permutations regarding to how the correlation is calculated. The case where two points both have fire or both have no fire is registered as 1. Of course positive values add to the average correlation, so when summing over all possible points, geographical areas which have not been burnt, in a particular year, will add the correlation just as much as points which have been. All plots and analysis have been done using a format of $1/-1$.

2. **Format of 1/0**: If we are interested in purely the correlation between fire occurrences, then the format of $1/-1$ does not quite work since this considers also two patches of no fire as a positive correlation. By using the format of 1 for a fire and 0 for no fire only points that have had a fire in a particular year will contribute to the correlation. Hence we are looking strictly at the correlation of fire occurrences.

It is worthwhile to note, that correlations in one format are not derivable from the other for as long as one does not use periodic boundary conditions. With periodic boundary conditions, since the the $1/-1$ format is just a rescaling of the $0/1$ format, correlations are related by :

$$4f(x_{12},t)_{1/0} - f(x_{12},t)_{1/-1} = 0. \tag{4.3.1}$$

We show this by substituting (4.2.10) into (4.2.8). To see why this does not work for non-periodic boundary conditions, consider the following example of a 3×3 grid:

$$\begin{matrix} 0 & 0 & 1 \\ 0 & 1 & 0 \\ 1 & 1 & 1 \end{matrix} \tag{4.3.2}$$

The first two correlations are as follows:

$$f(r)_{1/0} = \left[\left(1, -\frac{19}{324}\right), \left(\sqrt{2}, \frac{43}{648}\right)\right], \tag{4.3.3}$$

$$f_p(r)_{1/0} = \left[\left(1, -\frac{5}{162}\right), \left(\sqrt{2}, -\frac{5}{162}\right)\right], \tag{4.3.4}$$

where f_p and f denote correlations using periodic and non periodic boundary conditions respectively, In the $1/-1$ format, the correlations become:

$$f(r)_{1/-1} = \left[\left(1, -\frac{29}{162}\right), \left(\sqrt{2}, \frac{77}{324}\right)\right] \tag{4.3.5}$$

$$f_p(r)_{1/-1} = \left[\left(1, -\frac{10}{81}\right), \left(\sqrt{2}, -\frac{10}{81}\right)\right] \tag{4.3.6}$$

We see that:

$$4f_p(r)_{1/0} - f_p(r)_{1/-1} = (0, 0) \tag{4.3.7}$$

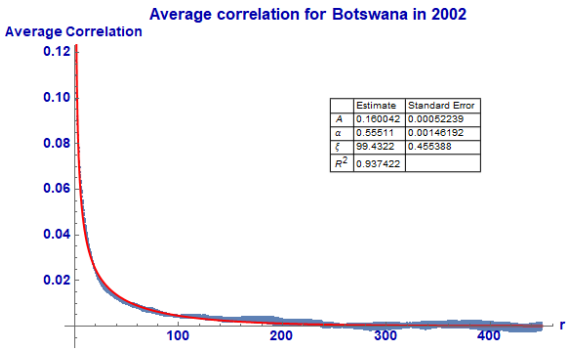
$$4f(r)_{1/0} - f(r)_{1/-1} = (-\frac{1}{18}, \frac{1}{36}) \neq (0, 0) \tag{4.3.8}$$

This relation can be shown for all distances and for any size grid. For a landscape such as Botswana and Kazakhstan, we implement non-periodic boundary conditions when calculating correlation functions, as periodic boundaries have no physical meaning. The non-derivability of these two formats is the reason we have to keep the two formats separate in the analysis.

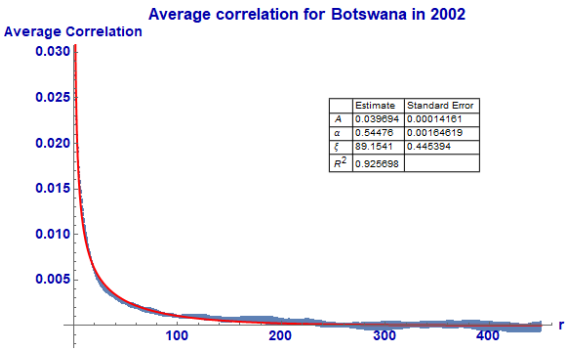
4.3.1.1 Botswana - 2002



FIGURE 4.10: *Overlay of region with fire occurrences for the year 2002.*

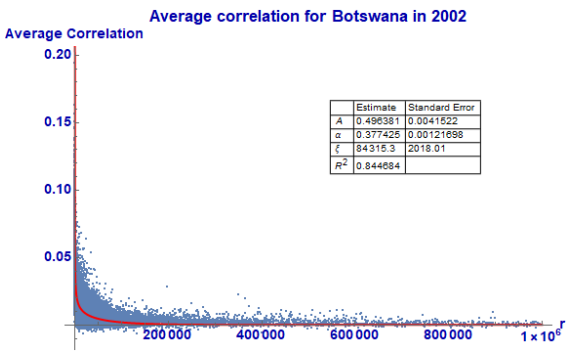


(A) *Two point correlation using* $1/-1$ *format.*

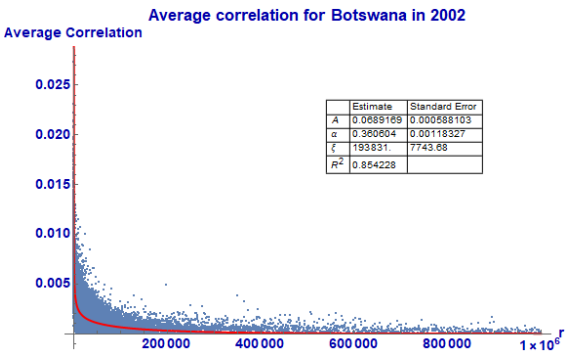


(B) *Two point correlation using* $1/0$ *format.*

FIGURE 4.11: *Two point correlation function analysis for 2002 using both formats in Botswana.*

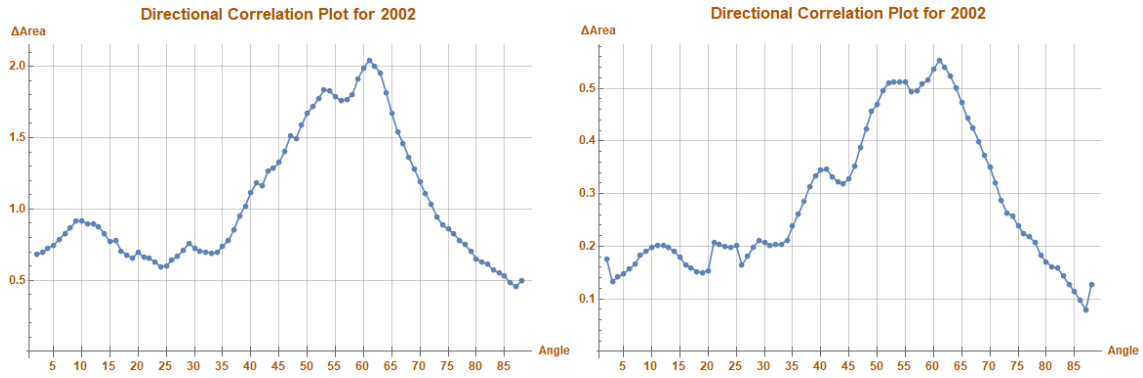


(A) *Three point correlations using* $1/-1$ *format.*



(B) *Three point correlations using* $1/0$ *format.*

FIGURE 4.12: *Three point correlation function analysis for 2002 using both formats in Botswana.*



(A) *Directional correlations using* $1/-1$ *format.* (B) *Directional correlations using* $1/0$ *format.*

FIGURE 4.13: *Directional correlation analysis for 2002 using both formats in Botswana.*

1. **Two-point correlation** Figure -4.11 : This year was chosen to represent the general standard of all other plots. The fit-statistics indicate the model fit remarkably well. The correlation length for both formats fall between 89 and 99 units, with each unit being equivalent to a $50m \times 50m$ cell, the correlation length is around 4.75 km. What can be seen is the more fires there are, the greater the amplitude A. In this year the amplitude is moderately low.

2. **Three-point correlation** Figure - 4.12 : The three point correlation is a lot more noisy, this is due to the random sampling approach that is adopted. The correlation length quoted needs to be cube rooted since the r-axis is in units of r^3. Most other plots tend to be a lot more noisy, especially at large values of r. It becomes expensive computationally to do a complete sampling of all three points.

3. **Directional correlations** Figure - 4.13 : In both formats the angle of greatest difference between correlation graphs occurs at roughly $55^o - 65^o$ and $125^o - 145^o$. This graph was produced using a moving average to reduce noise in the plots. A difference of the area in the order of 1 is above the the other years. The higher this value the more the more transnational invariance was broken. Indicating that there was an external driver in the spreading of the fire.

4.3.1.2 Botswana - 2008

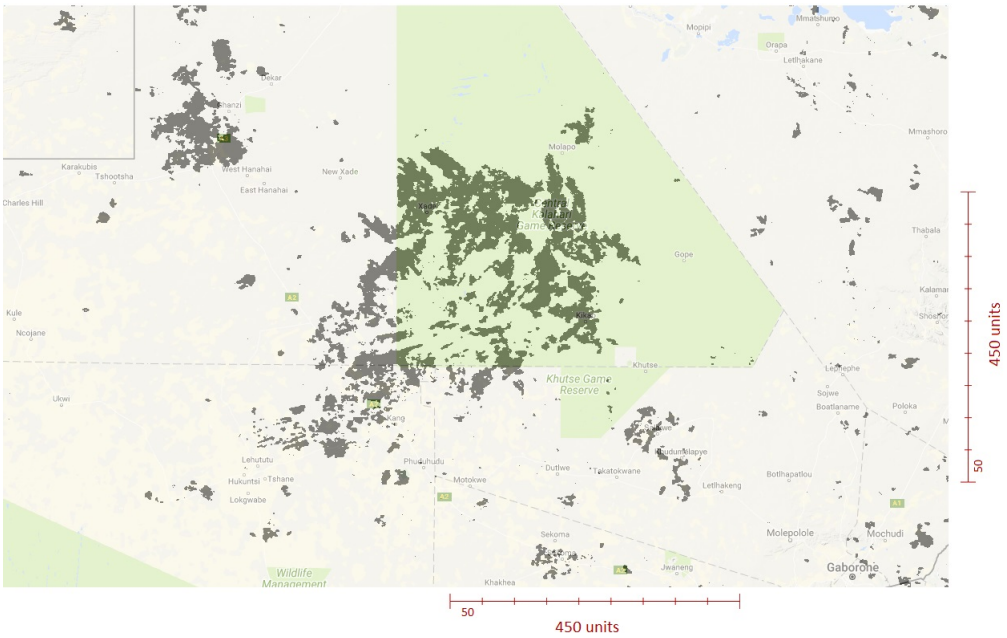
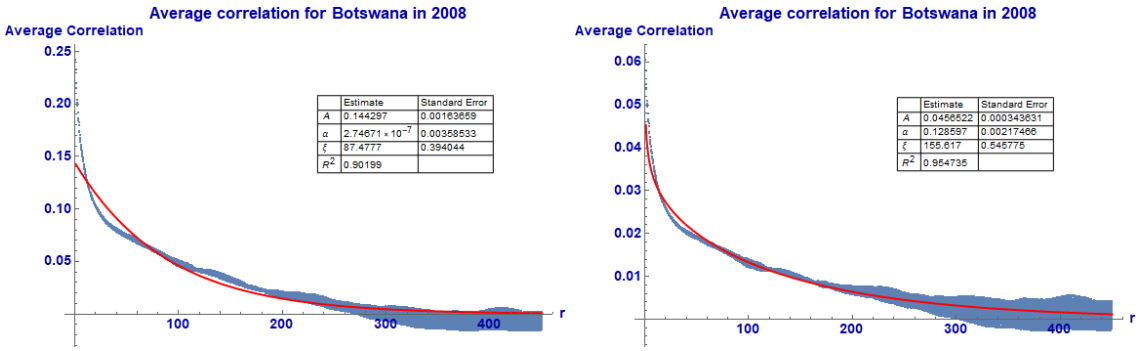
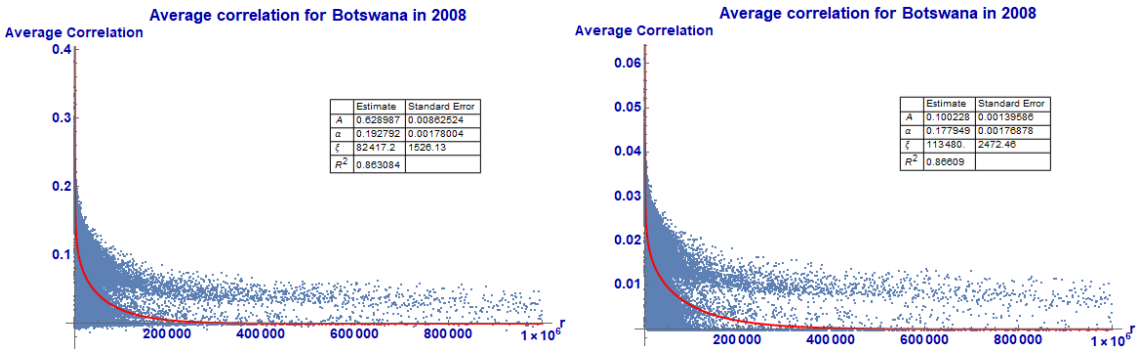


FIGURE 4.14: *Overlay of region with fire occurrences for the year 2008.*



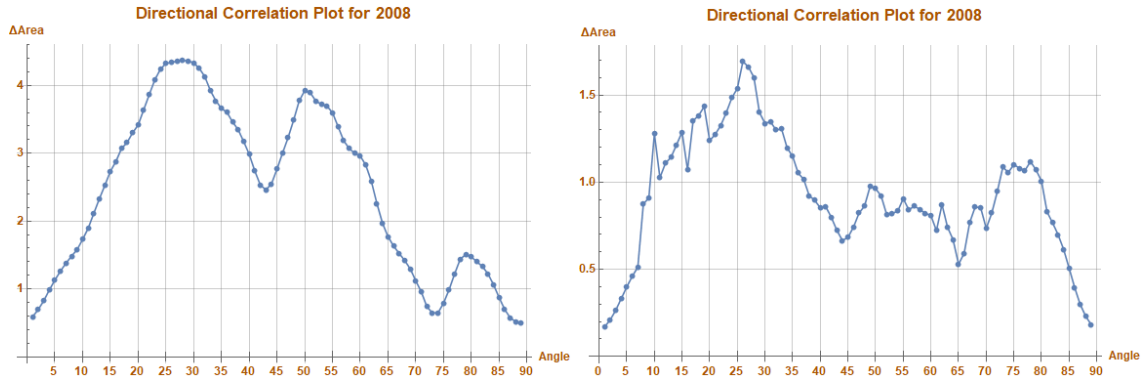
(A) *Two point correlation using* $1/-1$ *format.* (B) *Two point correlation using* $1/0$ *format.*

FIGURE 4.15: *Two point correlation function analysis for 2008 using both formats in Botswana.*



(A) *Three point correlations using* $1/-1$ *format.* (B) *Three point correlations using* $1/0$ *format.*

FIGURE 4.16: *Three point correlation function analysis for 2008 using both formats in Botswana.*



(A) *Directional correlations using* $1/-1$ *format.* (B) *Directional correlations using* $1/0$ *format.*

FIGURE 4.17: *Directional correlation analysis for 2008 using both formats in Botswana.*

1. **Two-point correlation** Figure -4.15 : This year was chosen to represent the worst fit scenario. In the two point function data, there appears to be a flat section between $r = 20$ and $r = 120$. This flatness means the model struggles to fit to the curve. It is curious that only this particular region of Botswana exhibits such behaviour and it is also only for the years 2006, 2008, 2010, 2014. Possible indication is that fires were perhaps put out, or patches purposely burnt, thus resulting in non-typical spread behaviour resulting in correlations that don't follow the model. The average correlation scale is larger than compared to 2002. It is a common feature that the greater, or closer to 1 this scale is, the more burnt patches one finds.

2. **Three-point correlation** Fig - 4.16 : The three point correlation is a lot more noisy compared to 2002. In addition we find this sort of double line behaviour. Due to lack of data, it is hard to say if there are two distinct lines, or if there is just data missing and it is in fact just one thick band.

3. **Directional correlations** Fig - 4.17 : The peak differences in directions occur at $15^o - 30^o$ and $105^o - 120^o$. The second peak in (b) is not as pronounced as in (a). This could mean that the directional correlation effect was more pronounced in the geographical setting since the $1/-1$ format shows a greater distinction between peaks.

4.3.1.3 Kazakhstan - 2003

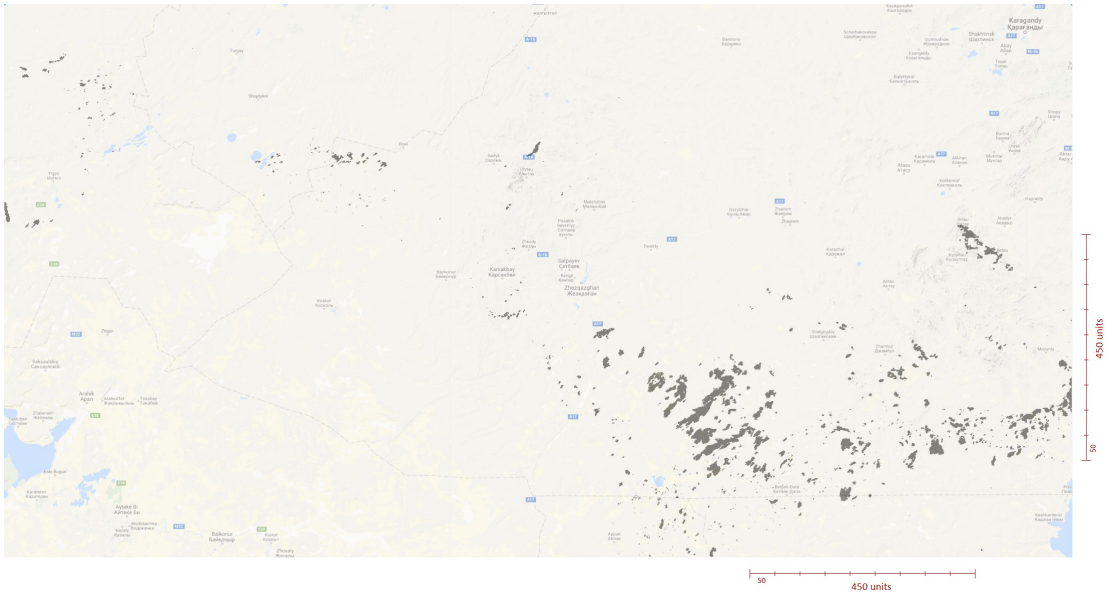
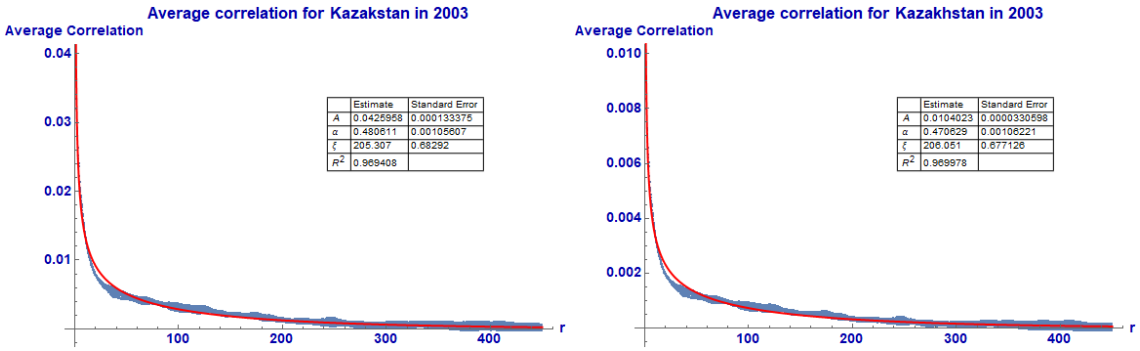
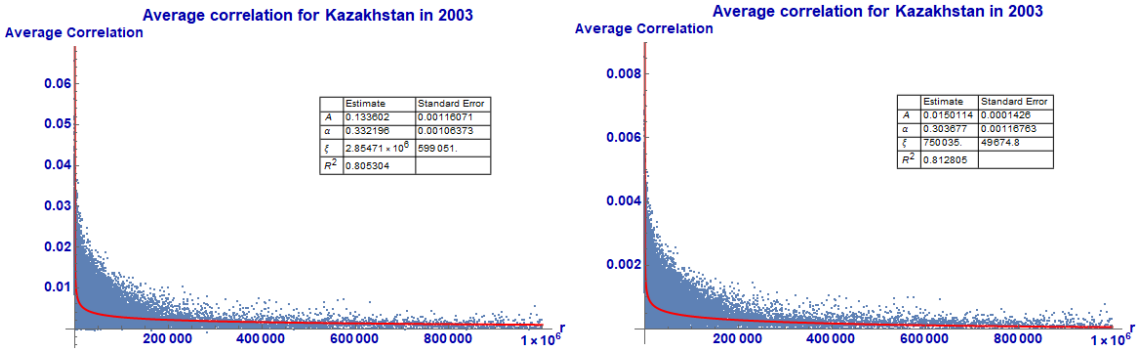


FIGURE 4.18: *Overlay of region with fire occurrences for the year 2003.*



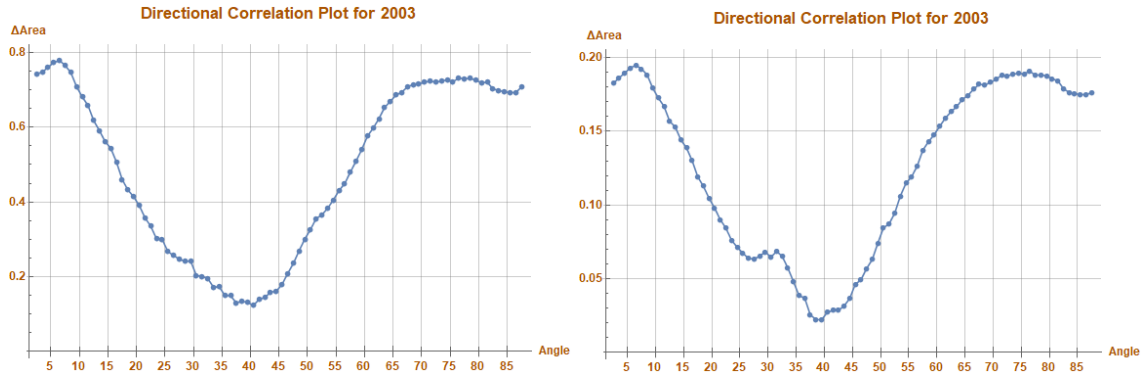
(A) *Two point correlation using* $1/-1$ *format.* (B) *Two point correlation using* $1/0$ *format.*

FIGURE 4.19: *Two point correlation function analysis for 2003 using both formats in Kazakhstan.*



(A) *Three point correlations using* $1/-1$ *format.* (B) *Three point correlations using* $1/0$ *format.*

FIGURE 4.20: *Three point correlation function analysis for 2003 using both formats in Kazakhstan.*



(A) *Directional correlations using* $1/-1$ *format.* (B) *Directional correlations using* $1/0$ *format.*

FIGURE 4.21: *Directional correlation analysis for 2003 using both formats in Kazakhstan.*

1. **Two-point correlation** Figure -4.19: Over all the years, the modeled two point function fits all the years very well. The correlation length of 205 units, or 10km is larger than that over the Botswana region. The burn areas are also not as big as in Botswana.

2. **Three-point correlation** Figure - 4.20b: Over all years the three point function results also behave regularly. With the same amount of noise, once again a result of the sampling method.

3. **Directional correlations** Figure - 4.21: The directional correlations here are interesting as one can see even in the actual layout of the fires there seems to be some directional preference. This is shown where the peak differences in direction are at $0^o - 15^o$ and $90^o - 105^o$. This is matched by Fig 4.18 which shows that the burning pattern is more dominant horizontally than it is vertically.

4.3.2 Error Estimates

Due to the lack of error thresholds in the analysed data, it is difficult to come up with an error analysis in developing the models. One can obtain a error estimate in the fitting procedure of the variables, but this is related more to the statistical error in how the program performs the regression analysis, rather than error in data itself. As a way to account for this, we performed a random sampling of the data. We then looked at the statistics of how the variables are fitted over 100 different sampling iterations. There are 3 180 000 possible pairs of points with length between the $r = 1$ and $r = 450$. For our random sampling, we randomly choose 7 000 possible pairs, and for each pair we sampled 1 000 00 locations on the grid. This is repeated 100 times, each time choosing new points and each time fitting the resultant sampling. By then looking at the mean, variance and standard deviation we can get a sense of the error in fitting of the data. This then can be applied to all future obtained fitted variables.

For the purpose of the sampling, we chose to use the region of Botswana for the year 2002. Below is an example of the sampling:

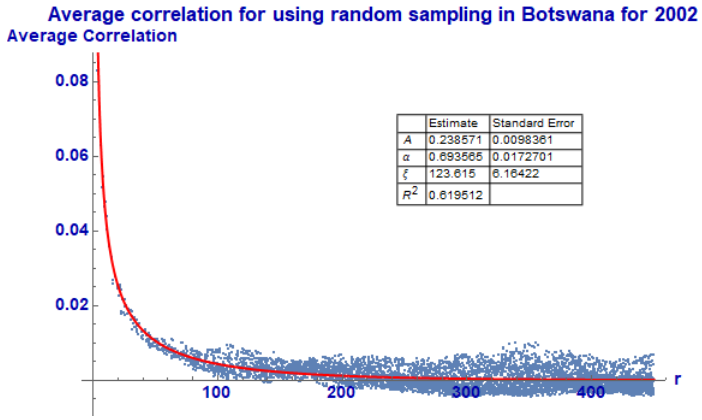


FIGURE 4.22: *Amplitude sampling statistics for both formats*

The R^2 value is not very high, and this is of course attributed by virtue of doing such a random sampling - increasing the number of samples increases the R^2 value. Comparing the obtained values to an exact sampling in Figure 4.11, the random sampled variables are all bigger. Below is a summary of the random sampling statistics in which we used the standard deviation as an error estimate in determining the values of A, α, χ for the two point functions and A, η, ζ for the three point function.

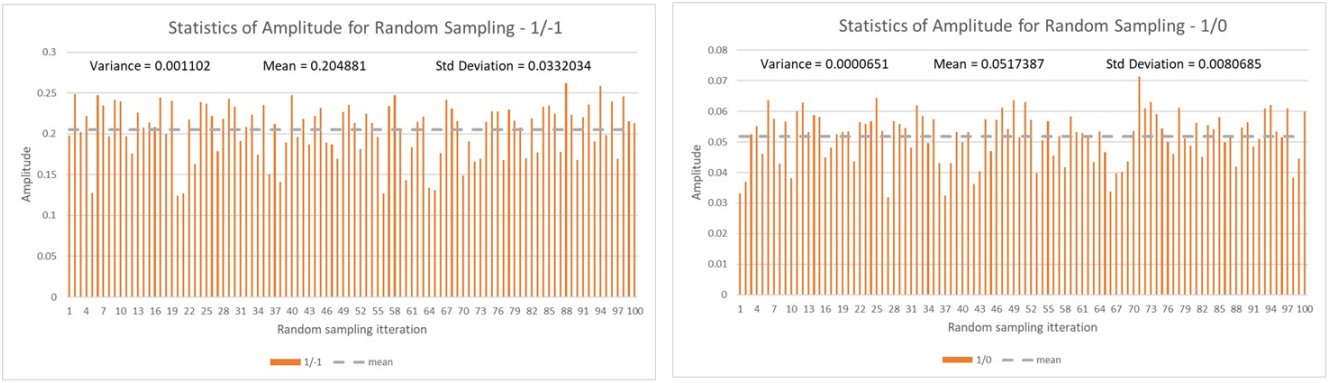


FIGURE 4.23: *Amplitude sampling statistics for both formats.*

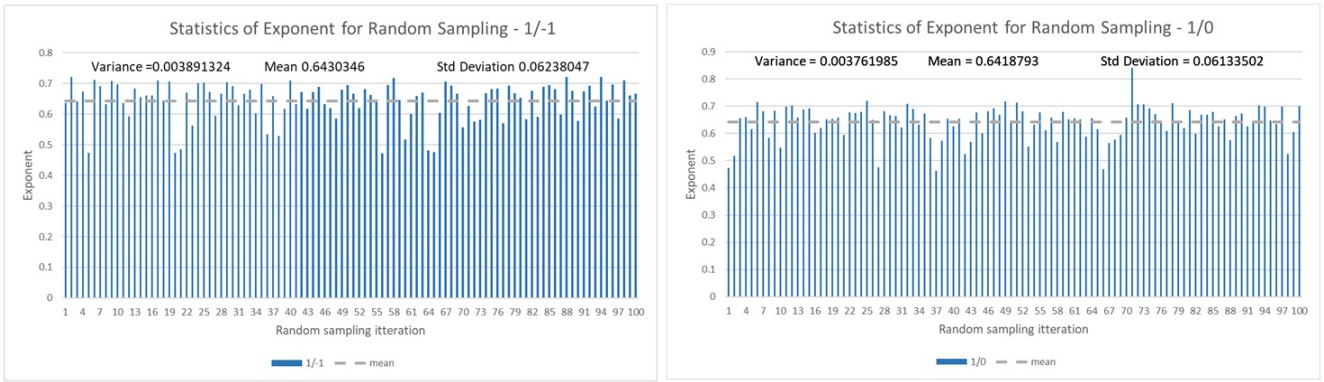


FIGURE 4.24: *Exponent sampling statistics for both formats.*

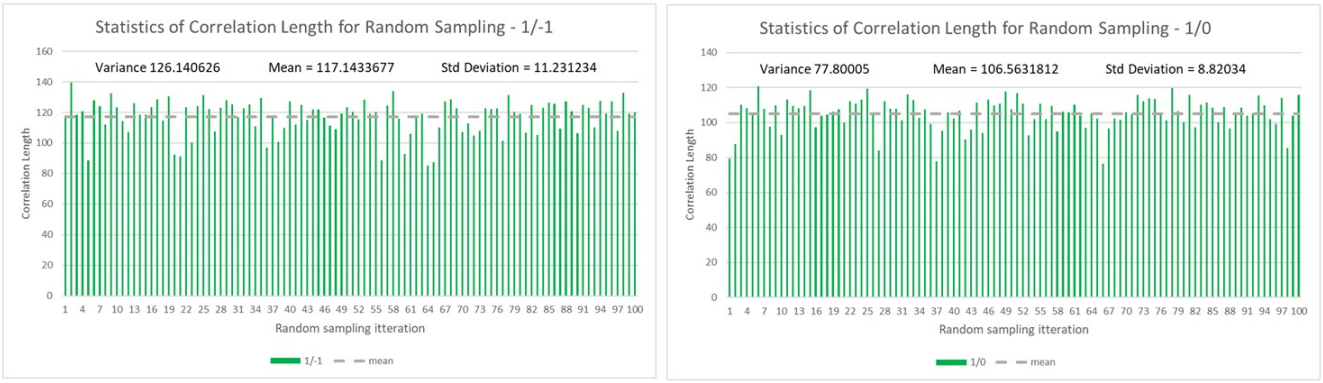


FIGURE 4.25: *Correlation length sampling statistics for both formats.*

4.3.3 All variable values

The following are two tables showing the results of the entire analysis across all 12 years with both formats and both regions:

Two Point Botswana														Mean
Year	2002	2003	2004	2005	2006	2007	2008	2009	2010	2011	2012	2013	2014	
1/-1														
Amplitude	0.160042	0.010639	0.011982	0.013611	0.163829	0.037179	0.144297	0.036824	0.352272	0.582137	0.096777	0.05579	0.041826	0.131323
Exponent	0.55511	0.289399	0.32764	0.24923	3.57E-07	0.205436	2.75E-07	0.27653	0.089725	0.240967	0.154132	0.205746	4.68E-05	0.199535
Correlation length	99.43218	11.34878	40.78842	19.74222	55.52497	24.42748	87.47765	32.57821	63.53911	162.618	34.42758	40.54717	41.33759	54.90687
Angular differences														
Max angle	60	10	50	85	60	27	30	5	26	80	83	55	82	
Min angle	0	80	10	45	75	45	0	35	7	75	30	10	42	
Area difference	1.5	0.02	0.07	0.15	4.5	0.84	3.8	0.23	13	7	1.7	1.29	1.4	
1/0														
Amplitude	0.039694	0.00333	0.002986	0.005304	0.041996	0.009457	0.045652	0.009078	0.07744	0.117923	0.022147	0.013177	0.010381	0.030659
Exponent	0.54476	0.803931	0.324311	0.804342	4.84E-06	0.224935	0.128597	0.259795	0.021969	0.147807	0.081952	0.163989	0.002128	0.269886
Correlation length	89.15409	49.82312	40.46473	142.9382	52.57568	25.69241	155.617	30.67333	54.18508	118.6306	28.71638	36.72485	42.30465	66.73078
Angular differences														
Max angle	60	10	50	85	60	27	27	5	25	60	90	50	80	
Min angle	5	90	20	42	73	42	0	50	3	45	37	5	45	
Area difference	0.4	0.0045	0.015	0.03	1	0.18	1.68	0.068	2.8	1.9	0.21	0.31	0.36	

** Colour refers to problem years

Three Point Botswana														Mean
Year	2002	2003	2004	2005	2006	2007	2008	2009	2010	2011	2012	2013	2014	
1/-1														
amplitude	0.496381	0.028345	0.034787	0.03511	0.5269	0.112015	0.628987	0.119498	0.798123	1.415984	0.381726	0.186793	0.12366	0.376024
exponent	0.377425	0.422748	0.293083	0.282585	0.17349	0.281219	0.192792	0.346639	0.156737	0.252356	0.373196	0.278547	0.141132	0.274765
correlation length	43.84993	15.67159	23.75522	25.51657	37.91155	29.9784	43.51837	19.47252	79.39657	46.66763	46.33425	30.27882	32.29682	36.5114
1/0														
amplitude	0.068917	0.003637	0.004393	0.00447	0.081418	0.014431	0.100228	0.015636	0.146575	0.34365	0.051099	0.024804	0.016295	0.06735
exponent	0.360604	0.426299	0.291617	0.282208	0.171039	0.277044	0.177949	0.345328	0.129508	0.239698	0.362458	0.276863	0.138729	0.267642
correlation length	57.87279	16.33878	23.90178	26.05354	38.92404	30.86757	48.4143	20.09039	90.17799	75.87858	50.73438	31.28532	32.54222	41.77551

Year	2002	2003	2004	2005	2006	2007	2008	2009	2010	2011	2012	2013	2014	Mean
Percentage Burnt														
Total	3.62492	0.289299	0.337692	0.372521	6.091	1.02893	7.87561	1.07946	14.698	20.3048	2.72494	1.53536	1.59596	4.735269
Central Kalahari	8.59987	26.7137	12.5242	29.1603	48.088	33.1975	54.1936	32.391	39.8679	16.737	29.9979	0.974009	58.705	30.08846
Weather Data														
rain (mm)	29.89998	28.22142	36.54797	26.81177	39.06341	25.32706	31.41468	34.65398	42.08947	41.74118	28.64136	29.54887	35.30227	33.02026
temp (°C)	22.6051	22.70162	22.57988	23.16414	21.98365	22.11147	22.25963	22.83802	22.58502	21.99065	22.4318	22.27289	22.1272	22.4347

FIGURE 4.26: *All fitted values for the region of Botswana. Cells with years coloured in orange are those with fits which don't follow our model very well - see Figure -4.15 for a detailed example.*

Two Point Kazakhstan														Mean
Year	2002	2003	2004	2005	2006	2007	2008	2009	2010	2011	2012	2013	2014	
1/-1														
Amplitude	0.063191	0.042596	0.091043	0.029304	0.024759	0.07667	0.020021	0.032741	0.010552	0.024079	0.011033	0.011893	0.008767	0.034358
Exponent	0.502494	0.480611	0.37119	0.621906	0.593833	0.55536	0.915057	0.656752	0.702398	0.484315	0.719829	0.68473	0.325949	0.585725
Correlation length	359.1749	205.3069	293.2377	159.3695	67.86162	323.97	471.9998	177.1595	34.60938	46.42104	49.84089	43.49492	29.31365	173.9815
Angular differences														
Max angle	10	7	16	20	70	0	5	42	82	80	82	90	15	
Min angle	65	38	70	73	35	36	47	53	50	33	35	30	57	
Area difference	1.256	0.655	1.858	0.156	0.144	0.986	0.093	0.155	0.024	0.258	0.172	0.106	0.085	
1/0														
Amplitude	0.015541	0.010402	0.022111	0.007342	0.00626	0.019033	0.004892	0.008155	0.002902	0.00613	0.002463	0.002633	0.003846	0.008593
Exponent	0.494183	0.470629	0.360887	0.624441	0.606849	0.552398	0.892358	0.653732	0.769161	0.505721	0.495234	0.46596	0.936735	0.602176
Correlation length	332.0778	206.0509	289.6267	163.2026	72.49253	326.8989	482.154	172.5557	48.5513	50.76545	21.78685	21.03982	555.9969	211.0153
Angular differences														
Max angle	7	10	20	20	65	2	2	42	80	85	82	80	15	
Min angle	63	40	65	73	35	37	45	52	42	35	32	30	58	
Area difference	0.329	0.173	0.440	0.041	0.032	0.218	0.020	0.039	0.006	0.063	0.043	0.025	0.020	

Three Point Kazakhstan														Mean
Year	2002	2003	2004	2005	2006	2007	2008	2009	2010	2011	2012	2013	2014	
1/-1														
amplitude	0.135882	0.133602	0.199018	0.087466	0.062894	0.151846	0.049751	0.082024	0.024723	0.06063	0.022692	0.022014	0.021678	0.081094
exponent	0.244323	0.332196	0.207181	0.371021	0.364465	0.235711	0.450177	0.343112	0.409366	0.329986	0.34708	0.330114	0.260619	0.325027
correlation length	111.539	141.858	141.1827	49.65763	33.13284	49.50771	53.49178	45.63326	15.02268	33.42995	17.03379	18.72962	61.00054	59.32458
1/0														
amplitude	0.016052	0.015011	0.023516	0.010947	0.008058	0.01976	0.005624	0.01039	0.003218	0.007763	0.002905	0.00282	0.00255	0.009893
exponent	0.224677	0.303677	0.179795	0.363411	0.360938	0.229058	0.422386	0.337891	0.418303	0.326714	0.349504	0.331552	0.249911	0.315217
correlation length	108.7373	90.85743	139.2649	52.92948	34.64633	52.83433	40.94964	47.88975	15.90787	34.47713	17.39665	19.1132	56.59611	54.73847

Year	2002	2003	2004	2005	2006	2007	2008	2009	2010	2011	2012	2013	2014	Mean
Percentage Burnt														
Total	1.45102	1.20778	2.6145	0.70797	0.666116	1.62073	0.411801	0.693835	0.263127	0.67777	0.265909	0.319002	0.246668	0.857402
Weather Data														
rain (mm)	24.94984	24.51808	22.50893	19.01691	21.98139	20.66282	18.30425	22.83487	19.8313	22.31585	19.46306	25.20437	21.09988	21.7455
temp (°C)	7.474171	6.311153	7.715287	7.163488	7.096081	7.414591	7.199297	6.563739	6.959989	5.894087	6.318634	7.907236	6.1285	6.934327

FIGURE 4.27: *Table summarizing all fitted variables relating to Kazakhstan.*

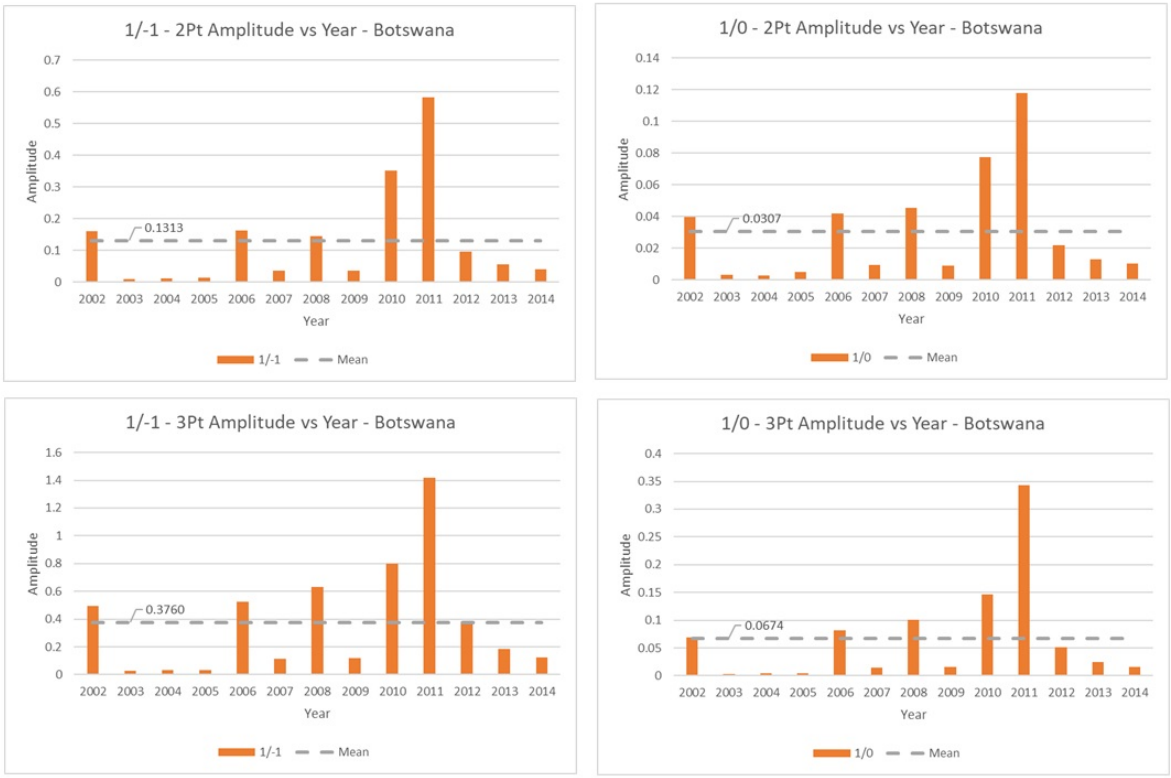


FIGURE 4.28: *Plots of amplitude with mean values - Botswana.*

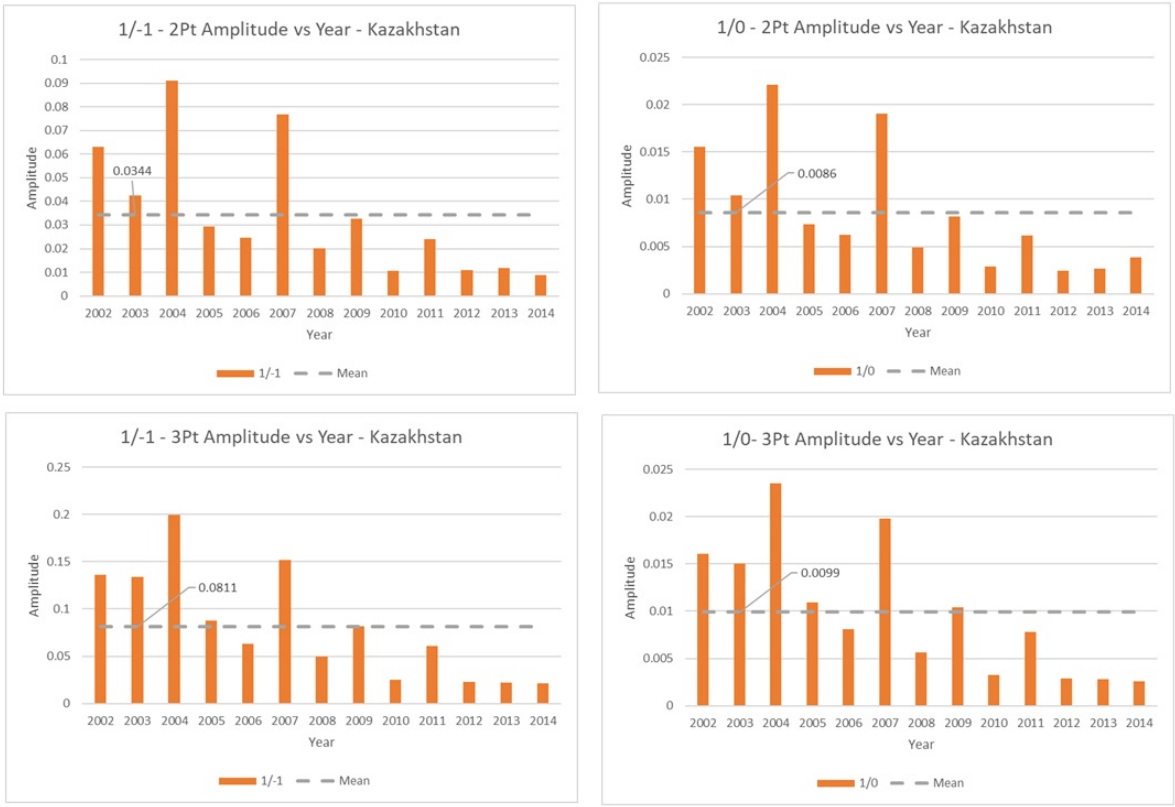


FIGURE 4.29: *Plots of amplitude with mean values - Kazakhstan.*

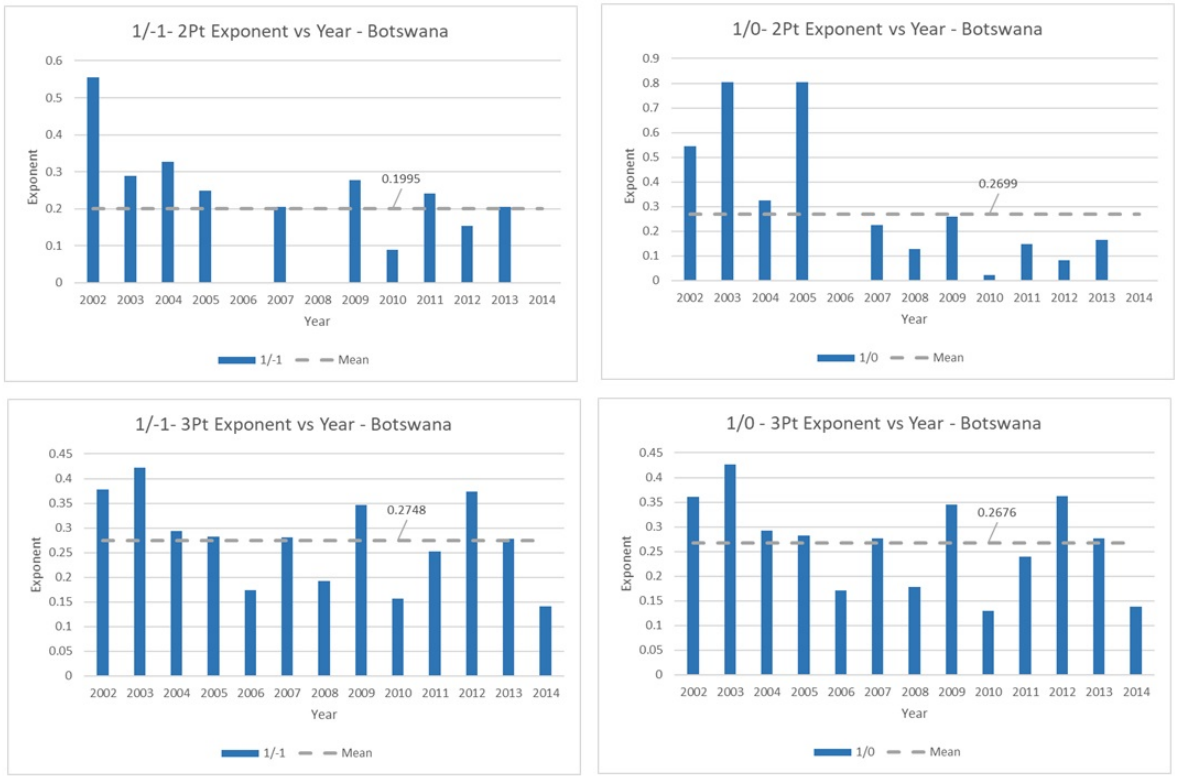


FIGURE 4.30: *Plots of exponents with mean values - Botswana.*



FIGURE 4.31: *Plots of exponents with mean values - Kazakhstan.*



FIGURE 4.32: *Plots of correlation lengths with mean values - Botswana.*



FIGURE 4.33: *Plots of correlation lengths with mean values - Kazakhstan.*

4.3.4 Comparison of Variables with Meteorological Data

It is known that weather variables such as rainfall, temperature, humidity and wind all have effects on how a fire will move, grow and self extinguish. The only data that we were able to get hold of was that of average rain fall(mm) and average temperature (^oC)[168]. Due to the lack of wind data, we have included the area difference. This is an indication of directional differences in the correlations - a small area difference indicates no directional preferences in burning patterns whereas a large difference indicates a directional preference. It can be speculated that if wind were to mainly blow in a particular direction, then the directional correlations will pick this up. No humidity, or terrain data was obtained and thus could not be included in the analysis. The goal of comparing variables is to find potential correlations between our models fitted variables and meteorological variables. In order to plot values on the same axis, all variables found in tables 4.26 and 4.27 were normalized according to a 1-0 normalization:

$$x_i' = \frac{x_i - x_{\min}}{x_{\max} - x_{\min}}. \tag{4.3.9}$$

Because data has a time scale of one year, we also included a comparison by offsetting the variable values with the weather data by one year. For example, the data point for the amplitude for year 2003 was compared with the rainfall, temperature, and area difference for 2002. The logic behind this, is that rainfall and temperature have a delayed effect on distribution and quality of fuel. These comparisons are displayed in plots which are shown displayed “One Year Offset”.

Lastly, we included a moving average comparison as moving averages allow one to clear out any noise in the data and highlight general trends. A correlation in the general trend between model variables and weather variables are of definite interest. The moving average is calculated using a two year scale:

$$x_i' = \frac{x_i + x_{i+1}}{2}. \tag{4.3.10}$$

The analysis is performed for both Botswana and Kazakhstan and for both formats of $1/0$ and $1/-1$

4.3.4.1 Botswana



FIGURE 4.34: *Weather comparison using the* 1/0 *format for Botswana.*



FIGURE 4.35: *Weather comparison using the* $1/-1$ *format for Botswana.*

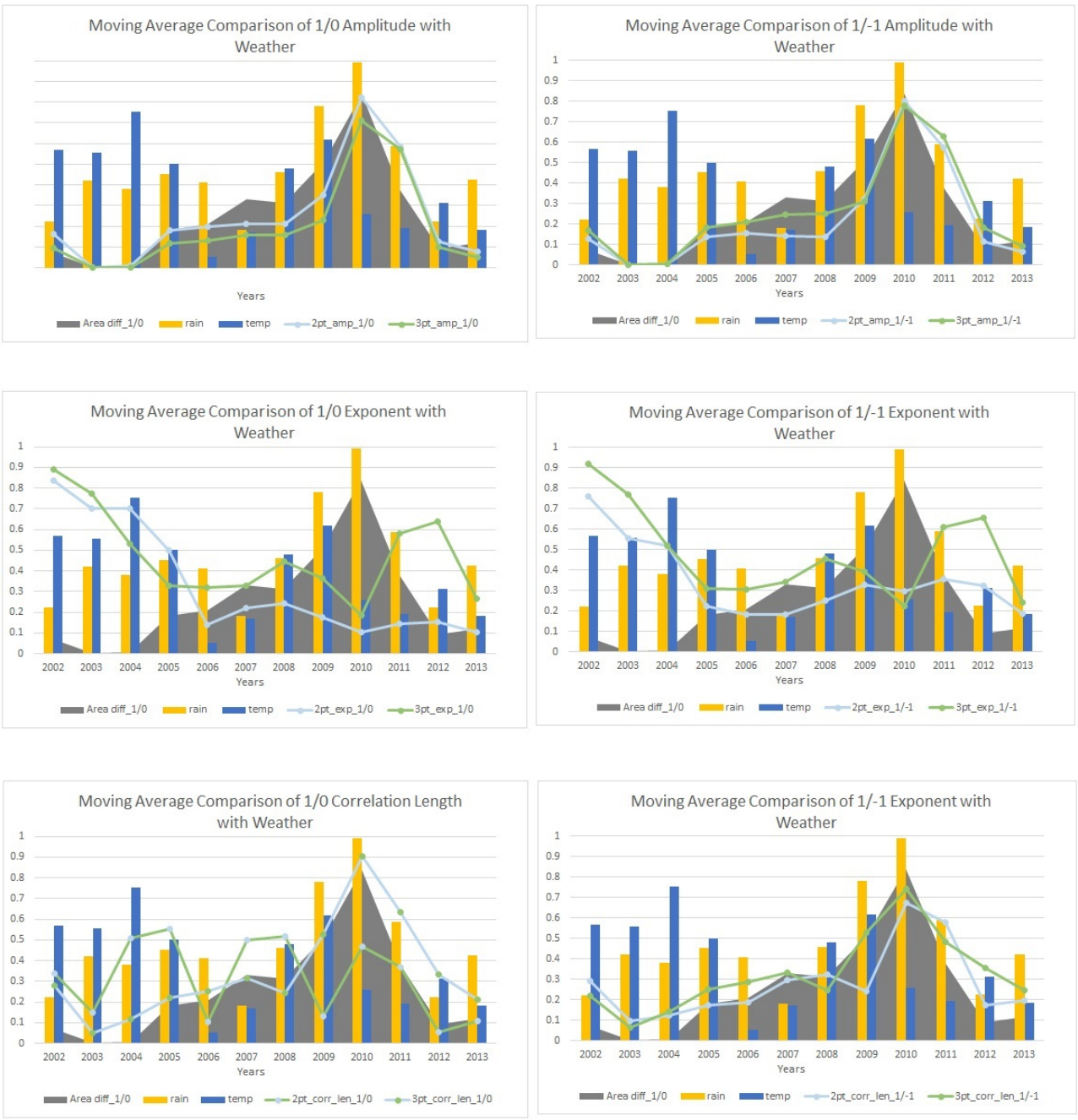


FIGURE 4.36: *Moving average weather comparison of both formats for Botswana.*

4.3.4.2 Kazakhstan

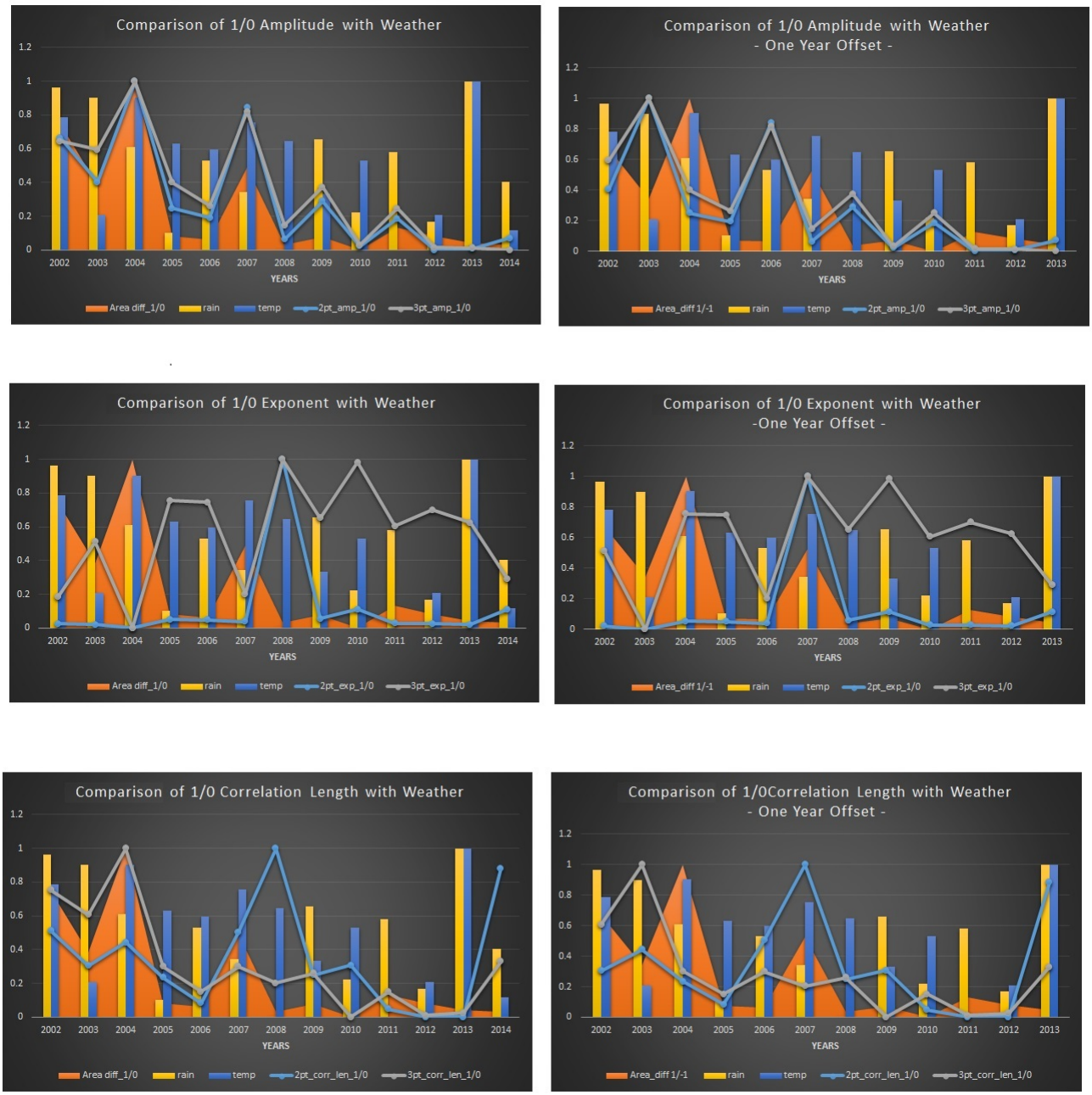
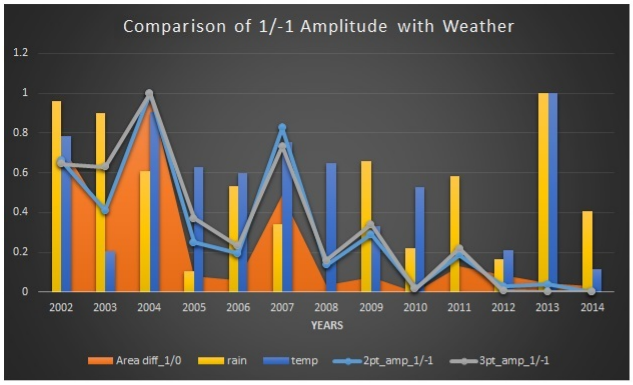
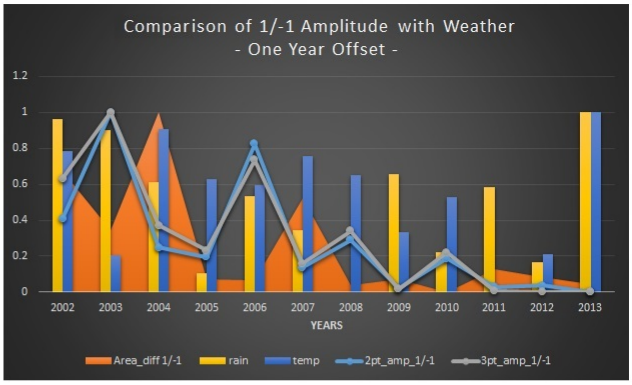
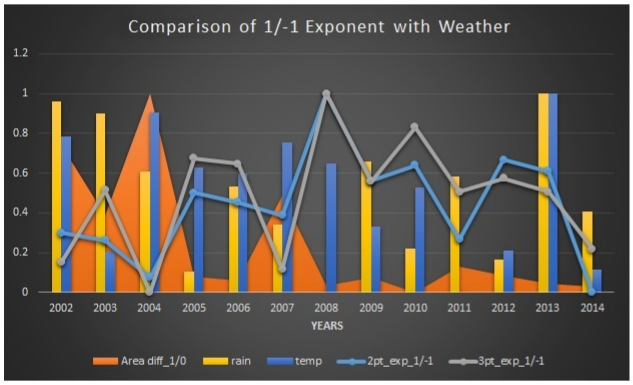
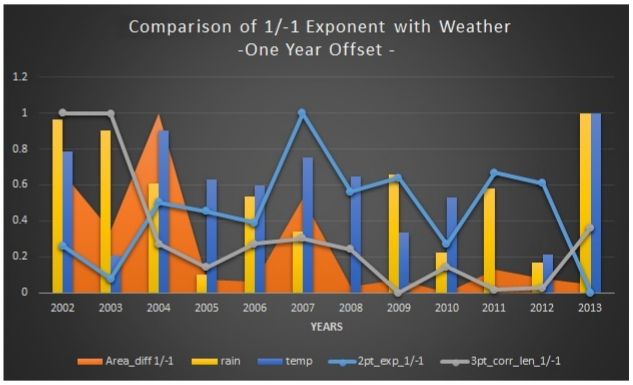


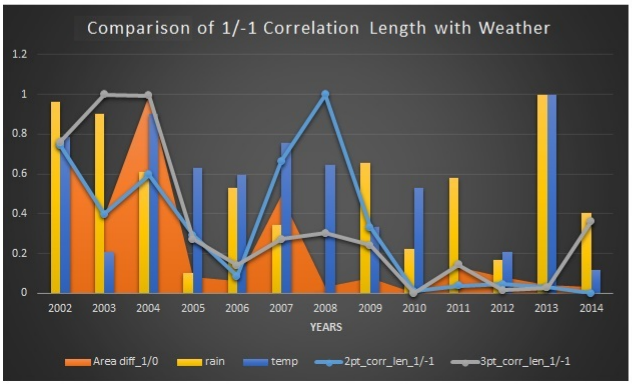
FIGURE 4.37: *Weather comparison using the* 1/0 *format for Kazakhstan.*











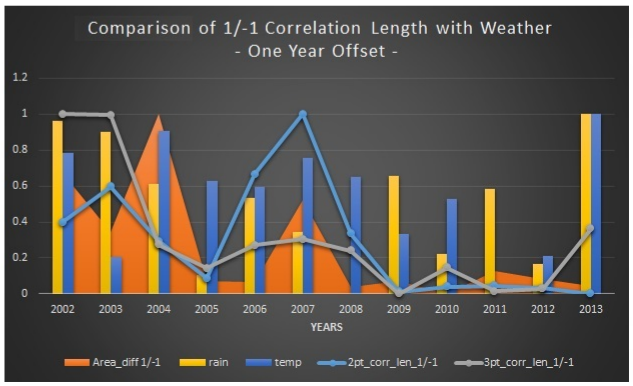


FIGURE 4.38: *Weather comparison using the* $1/-1$ *format for Kazakhstan.*

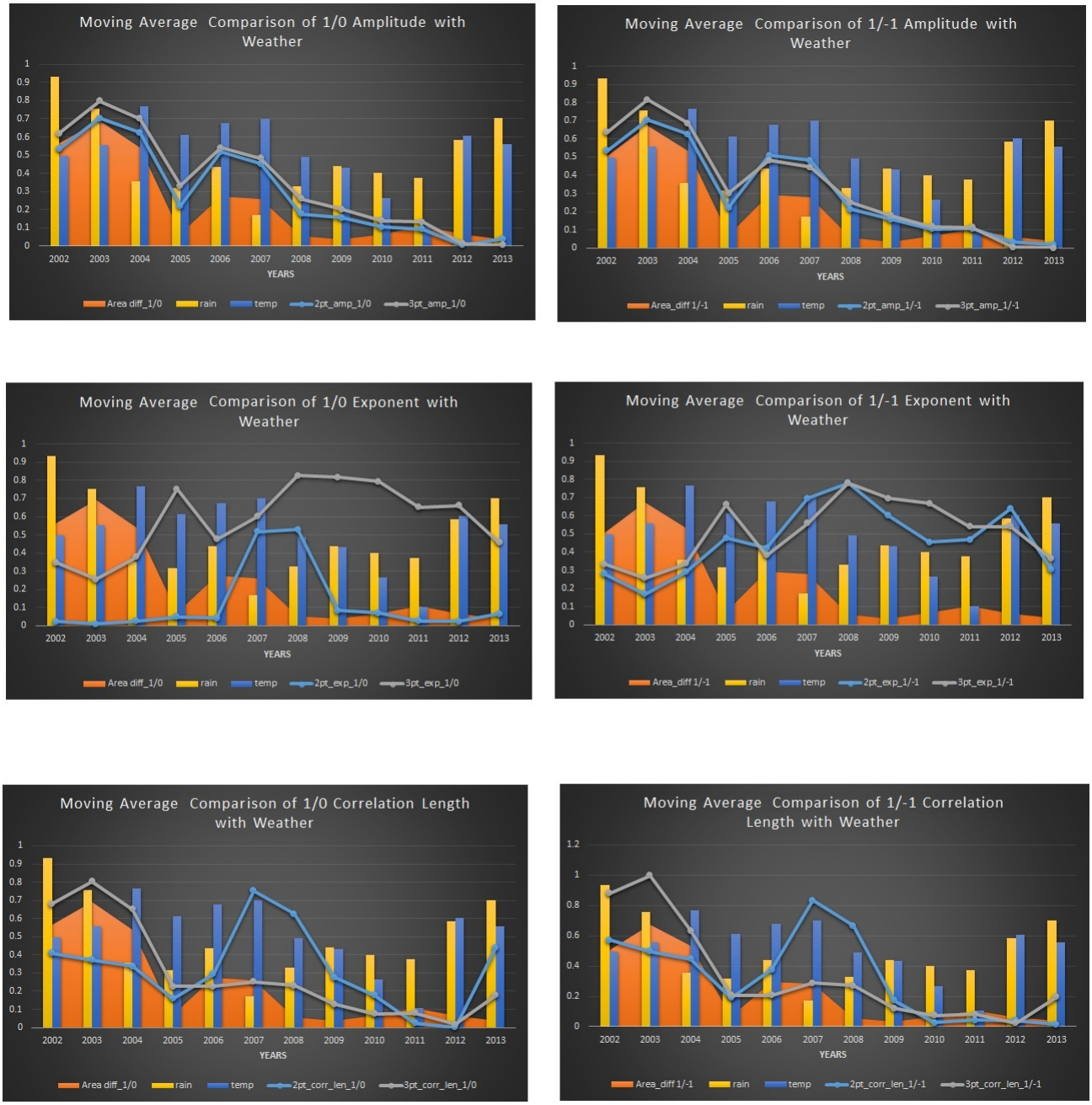
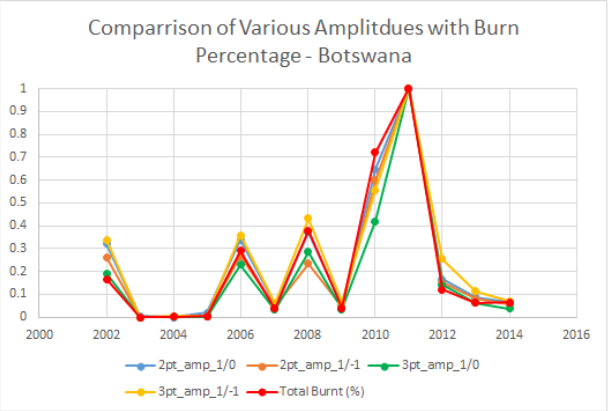


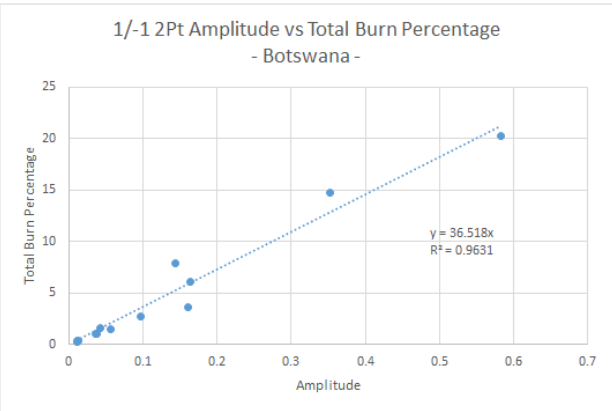
FIGURE 4.39: *Moving average weather comparison of both formats for Kazakhstan.*

Out of all the relationships, the one which exhibited strongest correlations is that of of the burn percentage of land and the amplitude of our model. This is shown for both Botswana and Kazakhstan, thus indicating that this is a feature of our descriptive nature of the model and not something specific about either area in particular. The simplest function to describe the realtionship is that of a straight line starting at the origin.

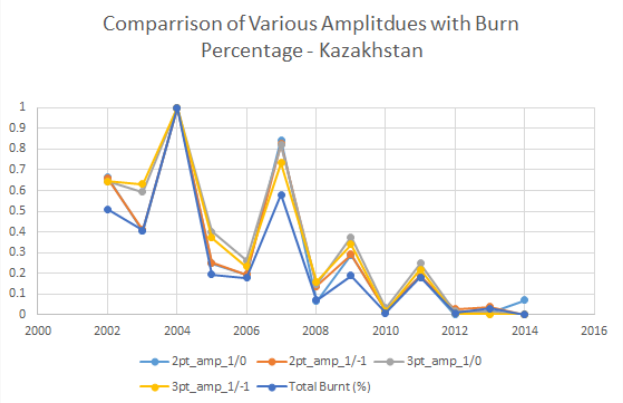
4.3.5 Comments

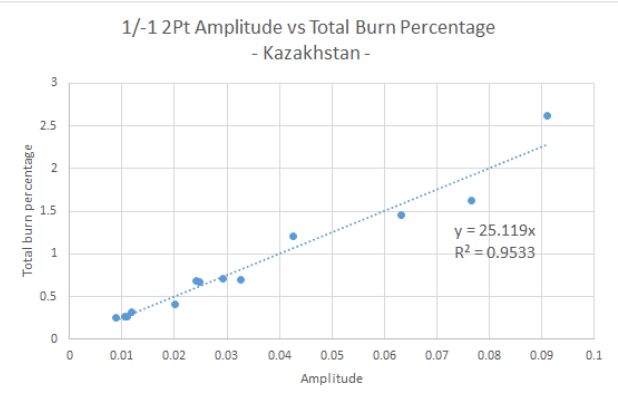
From the analysis above, we found the following relationships:





(A) *Plot illustrating the relationship of amplitude with total burn area of Botswana.*





(B) *Plot illustrating the relationship of amplitude with total burn area of Kazakhstan.*

FIGURE 4.40: *The amplitudes across both the two point and three point functions show linear relationships to the percentage of the total landscape within this particular region of Botswana and Kazakhstan that are burnt.*

- All variables in both regions of the $1/0$ format were closely related with the respective variables of the $1/-1$ format. All showed linear relationships.
- When using a moving average of the data in tables 4.26 we observed a strong linear relationship between the correlation lengths of the two point and three point functions for the $1/-1$ format in the region of Botswana. Testing of the other variables, showed some relationship, but nothing statistically significant enough.
- Initially, a comparison between our wind speed and our directional correlations was supposed to be done, however, the lack of decent wind data over the same set of years, made the comparison difficult. In all years there was a maximum and minimum difference between angles. However, for years 2003, 2004 and 2009 for Botswana, and 2010, 2014 for Kazakhstan, these differences were relatively very small. This suggests that there were no real external influences on how the fire would propagate. The years in Kazakhstan where significant difference in directions occurs, can actually be seen visually in Figure: 4.18 that the preference in particular directions exist. With the directional correlation tools, we are able to quantify this.
- Deciding the range r over which the analysis would be performed was not a straight forward task. In the testing phase of the model, it appeared that roughly 10% of the grid size should be used. However, since that was tested using the Ising model, we knew exactly what to look for. In this case, there was

no strong reason to choose our value of $r = 450$, other than it appeared that the fitting procedure was stable at this range. By stable we mean fitted parameter values didn't change a lot as we changed the sampling range r. Around this range most of these changes are very small. There are however, certain sampling values of $200r < 600$ that change parameter values significantly.

- The two point function was done exactly - we took every possible combination of pairs of points and moved that pair at every possible location on the grid. This was done using a combination of inbuilt Mathematica functions as well as a written code. Due to computational efficiency, this "exact" sampling was not possible for the three point functions. Reason being is that there are orders of magnitude more ways of choosing three points and moving them on all possible locations on the grid than there are for two points. For this reason, we opted to do a random sampling for the three point functions, as to get a large enough sample pool, is still computationally expensive. With more time and greater coding efficiency, an exact sampling can be achieved. Where this exact sampling will come useful in determining if results like that in Figure :4.16 are just artifacts of the random sampling, or there is actual structure.

- A strong relationship between all the amplitudes and the percentage of total landscape burnt was found. For Botswana, this linear relationship is given by a gradient of $m_B = 36.518$ and for Kazakhstan, $m_K = 25.119$ (see Figures 4.21a and 4.21b). The best fit line was set to have intercept zero, as there is no physical sense to have a non-zero, or even negative, amplitude for a region which has not had any fires. The difference in areas showed some power law relationship with the amplitudes with ab R^2 value between 70 and 80.

4.4 Conclusion

Firstly, it needs to be emphasized that the data given is sensitive only to changes over an entire year. We cannot differentiate between patches that have been burnt multiple times. This means that the correlations are not related to fires that occur at a single event in time. Rather, they show correlations between different fires at different times in a year. It would be interesting to apply our analysis on a single burning event and observe how well the proposed model stands. We suspect that it should indeed still work. Moreover, such experiments may shed more light on what relation the variables σ, η, ξ, ζ have with the external environment. Indeed, if there is true scale invariance, then the emergent patterns at a shorter temporal scale should still exhibit scale invariance, thus our model here will still be valid.

The odd results obtained in the region of Botswana need to be noted. It appears that the four years, whereby the central Kalahari game reserve shares a large percentage of the total burnt area, are the same four years that the data does not fit the model. What occurs in the data is a small region where the curve straightens out (see Figure 4.15). This straightening of the data signifies perhaps something special occurred that forced the fire to burn in a particular way - being a game reserve it could have been something like intended burning of land. The fact that this only happens for these few years, signifies that the model successfully describes how fire propagates over the timescale of one year. It would be worth performing the analysis over different landscapes. The distinction between the two formats did not show any significantly

different behaviour. Because the $1/-1$ contains geographical information, one would need more geographical data to really investigate how the two formats differ.

Before the smaller regions were chosen, a full analysis was performed on the larger landscapes. The results in these initial tests showed similar behaviour. Our model fit the data very well - in fact, Figure 4.2 (a) is the plot of the original larger Botswana region. What we noticed in the first trial was that these odd effects (Botswana 2002, 2006, 2008, 2014) were not nearly as apparent. Moreover, the directional correlations were a lot smoother. As the spatial scale becomes smaller, the data is more susceptible to changes in the environment. It is unfortunately not yet clear what how exactly factors like vegetation growth rate, rain and temperature have on the model. In other words, it is not clear how we can relate the fitted variables in the functions 4.2.14 and 4.2.15 with real external variables. Thus, due to a lack of additional data, as of now, we cannot conclusively relate weather variables to our model variables.

However, we have successfully shown the following:

- For a given landscape the amplitude in our two point and three point functions directly correlate to the extent of burning. Since amplitudes behave as a sort of burning probability, it would be interesting to compare the fuel percentage within the landscape. This may enable us to define the percolation threshold using our model, whereby the critical value is given by some amplitude.

- With the tools of correlation function analysis, we have shown a stronger test for scale invariance. The test can scale up or down to any grid size. Using the implementation of our Mathematica code, we can perform the two point function within minutes. Although the variables do not demonstrate consistent behaviour throughout the year, with the average values, we can then perform simulations of a how a fire would propagate in a given year. With the acquisition of more data over diverse regions and different time-scales, the model can become more robust yielding greater predictive power.

From this initial analysis, simulations need to be created to to see how effectively our model can simulate realistic fire patterns by considering wind speed, topography, vegetation distribution, rain, temperature and other important factors. Recreating such real life fire scenarios that also exhibit self extinguishing behaviour would be a good test for our model. Performing this kind of analysis on bigger data sets, and comparing our future simulations with existing models will be the task of future work.

Bibliography

[1] A. Shomer. "A pedagogical explanation for the non-renormalizability of gravity". In: *arxiv* (2007). URL: https://arxiv.org/abs/0709.3555.

[2] Elias Kiritsis. *Introduction to superstring theory*. Vol. B9. Leuven notes in mathematical and theoretical physics. Leuven: Leuven U. Press, 1998. ISBN: 9789061868941. arXiv: hep-th/9709062 [hep-th]. URL: https://inspirehep.net/record/448134/files/arXiv:hep-th_9709062.pdf.

[3] David Tong. "String Theory". In: (2009). arXiv: 0908.0333 [hep-th].

[4] Joseph Polchinski. *Volume 1: An Introduction to the Bosonic String*. Cambridge University Press, 1998. ISBN: 9780511816079. URL: https://doi.org/10.1017/CBO9780511816079.

[5] B. Green, G.Shwartz, and E. Witten. *Superstring Theory: Volume 1*. Cambridge University Press, 1988. ISBN: 978-1107029118.

[6] Juan Martin Maldacena. "The Large N limit of superconformal field theories and supergravity". In: *Int. J. Theor. Phys.* 38 (1999). [Adv. Theor. Math. Phys.2,231(1998)], pp. 1113–1133. DOI: 10.1023/A:1026654312961,10.4310/ATMP.1998.v2.n2.a1. arXiv: hep-th/9711200 [hep-th].

[7] C. M. Hull and P. K. Townsend. "Unity of superstring dualities". In: *Nucl. Phys.* B438 (1995). [,236(1994)], pp. 109–137. DOI: 10.1016/0550-3213(94)00559-W. arXiv: hep-th/9410167 [hep-th].

[8] Edward Witten. "String theory dynamics in various dimensions". In: *Nucl. Phys.* B443 (1995). [,333(1995)], pp. 85–126. DOI: 10.1016/0550-3213(95)00158-O. arXiv: hep-th/9503124 [hep-th].

[9] D. Tong. *String Theory University of Cambridge Part III Mathematical Tripos*. URL: http://www.damtp.cam.ac.uk/user/tong/string/string.pdf.

[10] P. Schwarz. *The Official String Theory Website*. URL: http://superstringtheory.com/index.html.

[11] W. Siegel. *Introduction to String Field Theory*. URL: http://insti.physics.sunysb.edu/~siegel/sft.pdf.

[12] P. Candelas et al. "Vacuum configurations for superstrings". In: *Nuclear Physics B* 258 (1985), pp. 46–74. ISSN: 0550-3213. DOI: https://doi.org/10.1016/0550-3213(85)90602-9. URL: http://www.sciencedirect.com/science/article/pii/0550321385906029.

[13] Wafic A Sabra and Owen Vaughan. "10D to 4D Euclidean supergravity over a Calabi-Yau three-fold". In: *Classical and Quantum Gravity* 33.1 (2016), p. 015010. URL: http://stacks.iop.org/0264-9381/33/i=1/a=015010.

[14] R.C. Rothermal. "A Mathematical Model for Prediction Fire Spreading in Wildland Fuels". In: (May 1927). URL: https://www.fs.fed.us/rm/pubs_int/int_rp115.pdf.

[15] S. Hantson, S. Pueyo, and E. Chuvieco. "Global fire size distribution: From power law to log-normal". In: 25 (Apr. 2016), pp. 403–412.

[16] Georges Aad et al. "Observation of a new particle in the search for the Standard Model Higgs boson with the ATLAS detector at the LHC". In: *Phys. Lett.* B716 (2012), pp. 1–29. DOI: 10.1016/j.physletb.2012.08.020. arXiv: 1207.7214 [hep-ex].

[17] M. Brak. *The Hierarchy Problem in the Standard Model and Little Higgs Theories*. URL: https://www.nikhef.nl/pub/theory/masters-theses/maarten_brak.pdf.

[18] P. J. Mohr, B. N. Taylor, and D. B. Newell. "CODATA recommended values of the fundamental physical constants: 2010". In: *Reviews of Modern Physics* 84 (Oct. 2012), pp. 1527–1605. DOI: 10.1103/RevModPhys.84.1527. arXiv: 1203.5425 [physics.atom-ph].

[19] S. Dickson. *Redubble*. URL: https://www.redbubble.com/people/mathartspd/portfolio?ref=carousel_portfolio.

[20] U. A. Whitcher C. F. Doran. *From Polygons to String Theory*. URL: https://www.math.hmc.edu/~ursula/notes/reflexivepolytopesarticle.pdf.

[21] V. Bouchard. "Lectures on complex geometry, Calabi-Yau manifolds and toric geometry". In: *arxiv* (2007). URL: https://arxiv.org/abs/hep-th/0702063.

[22] T Hübsch. "Calabi-Yau Manifolds: A Bestiary for Physicists". In: World Scientific, 1992.

[23] F. Brickell and R.S Clark. "Differentiable Manifolds". In: Van Nostrand Reinhold Company London, 1970.

[24] C. Koppensteiner. *Complex Manifolds*. URL: http://caramdir.at/uploads/math/piii-cm/complex-manifolds.pdf.

[25] S. Katz D. A. Cox. "Mirror Symmetry and Algebraic Geometry - Mathematical Surveys and Monographs". In: American Mathematical Society, 1999.

[26] C. Magyar and U. Whitcher. "Strong arithmetic mirror symmetry and toric isogenies". In: *ArXiv e-prints* (Oct. 2016). arXiv: 1610.01011 [math.AG].

[27] P. Dimitrov. *Polynomials and Polytopes*. URL: http://www.cim.mcgill.ca/~pdimit/polyeq-convexpoly.pdf.

[28] NASA/WMAP Science Team. *Universe 101*. URL: https://map.gsfc.nasa.gov/universe/uni_matter.html.

[29] E. L. Wright. *Ned Wright's Cosmology Tutorial*. URL: http://www.astro.ucla.edu/~wright/density.html.

[30] A. H. Guth. "Inflationary universe: A possible solution to the horizon and flatness problems". In: *Physical Review D* 347.23 (1981). URL: https://doi.org/10.1103/PhysRevD.23.347.

[31] J. Martens. "Group Compactifications and Moduli Spaces". In: *ArXiv e-prints* (June 2017). arXiv: 1706.00934 [math.AG].

[32] P. Gallardo, J. Martinez-Garcia, and Z. Zhang. "Compactifications of the moduli space of plane quartics and two lines". In: *ArXiv e-prints* (Aug. 2017). arXiv: 1708.08420 [math.AG].

[33] Cumrun Vafa. "Lectures on strings and dualities". In: *High energy physics and cosmology. Proceedings, Summer School, Trieste, Italy, June 10-July 26, 1996*. 1997, pp. 66–119. arXiv: hep-th/9702201 [hep-th].

[34] L. E. Ibáñez and A. M. Uranga. *String Theory and Particle Physics*. Cambridge University Press, 2012. ISBN: 0521517524.

[35] Thomas C. Bachlechner et al. "Supersymmetric Vacua in Random Supergravity". In: *JHEP* 01 (2013), p. 136. DOI: 10.1007/JHEP01(2013)136. arXiv: 1207.2763 [hep-th].

[36] I-Sheng Yang. "Probability of Slowroll Inflation in the Multiverse". In: *Phys. Rev.* D86 (2012), p. 103537. DOI: 10.1103/PhysRevD.86.103537. arXiv: 1208.3821 [hep-th].

[37] J. Martin, C. Ringeval, and V. Vennin. "Encyclopaedia Inflationaris". In: *arxiv* (2013). URL: https://arxiv.org/abs/1303.3787.

[38] J. Frazer and A. R. Liddle. "Multi-field inflation with random potentials: field dimension, feature scale and non-Gaussianity". In: *Journal of Cosmology and Astroparticle Physics* 2012.02 (2012), p. 039. URL: http://stacks.iop.org/1475-7516/2012/i=02/a=039.

[39] R. Easther et al. "Simple Predictions from Multifield Inflationary Models". In: *Phys. Rev. Lett.* 112 (16 2014), p. 161302. DOI: 10.1103/PhysRevLett.112.161302. URL: https://link.aps.org/doi/10.1103/PhysRevLett.112.161302.

[40] J. Frazer. "Predictions in multifield models of inflation". In: *arxiv* (2013). URL: https://arxiv.org/abs/1303.3611.

[41] R. Easther and L. C. Price. "Initial conditions and sampling for multifield inflation". In: *Journal of Cosmology and Astroparticle Physics* 2013.07 (2013), p. 027. URL: http://stacks.iop.org/1475-7516/2013/i=07/a=027.

[42] "Generating functionals for quantum field theories with random potentials". In: *Journal of High Energy Physics* 2016.01 (Jan. 2016), p. 107. URL: https://doi.org/10.1007/JHEP01(2016)107.

[43] M. Tegmark. "What does inflation really predict?" In: *Journal of Cosmology and Astroparticle Physics* 2005.04 (2005), p. 001. URL: http://stacks.iop.org/1475-7516/2005/i=04/a=001.

[44] A. Edelman. *Random Matrix Theory*. URL: https://web.eecs.umich.edu/~rajnrao/Acta05rmt.pdf.

[45] M. L. Mehta. "Random Matrices". In: Elsevier, 2004.

[46] A. Aazami and R. Easther. "Cosmology from random multifield potentials". In: *Journal of Cosmology and Astroparticle Physics* 2006.03 (2006), p. 013. URL: http://stacks.iop.org/1475-7516/2006/i=03/a=013.

[47] D. Marsh, L. McAllister, and T. Wrase. "The wasteland of random supergravities". In: *Journal of High Energy Physics* (2012). URL: https://doi.org/10.1007/JHEP03(2012)102.

[48] D. Battefeld, T. Battefeld, and S. Schulz. "On the unlikeliness of multi-field inflation: bounded random potentials and our vacuum". In: *Journal of Cosmology and Astroparticle Physics* 2012.06 (2012), p. 034. URL: http://stacks.iop.org/1475-7516/2012/i=06/a=034.

[49] L. McAllister et al. "Charting an Inflationary Landscape with Random Matrix Theory". In: *Journal of Cosmology and Astroparticle Physics* 2013.11 (2013), p. 040. URL: http://stacks.iop.org/1475-7516/2013/i=11/a=040.

[50] J. Frazer and A. R. Liddle. "Exploring a string-like landscape". In: *Journal of Cosmology and Astroparticle Physics* 2011.02 (2011), p. 026. URL: http://stacks.iop.org/1475-7516/2011/i=02/a=026.

[51] Yu Nakayama. "Scale invariance vs conformal invariance". In: *Phys. Rept.* 569 (2015), pp. 1–93. DOI: 10.1016/j.physrep.2014.12.003. arXiv: 1302.0884 [hep-th].

[52] Joshua D. Qualls. "Lectures on Conformal Field Theory". In: (2015). arXiv: 1511.04074 [hep-th].

[53] Matthias R. Gaberdiel. "An Introduction to conformal field theory". In: *Rept. Prog. Phys.* 63 (2000), pp. 607–667. DOI: 10.1088/0034-4885/63/4/203. arXiv: hep-th/9910156 [hep-th].

[54] Harry H. Denman. "Invariance and Conservation Laws in Classical Mechanics. II". In: *Journal of Mathematical Physics* 7.11 (1966), pp. 1910–1915. DOI: 10.1063/1.1704843. eprint: https://doi.org/10.1063/1.1704843. URL: https://doi.org/10.1063/1.1704843.

[55] Daniel K. Brattan, Omrie Ovdat, and Eric Akkermans. "On the landscape of scale invariance in quantum mechanics". In: (2018). arXiv: 1804.10213 [hep-th].

[56] P. Candelas et al. "Vacuum configurations for superstrings". In: *Nuclear Physics B* 258 (1985), pp. 46 –74. ISSN: 0550-3213. DOI: https://doi.org/10.1016/0550-3213(85)90602-9. URL: http://www.sciencedirect.com/science/article/pii/0550321385906029.

[57] P. Candelas et al. "Complete intersection Calabi-Yau manifolds". In: *Nuclear Physics B* 298.3 (1988), pp. 493 –525. ISSN: 0550-3213. DOI: https://doi.org/10.1016/0550-3213(88)90352-5. URL: http://www.sciencedirect.com/science/article/pii/0550321388903525.

[58] P. Candelas, C.A. Lütken, and R. Schimmrigk. "Complete intersection Calabi-Yau manifolds (II).: Three generation manifolds". In: *Nuclear Physics B* 306.1 (1988), pp. 113 –136. ISSN: 0550-3213. DOI: https://doi.org/10.1016/0550-3213(88)90173-3. URL: http://www.sciencedirect.com/science/article/pii/0550321388901733.

[59] M. Gagnon and Q. Ho-Kim. "An Exhaustive list of complete intersection Calabi-Yau manifolds". In: *Mod. Phys. Lett.* A9 (1994), pp. 2235–2243. DOI: 10.1142/S0217732394002094.

[60] N. Hitchin. "Generalized Calabi-Yau manifolds". In: *ArXiv Mathematics e-prints* (Sept. 2002). eprint: math/0209099.

[61] Michael R. Douglas. "The statistics of string/M theory vacua". In: *Journal of High Energy Physics* 2003.05 (2003), p. 046. URL: http://stacks.iop.org/1126-6708/2003/i=05/a=046.

[62] P. Candelas, M. Lynker, and R. Schimmrigk. "Calabi-Yau Manifolds in Weighted P(4)". In: *Nucl. Phys.* B341 (1990), pp. 383–402. DOI: 10.1016/0550-3213(90)90185-G.

[63] Victor V. Batyrev and Lev A. Borisov. "On Calabi-Yau complete intersections in toric varieties". In: (1994). arXiv: alg-geom/9412017 [alg-geom].

[64] A.C. Avram et al. "The web of Calabi-Yau hypersurfaces in toric varieties". In: *Nuclear Physics B* 505.3 (1997), pp. 625 –640. ISSN: 0550-3213. DOI: https://doi.org/10.1016/S0550-3213(97)00582-8. URL: http://www.sciencedirect.com/science/article/pii/S0550321397005828.

[65] Maximilian Kreuzer and Harald Skarke. "Reflexive polyhedra, weights and toric Calabi-Yau fibrations". In: *Rev. Math. Phys.* 14 (2002), pp. 343–374. DOI: 10.1142/S0129055X0200120X. arXiv: math/0001106 [math-ag].

[66] Ross Altman et al. "A Calabi-Yau Database: Threefolds Constructed from the Kreuzer-Skarke List". In: *JHEP* 02 (2015), p. 158. DOI: 10.1007/JHEP02(2015)158. arXiv: 1411.1418 [hep-th].

[67] James Gray, Alexander Haupt, and Andre Lukas. "Calabi-Yau Fourfolds in Products of Projective Space". In: (June 2013).

[68] Maximilian Kreuzer and Harald Skarke. "Calabi-Yau 4-folds and toric fibrations". In: *Journal of Geometry and Physics* 26.3 (1998), pp. 272 –290. ISSN: 0393-0440. DOI: https://doi.org/10.1016/S0393-0440(97)00059-4. URL: http://www.sciencedirect.com/science/article/pii/S0393044097000594.

[69] Lara B. Anderson et al. "A new construction of Calabi–Yau manifolds: Generalized CICYs". In: *Nucl. Phys.* B906 (2016), pp. 441–496. DOI: 10.1016/j.nuclphysb.2016.03.016. arXiv: 1507.03235 [hep-th].

[70] Rhys Davies. "The Expanding Zoo of Calabi-Yau Threefolds". In: *Adv. High Energy Phys.* 2011 (2011), p. 901898. DOI: 10.1155/2011/901898. arXiv: 1103.3156 [hep-th].

[71] Philip Candelas and Rhys Davies. "New Calabi-Yau Manifolds with Small Hodge Numbers". In: *Fortsch. Phys.* 58 (2010), pp. 383–466. DOI: 10.1002/prop.200900105. arXiv: 0809.4681 [hep-th].

[72] Yang-Hui He. "Calabi-Yau Geometries: Algorithms, Databases, and Physics". In: *Int. J. Mod. Phys.* A28 (2013), p. 1330032. DOI: 10.1142/S0217751X13300329. arXiv: 1308.0186 [hep-th].

[73] M. Kreuzer and H. Skarke. "On the Classification of Reflexive Polyhedra". In: *Communications in Mathematical Physics* 185.2 (1997), pp. 495–508. ISSN: 1432-0916. DOI: 10.1007/s002200050100. URL: https://doi.org/10.1007/s002200050100.

[74] Maximilian Kreuzer and Harald Skarke. "Classification of reflexive polyhedra in three-dimensions". In: *Adv. Theor. Math. Phys.* 2 (1998), pp. 853–871. DOI: 10.4310/ATMP.1998.v2.n4.a5. arXiv: hep-th/9805190 [hep-th].

[75] Maximilian Kreuzer and Harald Skarke. "Complete classification of reflexive polyhedra in four-dimensions". In: *Adv. Theor. Math. Phys.* 4 (2002), pp. 1209–1230. DOI: 10.4310/ATMP.2000.v4.n6.a2. arXiv: hep-th/0002240 [hep-th].

[76] Washington Taylor. "On the Hodge structure of elliptically fibered Calabi-Yau threefolds". In: *JHEP* 08 (2012), p. 032. DOI: 10.1007/JHEP08(2012)032. arXiv: 1205.0952 [hep-th].

[77] Washington Taylor and Yi-Nan Wang. "A Monte Carlo exploration of threefold base geometries for 4d F-theory vacua". In: *JHEP* 01 (2016), p. 137. DOI: 10.1007/JHEP01(2016)137. arXiv: 1510.04978 [hep-th].

[78] Xin Gao and Pramod Shukla. "On Classifying the Divisor Involutions in Calabi-Yau Threefolds". In: *JHEP* 11 (2013), p. 170. DOI: 10.1007/JHEP11(2013)170. arXiv: 1307.1139 [hep-th].

[79] Ralph Blumenhagen, Benjamin Jurke, and Thorsten Rahn. "Computational Tools for Cohomology of Toric Varieties". In: *Adv. High Energy Phys.* 2011 (2011), p. 152749. DOI: 10.1155/2011/152749. arXiv: 1104.1187 [hep-th].

[80] James Gray et al. "Calabi-Yau Manifolds with Large Volume Vacua". In: *Phys. Rev.* D86 (2012), p. 101901. DOI: 10.1103/PhysRevD.86.101901. arXiv: 1207.5801 [hep-th].

[81] Philip Candelas, Andrei Constantin, and Harald Skarke. "An Abundance of K3 Fibrations from Polyhedra with Interchangeable Parts". In: *Commun. Math. Phys.* 324 (2013), pp. 937–959. DOI: 10.1007/s00220-013-1802-2. arXiv: 1207.4792 [hep-th].

[82] Volker Braun. "On Free Quotients of Complete Intersection Calabi-Yau Manifolds". In: *JHEP* 04 (2011), p. 005. DOI: 10.1007/JHEP04(2011)005. arXiv: 1003.3235 [hep-th].

[83] Philip Candelas et al. "Triadophilia: A Special Corner in the Landscape". In: *Adv. Theor. Math. Phys.* 12.2 (2008), pp. 429–473. DOI: 10.4310/ATMP.2008.v12.n2.a6. arXiv: 0706.3134 [hep-th].

[84] Maximilian Kreuzer and Harald Skarke. "PALP: A Package for analyzing lattice polytopes with applications to toric geometry". In: *Comput. Phys. Commun.* 157 (2004), pp. 87–106. DOI: 10.1016/S0010-4655(03)00491-0. arXiv: math/0204356 [math.NA].

[85] Andreas P. Braun et al. "PALP - a User Manual". In: *Strings, gauge fields, and the geometry behind: The legacy of Maximilian Kreuzer*. Ed. by Anton Rebhan et al. 2012, pp. 461–550. DOI: 10.1142/9789814412551_0024. arXiv: 1205.4147 [math.AG]. URL: https://inspirehep.net/record/1115315/files/arXiv:1205.4147.pdf.

[86] N.J.A Sloane. *The On-Line Encyclopedia of Integer Sequences - Number A090045*. URL: http://oeis.org.

[87] Yang-Hui He, Seung-Joo Lee, and Andre Lukas. "Heterotic Models from Vector Bundles on Toric Calabi-Yau Manifolds". In: *JHEP* 05 (2010), p. 071. DOI: 10.1007/JHEP05(2010)071. arXiv: 0911.0865 [hep-th].

[88] Victor V. Batyrev. "Dual polyhedra and mirror symmetry for Calabi-Yau hypersurfaces in toric varieties". In: *J. Alg. Geom.* 3 (1994), pp. 493–545. arXiv: alg-geom/9310003 [alg-geom].

[89] DH Stamatis. "Six Sigma and Beyond: Statistics and Probability Vol 3". In: CRC Press, 2002.

[90] Philip Candelas, Andrei Constantin, and Challenger Mishra. "Calabi-Yau Threefolds With Small Hodge Numbers". In: (2016). arXiv: 1602.06303 [hep-th].

[91] Samuel B. Johnson and Washington Taylor. "Calabi-Yau threefolds with large $h^{2,1}$". In: *JHEP* 10 (2014), p. 23. DOI: 10.1007/JHEP10(2014)023. arXiv: 1406.0514 [hep-th].

[92] Volker Braun. "Toric Elliptic Fibrations and F-Theory Compactifications". In: *JHEP* 01 (2013), p. 016. DOI: 10.1007/JHEP01(2013)016. arXiv: 1110.4883 [hep-th].

[93] Washington Taylor and Yi-Nan Wang. "Non-toric bases for elliptic Calabi–Yau threefolds and 6D F-theory vacua". In: *Adv. Theor. Math. Phys.* 21 (2017), pp. 1063–1114. DOI: 10.4310/ATMP.2017.v21.n4.a6. arXiv: 1504.07689 [hep-th].

[94] Lara B. Anderson et al. "Multiple Fibrations in Calabi-Yau Geometry and String Dualities". In: *JHEP* 10 (2016), p. 105. DOI: 10.1007/JHEP10(2016)105. arXiv: 1608.07555 [hep-th].

[95] Monika Lynker, Rolf Schimmrigk, and Andreas Wisskirchen. "Landau-Ginzburg vacua of string, M theory and F theory at c = 12". In: *Nucl. Phys.* B550 (1999), pp. 123–150. DOI: 10.1016/S0550-3213(99)00204-7. arXiv: hep-th/9812195 [hep-th].

[96] Lara B. Anderson, Yang-Hui He, and Andre Lukas. "Heterotic Compactification, An Algorithmic Approach". In: *JHEP* 07 (2007), p. 049. DOI: 10.1088/1126-6708/2007/07/049. arXiv: hep-th/0702210 [HEP-TH].

[97] Maxime Gabella, Yang-Hui He, and Andre Lukas. "An Abundance of Heterotic Vacua". In: *JHEP* 12 (2008), p. 027. DOI: 10.1088/1126-6708/2008/12/027. arXiv: 0808.2142 [hep-th].

[98] Peng Gao, Yang-Hui He, and Shing-Tung Yau. "Extremal Bundles on Calabi–Yau Threefolds". In: *Commun. Math. Phys.* 336.3 (2015), pp. 1167–1200. DOI: 10.1007/s00220-014-2271-y. arXiv: 1403.1268 [hep-th].

[99] Lara B. Anderson et al. "Heterotic Line Bundle Standard Models". In: *JHEP* 06 (2012), p. 113. DOI: 10.1007/JHEP06(2012)113. arXiv: 1202.1757 [hep-th].

[100] Alexei A. Starobinsky. "A New Type of Isotropic Cosmological Models Without Singularity". In: *Phys. Lett.* 91B (1980), pp. 99–102. DOI: 10.1016/0370-2693(80)90670-X.

[101] A.D.Linde. "A new inflationary universe scenario: A possible solution of the horizon, flatness, homogeneity, isotropy and primordial monopole problems". In: *Physics Letters B* 108.6 (1982), pp. 389–393. URL: https://doi.org/10.1016/0370-2693(82)91219-9.

[102] A. Albrecht and P. J. Steinhardt. "Cosmology for Grand Unified Theories with Radiatively Induced Symmetry Breaking". In: *Physical Review Letters* 1220.48 (1982). URL: https://doi.org/10.1103/PhysRevLett.48.1220.

[103] David H. Lyth and Antonio Riotto. "Particle physics models of inflation and the cosmological density perturbation". In: *Phys. Rept.* 314 (1999), pp. 1–146. DOI: 10.1016/S0370-1573(98)00128-8. arXiv: hep-ph/9807278 [hep-ph].

[104] Volker Braun et al. "A Heterotic standard model". In: *Phys. Lett.* B618 (2005), pp. 252–258. DOI: 10.1016/j.physletb.2005.05.007. arXiv: hep-th/0501070 [hep-th].

[105] Volker Braun et al. "The Exact MSSM spectrum from string theory". In: *JHEP* 05 (2006), p. 043. DOI: 10.1088/1126-6708/2006/05/043. arXiv: hep-th/0512177 [hep-th].

[106] Vincent Bouchard and Ron Donagi. "An SU(5) heterotic standard model". In: *Phys. Lett.* B633 (2006), pp. 783–791. DOI: 10.1016/j.physletb.2005.12.042. arXiv: hep-th/0512149 [hep-th].

[107] L. B. Anderson et al. "Two Hundred Heterotic Standard Models on Smooth Calabi-Yau Threefolds". In: *Phys. Rev.* D84 (2011), p. 106005. DOI: 10.1103/PhysRevD.84.106005. arXiv: 1106.4804 [hep-th].

[108] Stuart Raby. "Searching for the Standard Model in the String Landscape: SUSY GUTs". In: *Rept. Prog. Phys.* 74 (2011), p. 036901. DOI: 10.1088/0034-4885/74/3/036901. arXiv: 1101.2457 [hep-ph].

[109] P. Athanasopoulos, A. E. Faraggi, and V. M. Mehta. "Light Z in heterotic string standardlike models". In: *Phys. Rev.* D89.10 (2014), p. 105023. DOI: 10.1103/PhysRevD.89.105023. arXiv: 1401.7153 [hep-th].

[110] T. Dereli and Robin W. Tucker. "String fields and the standard model". In: *Phys. Rev. Lett.* 82 (1999), pp. 4184–4187. DOI: 10.1103/PhysRevLett.82.4184. arXiv: hep-th/9808059 [hep-th].

[111] Dieter Lust. "String Landscape and the Standard Model of Particle Physics". In: *Recent developments in theoretical and experimental general relativity, gravitation and relativistic field theories. Proceedings, 11th Marcel Grossmann Meeting, MG11, Berlin, Germany, July 23-29, 2006. Pt. A-C.* 2007, pp. 148–176. DOI: 10.1142/9789812834300_0009. arXiv: 0707.2305 [hep-th]. URL: https://inspirehep.net/record/755895/files/arXiv:0707.2305.pdf.

[112] Evgeny I. Buchbinder, Andrei Constantin, and Andre Lukas. "A heterotic standard model with $B-L$ symmetry and a stable proton". In: *JHEP* 06 (2014), p. 100. DOI: 10.1007/JHEP06(2014)100. arXiv: 1404.2767 [hep-th].

[113] Lara B. Anderson et al. "A Comprehensive Scan for Heterotic SU(5) GUT models". In: *JHEP* 01 (2014), p. 047. DOI: 10.1007/JHEP01(2014)047. arXiv: 1307.4787 [hep-th].

[114] R. Altman. *Toric Calabi-Yau Database*. URL: http://www.rossealtman.com/.

[115] Shamit Kachru et al. "De Sitter vacua in string theory". In: *Phys. Rev.* D68 (2003), p. 046005. DOI: 10.1103/PhysRevD.68.046005. arXiv: hep-th/0301240 [hep-th].

[116] Michele Cicoli, Joseph P. Conlon, and Fernando Quevedo. "General Analysis of LARGE Volume Scenarios with String Loop Moduli Stabilisation". In: *JHEP* 10 (2008), p. 105. DOI: 10.1088/1126-6708/2008/10/105. arXiv: 0805.1029 [hep-th].

[117] Ross Altman et al. "New Large Volume Solutions". In: (2017). arXiv: 1706.09070 [hep-th].

[118] Gerard 't Hooft. "Naturalness, chiral symmetry, and spontaneous chiral symmetry breaking". In: *NATO Sci. Ser. B* 59 (1980), pp. 135–157. DOI: 10.1007/978-1-4684-7571-5_9.

[119] Yang-Hui He, Vishnu Jejjala, and Luca Pontiggia. "Patterns in Calabi–Yau Distributions". In: *Commun. Math. Phys.* 354.2 (2017), pp. 477–524. DOI: 10.1007/s00220-017-2907-9. arXiv: 1512.01579 [hep-th].

[120] Mariana Grana. "Flux compactifications in string theory: A Comprehensive review". In: *Phys. Rept.* 423 (2006), pp. 91–158. DOI: 10.1016/j.physrep.2005.10.008. arXiv: hep-th/0509003 [hep-th].

[121] Michael R. Douglas and Shamit Kachru. "Flux compactification". In: *Rev. Mod. Phys.* 79 (2007), pp. 733–796. DOI: 10.1103/RevModPhys.79.733. arXiv: hep-th/0610102 [hep-th].

[122] Iosif Bena et al. "Giant Tachyons in the Landscape". In: *JHEP* 02 (2015), p. 146. DOI: 10.1007/JHEP02(2015)146. arXiv: 1410.7776 [hep-th].

[123] Hirosi Ooguri and Cumrun Vafa. "Non-supersymmetric AdS and the Swampland". In: (2016). arXiv: 1610.01533 [hep-th].

[124] Ben Freivogel and Matthew Kleban. "Vacua Morghulis". In: (2016). arXiv: 1610.04564 [hep-th].

[125] Hinshaw G. et al. "Nine-year Wilkinson Microwave Anisotropy Probe (WMAP) Observations: Cosmological Parameter Results". In: *apjs* 208, 19 (Oct. 2013), p. 19. DOI: 10.1088/0067-0049/208/2/19. arXiv: 1212.5226.

[126] P. A. R. Ade et al. "Planck 2015 results. XIII. Cosmological parameters". In: *Astron. Astrophys.* 594 (2016), A13. DOI: 10.1051/0004-6361/201525830. arXiv: 1502.01589 [astro-ph.CO].

[127] P. A. R. Ade et al. "Planck 2015 results. XX. Constraints on inflation". In: *Astron. Astrophys.* 594 (2016), A20. DOI: 10.1051/0004-6361/201525898. arXiv: 1502.02114 [astro-ph.CO].

[128] A. Linde. "Hybrid inflation". In: *Phys. Rev. D* 49 (2 1994), pp. 748–754. DOI: 10.1103/PhysRevD.49.748. URL: https://link.aps.org/doi/10.1103/PhysRevD.49.748.

[129] Daniel Baumann and Liam McAllister. *Inflation and String Theory*. Cambridge University Press, 2015. ISBN: 9781107089693, 9781316237182. arXiv: 1404.2601 [hep-th]. URL: https://inspirehep.net/record/1289899/files/arXiv:1404.2601.pdf.

[130] Frederik Denef and Michael R. Douglas. "Distributions of flux vacua". In: *JHEP* 05 (2004), p. 072. DOI: 10.1088/1126-6708/2004/05/072. arXiv: hep-th/0404116 [hep-th].

[131] Michael R. Douglas. "Basic results in vacuum statistics". In: *Comptes Rendus Physique* 5 (2004), pp. 965–977. DOI: 10.1016/j.crhy.2004.09.008. arXiv: hep-th/0409207 [hep-th].

[132] Frederik Denef and Michael R. Douglas. "Distributions of nonsupersymmetric flux vacua". In: *JHEP* 03 (2005), p. 061. DOI: 10.1088/1126-6708/2005/03/061. arXiv: hep-th/0411183 [hep-th].

[133] Richard Easther and Liam McAllister. "Random matrices and the spectrum of N-flation". In: *JCAP* 0605 (2006), p. 018. DOI: 10.1088/1475-7516/2006/05/018. arXiv: hep-th/0512102 [hep-th].

[134] A. J. Bray and D. S. Dean. "Statistics of Critical Points of Gaussian Fields on Large-Dimensional Spaces". In: *Physical Review Letters* 98.15, 150201 (Apr. 2007), p. 150201. DOI: 10.1103/PhysRevLett.98.150201. eprint: cond-mat/0611023.

[135] T. Battefeld. *Random Potentials in Cosmology*. URL: https://indico.cern.ch/event/438475/session/2/contribution/118/attachments/1152245/1654653/DE_Thursday_Battefeld_0178_f4e087509ceb83bcef6edcf3c7bc29f4332855ac.pdf.

[136] Francisco G. Pedro and Alexander Westphal. "The Scale of Inflation in the Landscape". In: *Phys. Lett.* B739 (2014), pp. 439–444. DOI: 10.1016/j.physletb.2014.10.022. arXiv: 1303.3224 [hep-th].

[137] Gaoyuan Wang and Thorsten Battefeld. "Vacuum Selection on Axionic Landscapes". In: *JCAP* 1604.04 (2016), p. 025. DOI: 10.1088/1475-7516/2016/04/025. arXiv: 1512.04224 [hep-th].

[138] Ali Masoumi and Alexander Vilenkin. "Vacuum statistics and stability in axionic landscapes". In: *JCAP* 1603.03 (2016), p. 054. DOI: 10.1088/1475-7516/2016/03/054. arXiv: 1601.01662 [gr-qc].

[139] Francisco G. Pedro and Alexander Westphal. "Inflation with a graceful exit in a random landscape". In: *JHEP* 03 (2017), p. 163. DOI: 10.1007/JHEP03(2017)163. arXiv: 1611.07059 [hep-th].

[140] Brian Greene et al. "Tumbling through a landscape: Evidence of instabilities in high-dimensional moduli spaces". In: *Phys. Rev.* D88.2 (2013), p. 026005. DOI: 10.1103/PhysRevD.88.026005. arXiv: 1303.4428 [hep-th].

[141] Michael Dine and Sonia Paban. "Tunneling in Theories with Many Fields". In: *JHEP* 10 (2015), p. 088. DOI: 10.1007/JHEP10(2015)088. arXiv: 1506.06428 [hep-th].

[142] Michael Dine. "Classical and Quantum Stability in Putative Landscapes". In: *JHEP* 01 (2017), p. 082. DOI: 10.1007/JHEP01(2017)082. arXiv: 1512.08125 [hep-th].

[143] Ali Masoumi, Alexander Vilenkin, and Masaki Yamada. "Inflation in random Gaussian landscapes". In: *JCAP* 1705.05 (2017), p. 053. DOI: 10.1088/1475-7516/2017/05/053. arXiv: 1612.03960 [hep-th].

[144] Richard Easther, Alan H. Guth, and Ali Masoumi. "Counting Vacua in Random Landscapes". In: (2016). arXiv: 1612.05224 [hep-th].

[145] Andrei Linde. "Random Potentials and Cosmological Attractors". In: *JCAP* 1702.02 (2017), p. 028. DOI: 10.1088/1475-7516/2017/02/028. arXiv: 1612.04505 [hep-th].

[146] Ali Masoumi, Alexander Vilenkin, and Masaki Yamada. "Initial conditions for slow-roll inflation in a random Gaussian landscape". In: *JCAP* 1707.07 (2017), p. 003. DOI: 10.1088/1475-7516/2017/07/003. arXiv: 1704.06994 [hep-th].

[147] Yang-Hui He et al. "Exploring the Potential Energy Landscape Over a Large Parameter-Space". In: *JHEP* 07 (2013), p. 050. DOI: 10.1007/JHEP07(2013)050. arXiv: 1301.0946 [hep-th].

[148] Mudit Jain and Vitaly Vanchurin. "Generating Functionals for Quantum Field Theories with Random Potentials". In: *JHEP* 01 (2016), p. 107. DOI: 10.1007/JHEP01(2016)107. arXiv: 1506.03840 [hep-th].

[149] I-Sheng Yang. "The Strong Multifield Slowroll Condition and Spiral Inflation". In: *Phys. Rev.* D85 (2012), p. 123532. DOI: 10.1103/PhysRevD.85.123532. arXiv: 1202.3388 [hep-th].

[150] Andrew R. Liddle, Anupam Mazumdar, and Franz E. Schunck. "Assisted inflation". In: *Phys. Rev.* D58 (1998), p. 061301. DOI: 10.1103/PhysRevD.58.061301. arXiv: astro-ph/9804177 [astro-ph].

[151] Evgeny I. Buchbinder, Ron Donagi, and Burt A. Ovrut. "Superpotentials for vector bundle moduli". In: *Nucl. Phys.* B653 (2003), pp. 400–420. DOI: 10.1016/S0550-3213(02)01093-3. arXiv: hep-th/0205190 [hep-th].

[152] James Gray et al. "STRINGVACUA: A Mathematica Package for Studying Vacuum Configurations in String Phenomenology". In: *Comput. Phys. Commun.* 180 (2009), pp. 107–119. DOI: 10.1016/j.cpc.2008.08.009. arXiv: 0801.1508 [hep-th].

[153] Joseph Cleveland et al. "Certified counting of roots of random univariate polynomials". In: (2014). arXiv: 1412.1717 [math.NA].

[154] Dhagash Mehta, Matthew Niemerg, and Chuang Sun. "Statistics of Stationary Points of Random Finite Polynomial Potentials". In: *J. Stat. Mech.* 1509.9 (2015), P09012. DOI: 10.1088/1742-5468/2015/09/P09012. arXiv: 1504.02786 [cond-mat.stat-mech].

[155] Tom Beer and I.G. Enting. "Fire spread and percolation modelling". In: *Mathematical and Computer Modelling* 13.11 (1990), pp. 77 –96. ISSN: 0895-7177. DOI: https://doi.org/10.1016/0895-7177(90)90065-U. URL: http://www.sciencedirect.com/science/article/pii/089571779090065U.

[156] G. Caldarelli et al. "Percolation in real wildfires". In: *EPL (Europhysics Letters)* 56.4 (2001), p. 510. URL: http://stacks.iop.org/0295-5075/56/i=4/a=510.

[157] T. Beer and I.G. Enting. "Fire spread and percolation modelling". In: *Mathematical and Computer Modelling* 13.11 (1990), pp. 77 –96. ISSN: 0895-7177. DOI: https://doi.org/10.1016/0895-7177(90)90065-U. URL: http://www.sciencedirect.com/science/article/pii/089571779090065U.

[158] I.P Sang and H. Tomohisa. *Forest fire modeling using cellular automata and percolation threshold analysis*. Aug. 2011.

[159] B.D Malamud, G.Morein, and D.L. Turcotte. "Forest Fires: An Example of Self-Organized Critical Behavior". In: *Science* 281 (5384 Jan. 1994), pp. 1840–1842. DOI: DOI:10.1126/science.281.5384.1840.

[160] S. Hantson, S. Pueyo, and E. Chuvieco. "Global fire size distribution is driven by human impact and climate". In: 24 (Jan. 2015), pp. 77–86.

[161] Jean-Francois Fortin, Benjamin Grinstein, and Andreas Stergiou. "Scale without Conformal Invariance: Theoretical Foundations". In: *JHEP* 07 (2012), p. 025. DOI: 10.1007/JHEP07(2012)025. arXiv: 1107.3840 [hep-th].

[162] Joseph Polchinski. "Polchinski, J.: Scale and conformal invariance in quantum field theory. Nucl. Phys. B. 303, 226". In: 303 (June 1988), pp. 226–236.

[163] P. Di Francesco, P. Mathieu, and D. Senechal. "Conformal Field Theory". In: Springer-Verlag, 1997.

[164] J. Polchinski. "Polchinski, J.: Scale and conformal invariance in quantum field theory. Nucl. Phys. B. 303, 226". In: 303 (June 1988), pp. 226–236.

[165] V. Riva and J. Cardy. "Scale and conformal invariance in field theory: A physical counterexample". In: 622 (May 2005).

[166] Google Maps. *Kazak small*. URL: https://drive.google.com/open?id=1rhWUv60jsEF5AY22k18z-detzIgH7WYH&usp=sharing.

[167] Google Maps. *Botswana small*. URL: https://drive.google.com/open?id=1FcfdtoFvsTr9HrA4vl4jjA_J8VPAIcOJ&usp=sharing.

[168] The World Bank Group. *Climate Change Knowledge Portal*. URL: http://sdwebx.worldbank.org/climateportal/index.cfm.